UNIVERSITÀ DEGLI STUDI FIRENZE

DIEF - Dipartimento di Ingegneria Industriale

PhD School: *Energetica e Tecnologie Industriali e Ambientali Innovative*

SCIENTIFIC AREA: ING-IND/09

IMPACTS OF GAS-TURBINE COMBUSTORS OUTLET FLOW ON THE AERO-THERMAL PERFORMANCE OF FILM-COOLED FIRST STAGE NOZZLES

PhD Candidate: ING. SIMONE CUBEDA

Tutor: PROF. ING. BRUNO FACCHINI

Academic Supervisor: DR. ING. LORENZO MAZZEI

Industrial Supervisor: DR. ING. LUCA INNOCENTI

PhD School Coordinator: PROF. ING. MAURIZIO DE LUCIA

PhD School Cycle: XXXII (2017-2019)

A mia moglie Elena e mio figlio Stefano

Ringraziamenti

Ringrazio innanzitutto il Prof. Bruno Facchini, Antonio Andreini e il mio manager Luca Innocenti, senza i quali questa esperienza di arricchimento tecnico e personale non avrebbe neanche potuto avere inizio. Ringrazio Lorenzo Mazzei che con immensa pazienza, professionalità ed amicizia è stato la fondamentale guida lungo questo percorso.

Non posso non ringraziare i miei colleghi Luca A., Gianluca, Francesco, Lorenzo, Alessio, Alberto, Roberto, Alessandro C., James, Alessandro D., Gabriele, Daniele e Simone i quali, oltre ad essere carissimi amici, mi hanno insegnato tantissimo in questi anni, trasferendo conoscenze e capacità tra lavoro in azienda e ricerca. Ugualmente prezioso è stato l'aiuto dei miei compagni in Università Tommaso B., Alessio, Lorenzo C. e Tommaso F..

Aggiungo i miei amici storici Silvio, Federico, Nicola, Alessandro, Sergio, Luca D., Luca M. e Alberto nonché i nuovi amici Luca B., Sabrina, la piccola Vittoria, Fulvio, Marina e il piccolo Tommaso, che in fondo sono la nostra famiglia fiorentina.

I ringraziamenti maggiori e la riconoscenza più grande vanno senza dubbio ai miei genitori Angelo e Carmela e mia sorella Valeria, i quali spero di rendere orgogliosi con i traguardi che loro hanno reso possibili. Saluto con affetto anche i miei suoceri Giancarlo e Sonia e mio cognato Andrea.

Non posso però non dedicare questo lavoro alla mia preziosa famiglia: mia moglie Elena e mio figlio Stefano, a cui ho rubato troppo del mio tempo ricevendo in cambio sostegno incondizionato e amore, che spero di ripagare con cura e dedizione da qui in avanti in misura ancora maggiore.

Infine intendo citare e ringraziare il consorzio FACTOR (progetto collaborativo cofinanziato dall'Unione Europea sotto la sovvenzione n° 265985 2010-2017) per il permesso di pubblicare i risultati qui riportati. Analoghi ringraziamenti vanno alla Regione Toscana (cofinanziatrice del progetto STech 2017-2019 nell'ambito del bando FAR-FAS 2014) e l'azienda Baker Hughes (coordinatrice di STech), grazie alle quali è stato possibile realizzare parte delle attività incluse in questa tesi.

Abstract

Modern aero-engine and industrial gas turbines typically employ lean-type combustors, which are capable of limiting pollutant emissions thanks to premixed flames, while sustaining high turbine inlet temperatures that increase the single-cycle thermal efficiency. In such technology gas-turbine first stage nozzles are characterised by a highly-swirled and temperature-distorted inlet flow field. However, due to several sources of uncertainty during the design phase, wide safety margins are commonly adopted, which can have a direct impact on the engine performance and efficiency.

Therefore, with the aim of increasing the knowledge on combustor-turbine interaction and improving standard design practices, two non-reactive test rigs were assembled at the University of Florence, Italy. The rigs, both accommodating three lean-premix swirlers within a combustion chamber and a first stage film-cooled nozzles cascade, were operated in similitude conditions to mimic an aero-engine and an industrial gas-turbine arrangements. The rigs were designed to reproduce the real engine periodic flow field on the central sector, allowing also to perform measurements far enough from the lateral walls. The periodicity condition was enforced by the installation of circular ducts at the injectors outlet section as to preserve the non-reactive swirling flow down to the nozzles inlet plane.

For the aero-engine simulator rig and as part of two previous PhD works, of which the present is a continuation, an extensive test campaign was conducted. The flow field within the combustion chamber was investigated via particle-image velocimetry (PIV) and the combustor-turbine interface section was experimentally characterised in terms of velocity, pressure and turbulence fields by means of a five-hole pressure plus thermocouple probe and hot-wire anemometers, mounted on an automatic traverse system. To study the evolution of the combustor outlet flow through the nozzles and its interaction with the film-cooling flow, such measurements have been also replicated slightly downstream of the airfoils' trailing edge. Lastly, the film-cooling adiabatic effectiveness distribution over the airfoils was evaluated via coolant concentration measurements based on pressure sensitive paints (PSP) application. As far as the industrial turbine rig is concerned, the same type of measurements were carried out except for PIV.

Within such experimental scenario, the core of the present work is related to numerical analyses. In fact, since the design of industrial high-pressure turbines historically relies on 1D, circumferentially-averaged profiles of pressure, velocity and temperature at the combustor/turbine interface in conjunction with Reynolds-averaged Navier-Stokes (RANS) models, this thesis describes how measurements can be leveraged to improve numerical modelling procedures. Within such context, hybrid scale resolving techniques, such as Scale-Adaptive Simulation (SAS), can suit the purpose, whilst containing computational costs, as also shown in the literature. Furthermore, the investigation of the two components within the same integrated simulation enables the transport of unsteady fluctuations from the combustor down to the first stage nozzles, which can make the difference in the presence of film cooling.

Contents

List of Figures

List of Tables

Nomenclature

Symbols

BFM	Back Flow Margin	$[-]$
BR	Blowing Ratio	$[-]$
c	Loss coefficient	$[-]$
C	Chord	$[m]$
C	Concentration	$[m]$
Ch	Chord	$[m]$
d	Wall distance	$[m]$
D	Diameter	$[m]$
D	Mass diffusivity	$[m^2/s]$
DR	Density Ratio	$[-]$
e	Internal energy	$[m^2/s^2]$
E	Energy	$[m^2/s^2]$
G	Momentum axial flux	$[kg/ms^3]$
h	Local height	$[m]$
H	Height	$[m]$
HTC	Heat Transfer Coefficient	$[W/m^2K]$
I	Momentum flux ratio	$[-]$
J	Diffusion term	$[Pa/s]$
k	Wavelength	$[m]$
k	Turbulent kinetic energy	$[m^2/s^2]$
l	Length Scale	$[m]$
L	Integral length Scale	$[m]$
Le	Lewis number	$[-]$

$LOTDF$	Lo
$LRTDF$	Lo
m	Ma
M	Blo
Ma	Ma
MR	Ma
$OTDF$	Ov
p	Pit
P	Pre
P	Pro
Pr	Pra
PR	Pre
q	En
r	Ra
R	Ra
Re	Re
$RTDF$	Ra
S	Me
S	Vo
Sc	Sch
Sn	Sw
t	Lo
t	Tir
T	Ter
Tu	Tu
TR	Ter
u	Vel
U	Av
v	Vel
V	Vel
VR	Vel
W	Mo
x	Ax

Greeks

α	Thermal diffusivity	$[m^2/s]$
δ	Kronecker symbol	$[-]$
Δ	Size	$[m]$
Δ	Difference	$[\cdot]$
ϵ	Dissipation rate	$[m^2/s^3]$
η	Effectiveness	$[-]$
η	Length scale	$[m]$
θ	Tangential angle	$[°]$
κ	Wave number	$[1/m]$
λ	Thermal conductivity	$[W/mK]$
μ	Molecular viscosity	$[m^2/s]$
ρ	Density	$[kg/m^3]$
τ	Shear stress	$[Pa]$
τ	Time	$[s]$
ϕ	Equivalence ratio	$[-]$
ϕ	Generic variable	$[\cdot]$
ϕ	Angle	$[°]$
Φ	Generic variable	$[\cdot]$
Ψ	Generic variable	$[\cdot]$
ω	Specific dissipation rate	$[1/s]$

Subscripts-Superscripts

$\bar{\cdot}$	Time-averaged quantity
$\tilde{\cdot}$	Favre-averaged quantity
$\hat{\cdot}$	Effective quantity
$\cdot'$	Fluctuating/unresolved quantity
$\cdot''$	Favre's fluctuating quantity
$\perp$	Perpendicular
0	Total quantity
30	Plane 30
40	Plane 40
41	Plane 41

ad	Adiabatic
air	Air
aw	Adiabatic wall
ax	Axial
c	Coolant
c	Cut-off
$cool$	Coolant
d	Dissipative
FC	Film cooling
fg	Foreign gas
g	Gas (main flow)
i	i-th item
in	Inlet
j	j-th item
k	k-th item
K	Kolmogorov
l	Length scale
L	Integral length scale
$main$	Main flow
$mean$	Mean value
mod	Modelled
n	Normal
nd	Non-dimensionalised
out	Outlet
p	Pressure
P	Pope
rad	Radial
ref	Reference
res	Resolved
rig	Rig
s	Static
sf	Secondary flows
sgs	SubGrid Scale
sw	Swirler
t	Total quantity

T
tan
tot
vK
x
w

Acronyms

$5HP$	Five Hole Probe
$ACARE$	Advisory Council for Aeronautics Research
CAD	Computer-Aided Drafting
CFD	Computational Fluid Dynamics
CFL	Courant-Friedrichs-Lewy
CMC	Ceramic Matrix Composite
CRZ	Corner Recirculation Zone
CS	Cold Streak
$CTRZ$	Central Toroidal Recirculation Zone
CVP	Counter-rotating Vortex Pair
$DACRS$	Dual Annular Counter Rotating axial Swirl
$DDES$	Delayed Detached Eddy Simulation
DES	Detached Eddy Simulation
DLE	Dry-Low Emission
DLN	Dry-Low NO_x
DLR	Deutsches zentrum fur Luft und Raumfahrt
DNS	Direct Numerical Simulation
DSM	Dynamic Smagorinsky Model
EEA	European Environment Agency
$ELBO$	Enhanced Lean Blow-Out
$EOTDF$	Enhanced Overall Temperature Distortion Factor
EU	European Union
$FACTOR$	Full Aerothermal Combustor-Turbine interactiOn Research
$FANS$	Favre Averaged Navier-Stokes
GE	General Electric

HPT	High Pressure Turbine
HWA	How Wire Anemometry
HS	Hot Streak
$ILPF$	Isentropic Light Piston Facility
IR	InfraRed
LE	Leading Edge
$LEAP$	Leading Edge Aviation Propulsion
LES	Large-Eddy Simulation
LPC	Lean Premixed Combustion
$LSRR$	Large Scale Rotating Rig
$LSTR$	Large Scale Turbine Rig
LTO	Landing-Take Off
NGV	Nozzle Guide Vane
NS	Navier-Stokes
OPR	Overall Pressure Ratio
$OTRF$	Oxford Turbine Research Facility
PA	Passage
$PANS$	Partially Averaged Navier-Stokes
$PITM$	Partially Integrated Transport Modelling
PIV	Particle Image Velocimetry
PSP	Pressure Sensitive Paint
PS	Pressure Side
PVC	Precessing Vortex Core
$RANS$	Reynolds Averaged Navier-Stokes
$RBDF$	Rotating Blow Down Facility
RMS	Root Mean Square
RSM	Reynolds Stress Model
RQL	Rich-burn quick-Quench Lean-burn
S-A	Spalart-Allmaras
SAS	Scale-Adaptive Simulation
$SBES$	Stress-Blended Eddy Simulation
SGS	SubGrid Scale
SM	Smagorinsky

SS	Suction Side
SST	Shear Stress Transport
$STech$	Smart Technologies
$TALON$	Technology for Advanced Low NO_x
$Taps$	Twin Annular Premix System
$TATEF$	Turbine Aero-Thermal External Flows
TBC	Thermal Barrier Coating
THT	Technologies for High Temperature
TIT	Turbine Inlet Temperature
TRF	Turbine Research Facility
uHC	Unburned Hydro-Carbon
ULN	Ultra Low NO_x
$uRANS$	Unsteady Reynolds Averaged Navier-Stokes
VB	Vortex Breakdown
$VLES$	Very Large-Eddy Simulation
$WALE$	Wall-Adpating Local Eddy viscosity
$WCTTF$	Warm Core Turbine Test Facility
WM	Wall Modelling

Chapter 1

Introduction

Contents

1.1 Development of modern gas turbines

The development of gas turbines for propulsion and industrial applications is being driven nowadays more and more by performance and efficiency targets, which are majorly dependent on overall pressure ratio and turbine inlet temperature, yet without neglecting other important aspects, such as durability, reliability and maintainability. Single cycle thermal efficiency is being approaching 50% for aero-engines and has overtaken 40% for industrial gas turbines, mainly through the progressive increase in Turbine Inlet Temperature (TIT) and, especially for aeronautic applications, Overall Pressure Ratio (OPR), as highlighted in Fig. 1.1 and 1.2.

Making reference to Fig. 1.1, it is evident how the TIT has far exceeded the melting point of hot gas path components materials. Notwithstanding the advances in material properties and the continuous improvements in manufacturing technologies, a more and more essential contribution is given by the development of innovative cooling techniques. This is also further hindered by the above mentioned increasing trend of

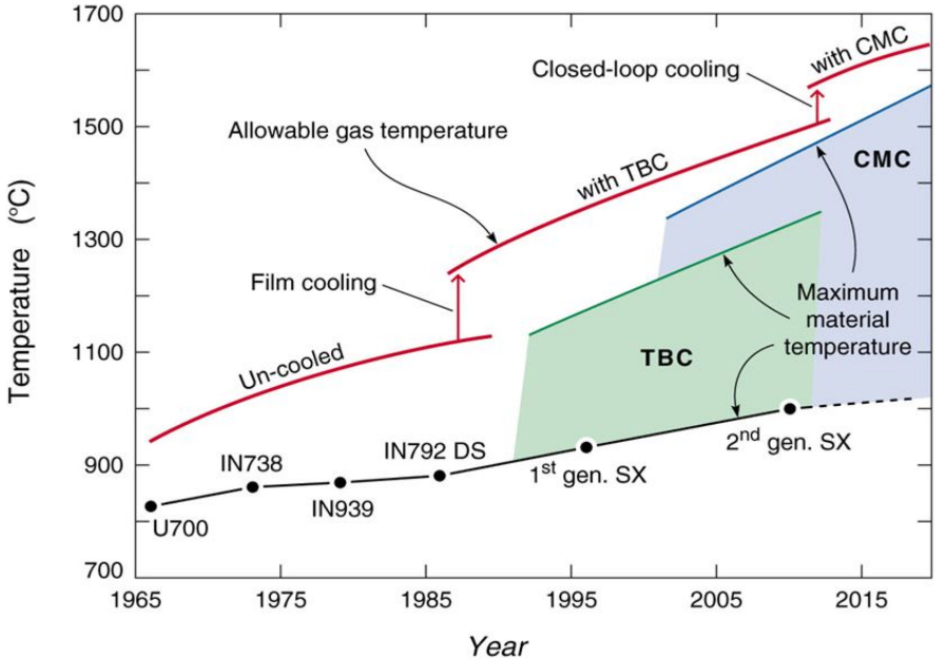

Figure 1.1: Turbine Inlet Temperature (*TIT*) historic and forecasted trend through time [1]

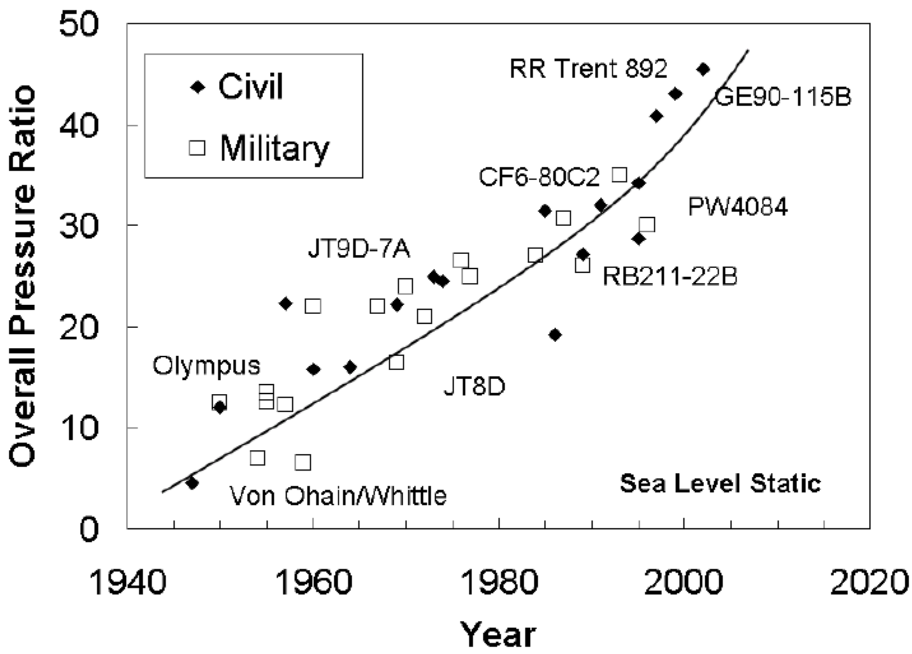

Figure 1.2: Overall Pressure Ratio (*OPR*) trend through time [2]

OPR. In fact, this implies a higher temperature at the compressor discharge that limits the cooling capacity of air. For these reasons, the definition of the most appropriate cooling scheme represents one of the most challenging tasks in the combustor and turbine design, since it directly determines the components life.

Nevertheless, much attention in the design of gas turbines is nowadays directed at meeting the strict regulations for what concerns emissions. In fact, civil air traffic is expected to grow by 4.1% annually [3], potentially leading to an increase of pollutant emissions caused by civil aviation. As at least a partial compensation, the Advisory Council for Aeronautics Research in Europe ($ACARE$) has set several ambitious goals to be achieved by 2050 from a 2000 baseline [4, 5]:

- 75% reduction in CO_2 per passenger kilometre;
- 90% reduction in NO_x emissions;
- 65% reduction in noise.

Even though 20% and 10% of the CO_2 reduction is expected to be achieved in the framework of respectively airframe and air traffic management and operations, these targets strongly affect the development of aero-engines.

Similarly, for what concerns industrial applications, the European Environment Agency (*EEA*) has set an ambitious implementation of new requirements under the *EU* Industrial Emissions Directive in order to significantly reduce pollutant emissions and thus minimise their potential harmful effects on the environment and human health. In particular, although emissions of SO_2 and dust from power plants have already decreased by more than three quarters since 2004, largely as a result of environmental regulation, new requirements concerning SO_2, NO_x and dust emissions were adopted in 2017. These are to be implemented by member state authorities by 2021, are based on 2016 reported emissions and need to be achieved by 2030, as listed hereafter [6]:

- 66-91% reduction in SO_2 (barely present in gas turbine fuels);
- 51-79% reduction in NO_x emissions;
- 56-82% reduction in dust.

For all these reasons the design of gas turbines is becoming a matter of optimisation of the whole system, requiring the accurate assessment of trade-offs with the aim of meeting such requirements. It is indeed worth mentioning, for example, that the improvement of overall efficiency through the increase in TIT and OPR comes at the cost of larger NO_x production.

In general terms, the exhaust gases of a gas turbine are typically composed of particulate material and different gaseous species, depending on the fuel composition and on the portion of air that does not take part to the combustion process. The main pollutant species are namely CO, unburned Hydro-Carbons (uHC) and, most importantly, NO_x, being extremely harmful to environment and human health. Apart from the specific fuel composition, CO and NO_x emissions mainly depend on the air/fuel ratio and on the combustion temperature.

As sketched in Fig. 1.3, they have an opposite trend: CO emissions, as well as uHC ones, reach their maximum for either very lean or very rich mixtures, due to incomplete combustion; on the other hand NO_x emissions have their maximum impact for air/fuel ratios slightly higher than the stoichiometric value, where combustion temperatures are high and residual oxygen is available for nitrogen oxidation. Based on this, two possible operation zones can be identified with the aim of reducing the nitrous oxides formation: the rich and the lean burn modes (see Fig. 1.3 for reference). Furthermore, since amongst the mechanisms contributing to the nitrous oxides formation, the most relevant one is exponentially related to temperature, as formulated by Zeldovich [7], combustion systems shall be able to operate at a trade-off temperature, where both species emissions are limited, as qualitatively shown in Fig. 1.4.

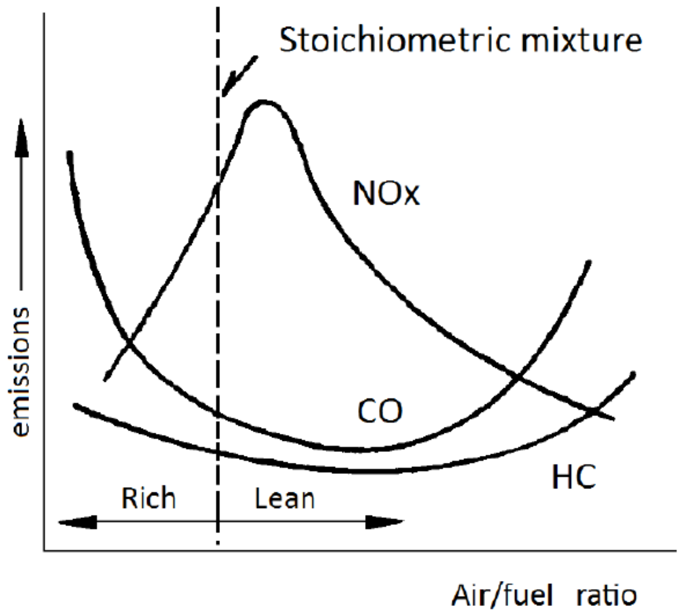

Figure 1.3: Dependence of NO_x, uHC and CO emissions with the air/fuel ratio [7]

Despite the overall standardisation of combustors, the need for always new requirements have pushed the manufacturers to recurrently adapt combustor characteristics and design procedures. In particular, several combustor configurations exist: the standard for aero-engines has rapidly set to annular combustors, since they allow to min-

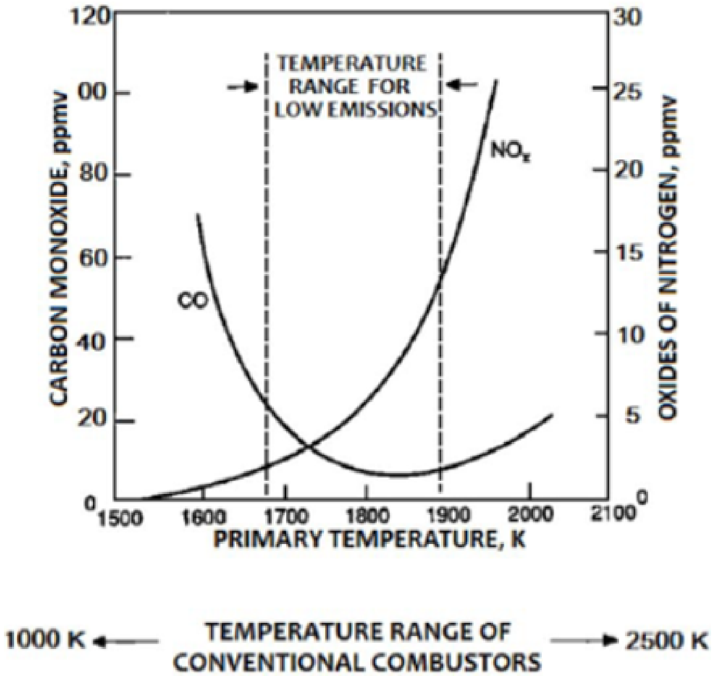

Figure 1.4: Dependence of NO_x, uHC and CO emissions with temperature [7]

imise pressure losses, front area and weight, while can and can-annular combustors are largely used in heavy-duty gas turbines, although more recently, and especially for small-size turbines, annular combustor are being employed.

Moreover, since NO_x emissions reduction has been the main technology driver in the last 30 years, two main configurations have been so far explored in the aero-engine framework. Referring back to Fig. 1.3, designers can either choose to move towards low air/fuel ratios in the primary zone followed by large mixing with dilution air, as in the RQL (Rich burn - quick Quench - Lean burn) concept, i.e. the standard for a long time, or to opt for equivalence ratios ϕ (i.e. actual-to-stoichiometric fuel/air ratios) significantly below the unity (lean burn combustion), as explored in the recent years.

On the other hand, the lean premixed combustion technology is already regarded as the most promising one to satisfy emissions requirements among industrial applications, since it is the only one able to meet the current NO_x legislation limits moving already towards single-digit ppm figures in certain areas. In the past diffusion flames represented the majorly employed combustion type, thanks to their reliable performance and reasonable stability characteristics [8].

By contrast, today's dry-low NO_x burners (to be distinguished from systems implementing water or steam to reduce temperature and hence NO_x emissions) operate by pre-mixing fuel and air within the injection system prior to reaching inside the combustion chamber. This Lean Premixed Combustion (LPC) concept allows to control CO production rising the residence time in the combustion chamber, without promoting NO_x creation, thanks to reduced temperatures.

One common issue of lean combustion technologies to be mentioned, however, is the occurrence of combustion instabilities, related to the coupling between pressure oscillations and thermal fluctuations, which are excited by the possibly unsteady heat release and need to be carefully accounted for since the design phase.

1.2 Aero-engine combustor technologies

1.2.1 Rich-Quench-Lean combustors

The majority of the currently employed aero-engines in the civil aviation sector is based on the RQL concept. This technology was proposed in the 1980s in order to achieve a significant reduction in NO_x emission. Bearing in mind the necessity to avoid flame blow out during the entire flight mission and with any kind of weather conditions, the basic idea consists in ensuring the flame stability through the combustion of a rich mixture in the primary zone. In addition, the “rich burn” condition (ϕ between 1.2 and 1.6) reduces the nitrogen oxides production thanks to the relatively low temperature and the limited concentration of oxygen containing intermediate species. Subsequently, the gas is diluted through the addition of primary air with the aim of quickly quenching the reactions and shifting as quick as possible towards the “lean burn” condition, with ϕ = 0.5 - 0.7. It appears therefore evident that the main focus and the technological issues lie in guaranteeing a rapid mixing to minimise the residence time at stoichiometric conditions, which the maximum NO_x production is associated with.

From a more practical point of view, the implementation of the RQL concept in a modern aero-engine is presented in Fig. 1.5. The flame in the primary zone is usually stabilised by means of swirlers, devices able to provide a tangential velocity component to air with the purpose of generating the “swirler breakdown” phenomenon and the recirculation of hot gas towards the injector. The secondary zone, immediately downstream of the mixing ports, completes the reaction of the unburned species (CO, uHC, smoke), whereas additional air is usually injected (not shown in the picture) to control the exit temperature profile.

The intrinsic characteristics of the operation of RQL combustors represents a severe limitation in optimizing the pollutants emissions. The critical switching from rich- to lean-burn conditions involves necessarily local values of $\phi \approx 1$. In addition, the applica-

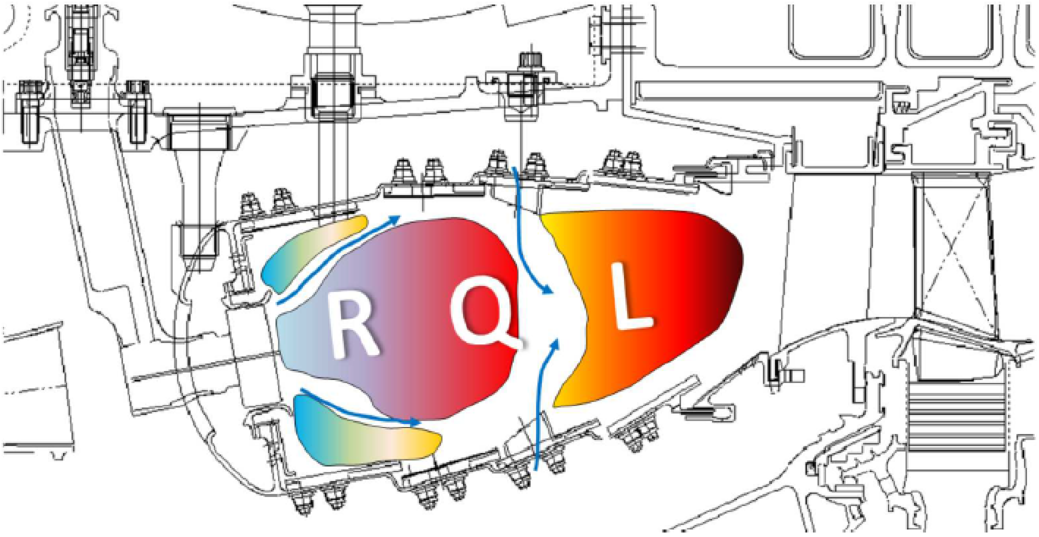

Figure 1.5: Sketch of a Rolls Royce Trent XWB *RQL* combustor [9]

tion of film cooling in the primary zone may locally produce stoichiometric conditions, undermining the efforts in reaching the low NO_x target. This is qualitatively illustrated in Fig. 1.6, where the ideal and real *RQL* process routes are reported.

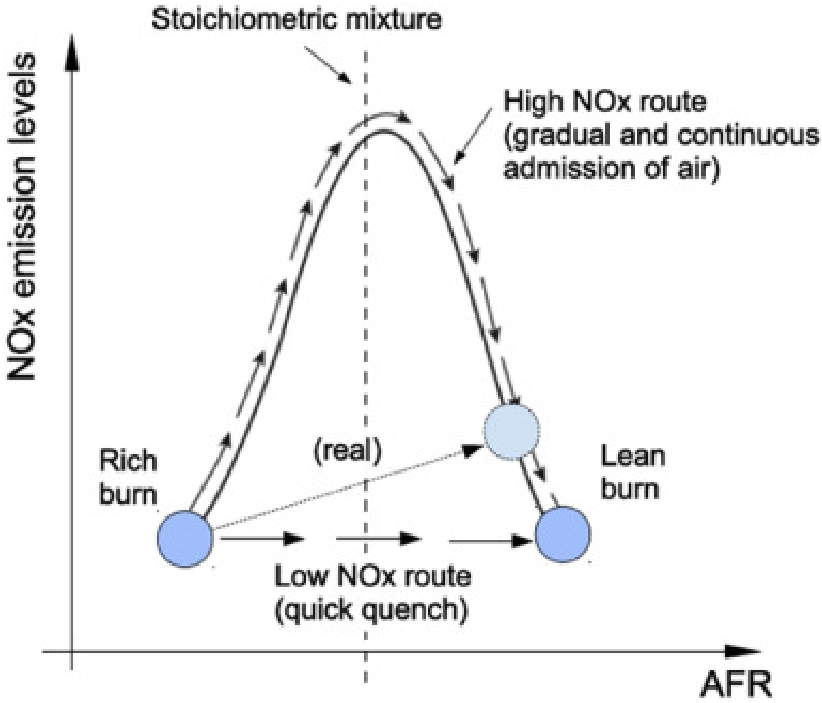

Figure 1.6: *RQL* concept: ideal and real process routes [9]

Nevertheless, the nitrous oxides do not represent the only type of pollution to be concerned about: the rich condition achieved in the primary zone, as well as the quenching in the proximity of the liners, entails also a significant production of unburned species, such as CO, uHC and smoke. The presence of the lean secondary zone is supposed to significantly reduce their emission by means of a high oxidiser concentration, provided that the temperature reduction due to mixing is sufficient to burn these species. For this reason, the equivalence ratio ϕ for both zones must be carefully selected to satisfy all emission requirements.

Recent advances have shown that significant reductions in residence time and NO_x production can be achieved without compromising the combustor stability and low-power performance. Use of fuel injectors capable of producing uniformly-dispersed small droplets, the rapid air jet mixing as well as the decrease in combustion volume, have demonstrated NO_x reduction of over 50% when compared to early annular combustors [10]. The compact design is advantageous also with regards to the thermal management of the liners, since it mitigates the issues related to the occurrence of stoichiometric conditions in the proximity of film cooled walls.

An example of advanced RQL combustor can be given by the TALON family (Technology for Advanced Low NO_x), developed by Pratt & Whitney. These combustors employ the proven and robust RQL technology, adding drastic improvements focused on obtaining a uniformly rich primary zone, optimized quench, advanced cooling and reduced residence time. The last member of the family, the TALON X, indicated the potential to achieve NO_x levels up to 70% below CAEP2 regulations [11] and it is equipped on the PW1000G geared turbo-fan.

Due to the intrinsic limits of RQL combustors, it is possible to understand the motivations that are pushing towards the implementation of the lean burn concept. Nevertheless, despite the efforts carried out in the last decades by the main aero-engine manufacturers in developing lean combustors, at the moment only few produce aero-engines equipped with this kind of technology.

Therefore, RQL combustors still receive significant attention aimed at their optimization, while at the same time huge efforts are in place for the development of the lean burn technology, since it is able to overcome the RQL limitations and meet the more and more stringent emission requirements, in spite of flame stability and reliability issues.

1.2.2 Lean burn combustors

The concept of a lean burn combustor is to operate with a premixed lean mixture in order to keep the combustion temperature at a lower level and therefore to inhibit the formation of NO_x. In parallel with this benefit, there are several issues that designers have to deal with: first of all, the lower combustion temperature leads to increased conversion times, that become similar to residence times for CO and uHC, and hence to higher emissions for these species [12]. Furthermore, lean combustors work closer to the flame extinction limit, which implies relevant issues in terms of flame stability. These become even more pressing if considering that aero-engine combustors are subjected to different operating regimes, from the idle to the take-off conditions, and that efficiency, stability and polluting emissions limitation must be always guaranteed through the whole Landing-Take Off (LTO) cycle. Therefore, a big effort has been put in recent years in trying to introduce lean combustion in the aero-engine combustors market.

The most used way to overcome the problem related to flame stability is the so called fuel staging: it consists in turning off individual or groups of burners, and thus increasing the equivalence ratio in the remaining ones. While this technique is widely used also on *Dry-Low-*NO_x industrial gas turbine combustors, the more pressing needs in terms of stability for aero-engine applications, led to modifications and refinements. In a staged combustor two separate zones are designed to improve the combustion performance: the first one operates at fairly high equivalence ratio, even if lower than stoichiometric, to achieve a good combustion efficiency and to minimise the production of CO and uHC. This "primary" zone guarantees the stability of combustion during idle and low power conditions. At higher power level, it acts as a pilot source of heat for the second "main" combustion zone, which is supplied with premixed fuel-air mixture. In this way, the engine globally works in lean conditions and the combustion process still results efficient and stable for a wide range of operating conditions.

Axially and radially staged combustors have been proposed, the drawback of which, however, lays in the large surface to be cooled, the slightly higher CO and uHC emissions than single annular chambers and, for the latter type, the relevant front area. Therefore the research steered towards developing single annular technologies with internally staged injectors, with the idea of combining the two domes into one with fuel staging, using two fuel manifolds. Emission performance characteristics have shown this approach to be highly promising, making it possible to reduce all types of emissions as compared to a double annular combustor.

Despite some drawbacks, mainly related to CO and uHC emissions and complexity, this architecture is nowadays considered as the most viable technology to be exploited [13], as current research heads towards the development of *Ultra Low* NO_x (ULN) combustors with single digit NO_x emissions. Fig. 1.7 shows a scheme of the GE Taps (Twin Annular Premix System) combustor: a single annular combustor currently mounted on the *GEnx* engines powering Boeing 787 aircraft.

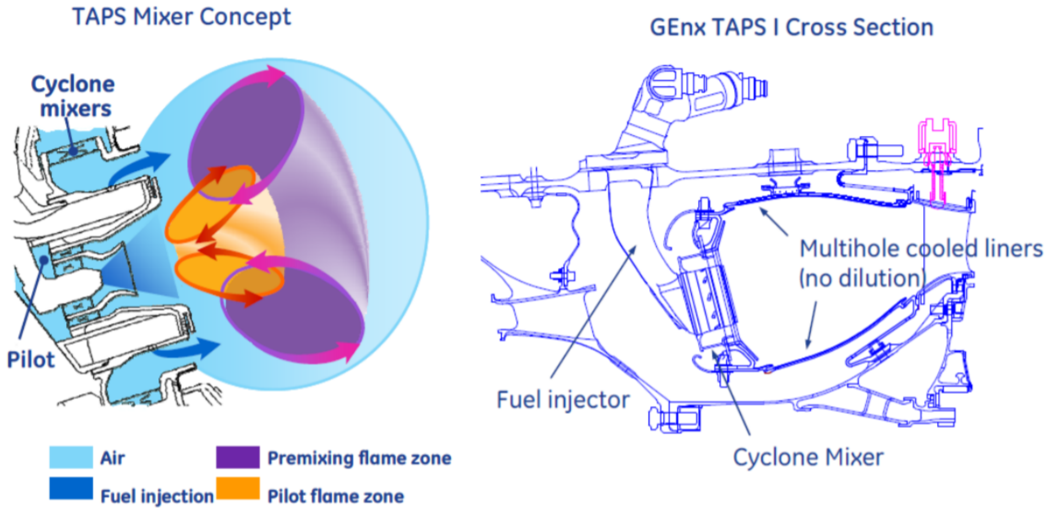

Figure 1.7: GE Taps combustor concept and section [14]

The combustion concept is a lean burn system in which each fuel injector contains a center pilot and concentric outer main. The central pilot flame is rich burn, where 100% of the fuel is directed at starting and low power operation, while at higher power approximately 70% of the air flow passes through the injector and most of the fuel is injected through the main swirler, thus providing a lean combustion.

A successive version of this combustor, the GE Taps II, is present in the *LEAP* (Leading Edge Aviation Propulsion) jet engine, equipping the Boeing 737max and Airbus A320neo aircraft families. With modern lean burn combustors being introduced, it is useful to highlight the differences with the formerly illustrated *RQL* technology, with reference to Fig. 1.8.

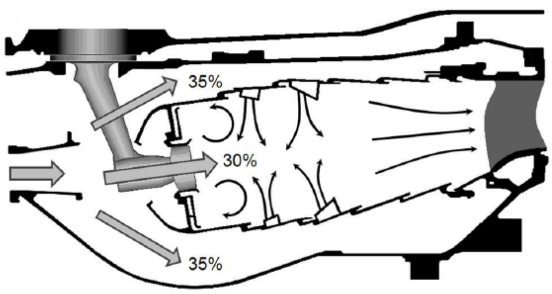

(a)

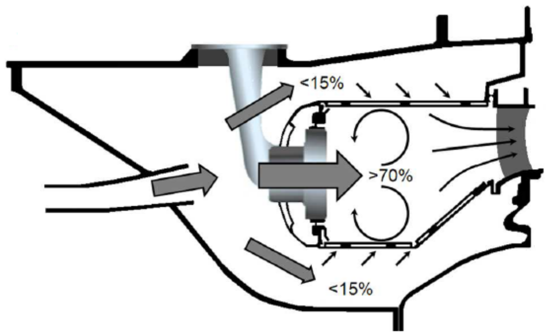

(b)

Figure 1.8: Air flow split and main flow field structures for *RQL* (a) and lean burn combustors (b) [15]

The main difference lays in the air flow split distribution: while in RQL combustors most of the airflow (65-70%) is used for dilution and cooling flows, since only a limited amount of air is needed in the rich burning primary zone, in lean burn combustors almost 70% of the air flow is injected in the primary zone to mix up with the fuel. As a consequence, a reduced amount of air is available for liner cooling, resulting in the necessity for studying more efficient cooling concepts. Another distinction is in the flow field promoted by the injection system. Even if in both configurations the swirling structures generated by the injection system play an important role in the primary zone combustion performance, for RQL combustors, where diffusive flames are adopted, the crucial part of the process consists in the rich-to-lean switch promoted by the dilution flows. Therefore these flow structures are the dominant ones within the combustion chamber flow field evolution and hence the focus of most of the design efforts. On the other hand, for lean combustors, the cooling flows interaction with the main flow is much more limited, due to the reduced flow. The flow structures created by the injection system itself thus play the major role in the swirl-stabilised combustion process and propagate through the chamber without being significantly altered.

1.3 Industrial gas-turbine lean-premix combustors

1.3.1 Dry-Low Emission combustors

Industrial gas turbine combustors make large use of the lean premixed technology, being nowadays the state of the art. In a practical LPC, fuel and air are premixed within the injector as to achieve a lean, uniform mixture inside the combustion chamber. The mixing process is favoured by premixer designs with enhanced turbulence levels in the nozzles, even if this results in increased pressure losses. Various approaches are used in swirl-stabilised combustion systems including fuel injection through the swirl vanes. With gaseous fuels, several injection points can be used to distribute the fuel over the injector.

One example is a GE burner commonly adopted in industrial lean-premixed gas turbines, which presents a Dual Annular Counter Rotating axial Swirl ($DACRS$) nozzle (see Fig. 1.9 for reference), where fuel is injected at the outer annulus and mixing with air is enhanced by the interaction of the two counter-swirled flows and gets completed through the converging nozzle. The $DACRS$ injector is also provided with the so-called Enhanced Lean Blow-Out ($ELBO$) pilot fuel, activated at partial loads and with low flame temperatures to guarantee operability at all working conditions. This consists of one or more discrete injections of either pure fuel or of a relatively rich fuel-air mixture, which, placed at convenient locations, helps sustain the reaction [16]. Similar injection concepts are employed also by the other major gas turbine manufacturers, such as Siemens, Solar Turbines and Rolls Royce [8].

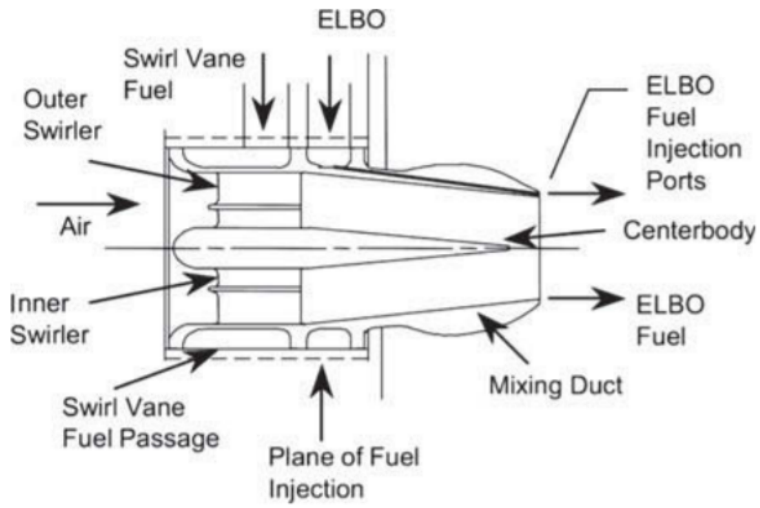

Figure 1.9: GE *DACRS* heavy-duty lean premixed injector[8]

In addition to the injection system technology, a proposed lean combustion method is “staged combustion”, which consists in fuel-staging operations and/or staged combustor architectures, in which combustion is respectively controlled in separate phases or zones to achieve an optimum performance [17]. With the former technique, typical of annular combustor, fuel can be supplied only to selected injector combinations based on different operating conditions. The full circle of injectors is utilised only at full power, while injector selection takes place at partial loads. This allows for raising the local equivalence ratio also at low-power operation in order to reduce CO and uHC emission and, at the same time, extend the lean blow-out limit [7].

In addition, it is to be noted that selective combustion can be applied even to more than one single circle of injectors, as in the case of the GE Dry-Low Emission (DLE) combustors, typically employed in aero-derivative gas turbines in replacement of standard annular chambers. Such combustors are composed of three circles of burners (outer, middle and inner as shown in Fig. 1.10) with different injectors count, being operated on different combinations as function of the actual working condition from partial to full load:

- *Starting* - Only the middle circle of burners is fuelled to pilot reaction;
- *Idle* - The middle circle as well as half inner circle of injectors are fuelled to increase load up to 5%;

- *Light load* - Both middle and inner circles of premixers are fuelled to ramp load up to 25%;
- *Intermediate load* - Reaction is switched from the inner to the outer circle of burners, while the middle circle is kept fuelled to sustain loads up to 50%;
- *Full load* - All premixers are in operation to reach the machine full load.

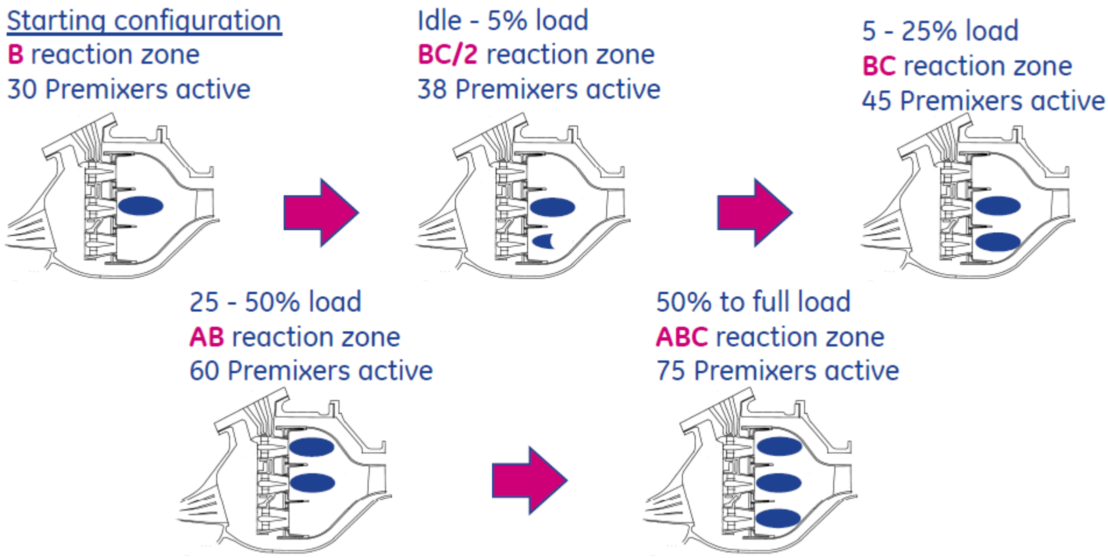

Figure 1.10: GE aero-derivative *DLE* combustor operating modes [18]

1.3.2 Dry-Low NO_x combustors

Dry-Low NO_x combustors are based on a "staged architecture", which has a lightly loaded primary zone, providing the temperature rise needed to drive the engine at low-power conditions, operating at equivalence ratios of around 0.8. At higher power settings, its main role is to act as a pilot source of heat for the main combustion zone, which is supplied with a fully premixed fuel-air mixture. When operating at maximum power conditions, the equivalence ratio in both zones is kept low at around 0.6 to minimise NO_x and smoke [7]. An example of staged combustor is the GE Dry-Low NO_x (*DLN*) of Fig. 1.10a, employed in heavy-duty machines, being now at the 2.6+ series. Fuel flow is injected in each combustion zone through the primary and secondary fuel nozzles so that the combustion system is arranged as a two-staged architecture. The operation of the *DLN* technology is based on four different modes, activated in sequence from ignition to base-load premix conditions, as shown in Fig. 1.11b with reference to the base *DLN1* series. Davis and Black [19] report the mode/operating range of such combustor technology, a brief summary of which is presented as follows:

- *Primary* - Fuel is injected to the primary nozzles only and flame is in the primary stage only, which makes this mode of operation useful to ignite, accelerate and operate the machine over low- to mid-loads, up to a pre-selected combustion reference temperature;

- *Lean-Lean* - Fuel is directed to both primary and secondary nozzles, flame is thus in both primary and secondary stages, with this mode of operation being employed for intermediate loads between two pre-selected combustion reference temperatures;

- *Secondary* - The secondary nozzles only are injected with fuel and host the flame, which represents a transition mode between lean-lean and premix;

- *Premixed* - With both primary and secondary nozzles being fuelled and the flame in the secondary zone only, this mode of operation is achieved at and near the combustion reference temperature design point, generating the lower CO and NO_x emissions.

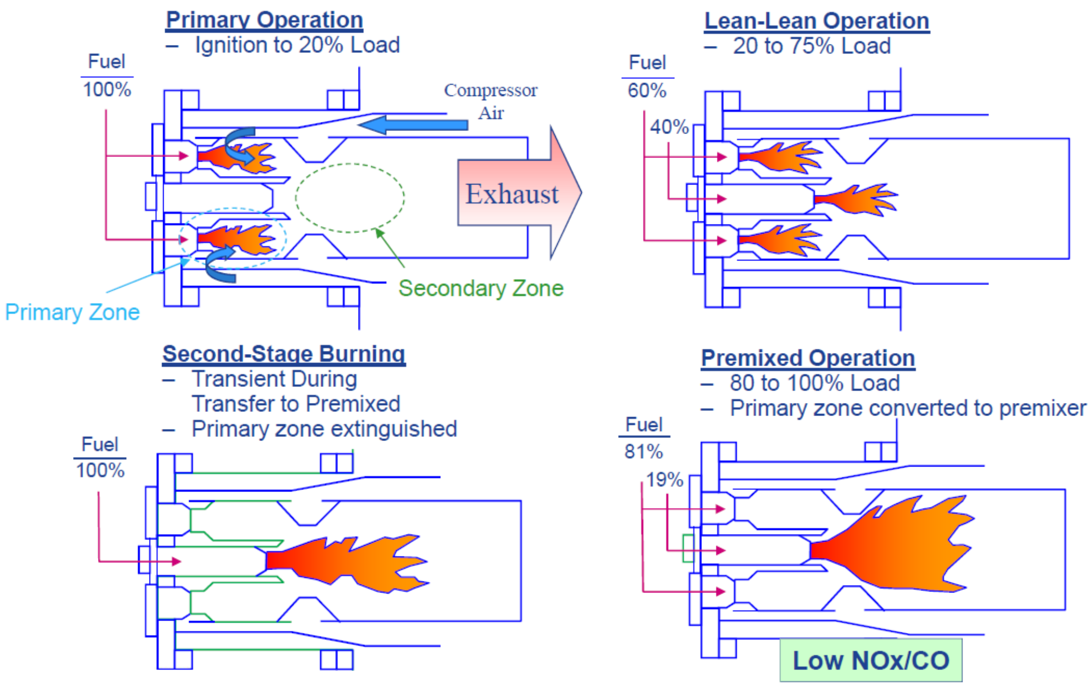

Figure 1.11: GE *DLN* combustor cross-section (a) [8] and operating modes (b) [18]

Another well established low-emission burner design is the former Alstom *EV* burner, shown in Fig. 1.12. The *EV* burner is the standard burner for all former-Alstom gas turbines. The burner is a dual fuel burner system for dry-low-NO_x natural gas combustion and for liquid fuel combustion with water injection. During startup the pilot fuel is injected over the central lance constituting a fuel enriched core flow. Similarly to the previously mentioned *LPC* systems, a broad stable range even at partial loads is therefore guaranteed through the pilot fuel, whereas at higher load the burner is operated as fully premixed in order to target lower emission values (see Fig. 1.12 for reference).

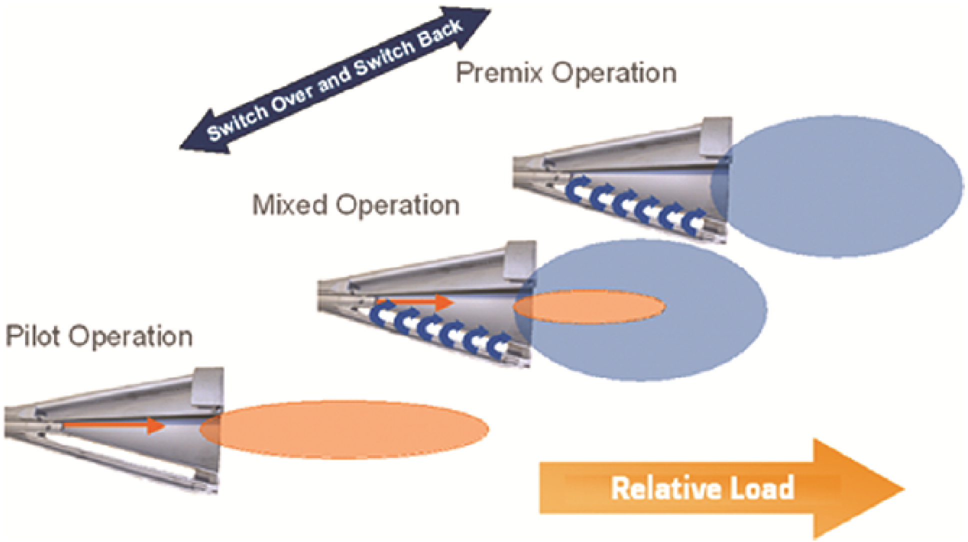

Figure 1.12: Former Alstom *EV* burner [8]

1.4 Aims, motivations and thesis outline

The so far depicted scenario, considering the technology involved in such modern gas-turbine lean combustors and the overall necessity for augmenting the thermodynamic cycle efficiency, poses the question of whether and to what extent the turbine operation can be affected by the combustor outlet flow. Therefore an increased knowledge on combustor-turbine interaction is needed, with the further objective of improving standard design practices and possibly reducing the commonly adopted wide safety margins.

For this sake, two non-reactive test rigs were assembled at the University of Florence, Italy. Both accommodating three lean-premix swirlers within a combustion chamber and a first stage film-cooled nozzles cascade, the rigs were operated in similitude conditions to mimic an aero-engine and an industrial gas-turbine arrangements. The rigs were designed to reproduce the real engine periodic flow field on the central sector, allowing also to perform measurements far enough from the lateral walls. The periodicity condition was enforced by the installation of circular ducts at the injectors outlet section as to preserve the non-reactive swirling flow down to the nozzles inlet plane.

For the aero-engine simulator rig, the flow field within the combustion chamber was investigated via particle-image velocimetry (*PIV*) in a previous work [20]. The combustor-turbine interface section was experimentally characterised in both test campaigns in terms of velocity, pressure and turbulence fields by means of a five-hole pressure plus thermocouple probe and hot-wire anemometers, mounted on an automatic traverse system. To study the evolution of the combustor outlet flow through the nozzles and its interaction with the film-cooling flow, such measurements have been also replicated slightly downstream of the airfoils' trailing edge. Lastly, the film-cooling adiabatic effectiveness distribution over the airfoils was evaluated via coolant concentration measurements based on pressure sensitive paints (*PSP*) application. Bacci [21] has extensively described the experimental measurements carried out on the aero-engine combustor simulator test rig.

Within such experimental scenario, the aim of the present work is pursued trough numerical analyses. In fact, since the design of industrial high-pressure turbines historically relies on 1D, circumferentially-averaged profiles of pressure, velocity and temperature at the combustor-turbine interface in conjunction with Reynolds-averaged Navier-Stokes (*RANS*) models, this thesis describes how measurements can be leveraged to improve numerical modelling procedures. Within the first project (*FACTOR*), hybrid scale resolving techniques, such as Scale-Adaptive Simulation (*SAS*), have been explored, proving to be able to suit the purpose, whilst containing computational costs, as also shown in the literature. Furthermore, the investigation of the two components within the same integrated simulation enables the transport of unsteady fluctuations from the combustor down to the first stage nozzles, which can make the difference in the presence of film cooling. For this reason, the experience gained during the *FACTOR* project could be exploited for the design of the *STech* rig.

In fact, in the recent years, some more knowledge has been built on combustor-turbine interaction and a number of works exist in the literature describing the combustor outlet flow features. However, the aero-engine combustor simulator developed within the *FACTOR* programme was the first project in which both temperature distortion and swirling flow were reproduced simultaneously through realistic components. This allowed for a heavy experimental campaign, resulting in an extensive characterisation of the phenomenon also from a numerical perspective. On the other hand, the industrial combustor-turbine rig realised for the *STech* programme is the first one in its genre housing real burners and high-pressure nozzles hardware of a heavy-duty gas turbine, including all the features of a real cooling system, typical of high-pressure turbine first-stage nozzles, designed to withstand to engine operating conditions.

As mentioned, it is the main focus of the present thesis, differentiating from previous works, to emphasise the gaps in the standard practices commonly employed within the design of high-pressure turbine components. This is performed by highlighting three fundamental aspects along with the fluid-dynamic analysis of nozzle guide vanes:

- *Inlet boundary conditions* - First it is questioned whether tangentially averaged quantities imposed at the turbine inlet is still a proper procedure to be adopted and what could be the impact of such an assumption in the presence of modern lean-premix burners;

- *Analysis domain* - Then the investigation focuses on the definition of the appropriate domain to be studied, i.e. whether it is convenient to keep the analyses of combustor and turbine separate for the correct evaluation of aerodynamics and heat transfer through the turbine;

- *Methodology* - With the increased availability of computational resources it is now possible to transfer the use of scale resolving techniques from the academic and research fields to the industry, which can enable the improvement of design practices yet relying on turbulence full modelling and steady simulations.

As the investigations carried out during this PhD course are related, on one hand, to the exploitation and comparison of performed measurements within the *FACTOR* project with *CFD* and, on the other, with the design phase of the *STech* rig, this is the proposed thesis structure:

- *Chapter 2* reports a review of the literature on the combustor-turbine interaction subject, which includes the definition of the main combustor outlet flow characteristics (Section 2.1) and the fundamental parameters of interest within the fluid-dynamic design of nozzles (Section 2.2). A brief review of past research follows (Section 2.3), with focus on the test facilities employed, while an overview of key aspects and previous *CFD* works is illustrated thereafter (Section 2.4);

- *Chapter 3* is composed of two parts, the first of which intends to briefly show the experimental rigs and the adopted measurement techniques (Section 3.1), whereas the second one is aimed at describing the numerical methodology implemented to obtain the results and outcomes of the present work (Section 3.2);

- *Chapter 4* includes the numerical analyses performed on the aero-engine combustor simulator rig to investigate over the nozzle guide vanes of a modern aeronautical lean-burn combustor engine, ranging from the aerodynamic (Section 4.2) to the heat transfer aspects (Section 4.3);
- *Chapter 5* illustrates the steps taken during the design of the industrial lean-premix combustor test bench housing a first stage nozzle cascade, from the definition of the combustor characteristics (Section 5.1) and the *NGV* module lateral walls (Section 5.2) to the first available experimental measurements (Section 5.3);
- *Chapter 6* lastly and briefly displays the concluding remarks on the work performed during this PhD course and reported in this manuscript.

Chapter 2

Literature review

Contents

2.1 Combustor outlet flow field

2.1.1 Typical characteristics

The study of the combustor flow structures is of fundamental importance for three main reasons:

- Combustion stabilisation,
- Interaction with cooling flows,

- Impact on the high pressure turbine.

The swirling flow typical of lean combustors is generally characterised by strong radial and axial pressure gradients setting up at the nozzle immediate exit, which results in the following main structures, as shown in Fig. 2.1:

- Central toroidal recirculation zone (*CTRZ*) - Located in the central region right downstream of the swirler, it is the bulk recirculating flow increasing the residence time, which is crucial for stabilising and completing the combustion process;
- Vortex breakdown (*VB*) - Realised by the opening of the swirling flow both laterally and towards the hub and casing surfaces, it also induces recirculation along the swirler axis, often empowering the *CTRZ*, in addition to interacting with the liners cooling flow;
- Corner recirculation zones (*CRZ*) - Present at the corners of the combustion chamber, they favour increased residence times and hence combustion;
- Precessing vortex core *PVC* - Vortical structure rolling around the *CTRZ* with a precessing motion.

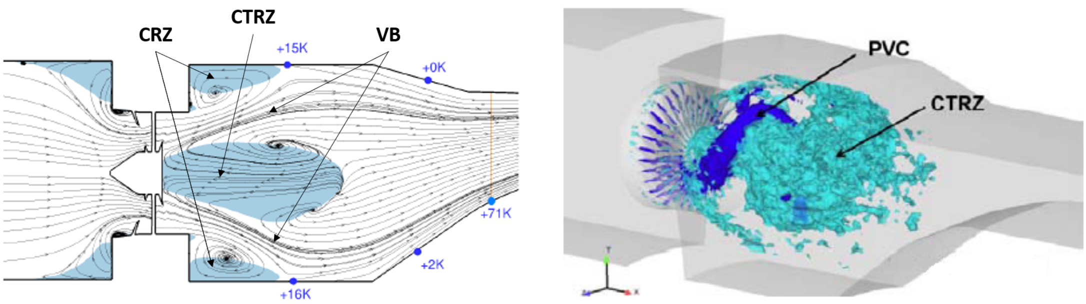

(a) (b)

Figure 2.1: Typical lean combustor vortical structures (central toroidal recirculation zone *CTRZ*, vortex breakdown *VB*, corner recirculation zones *CRZ*) on a central plane (a) and (precessing vortex core *PVC*) three dimensional (b) [22]

It is furthermore interesting to note that the reasons leading to the formation of the PVC are not fully understood yet, but it is usually identified by an asymmetric, large scale, coherent flow feature, generally assuming a corkscrew shape, with the potential to cause large-scale flow field instability within a swirling flow [23].

In the recent years, several authors have conducted experimental campaigns to detail problems related to combustion instabilities [8] and interaction between swirling flows and liner cooling schemes [24, 25, 26]. Berrino et al. [27, 28] investigated the flow field downstream of an ultra low NO_x injection system unveiling that, in such kind of higly swirling flows, the chemical combustion process, in the form of heat release, plays an important role in the flow field stabilisation. Moreover, unsteady phenomena, e.g. $CTRZ$ and PVC, were found to be damped or even erased when experiments shifted from non- to reactive conditions, on the same injector geometries [29, 30, 31, 32, 33]. Therefore, differences between reacting and non-reacting cases exist and might affect the combustor outlet characteristics if the two are directly compared, without any adjustments [23].

In general, the flow field at the outlet of a swirl-stabilised annular combustor is therefore characterised by aggressive swirl angles and non-uniform temperature: this occurs not only in the radial direction, due to the mixing of liner coolant (dilution air in RQL combustors) and core flow, but also in the circumferential direction, because of the discrete position of fuel injectors and the relatively short length of lean burn chambers. This is particularly emphasised in lean combustors, since a reduced amount of air is used for liner cooling, which hardly interacts with the main flow.
As a consequence, modern combustors outlets are generally characterized by marked hot streaks that combine the following characteristics:

- total temperature non-uniformities,
- residual swirl,
- high turbulence intensity.

2.1.2 Temperature distortion

The measured combustor exit temperature field of a modern Rolls-Royce engine is shown in Fig. 2.2 [34]: both circumferential and radial temperature gradients can be observed.

Cha et al. [35] presented the experimental study of an RQL aero-engine combustion chamber, tested in similitude conditions, without fuel injection. The test rig included the full annular liner with burners and injection systems. Since a cold flow test is considered, CO_2 is used as a non-reactive tracer to reproduce the hot fluid distribution within the combustion chamber. Fig. 2.3 reports the corrected CO_2 concentration, obtained on the combustor outlet section. A wavy-shaped hot streak is present on the investigated plane, with the maximum peaks located roughly at the mean radius of the channel. The cold zones are positioned along the endwalls and are more extended near the casing.

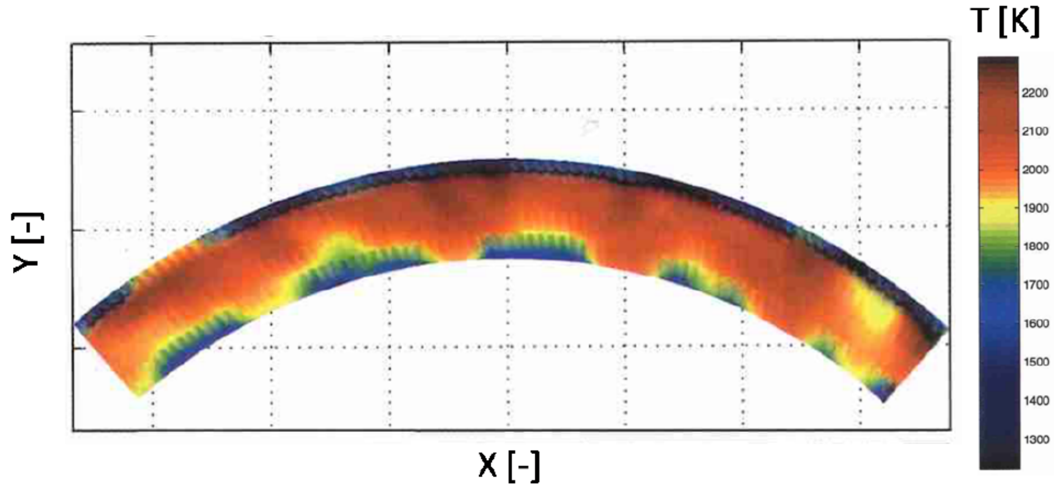

Figure 2.2: Temperature field measured at the outlet of a military engine [34]

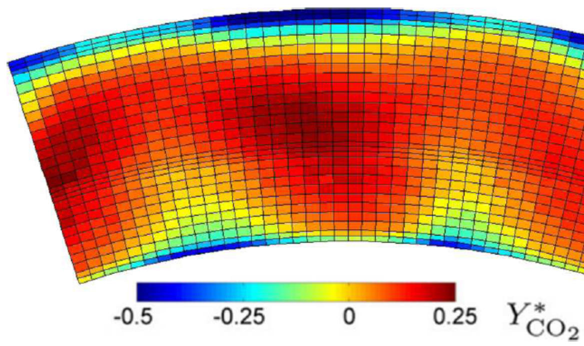

Figure 2.3: Measured CO_2 concentration distribution at the outlet of an aero-engine combustor run in similitude conditions [35]

Furthermore, Fig. 2.4 reports the non-dimensional total temperature distribution obtained by Povey et al. [36] downstream of a hot streak generator. The map covers two NGV pitches and clearly shows the presence of well defined hot spots, placed centrally in radial direction. In this case, the cold fluid covers very well the endwalls without marked tangential gradients.

To quantify and characterise the degree of non-uniformity of the temperature field at combustor outlet, lots of different parameters have been defined. In particular, two coefficients: the Overall Temperature Distortion Factor ($OTDF$, or also "pattern factor") and the Radial Temperature Distortion Factor ($RTDF$, or also "profile factor") have been proposed by Povey and Qureshi [37] (with r and θ being respectively the radial and circumferential directions). The former highlights the difference between maximum and mean temperature over the whole combustor outlet section, whereas the latter expresses the difference between the maximum circumferentially-averaged

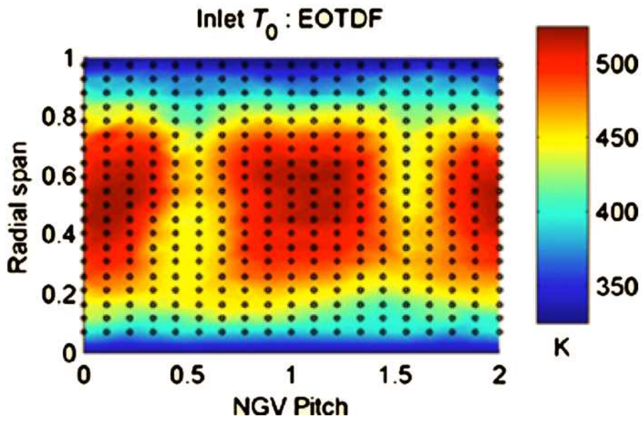

Figure 2.4: Measured non-dimensional temperature field measured at the outlet of a hot streak generator [36]

temperature and mean temperature:

$$OTDF = \frac{max\left(T\left(r,\theta\right)_{40}\right) - \bar{T}_{40}}{\bar{T}_{40} - \bar{T}_{30}} \tag{2.1a}$$

$$RTDF = \frac{max\left(T\left(r\right)_{40}\right) - \bar{T}_{40}}{\bar{T}_{40} - \bar{T}_{30}} \tag{2.1b}$$

Where subscripts 30 and 40 refer respectively to the combustor inlet and outlet planes. Similarly, it is possible to define the correspondent local parameters Local Overall Temperature Distortion Factor ($LOTDF$) and Local Radial Temperature Distortion Factor ($LRTDF$), in order to have respectively a 2D map or a circumferentially-averaged 1D profile at the outlet plane.

$$LOTDF = \frac{T\left(r,\theta\right)_{40} - \bar{T}_{40}}{\bar{T}_{40} - \bar{T}_{30}} \tag{2.2a}$$

$$LRTDF = \frac{T\left(r\right)_{40} - \bar{T}_{40}}{\bar{T}_{40} - \bar{T}_{30}} \tag{2.2b}$$

However, to reduce the measurement efforts, the combustor/turbine interface is usually analysed by developing non-reacting test rigs that simulate the flow of real combustors. In such context alternative definitions of Eq. 2.1 and Eq. 2.2 are preferably employed to describe the flow at the combustor outlet plane introducing the cooling flow temperature [37]:

$$LOTDF_{rig} = \frac{T\left(r,\theta\right)_{40} - \bar{T}_{40}}{\bar{T}_{40} - T_{cool}} \tag{2.3a}$$

$$LRTDF_{rig} = \frac{T\left(r\right)_{40} - \bar{T}_{40}}{\bar{T}_{40} - T_{cool}} \tag{2.3b}$$

2.1.3 Residual swirl

Modern low emission combustion chambers make use of strongly swirled flows in order to provide an adequate flame stabilization. A high swirl number is imposed to the flow by means of appropriate systems located in the burners. The definition of swirl number Sn is the following:

$$Sn = \frac{G_\theta}{R_{sw,out} G_{ax}} \tag{2.4}$$

Where G_θ is the axial flux of tangential momentum, $R_{sw,out}$ is the swirler outer radius and G_{ax} is the axial flux of axial momentum. Swirl numbers higher than 0.6 are often adopted in modern combustors. The intensity of the tangential velocity component makes swirl persist downstream, up to the nozzle guide vanes of the high-pressure turbine. This is particularly emphasised for lean burn combustors, where two aspects contribute to maintain swirl further down to combustor outlet. On one hand, this is dictated by the use of very high swirl numbers needed to enforce flame stabilization and enhance mixing, while, on the other, this derives from the absence of dilution jets that would tend to dissipate swirl, whereas liner coolant flow rate is lower and hence more segregated on the inner and outer chamber surfaces.

The swirl generated in a hot streak simulator was experimentally measured by Povey et al. [36], as reported in Fig. 2.5 in the form of vector plot and yaw angle distributions at 20% and 80% of the radial span. The swirl intensity in proximity of the endwalls (20%-80% span) is characterized by maximum and minimum peaks in yaw angle of about 50% and -50%.

Povey et al. [36] applied such swirl profile to the inlet section of the *MT1* high-pressure turbine stage, investigating the related effects both experimentally and numerically. With the nozzles-to-swirlers count being 1:2, results show that the nozzle aerodynamics is considerably altered by swirl, resulting in relevant changes in the rotor incidence, up to +4% from midspan to tip and -6% near the hub, with respect to a uniform inlet flow field case. Furthermore experimental and numerical data have re-

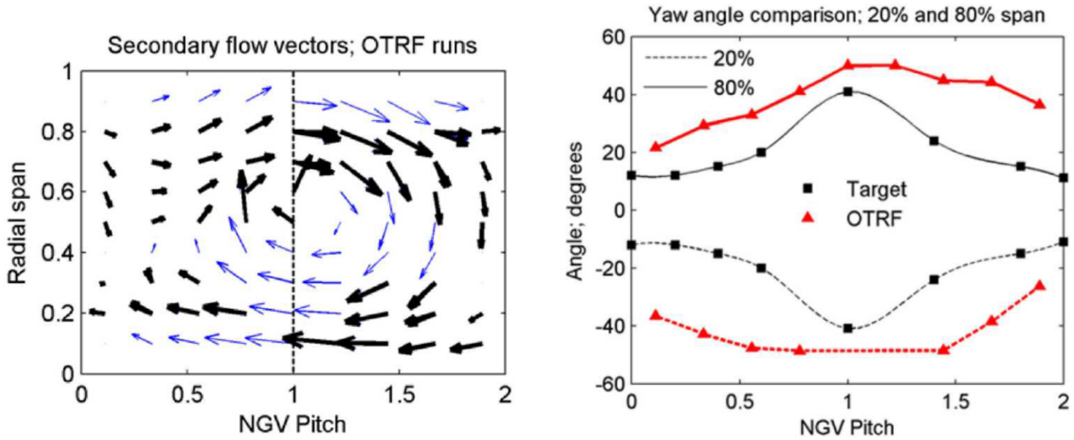

(a) (b)

Figure 2.5: Swirl vectors (a) and pitch angles (b) at a combustor simulator outlet plane [36]

vealed that swirling inflow is responsible for up to 35% decrease in endwall film-cooling adiabatic effectiveness in contrast with a 10-20% increase in Nusselt number.

2.1.4 Turbulence intensity

Among all the data collected on the different test facilities, little attention appears to be paid on the characterization of the turbulence field at the exit of the combustion systems (a very first explanation is that it is complex to measure such fields in realistic conditions). Depending on the way turbulence intensity is defined, most authors report values between 20 and 30% at the turbine inlet [38, 35, 39].

In specific contexts, such turbulence intensities can significantly affect the flow in the turbine. It has been shown indeed that large scale turbulence can enhance the heat transfer on the nozzle walls and promote earlier boundary layer transition [40]. Barringer et al. [41] also report that a turbulence intensity increase at the nozzle inlet leads to broadened wakes and improves mixing at the nozzle exit. Very few studies are available on the interaction between turbulence and hot streak, except for the experimental investigations [42, 43] on the rig of the University of Texas at Austin. They observed that the mainstream turbulence intensity (Tu = 3.5% or 20%) has very little impact on the hot streak attenuation and that under moderate turbulent conditions the hot streak remains more compact with higher temperature gradients. Finally, the authors report that the proper combination of nozzle film cooling and high turbulence can help reduce the hot streak peak temperature by 74%. In fact, in their specific configuration, the film cooling on the suction side nearly eliminates the hot streak on this side of the nozzle.

However, most of the experimental results published on this topic were obtained in test rigs where turbulence is generated by calibrated grids. Only recently, Cha et al. [44] reported experimental and numerical computations of turbulence at the exit of an *RQL* combustor fitted on the Loughborough University isothermal test rig. The turbulence intensity (expressed as the ratio between *RMS* and mean axial velocity at the investigation plane) measured by means of Hot Wire Anemometry (*HWA*) was found to be around 30-35% at the combustor/turbine interface plane both experimentally and through *LES*, as illustrated in Fig. 2.6. The length scale was instead comprised between 15 and 25% of the nozzle chord.

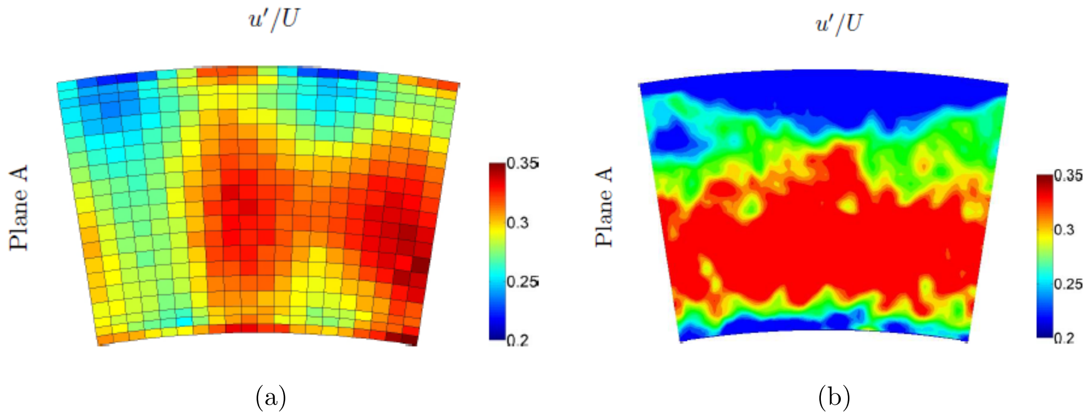

Figure 2.6: Experimental (a) and numerical (b) maps of turbulence intensity at a combustor simulator outlet [35]

2.2 First stage nozzles flow field

2.2.1 Pressure losses

In an axial flow turbine, high pressure nozzle guide vanes (*NGVs*) are the first stage nozzles that direct the airflow onto the turbine buckets while converting pressure into kinetic energy by imposing acceleration to the air flow thanks to their converging geometry. The design of *NGVs* needs to accomodate a lot of requirements dictated by aerodynamics, heat transfer and structural mechanics aspects. With the latter not being part of the present work, aerodynamics imposes the research for the minimum pressure losses and hence best efficiency, whereas the heat transfer discipline seeks for an optimum cooling system that is able to help the nozzle sustain the prescribed thermal loads.

Aerodynamic losses are generally described in terms of total pressure drop across the cascade, for which Ligrani [45] has provided a full review of utilised definitions, such as the following:

$$c'_p = \frac{\bar{P}_{0,in} - P_{0,out}}{\bar{P}_{0,in} - P_{s,out}} \tag{2.5a}$$

$$c''_p = \frac{\bar{P}_{0,in} - P_{0,out}}{\rho \frac{v^2_{out}}{2}} \tag{2.5b}$$

Where P is pressure, while the subscripts in and out indicate the cascade inlet and outlet positions respectively, $\rho \frac{v^2_{out}}{2}$ is the dynamic pressure contribution and the bar symbol indicates mass or area averaging at a certain section. An integral quantity can be derived simply by averaging also $P_{0,out}$, $P_{s,out}$ and $\rho \frac{v^2_{out}}{2}$.

Although categorising all the sources of pressure losses in axial turbine nozzles is complex, since different phenomena combine with each other, it is common use to simplify them down to three main sources [46]:

- *Profile losses* - Given by skin friction or separation occurring on the airfoil in the case of a uniform two-dimensional flow across a cascade;
- *Endwall losses* - Due to skin friction on the endwalls;
- *Secondary losses* - Associated to the non-uniformities of the three-dimensional flow through the cascade, i.e. to the secondary structures present inside the main flow.

Profile losses are generally expressed in terms of momentum thickness at blade trailing edge (TE) and, since they increase with blade load, they strongly depend on parameters like pitch-to-chord ratio and flow deflection. Several methods [47, 48] exist to evaluate this source of losses and to determine the optimum values for such parameters. Another major source of profile loss is caused by the finite thickness of the blade TE, since this generates a low-pressure wake region behind it, which induces the mixing between pressure (PS) and suction side (SS) boundary layers.

Secondary flow structures, with their associated losses, are the most complex, since may be defined as the difference between the actual and an ideal axisymmetric flow [49]. The fundamental features of secondary flow patterns in nozzle guide vane passages were proposed by Langston [50], through the characterisation of a linear cascade, whose work, even if it is acknowledged that several differences between annular and linear cascade flow fields exist, is recognised as highly significant in establishing the basic mechanisms applying to all cascades [51]. The main secondary flow structures, with reference to Fig. 2.7 [52], are the following:

- *Passage vortex* - The reduced velocity in the boundary layer causes an overturning of the flow towards the suction side, which creates a counter-rotating vortex on both inner and outer endwalls;

- *Horseshoe vortex* - On the stagnation point at the airfoil leading edge and close to the endwalls, the boundary layer flow is split into a *pressure* and a *suction vortex*, with a *horseshoe* fashion, which are then convected inside the passage, with the pressure leg enforcing the passage vortex, while the suction leg acquires an opposite sense of rotation and is sometimes labelled as *corner vortex* [50].

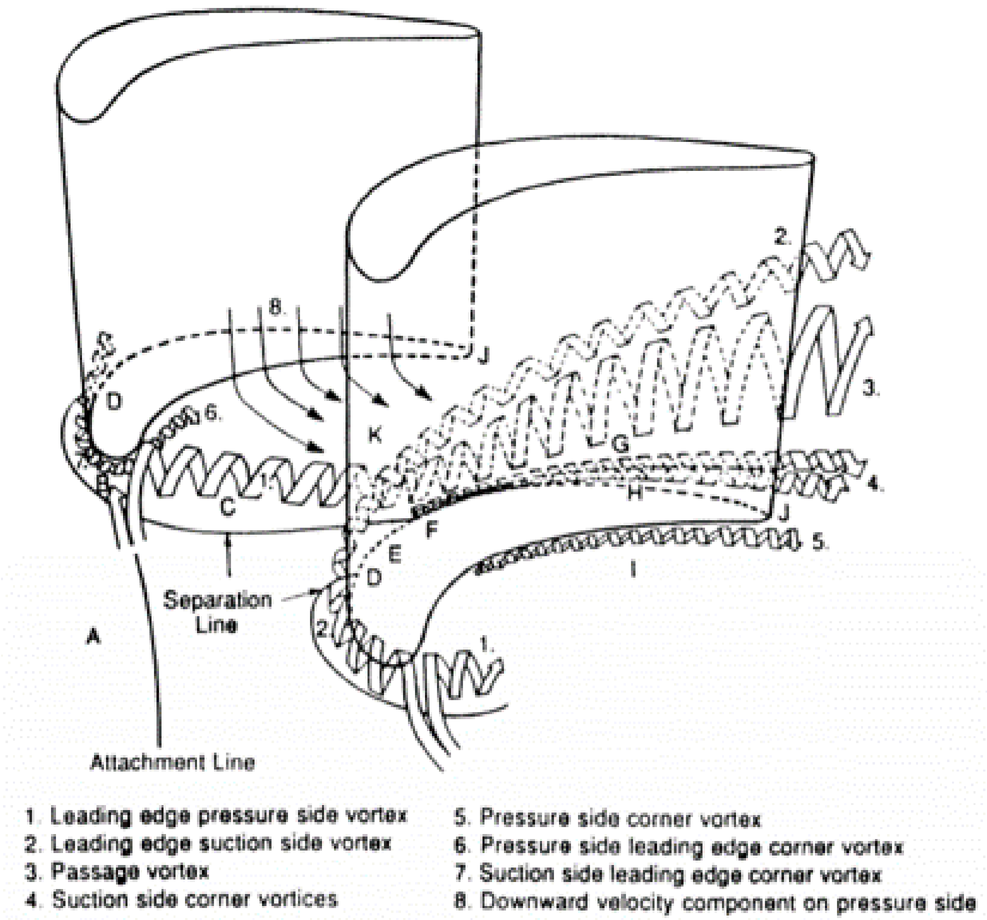

Figure 2.7: Categorisation of vortices generated by the boundary layer separation over turbine nozzles [52]

Additional sources of pressure loss are exit Mach number and inlet turbulence intensity, both with a proportional relationship. An analogue effect is given by the presence of film cooling, which, again, tends to augment pressure losses [45].

2.2.2 Film cooling

Cooling in gas-turbine flowpath components is usually realised by means of bleed air extracted from the compressor module at appropriate stages, although other fluids may be employed for such purpose, such as water, which however is possible only when water sources are available, e.g. in combined-cycle power plants. Such bleeding constitutes a penalty to the thermodynamic cycle, since work is performed to compress it, but none or limited power can be extracted through expansion in the turbine.

In the case of high-pressure nozzles or buckets, two forms of cooling scheme exists, i.e. internal and external, the latter being present in combination with the former. In the specific case of first stage nozzles, i.e. the component of main interest in this work, both schemes are typically present, since the component needs to withstand the highest temperature in the whole turbine module. Internal cooling typically consists in the conjunction of impingement inserts and pin-fin batteries, while external cooling is performed via film-cooling, that is air flowing through discrete holes and over the blade surface in a film fashion, as reported in Fig. 2.8 [53].

Moreover, cooling air is commonly extracted from the compressor discharge, since the maximum pressure available in the thermodynamic cycle is necessary to guarantee a positive back flow margin (BFM) in all operating conditions. This indicates that the cooling air pressure is always higher than the discharge flowpath one, i.e. cooling positive flow is ensured. BFM is usually defined as follows, with $P_{c,in}$ being the cooling inlet pressure and P_g the flowpath gas pressure:

$$BFM = \frac{P_{c,in}}{P_g} - 1 \tag{2.6}$$

Furthermore, in addressing film cooling effectiveness, specific design parameters shall be considered, i.e. blowing (BR, or M), velocity (VR), density (DR) and momentum ratios (I):

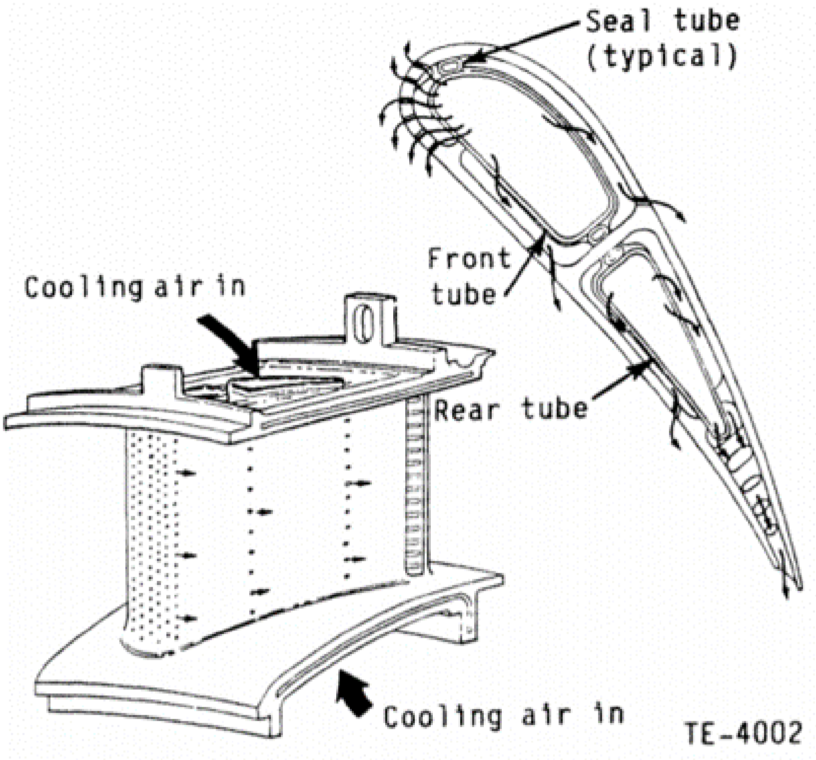

Figure 2.8: Typical internal and film-cooling scheme of a high pressure nozzle [53]

$$BR\ (M) = \frac{(\rho V)_c}{(\rho V)_g} \tag{2.7a}$$

$$VR = \frac{V_c}{V_g} \tag{2.7b}$$

$$DR = \frac{\rho_c}{\rho_g} \tag{2.7c}$$

$$I = \frac{(\rho V^2)_c}{(\rho V^2)_g} \tag{2.7d}$$

L'Ecuyer and Soechting [54] have also classified the characteristic regimes by which film cooling effectiveness can be categorised, based on a flat plate reference geometry, that are:

- *Mass addition* - Effectiveness level increases with BR, as per the increased thermal capacity of the coolant, while its distribution is independent of DR and VR;

- *Mixing* - Effectiveness distribution depends on BR, DR due to the opposing influence of increased thermal capacity and increased coolant-freestream mixing and penetration;

- *Penetration* - Effectiveness distribution is dominated by a complex interaction of excessive coolant penetration and augmented turbulent diffusivity of the coolant due to a high VR.

Based on Pedersen et al. [55] data, who considered a flat plate with a single row of holes, 35° injection angle and 3 pitch-to-diameter ratio, the just listed regimes are defined as per the following:

- *Mass addition* - $VR < 0.25$;
- *Mixing* - $0.25 < VR < 0.8$;
- *Penetration* - $VR > 0.8$;

The fundamental parameter for assessing film cooling performance is the adiabatic effectiveness η_{ad}, which is defined as:

$$\eta_{ad} = \frac{T_g - T_{aw}}{T_g - T_{c,out}} \tag{2.8}$$

Where T_{aw} is the adiabatic wall temperature, i.e. the temperature at the wall surface in case no heat flux is allowed to be exchanged between fluid and solid. Based on this, η_{ad} represents the normalised adiabatic wall temperature corresponding to the gas temperature adjacent to the surface. Fig. 2.9 shows a typical distribution of film-cooling adiabatic effectiveness as per different BR values.

Ideally a film of coolant would be introduced onto the surface of an airfoil using a slot angled almost tangential to the surface, since this would provide a uniform layer that remains attached to the surface. However, long slots would seriously reduce the structural strength of the airfoil, thus are not feasible. As a consequence, coolant is typically introduced using rows of holes, with the film cooling performance being dependent on the hole geometry and the layout configuration of the holes. Furthermore, various factors associated with the coolant and the mainstream flows nature are key in the determination of film cooling performance, among which the most relevant are blowing ratio, density ratio and curvature.

Baldauf et al. [57] have studied the dependence of film cooling effectiveness on blowing ratio BR (varying from 0.2 to 2.5) for a 30° inclined cylindrical-holes row

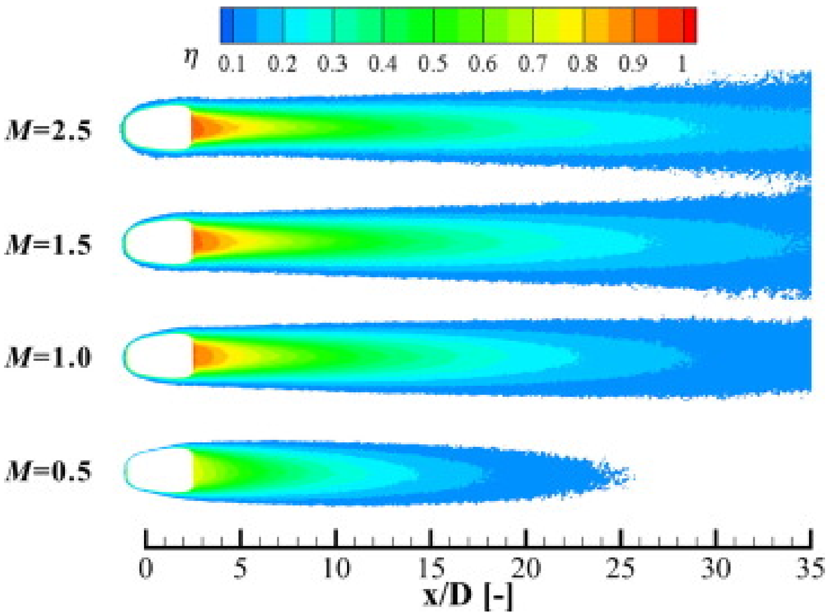

Figure 2.9: Typical distribution of film-cooling adiabatic effectiveness as function of blowing ratio M [56]

on a smooth flat surface. Fig. 2.10 reports the increasing trend of effectiveness peak until $BR = 0.6$, while from $BR = 0.85$ onwards such peak level reduces in addition to moving farther from the injection point. This is a clear indication of the jet separating from the surface, i.e. the onset of the penetration regime.

Similarly, the non-dimensional temperature along the centerline of a cooling jet exiting a cylindrical hole is illustrated in Fig. 2.11 for three different momentum ratios I. The jet is shown to be attached, detached then reattached or fully detached for respectively $I < 0.4$, $0.4 < I < 0.8$ and $I > 0.8$.

As far as density ratio is concerned, common engine values are $DR \approx 2$, while often experimental test rigs are operated in closer or even isothermal conditions, depending on the adopted measurement technique, which makes $DR \approx 1$. Thole et al. [58], Pedersen et al. [55] and Baldauf et al. [57] have found that maximum average film effectiveness on a smooth flat surface with $DR = 2$ can be 20% higher than with $DR = 1.2$ near the whole, while values were comparable farther downstream. Narzary et al. [59] studied the effect of DR on a prismatic blade, confirming that film cooling effectiveness increases with DR, in addition to being also affected by secondary flows, since, for instance, its distribution is spatially altered by the passage vortex on the suction side, as highlighted in the right-half of Fig. 2.12.

Furthermore, as also reported by Mayle et al. [60], Ito et al. [61] and Boyle and Ameri [62], Fig. 2.12 shows the effect of curvature on film effectiveness. In fact, concave

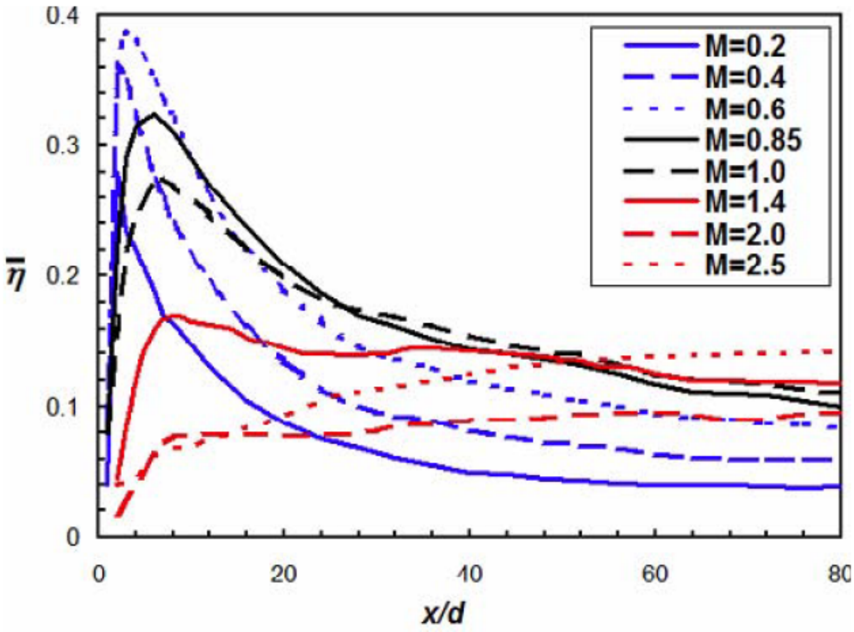

Figure 2.10: Distribution of film-cooling adiabatic effectiveness as per varying blowing ratios M [57]

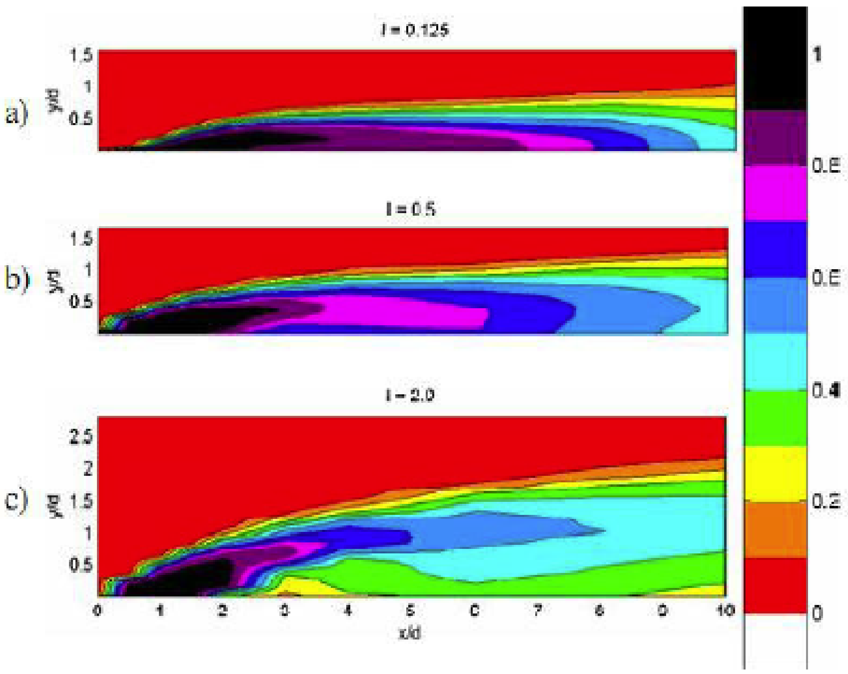

Figure 2.11: Attached, detached then reattached and fully detached film-cooling jet as function of momentum ratio I [58]

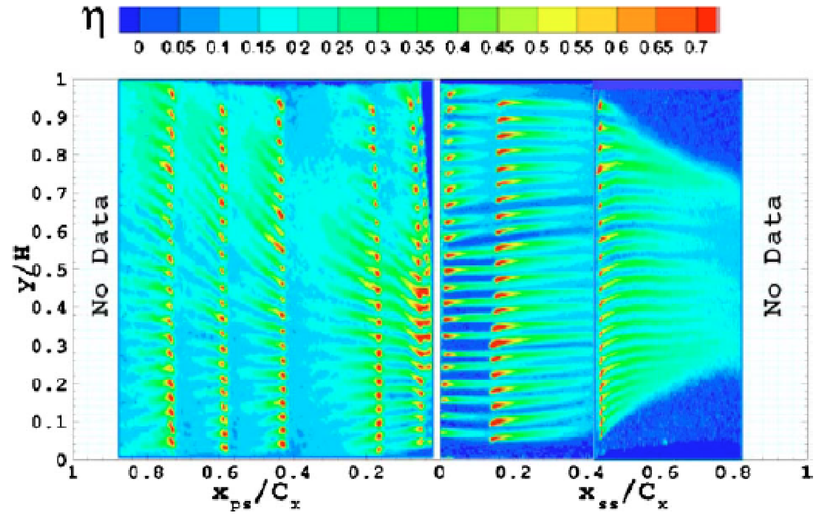

Figure 2.12: Film cooling adiabatic effectiveness on a prismatic blade affected by secondary flows [59]

surfaces (airfoil's pressure side) present a film effectiveness roughly 20% decreased with respect to flat plates, whereas convex surfaces (airfoil's suction side) have about 20% increased film effectiveness, at fixed BR. This is ascribable to the pressure gradient, which moves the cooling jets away from concave surfaces, while favours the jets attachment on convex surfaces.

Lastly, the study of the physics involved in film cooling include also the interaction of the coolant with the main stream in terms of the vortical structures generated, which is known in literature as "jet in crossflow". Such structures are reported in Fig. 2.13 and listed hereafter:

- *Jet shear-layer vortices* - Generated by the instability of the annular layer, which is subjected to shear stress and tends to separate at the hole exit in a ring fashion;
- *Horse-shoe vortex* - Created in a similar way to the flow structures forming in correspondence of solid obstacles, this can be responsible of the lateral spreading of coolant over the surface;
- *Counter-rotating vortex pair (CVP)* - Generated immediately downstream of the hole exit, these vortices are strengthened but also bent by the interaction with the cross flow in a kidney-shaped structure, which, although the causes of its formation are not universally recognised [63, 64], makes them responsible for mixing and either promote the lateral spreading of the jet or sometimes induce its lifting with a negative effect;

- *Wake vortices* - Caused by the separation of the boundary layer on the surface right behind the jet, these get lifted off by the jet itself and dragged downstream.

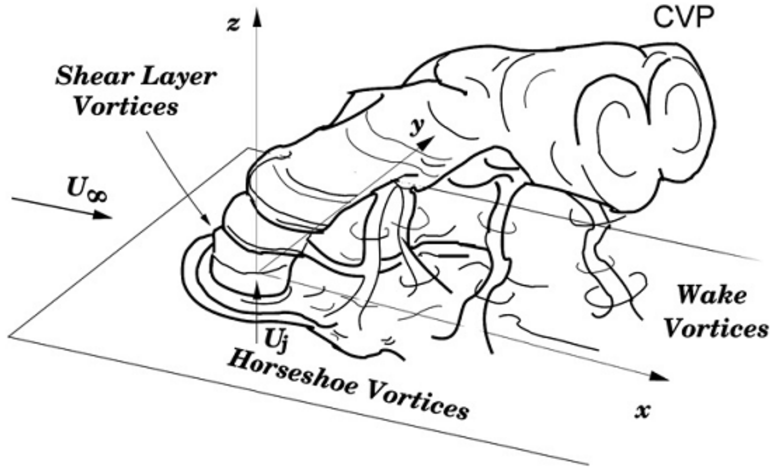

Figure 2.13: Jet in crossflow vortical structures [65]

Moreover, it is to be emphasised how the injection angle and VR need to be controlled appropriately, since, as already mentioned, high VR values lead to the full penetration and detachment of the jet, which then follows the mainstream flow, while suitable VR values have the jet kept attached to the surface, targeting the desired protection effect. In addition, as coolant and free stream flows undertake turbulent mixing at the hole exit, conveniently, neighbouring jets can merge together building up a blanket of coolant at some distance downstream, based on the jet spacing, which can be enhanced by realising multiple-row and staggered holes arrangements.

2.3 Review of past researches

2.3.1 Demonstrative early stage rigs

The very first facilities built in the early 1980s were designed for proof-of-concept investigations on the combustor/turbine interaction subject. It is not intended here to present them in details but the three most important ones are introduced:

- The Warm Core Turbine Test Facility ($WCTTF$) located at the Nasa Lewis Research Center (Cleveland, Ohio) was developed in 1983 [66]. The scaled down high pressure turbine stage shown in Fig. 2.14 is fed by the burnt mixture of a primary flow can-annular combustors with added cooling air from four slots, providing only a radially distorted temperature field, which affects only secondary flow structures, not altering efficiency.

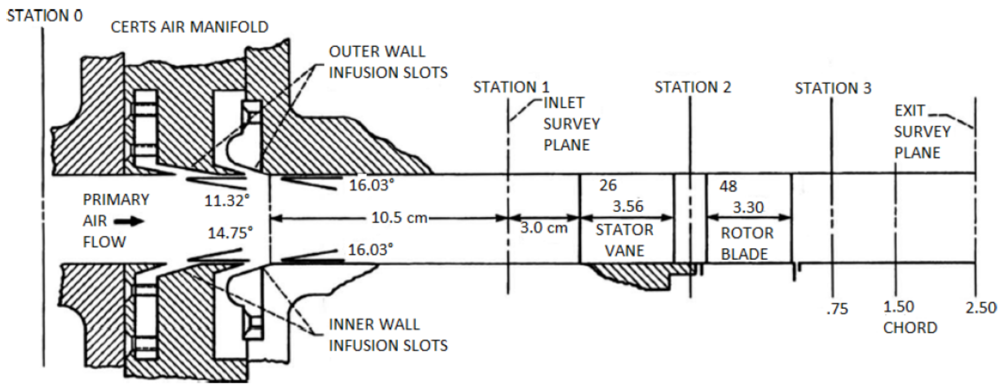

Figure 2.14: Warm Core Turbine Test Facility ($WCTTF$) at the Nasa Lewis Research Center (Cleveland, Ohio) [66]

- The Large Scale Rotating Rig ($LSRR$) located at the United Technologies Research Center (East Hartford, Connecticut) [67] was as well realized in 1983. For this facility, the hot streak was simulated by a local density change in an isothermal flow through the injection of CO_2 upstream of the turbine parts, as sketched in Fig. 2.15.

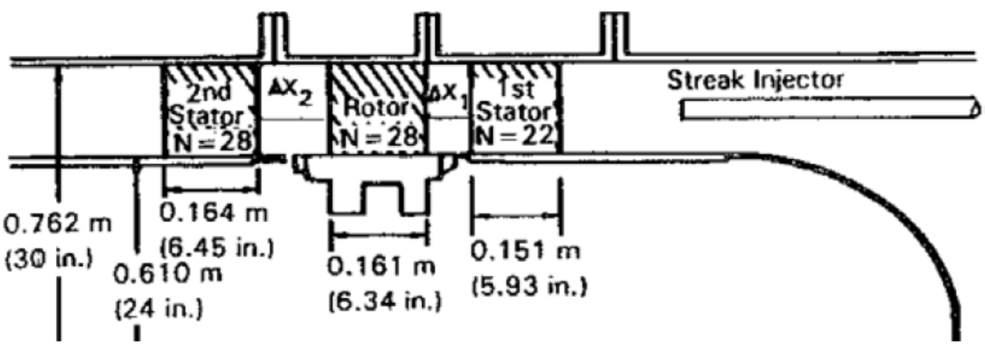

Figure 2.15: Large Scale Rotating Rig ($LSRR$) at the United Technologies Research Center (East Hartford, Connecticut) [67]

- The Rotating Blow-Down Facility ($RBDF$) at the Massachusetts Institute of Technology (Cambridge, Massachusettes) was developed in 1989. The facility was specifically designed to reproduce both radial and circumferential non-uniformities, by means of respectively a controllable heat exchanger and a by-pass duct as illustrated in Fig. 2.16.

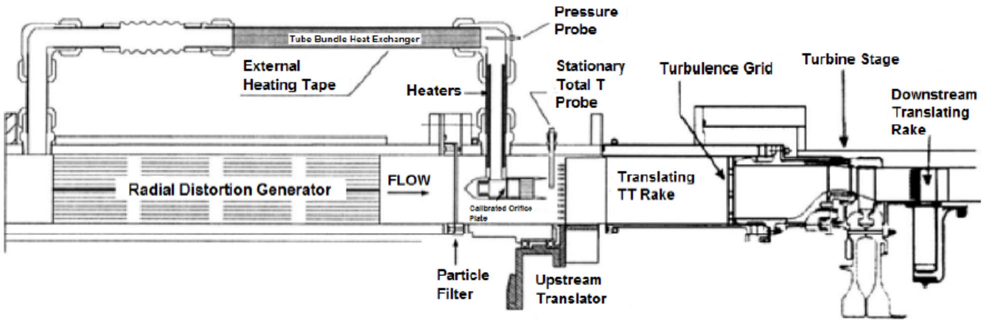

Figure 2.16: Rotating Blow-Down Facility ($RBDF$) rig at the Massachusetts Institute of Technology (Cambridge, Massachusettes) [68]

2.3.2 Engine representative recent rigs

More realistic test rigs started to operate about twenty years ago in the USA and UK. They differ from the previous ones by more engine representative layouts, more complex and heavy instrumentation and a blow-down operating mode whereas early facilities operated continuously. These facilities were designed to get a deep insight on the hot streak interaction with turbines and provided a large amount of information. A very brief overview of these rigs follows:

- The Isentropic Light Piston Facility ($ILPF$), built at QinetiQ (Hampshire, UK) in 2002, represents the first large test facility for studying combustor hot streaks in Europe [69]. A piston was used to rapidly compress air to feed a high pressure turbine stage in a blow-down mode. The rig constitutes a widely used reference for hot streak transport studies.

- The Turbine Research Facility (TRF) located at the Air Force Research Laboratory (Dayton, Ohio) dates to 2004. A heated and pressurized nitrogen tank was discharged through a combustor emulator (see Fig. 2.17) feeding the turbine and allowing to set some parameters of interest as Mach and Reynolds numbers, turbulence intensity, corrected speed and gas-blades temperature ratio as to study the alteration of aerodynamics and heat transfer on the nozzles due to the non-uniform pressure and temperature field [70].

- The University of Texas at Austin in 2004 has conducted an experimental campaign [43] on a linear rig installed in a low speed wind tunnel featuring an array of electrical resistances to generate a hot streak and three scaled-up film-cooled nozzles, as illustrated in Fig. 2.18. The work aimed at reducing the hot spot strength by adequate positioning of the hot streak and the use of film cooling.

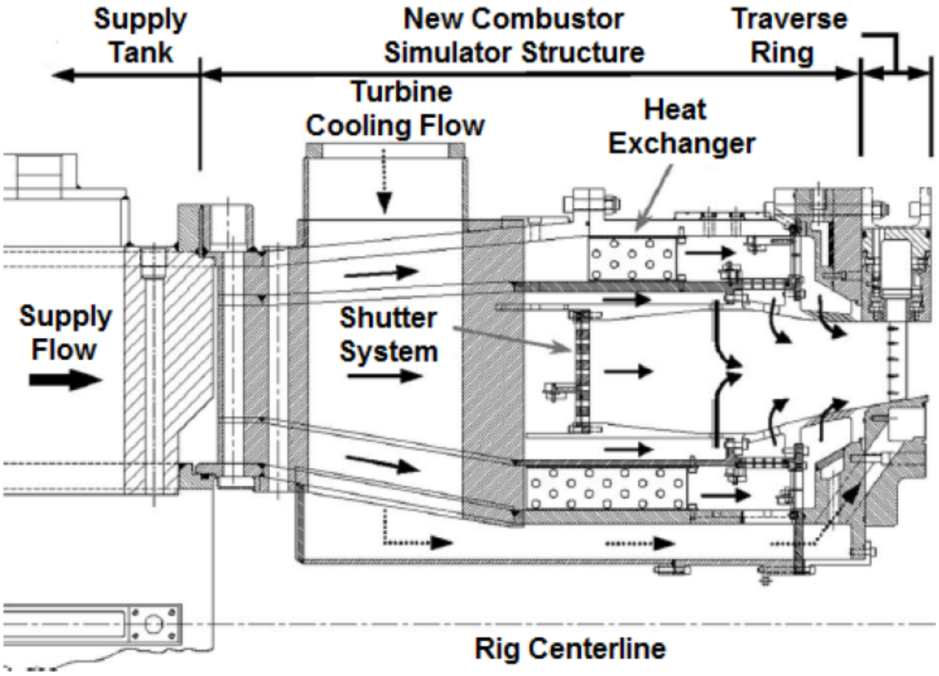

Figure 2.17: Turbine Research Facility (*TRF*) rig at the Air Force Research Laboratory (Dayton, Ohio) [70]

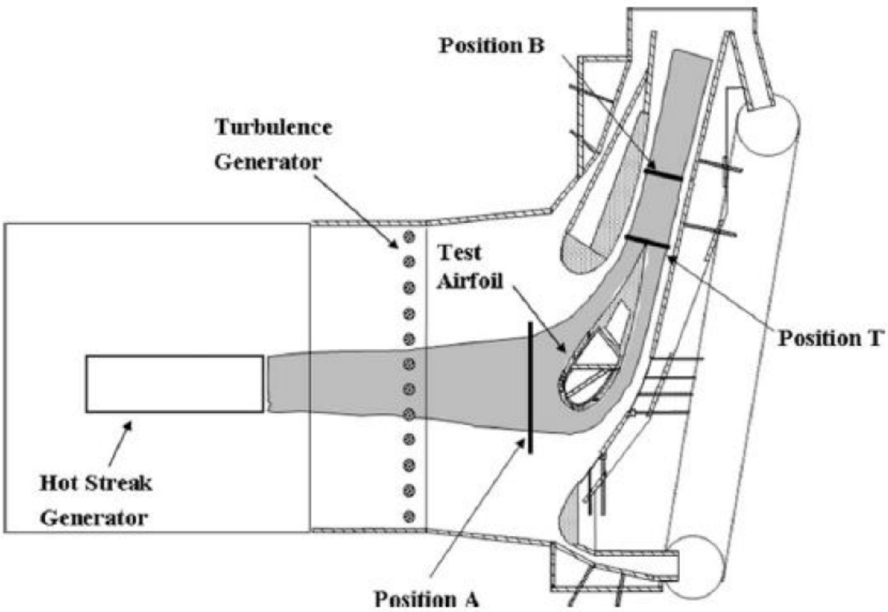

Figure 2.18: The linear cascade of the University of Texas at Austin [43]

- The University of Oxford (UK) recently presented a new linear blow-down experimental facility at the Osney laboratory (see Fig. 2.19) dedicated to the combustor/turbine interaction for heavy duty gas turbines [71]. Special insight was put on the interaction between the wake shed from the combustor lateral wall and the nozzles, typical of can-type combustors, allowing also for testing different streak-to-nozzle clocking positions yet with an isothermal flow.

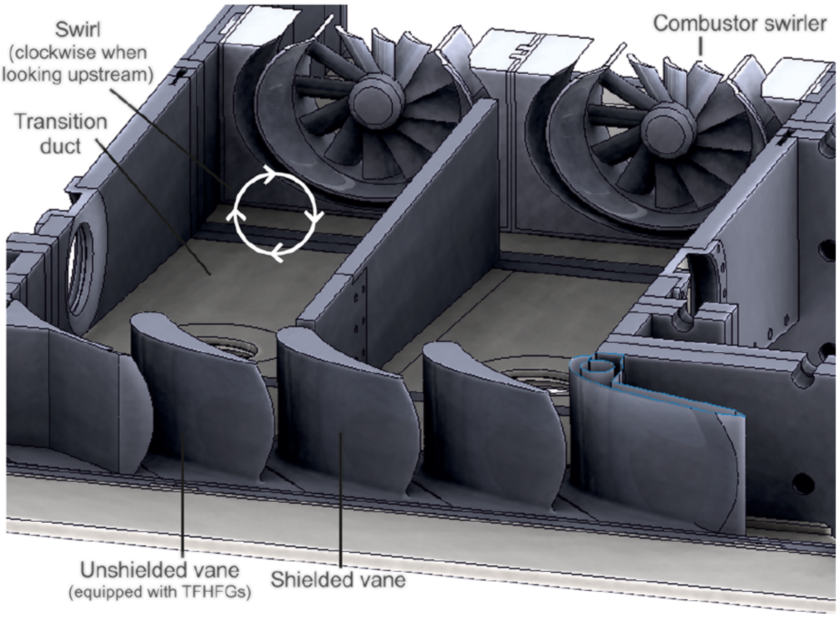

Figure 2.19: The linear cascade of the University of Oxford (UK) at Osney laboratory [71]

2.3.3 Lean-burn combustor simulators

Although all the previously listed works have contributed to build the knowledge on combustor/turbine interaction, none of these really presented realistic swirling flows, with turbulence and pressure profiles artificially realised by means of grids or dilution holes. By contrast, some very recent works have included the presence of actual swirling devices, as to better account for the impacts on secondary flows, pressure losses and nozzles film-cooling. As it is the aviation industry to drive most gas-turbine technology progresses, such modern rigs had the objective to study lean burn combustors. These are:

- The Oxford (UK) Turbine Research Facility ($OTRF$) was upgraded and changed name from the former Isentropic Light Piston Facility ($ILPF$) in 2008, as part of the Brite-Euram Turbine Aerothermal External Flows programme ($TATEFII$), when it was equipped with a well-defined temperature profile (Enhanced-$OTDF$) generator, enabling the investigation of hot-streak to NGV clocking effect. Later in 2011, the facility was further equipped with a lean-burn combustor representative swirl generator (see Fig. 2.20). The design process [72] ended up with a swirler able to generate maximum pitch and yaw angles of about ±50° at the combustor simulator outlet, with approximately constant temperature field. Qureshi et al. [51] carried out an experimental and numerical investigation on this test case to evaluate *NGV* aerodynamics and heat transfer in the presence of aggressive swirl. *CFD* calculations showed that the swirling structure is divided, by the nozzle *LE*, in two vortices being convected into the passages and responsible for the measured non-uniformities in heat transfer and aerodynamic load. In addition, Hall et al. [23] reported the challenges encountered during the design of combustor simulators with strong swirl and temperature distortion, since it is impossible to develop simulators identical to the real geometry, as it is impossible to replicate the unsteady phenomena stabilised by the combustion process in real applications that significantly alter the overall flow field.

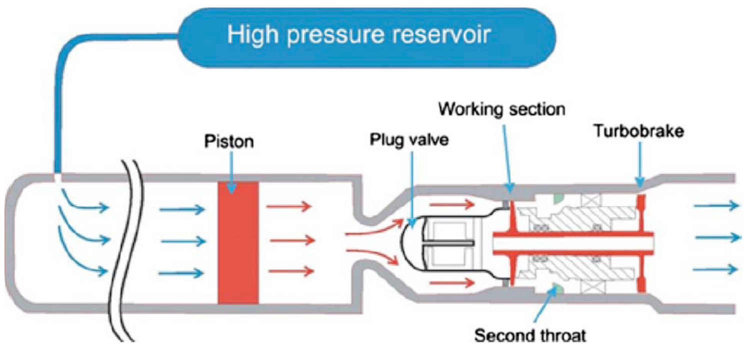

(a)

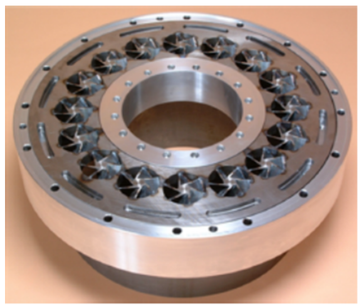

(b)

Figure 2.20: Oxford (UK) Turbine Research Facility (*OTRF*) rig (a) and swirlers module (b) [36]

- The Large Scale Turbine Rig (*LSTR*) at Darmstadt University (Germany), a scaled-up 1.5-stage low Mach number turbine, equipped with a lean combustor simulator [73] is illustrated in Fig. 2.21. Angles of ±15° can be achieved at the turbine inlet. *CFD* calculations carried out on such test case [74] have shown that the stage efficiency reduction of a given nozzle geometry can be as much as 2% shifting from either uniform or tangentially averaged inlet conditions to actual 2D conditions, for which both swirl and turbulence are considered.

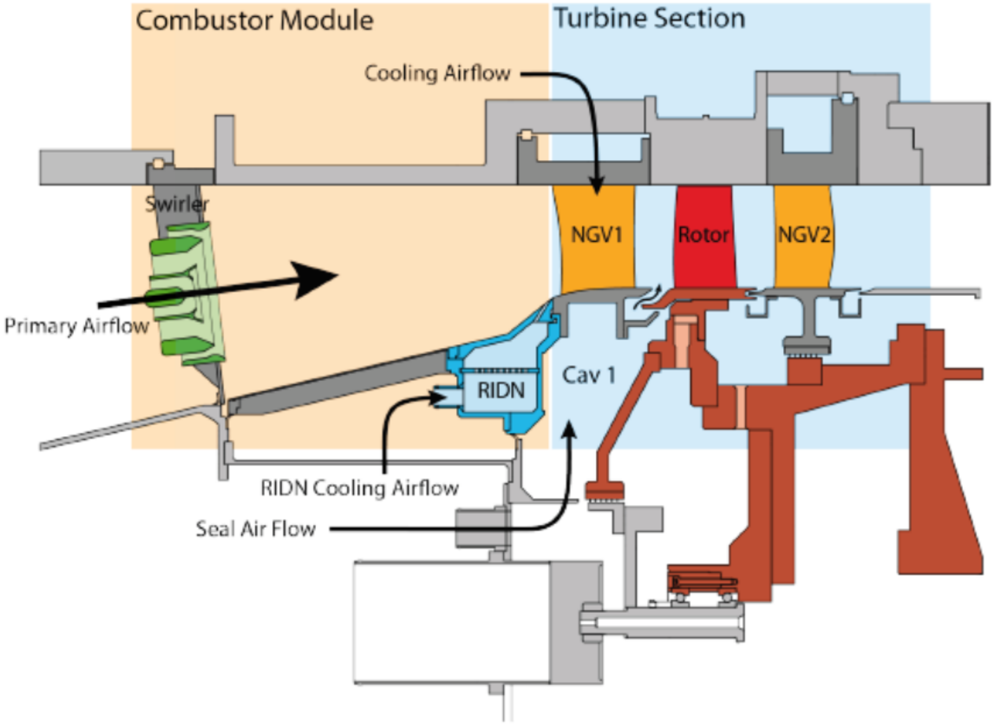

Figure 2.21: Large Scale Turbine Rig (*LSTR*) at Darmstadt University (Germany) [74]

2.4 CFD analyses of combustor/turbine interaction

2.4.1 Key aspects

Experimental investigations on combustor/turbine interaction are technically difficult and economically expensive. As modern aero-engines and many industrial turbines employ annular combustion chambers, these cannot be reproduced by simply isolating a limited sector of the chamber, since lateral walls would alter the periodicity of the flow [75].

This results in the necessity for related test rigs of reproducing the full annulus or, at least, a sector wide enough as to be engine representative. In addition, the design and operation of reactive rigs present several problems, usually bypassed by the adoption of cold experimental configurations, which however are unable to completely reproduce the flow field of real combustion chambers, since the combustion process itself plays an essential role in the flow dynamics.

For these reasons, the development of accurate *CFD* tools is fundamental as to get a better and wider understanding of the physics involved along with combustor/turbine interaction. In literature it is shown that the use of state-of-the-art numerical tools for the study of the subject present some technical limitation, at least until recent times.

In fact, the flow field within the combustion chamber and the one through the turbine are very different from one another, which preferably requires specific numerical features for solving the two. These are summarized as follows:

- *Solution algorithm* - A low-Mach (quasi-incompressible) reactive flow is present in the combustion chamber, while the high pressure turbine (*HPT*) usually operates with high-Mach or even transonic flows. The resolution of low- and high-Mach flows usually requires different algorithms in order to ensure stability and accuracy to the solution. In most cases, the combustor is solved by a pseudo-incompressible low-Mach approach or a pressure-based compressible solver, while density-based solvers are generally used in the turbine. Even though this differentiation is still common, nowadays modern compressible solvers have more and more widened their range of applicability.

- *Solver features* - To cope with stator-rotor interfaces, turbomachinery solvers shall include sliding meshes, mixing-plane and frozen-rotor interfacing options, in addition to specific shock capturing techniques if needed. For the combustion chamber, on the other hand, additional equations for the reactive flow are essential.

- *Grid requirements* - Since the combustion chamber is a very heterogeneous component, including cooling holes, swirlers and other complex geometrical features, it is common practice to simplify the meshing process by the implementation of unstructured grids, whereas airfoils are mostly modelled with structured ones, which ensures a higher quality of the boundary layer solution.

- *Turbulence resolution* - Combustion chambers flow is typically unsteady and characterized by fluctuating structures (e.g. *PVC* vortices), which calls for the use of *LES*, hybrid *RANS-LES* or at least unsteady *RANS* (*uRANS*) approaches with the intent of providing more accurate solutions. Despite *LES* being nowadays the state of the art in industry for combustors and the increasing interest in spreading its use to high pressure turbines [76], its computational cost remains prohibitive for the current industrial practice.

2.4.2 Past CFD studies

The simultaneous simulation of combustor and turbine has been carried out so far, as available in the open literature, via two possible approaches, namely "integrated" and "coupled". The former consists in the use of a single solver for the combustor

and turbine modules, with the advantage of handling one single and coherent domain, although time step sizes shall be properly chosen due to the different flow timescales of the two components. On the contrary, the latter enables to maximise the benefits from different solvers being optimised and hence employed within their best application ranges, with freedom to march at different time step sizes, even if this comes at the cost of more complex set-up and information-exchange phases.
Hereafter is a brief overview of previous works adopting one of the two possible schemes:

- The "coupled" approach was firstly investigated during a long-term research programme in Stanford with the aim of simulating all the components of a turboengine at the same time [77], as sketched in Fig. 2.22. This was realised by coupling a pseudo-incompressible low-Mach *LES* solver for the combustion chamber to a compressible *uRANS* solver for compressor and turbine. An overall converged solution was obtained by exchanging information between the solvers during the simulation: if only combustor and turbine are to be mentioned, body forces were used to drive the mean flow field at the *LES* outlet obtained by the steady *RANS* downstream, while inlet conditions for *RANS* were obtained by time averaging the *LES* solution [78].

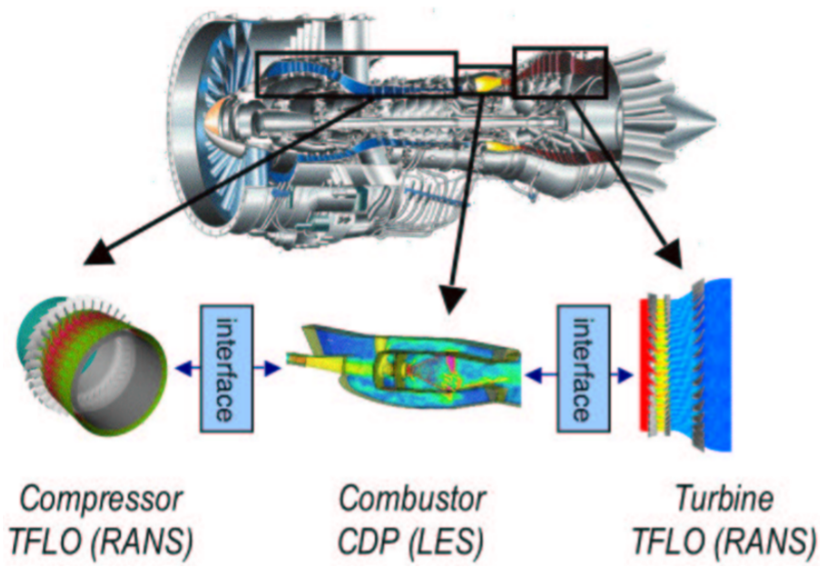

Figure 2.22: Interfaces definition for the study of compressor (*RANS*), combustor (*LES*) and turbine (*RANS*) [78]

- Klapdor [79] and Klapdor et al. [80] made use of an "integrated" approach by developing an in-house ad-hoc code to handle both the low-Mach reactive flow in the combustion chamber and the transonic flow through the turbine. This was achieved in two steps: first by extending an incompressible *SIMPLE* solver to all Mach number flows, then modifying it to allow for dealing with combustion and successfully studying combustor/turbine interaction. Particular attention was paid to the effect of the nozzles' presence on an *RQL* combustor outlet flow field, as shown in Fig. 2.23.

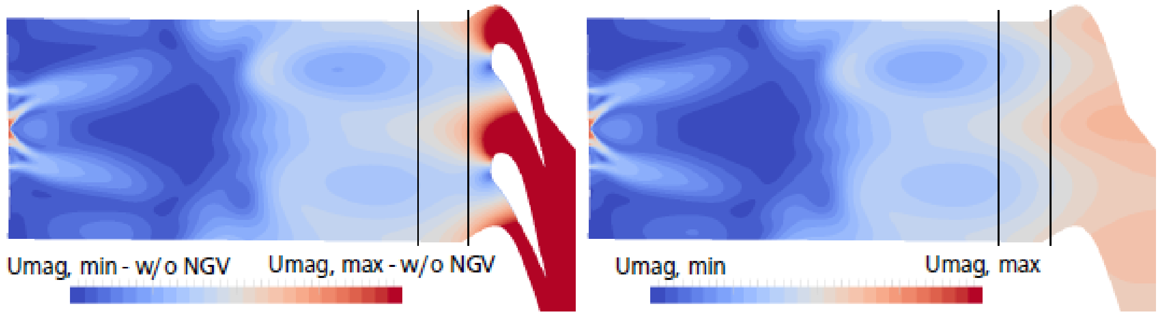

Figure 2.23: Distribution of velocity magnitude on a circumferential cut plane with and without nozzles [79]

- The "coupled" procedure was also utilised by Collado-Morata [81], who set up the compressible *LES* pressure-based code *AVBP* and the compressible *uRANS* density-based solver *ElsA* on simple test cases and then on an *RQL*-combustor/turbine arrangement (see Fig. 2.24 for reference). An overall convergence is reached by exchanging all time-averaged characteristic variables downstream to the *uRANS* solver, while transferring pressure upstream to *LES*.

- Another interesting piece of work on combustor/turbine interaction involving "coupled" numerical simulations was performed more recently by Vagnoli [82]. Two different codes were employed based on the *OpenFOAM* platform to solve the combustor (pressure-based *PIMPLE* algorithm *uRANS*/*LES*) and the turbine flows (density-based dual time-stepping technique *uRANS*/*LES*). Characteristic variables are exchanged to the downstream subdomain, while the pressure wave is transferred backwards. This approach was exploited to study the migration of the hot streak generated by a lean-burn combustor through a nozzle cascade, as shown in Fig. 2.25;

- One further "coupled" approach example is the one of Insinna [83] between two *RANS* simulations of combustor and turbine separately, based on the ANSYS® pressure-based *SIMPLE* solver and a density-based in-house code. The procedure was successfully applied to a realistic lean-burn-combustor/turbine test case as depicted in Fig. 2.26, together also with an extension to the use of *SAS* into the combustion chamber and *uRANS* in the turbine.

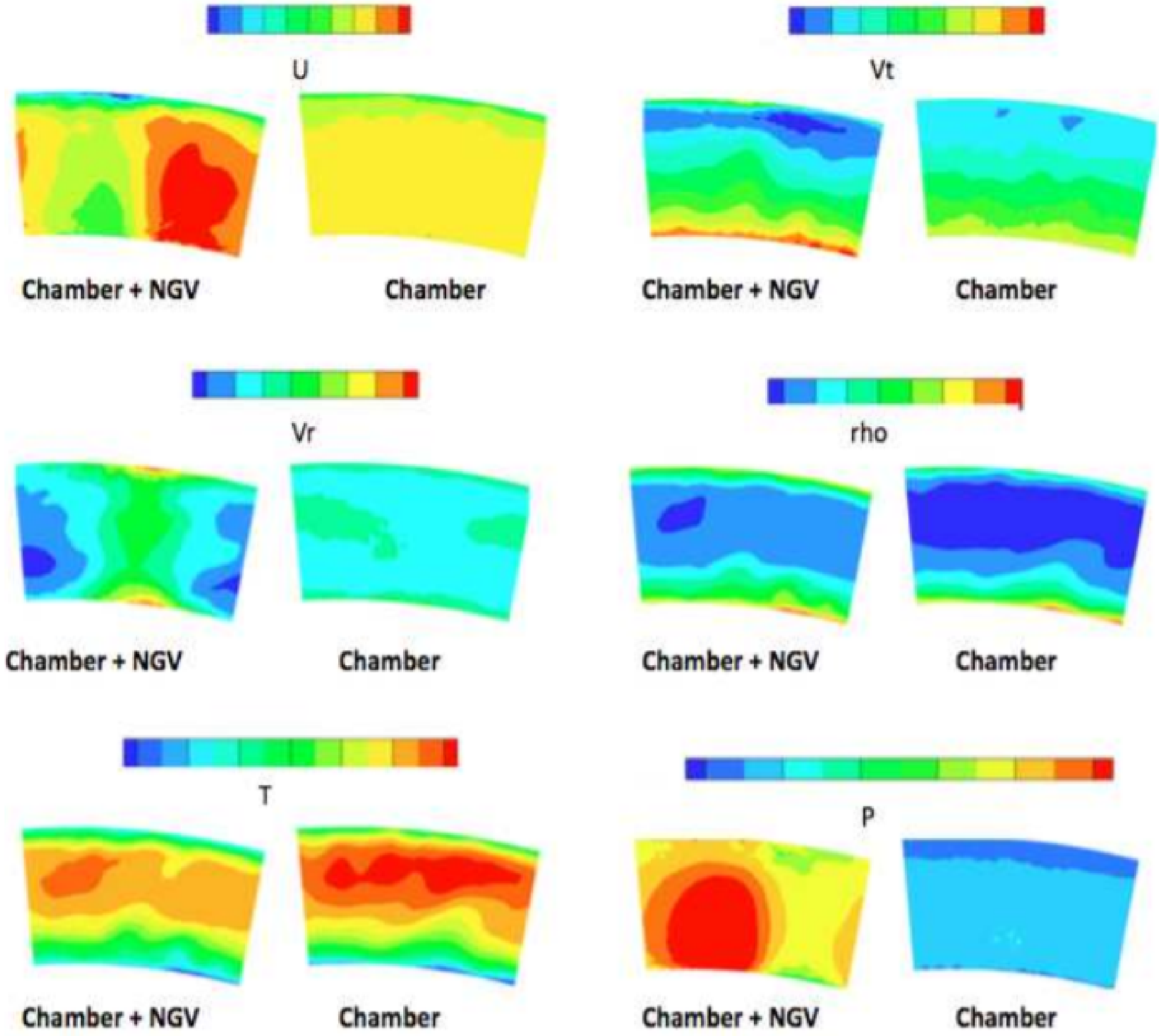

Figure 2.24: Mean aerodynamic quantities at the combustor/turbine interface with and without nozzles [81]

- Lastly, it is worth mentioning the extensive work performed by Koupper [22], who, in the framework of the FACTOR programme [75], reproduced an experimental lean-burn combustor simulator by means of a single sector model with periodic boundary conditions and including both the combustor chamber and the first stage nozzles in an "integrated" manner. Most relevant quantities were found to be well captured by *LES* (pressure-based code *AVBP*) with respect to experimental data at the interface plane (including turbulence [22]). Moreover, *LES* demonstrated to be able to discriminate the presence of a pronounced hot streak and swirling flow and its propagation through the nozzles [84], as reported by the non-dimensional temperature contours in Fig. 2.27.

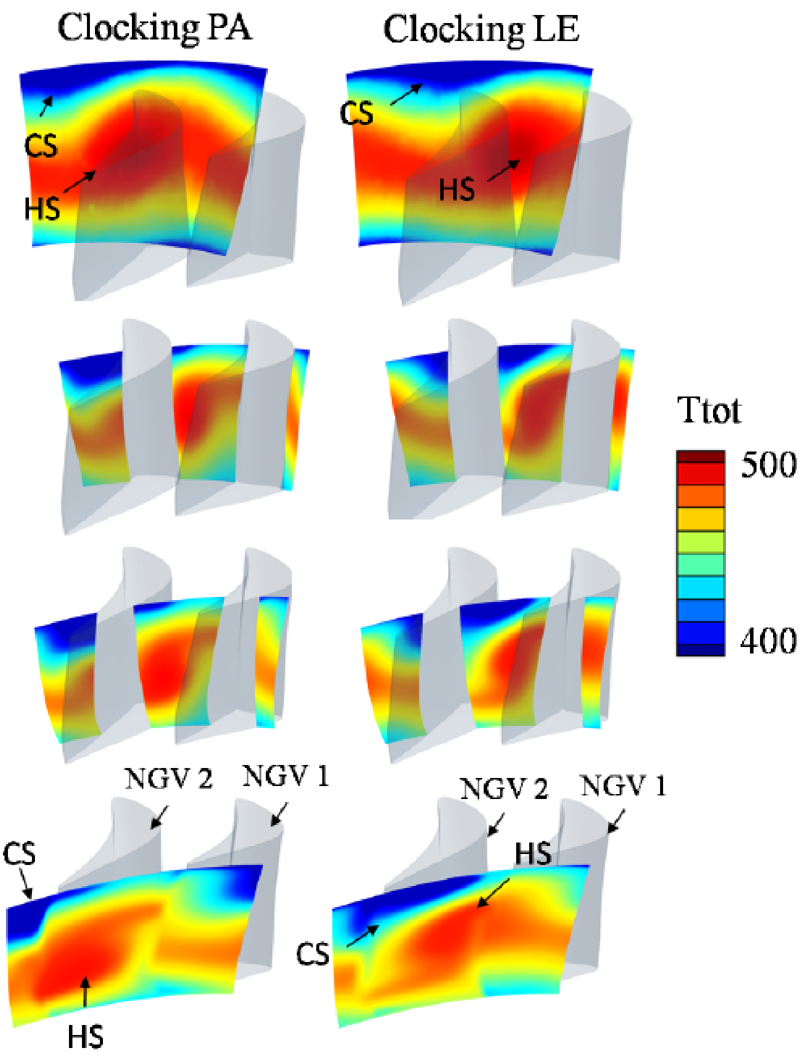

Figure 2.25: Total temperature contours through the nozzles based on the hot streak (*HS*) clocking with the vane passage (*PA*) or leading edge (*LE*) [82]

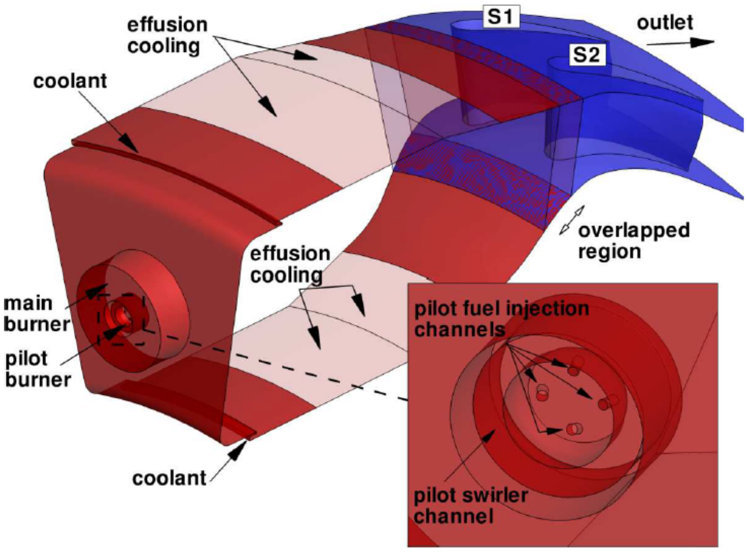

Figure 2.26: Combustor/turbine simulation domain with an overlapped region for the application of the “coupled” approach [83]

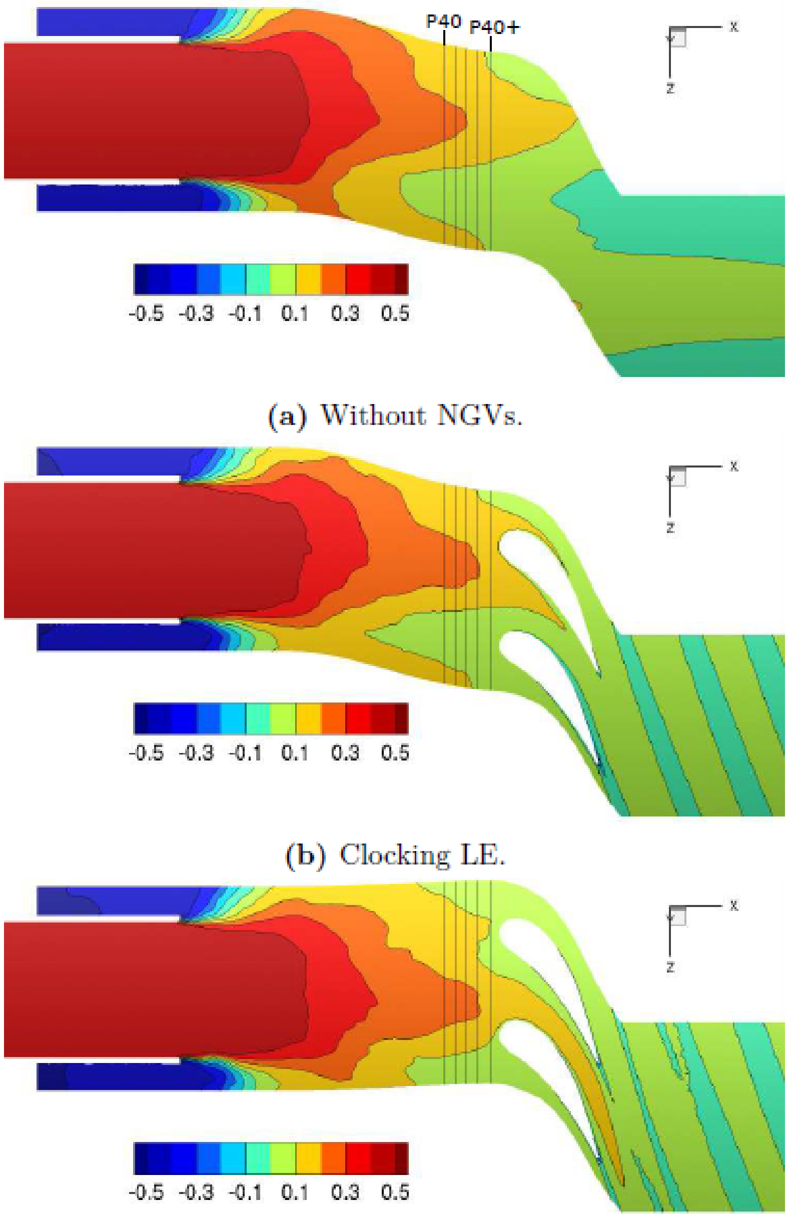

(a) Without NGVs.

(b) Clocking LE.

(c) Clocking PA.

Figure 2.27: Non-dimensional temperature contours at the midspan plane from the combustor through the nozzles without *NGVs* (a) and based on the swirlers clocking with the vanes leading edge *LE* (b) or passagge *PA* (c) [22]

Chapter 3

Methodologies

Contents

3.1 Experimental apparatuses and techniques

3.1.1 FACTOR test rig overview

As there is currently little experimental data regarding a turbine operated with realistic lean-burn combustor outflow conditions, the European project *FACTOR* (Full Aerothermal Combustor-Turbine interactiOn Research) has promoted such subject of study. An experimental facility was developed, within the project, at the *DLR* (*Deutsches zentrum fur Luft und Raumfahrt* - Gottingen, Germany). The research center, hosting a modern aero-engine combustor simulator and a 1.5 high pressure turbine stage (one stage plus a strut module), was operated at realistic Reynolds and Mach numbers. A sketch of it is reported in Fig. 3.1.

The main objective of the project was to carry out measurements, by means of the most advanced techniques, on this infrastructure, in order to create a wide database

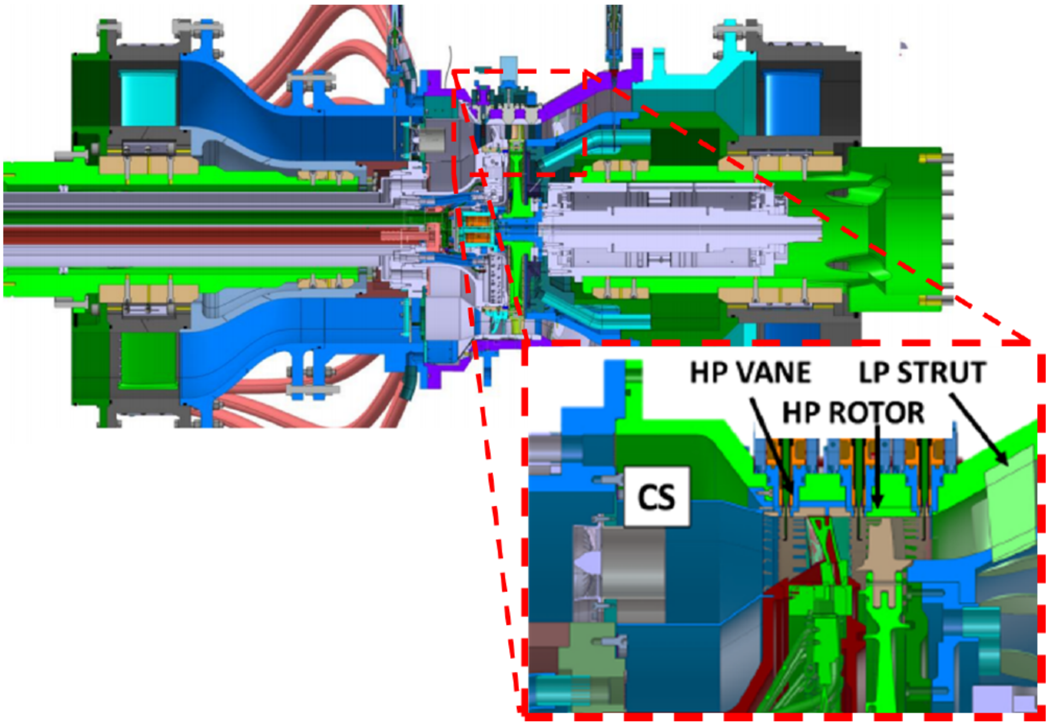

Figure 3.1: Sectional view of the *FACTOR* full annular rig

to set up boundary conditions and make comparisons with conventional and advanced *CFD* methods dedicated to the modelling of this interface area. A large test campaign was scheduled to improve the knowledge of such complex system, through a massive investigation. Probe traversing were realised to measure velocity, pressure and temperature at several axial positions, as well as "Raman" spectrography for the measurement of gas temperature in addition to infrared (*IR*) thermography to evaluate surface temperatures, adiabatic effectiveness and heat transfer coefficient on nozzles, buckets and struts.

An initial planning of the experimental campaign can be found in the summary of Battisti et al. [85], even if it was subjected to some change over the course of the project due to challenges related to instrumentation integration and time constraints. The experimental campaign was scheduled to be completed by the end of 2017, but got prolonged until early 2019.

As a preliminary and preparation activity to the operation of the full bench, a non-reactive test rig with a more limited scope, but with the same main design features, was installed at the Technologies for High Temperature (*THT*) laboratory of the *University of Florence*, Italy, as illustrated in Fig. 3.2. The rig is composed of a trisector combustor simulator coupled with a high-pressure *NGV* cascade, as sketched in Fig. 3.3a. The combustor simulator was designed to be able to replicate the most relevant flow structures and mixing phenomena that take place inside a modern lean burn combustor and hence to achieve an engine representative combustor outflow. In particular the rig is capable to simulate both the presence of enhanced temperature distortions and an aggressive swirl field with the purpose of investigating their combined effects on the high pressure turbine and covering an aspect where a lack of literature data exists.

Figure 3.2: Photograph of the *FACTOR* test rig cell

Focusing on the combustor side and looking at Fig. 3.3b, a heated mainstream flow reaches a plenum chamber with the objective to slow down the flow and damp possible non-uniformities, prior to getting inside the combustion chamber through three axial swirlers. Two separate coolant flows, at ambient temperature, reach two annular (inner and outer) coolant cavities, via three pipes each. From these cavities, acting as plenum chambers, the cooling flows feed the inner the outer laser-drilled multi-perforated liners, reaching into the combustion chamber. The combination between the hot swirling mainstream and the cold liner coolant permits to achieve the desired aerothermal field at the combustor outlet after a significant annulus contraction, which, as a consequence, makes the flow accelerate towards the *NGVs*. The red arrows show the path of the

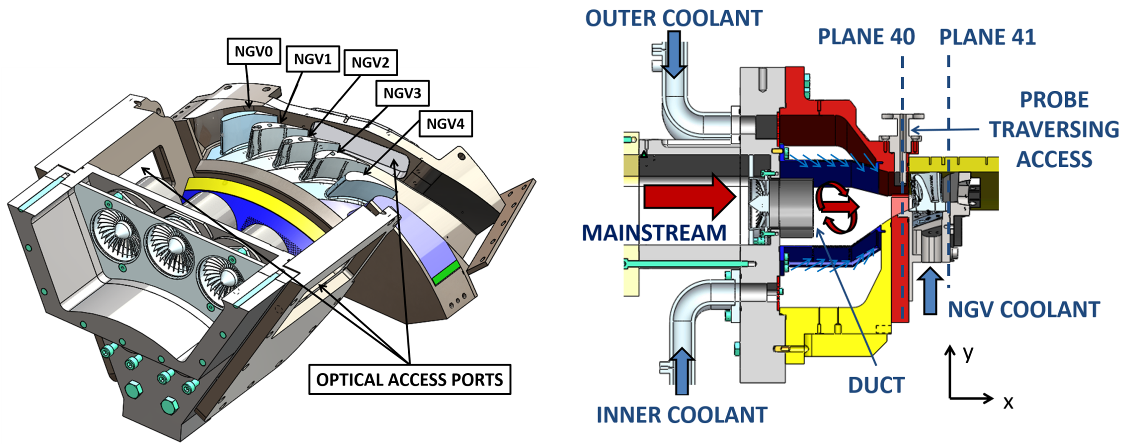

(a) (b)

Figure 3.3: *FACTOR* trisector rig layout: 3D CAD model (a) and sectional view (b)

heated mainstream, while blue ones represent the liner cooling flows.

Still with reference to Fig. 3.3b, the *NGV* module is identified by the grey component, where the *NGV* airfoils are hosted, and is provided with a plenum chamber to feed the film-cooling system, as indicated by the blue arrow. The yellow component, on the other hand, constitutes the outer casing and hosts the instrumentation accesses for probes traversing on the *NGVs* exit plane. The discharge component, not shown in Fig. 3.3 is an annular, right-turning duct, designed in order to follow the *NGVs* exit flow direction. Fig. 3.3b also shows the locations of the measurement planes at combustor and *NGVs* exit, *Plane 40* and *41* respectively.

Each module of the rig was designed as per the trend of development of modern aero-engines, in terms of liner coolant-mainstream air flow split in the combustion chamber, aggressive swirl and distorted temperature profiles at combustor exit and engine-representative film cooling system on the nozzles.
Starting from the specifications of the full annular combustor simulator of the *FACTOR* project at the *DLR*, the trisector rig, installed at the *THT* lab, was designed by *Safran* and *Avio Aero* (the industrial partners of the project) in order to precisely mimic a recent lean burn engine configuration and with the intent of capturing all physical scales at the combustor-turbine interface.

To ease operability and allow for the use of different measurement techniques, no combustion was enforced in the chamber and hence the temperature profile is obtained only by the mixing of hot (531 K) and cold (ambient) air streams, fed respectively to the swirlers and the cooling system (liner effusion and nozzles film-cooling). The axial swirlers consist of 30 flat nozzles disposed around a central hub, as designed by *Avio*

Aero, in order to create a representative flow field in the chamber without the effect of combustion and reach the target flow field and temperature patterns at combustor exit.

The inner and outer liners are multiperforated with different patterns of effusion holes, aligned with the streamwise direction (no compound angle) in a staggered configuration. Moreover the geometry of the chamber is not scaled with respect to a real engine (1:1 scale) and the combustor simulator key features are representative of a lean burn technology:

- A flow split with 65% of air mass flow going through the swirlers and 35% used for liner cooling;
- Liners are provided with an effusion cooling system, and no dilution holes are inserted;
- The inner liner is strongly convergent towards the final part of the chamber, with an angle of 35° (with respect to the horizontal axis).

The trisector configuration was adopted in order to better isolate the central sector flow field, target of all the measurements, and make it less sensitive to the presence of the rig lateral walls. The same configuration has been used in several works such as the ones carried out by Andreini et al. [86], Wurm et al. [87] and Meier et al. [88]. The results of preliminary CFD evaluations to verify this assumption can be found in the work of Koupper et al. [75].

An adaptive flange is located on *Plane 40*, to install the automatic traverse system, that was used for the probes handling. In order to perform optical measurements, such as Particle Image Velocimetry (PIV), the test rig includes two wide lateral pyrex windows, located at both sides of the combustor simulator. In order to achieve the test target, i.e. generating a lean burn representative flow field on *Plane 40*, ducts (35, 45 or 55 mm long, that is about 22, 29 and 35% of the total chamber axial extension) could be installed at the swirlers exit section. By doing so, the heated swirling mainflow is prevented from interacting with the cooling flows in addition to delaying the swirling structure opening, which occurs as soon as the mainflow enters the combustion chamber, with consequent loss of tangential momentum. This is comparable to shortening the combustion chamber.

At the end of the preliminary experimental validation, carried out by means of five hole probe measurements on *Plane 40*, the results of which are reported by Caciolli [20] and Bacci et al. [89], the configuration with the 55 mm ducts was chosen. This allowed to achieve the flow field illustrated in Fig. 3.4, defined by contours of temperature and flow angles patterns. Flow angles beyond ±50°, where achieved in a well-defined rotating structure.

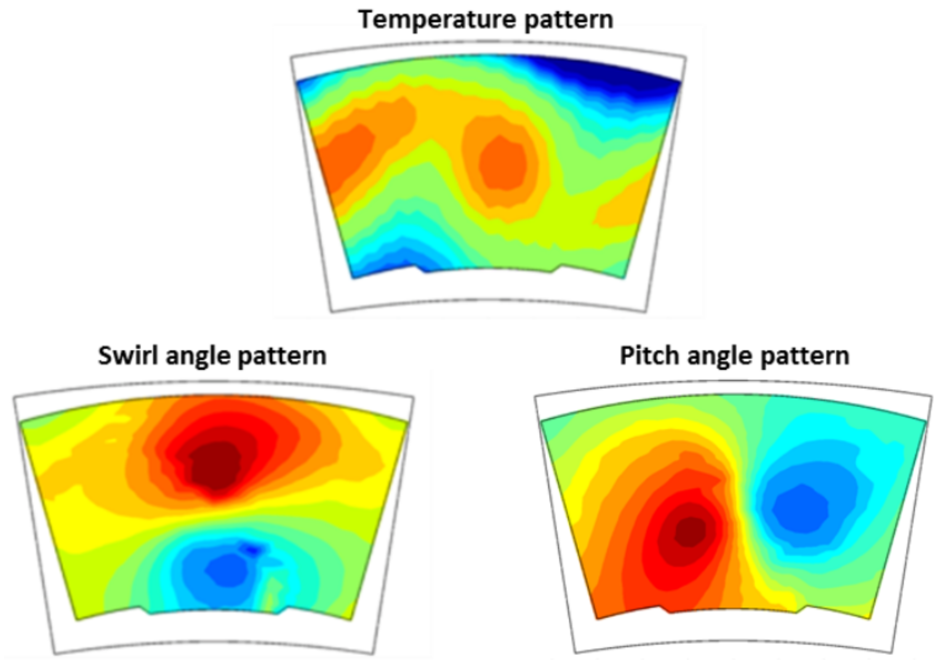

Figure 3.4: *FACTOR* - Temperature and flow angles patterns measured on *Plane 40* [89]

The aerodynamic design of the investigated nozzle guide vane and its cooling scheme definition were carried out by the *FACTOR* industrial partner *Rolls Royce*. The results coming from the preliminary *Plane 40* investigation [20, 89] were used as input. A CAD model of the *NGV* airfoil is reported in Fig. 3.5: the tip is at a constant radius of 280 mm, while the first part of the inner endwall has an increasing radius, to match with the converging shape of the inner liner, up to a 240 mm constant value in the final part.

An *NGV*-to-swirler count ratio of 2 was used, in order to provide a *CFD*-friendly domain. Furthermore, one *NGV* has the leading edge aligned with the swirler axis, while the adjacent one is clocked halfway between two swirlers. An aspect ratio (H/C_{ax}) of 1.04 and a pitch-chord ratio (p/C_{ax}) of 1.06 are achieved, considering the constant-height part of the *NGV*. According to preliminary evaluations and *CFD* calculations, the exit Mach number, in the abscence of film cooling, was around 0.75, with the *NGV* exit flow angle being about 74°.

Fig. 3.5 also illustrates the film cooling scheme characteristics: 8 cylindrical film cooling holes rows, four of which are shower-head rows, close to the leading edge (*LE*) position, whereas the remaining are positioned on the pressure side (*PS*), with no holes on the suction side (*SS*) far away from the leading edge. The holes positioning

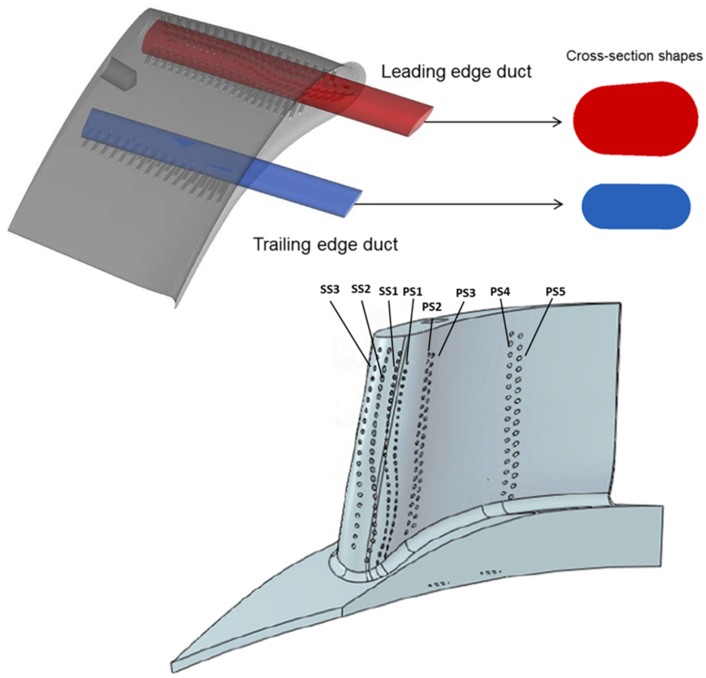

Figure 3.5: *FACTOR* - *NGV* 3D model and film cooling scheme

and inclination was defined in order to adapt to the expected flow field at the *NGV* inlet and, therefore, to the expected stagnation line position. Moreover, the blowing ratio (BR) is on average below or equal to 2, while the velocity ratio and penetration regime (VR) are generally higher than the evaluated threshold (as per L'Ecuyer and Soechting [54] in the flat plate configuration), yet considered low enough to guarantee a satisfactory attachment of the cooling flow over the *NGV* surface.

The test rig nominal design and operating point was established in order to match the most important non-dimensional parameters, which control the behaviour of mainstream and cooling flows at engine representative values. The parameters chosen to describe the physics of the flow in the combustor simulator are mainstream and liner cooling flows Reynolds numbers (Re_g, Re_c) and mainstream Mach number at the swirler exit (Ma_g). Moreover, the multiperforated plates can be characterised by the blowing ratio $BR_c = \frac{\rho_c V_c}{\rho_g V_g}$ and by the momentum flux ratio $I_c = \frac{\rho_c V_c^2}{\rho_g V_g^2}$, as already reported in Eq. 3.4, 3.5 and 3.6. Pressure drops across swirlers and liners (defined as $\frac{P_{0,in} - P_{s,out}}{P_{0,in}}$) are about 3.5 and 5% respectively, at design point conditions. A main-to-coolant temperature ratio of 1.77 is achieved by heating the mainflow up to 531 K and keeping the liner coolant at ambient temperature. Concerning the *NGV* investigation, Reynolds and Mach number on *Plane 40* (Re_{40}, Ma_{40}) were accounted for as well as the Mach number at *NGV* exit (Ma_{41}).

For the nominal operating point the NGV coolant mass flow rate is 7.5% of the total mainstream mass flow rate at NGV inlet ($W = \dot{m}_{fc}/\dot{m}_M = 0.075$). Beside the nominal operating point, an isothermal point, i.e. with all flows at ambient temperature, was to be defined, since some of the adopted measurement techniques had to be operated at ambient temperature, finding a good trade-off between the necessities of matching Mach and Reynolds numbers at such condition as well.

Four different experimental techniques were exploited for the characterisation of the combustor simulator and the high pressure NGV module. At the first stage, with only the combustor simulator installed, the focus was placed on the evaluation of the flow field and the mixing phenomena inside the combustor simulator by means of particle image velocimetry (PIV). Standard 2D PIV was employed to investigate three different planes: plane 1 of Fig. 3.6 is the chamber symmetry plane (0° azimuthal coordinate), halving the central swirler, while plane 2 and 3 are axial planes. Measurements were taken at warm conditions, in addition to isothermal ones, since the wide lateral pyrex windows could not withstand temperatures higher than 450 K.

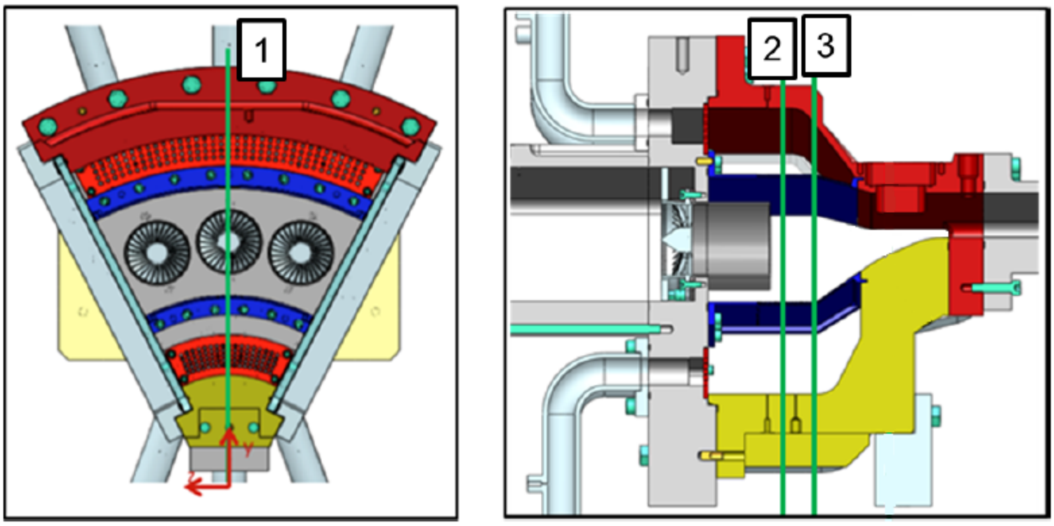

Figure 3.6: *FACTOR* - PIV measurement positions

After the test rig upgrade with the NGV module, the evaluation of the overall aerothermal field at combustor exit was carried out by means of five hole probe ($5HP$) traversing. *Plane 40* is the nominal combustor exit plane and it is located about half an axial chord ($\approx 20mm$) upstream of the NGV leading edge position and about 156 mm downstream the swirlers (101 mm downstream the duct exit). Five hole probe measurements on *Plane 40* have been conducted both in nominal and isothermal conditions to evaluate any differences in the aerodynamic field and to validate the results obtained by those measurements techniques requiring isothermal conditions against design conditions.

The combustor simulator characterisation was then completed with the evaluation of turbulence intensity and unsteady structures at combustor exit in isothermal conditions. Hot wire anemometry (*HWA*) probe traversing was employed, which, with the sensor element being in-axis with its support, allowed for measurements at the exact *Plane 40*.

Afterwards, the investigation of the overall flow field at NGV exit was conducted: it was carried out in both nominal and isothermal conditions with five hole probe traversing at *Plane 41*, an axial plane placed about 9 mm (≈ 0.24 axial chords) downstream of the NGV trailing edge ($\approx 67.5mm$ downstream of *Plane 40*). The same measurement plane was also investigated by means of hot wire anemometry traversing, in isothermal conditions.

Lastly, adiabatic effectiveness measurements on the NGV airfoils were performed in order to study the impact of the highly swirling combustor outflow on the film cooling performance. As for the hot wire test, the adopted pressure sensitive paint (*PSP*) technique required the tests to be run in cold isothermal conditions.

Since *PSP* is a way to measure oxygen concentration, the paint is suitable for gas concentration technique based on the heat and mass transfer analogy [90], with the ultimate goal of evaluating the adiabatic effectiveness. In fact, *PSP* are capable of emitting within the red wavelength, when illuminated with UV light, at an inversely proportional intensity with respect to the oxygen partial pressure on the investigated surface. In addition, it is generally necessary to run two consecutive tests in order to successfully conduct this measurement on an airfoil profile:

1. Firstly air is used for both main and coolant flows in order to obtain the pressure distribution over the inspected surface, which is needed to properly scale the results of the second test;

2. Secondly a tracer gas is adopted as coolant flow as to retrieve its wall concentration and hence the adiabatic effectiveness.

Therefore, with the set of equations for heat and mass transfer having the same modelling expressions [91], if the boundary conditions of the two analogous problems are the same and if the molecular and turbulent Schmidt numbers (Sc, Sc_T) are identical to molecular and turbulent Prandtl numbers (Pr, Pr_T) respectively (i.e. molecular and turbulent Lewis numbers Le and Le_T equal to one as shown below), the solutions of the heat and mass transfer phenomena are identical.

$$Le = \frac{Pr}{Sc} = \frac{\alpha}{D} \approx 1 \tag{3.1a}$$

$$Le_T = \frac{Pr_T}{Sc_T} = \frac{\alpha_T}{D_T} \approx 1 \tag{3.1b}$$

Assuming therefore the heat-mass transfer analogy valid, if a tracer gas without free oxygen is used as coolant in a film cooling system (CO_2 in this case, to respect the density ratio of 1.5 of the nominal conditions), it is straightforward to replace the temperature definition of film-cooling adiabatic effectiveness (see Section 2.2.2 for reference) by mass fractions of oxygen [90]:

$$\eta_{ad} = \frac{T_{main} - T_{ad}}{T_{main} - T_{cool}} = \frac{C_{main} - C_w}{C_{main}} \tag{3.2}$$

Where C_{main} is the oxygen concentration of main free stream and C_w is the oxygen concentration in proximity of the wall. In order to express Eq. 3.2 in terms of partial pressure of oxygen, as measured with *PSP*, the expression of adiabatic effectiveness is elaborated using the molecular weights [92]:

$$\eta_{ad} = \frac{C_{main} - C_w}{C_{main}} = 1 - \frac{1}{1 + \left(\frac{P_{O_2,air}/P_{O_2,ref}}{P_{O_2,fg}/P_{O_2,ref}} - 1\right)\frac{W_{fg}}{W_{air}}} \tag{3.3}$$

Subscripts fg and air stand for a case with foreign gas (without free oxygen) and air injection trough cooling system respectively. Moreover ref is used to identify a reference case.

The full experimental test matrix is thus eventually summarised in Table 3.1. As Bacci [21] has shown that limited differences are to be expected between isothermal and nominal conditions, the objectives of these measurements are basically two:

- evaluate the effect of a highly swirling, highly turbulent and temperature-distorted inflow on the adiabatic effectiveness of a film cooled *NGV*, as well as on the resulting flow field, secondary flows and turbulence pattern at its exit;
- investigate the hot streaks migration through the cascade, their interactions with film cooling and their effects on secondary flows.

			PIV	5HP	HWA	PSP
Combustion chamber	**Sym. plane 1**	isothermal	x			
		warm	x			
	Plane 2	isothermal	x			
		warm	x			
	Plane 3	isothermal	x			
		warm	x			
Combustor Exit	**Plane 40**	isothermal		x	x	
		nominal		x		
NGV Module	**Plane 41**	isothermal		x	x	
		nominal		x		
	Airfoils	isothermal				x

Table 3.1: *FACTOR* - Experimental campaign test matrix

3.1.2 STech test rig overview

In the framework of the *STech* (Smart Technologies) programme, a co-funded project by *Regione Toscana* and coordinated by the turbomachinery industrial partner *Baker Hughes*, an experimental non-reactive test rig was realised at the *THT* (Technologies for High Temperature) laboratory at the *University of Florence*, Italy. The rig, a picture of which is reported in Fig. 3.7, is composed of real turbomachinery hardware from a *Baker Hughes'* heavy-duty gas turbine. In particular, as schematically represented in Fig. 3.8, it houses three real lean-premix burners and a real film-cooled first-stage nozzle doublet (i.e. 3 vane passages) to form a trisector geometry. It is also to be noted that the swirlers have been filled with grey colour to protect the Baker Hughes' intellectual property.

The scope of the rig was to perform measurements and make comparisons against the *CFD* predictive tools and design practice currently in use at *Baker Hughes.* As lean combustion applied to industrial gas turbines is not novel technology, it was decided to simplify the characterisation of the combustion chamber flow field and to focus the test campaign more on the nozzles module. At the same time the experience gained at the *University of Florence* within the *FACTOR* project was leveraged in the design of the *STech* rig. Probe traversing were realised to measure velocity, pressure, temperature and turbulence upstream and downstream of the nozzles, while infrared (*IR*) thermography was employed to evaluate surface temperatures and adiabatic effectiveness. It is also planned to measure the heat transfer coefficient on the nozzles surface in a subsequent phase of the project by means of *IR* thermography and transient technique. Due to the technical complexities faced during the design and the procurement phases,

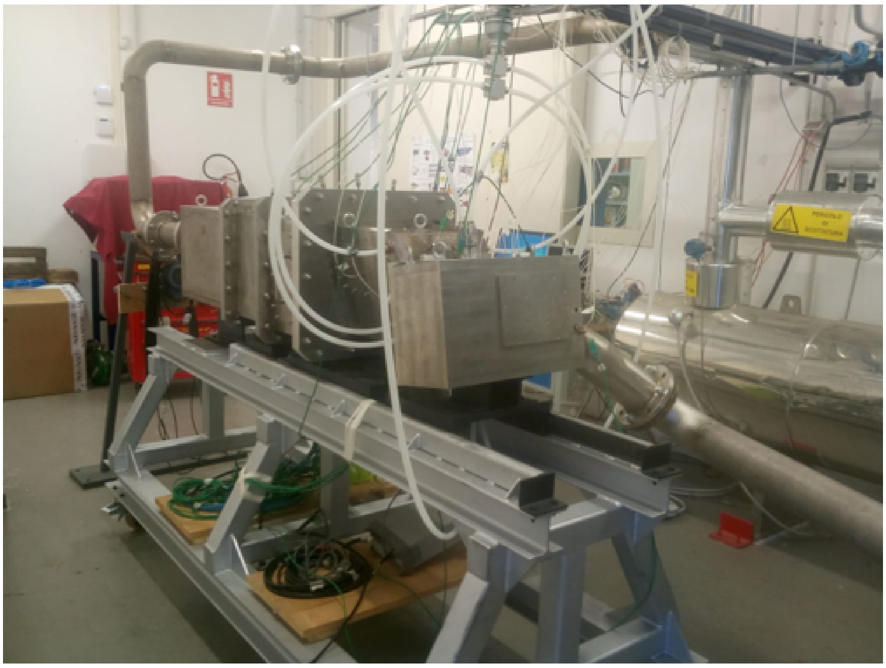

Figure 3.7: Photograph of the *STech* test rig cell

the experimental campaign kick-off has undergone some delay, with the end expected in the first half of 2020.

Despite the combustor simulator being composed of real engine hardware, a preliminary investigation was carried out to make sure that the rig was capable of emulating the main flow characteristics at the turbine inlet section in a similar way to the expected real engine ones. This was done by matching the engine Mach number through the nozzles (it was not possible to exactly replicate also the Reynolds number for limitations to the rig maximum flow rate and pressure) and by reproducing the engine temperature and velocity profiles at the combustor/turbine interface.

With reference to Fig. 3.8, a plenum chamber is placed upstream of the burners to reduce the incoming flow velocity and equalise pressure. Then the warm flow (red arrow) is injected through three swirlers into the combustion chamber, replicating the real geometry. Coolant flow (blue arrows) is injected from annular plena over the chamber liners, to reduce the main flow temperature in correspondence of the endwalls, via dedicated "nuggets" (a battery of multiple hole rows). As a common feature to lean combustors, the chamber annulus reduces in proximity of the nozzles sector with, in addition, a decrease in both minimum and maximum radii as per the real component features, which makes the flow accelerate towards the turbine vanes.

Still with reference to Fig. 3.8, the NGV module is placed downstream of the combustion chamber, hosting the NGV airfoils, which are internally cooled plus presenting

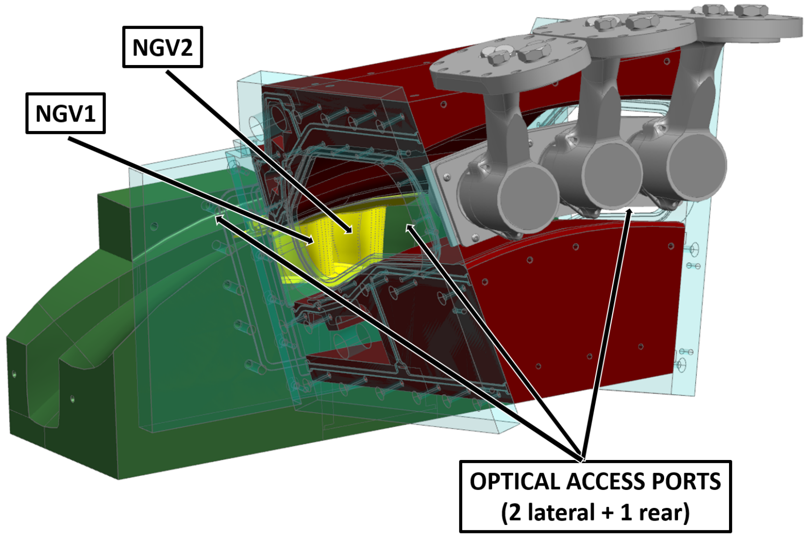

(a)

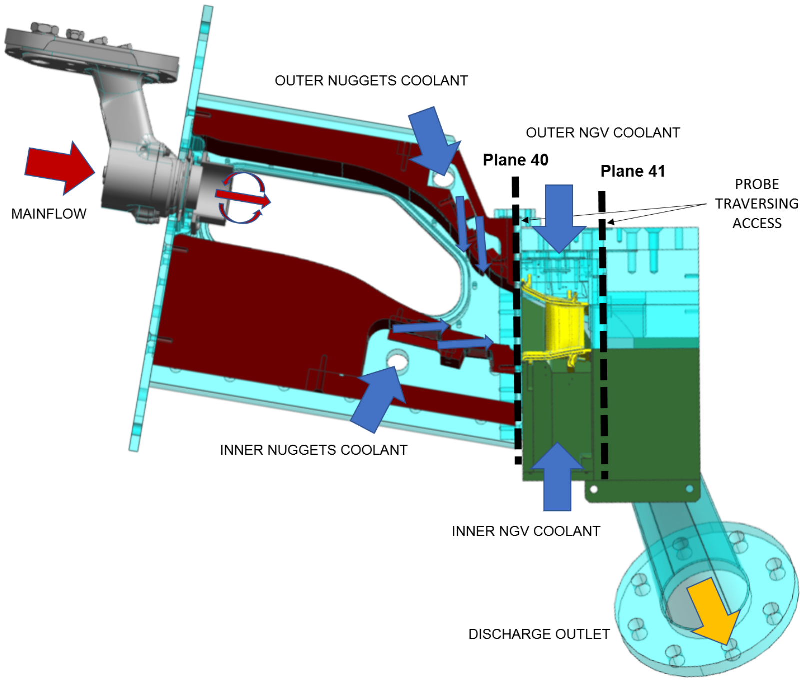

(b)

Figure 3.8: *STech* trisector rig layout: 3D CAD model (a) and sectional view (b)

external film cooling. Further blue arrows in the picture indicate such cooling flow. At the nozzles exit is an ad-hoc diffuser duct, which collects the nozzles discharge air and recover part of the static pressure, prior to directing it to the exhaust system.

As mentioned the rig swirlers are real burners, unless for the fact that they are operated in non-reactive conditions for ease of installation, operation and measurement.

Since combustion is not present, the temperature profile is obtained only by the mixing of hot (573 K) and cold (ambient) air streams, i.e. respectively main and cooling flows. As typical of lean combustors, main flow rate is largely higher than cooling one (in a ratio of roughly 80:20). The trisector configuration was employed to isolate the central sector, where measurements are possible far away from the lateral walls.

As in the previous case the automatic traverse system can be installed either on *Plane 40* or *Plane 41*, based on the section of interest. Furthermore, pyrex windows provision is present on the lateral walls of the combustion chamber, in order to grant the optical access necessary for the tests with *PSP* in addition to the planned HTC measurements and the possibility to perform *PIV* on the chamber in the future. In order to enforce periodicity on the central sector of *Plane 40*, it was necessary to install ducts at the immediate outlet section of the injectors (several lengths were tested: ≈ 0.5x, 0.75x and 1x the swirler outer diameter), which preserves the tangential momentum for a longer distance.

At the initial stage of the test campaign five-hole probe measurements were taken at *Plane 40* with all the three duct lengths, concluding that the "1xD" was the proper size to have a sufficiently periodic flow field at the combustor/turbine interface central plane. The resulting flow field is reported in Fig. 3.9, in terms of temperature and flow angles patterns.

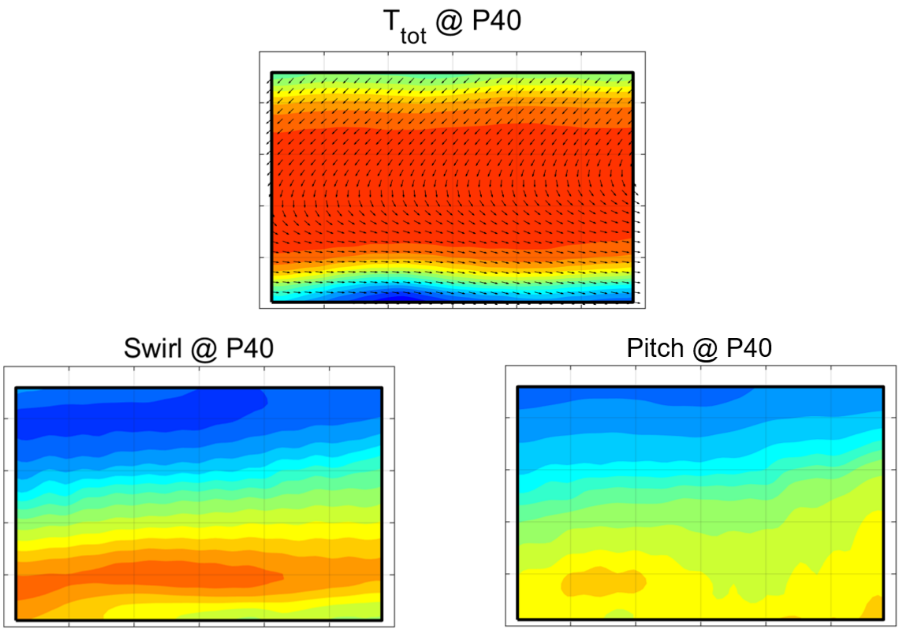

Figure 3.9: *STech* - Temperature and flow angles patterns measured on *Plane 40*

The first stage nozzle mounted on the rig is as well a real component of a *Baker*

Hughes heavy-duty gas turbine and was designed according to the company's standard practices for aerodynamics, heat transfer and structural mechanics. A *CAD* model of the nozzle doublet is reported in Fig. 3.10: as mentioned it is internally cooled plus presenting external film cooling.

An *NGV*-to-swirler count ratio of 1 was used, with the central swirler axis aligned with the central vane passage. Unfortunately, further and more detailed information about the airfoil geometry and cooling scheme cannot be disclosed to protect the company's intellectual property.

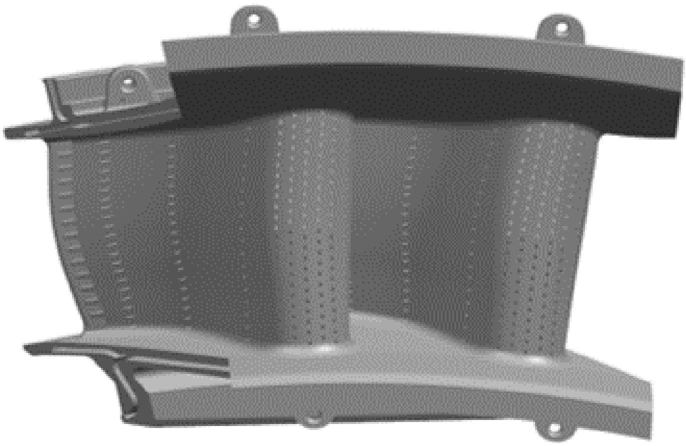

Figure 3.10: *STech* - *NGV* 3D model

The nominal design and operating point was defined as to match the main non-dimensional parameters, in order to operate in similitude conditions or, when not possible, in engine representative values. The mainstream and liner flows Reynolds numbers (Re_g, Re_c) were accounted for in the definition of the design point, although it was not possible to fully respect the Reynolds number similitude due to the limitations in the maximum flow rate and pressure in the test bench. By contrast, the mainstream Mach number (Ma_g) was respected at both the turbine inlet and outlet planes (*Plane 40* and *Plane 41*), which was essential as to replicate the same pressure profile on the airfoils as in engine conditions. Moreover, the combustion chamber nuggets and film-cooling (as much as possible) were characterised by the blowing ratio $BR = \frac{\rho_c V_c}{\rho_g V_g}$ and the momentum flux ratio $I = \frac{\rho_c V_c^2}{\rho_g V_g^2}$, which were maintained the same as in engine conditions by keeping almost the same mass flow $MR = \frac{\rho A V_c}{\rho A V_g}$, temperature $TR = \frac{T_c}{T_g}$ and pressure ratios $PR = \frac{p_c}{p_g}$, as per the following expressions:

$$BR = \frac{\rho V_c}{\rho V_g} \propto \frac{\dot{m}_c}{\dot{m}_g} \tag{3.4a}$$

$$\frac{BR_{rig}}{BR_{engine}} = \frac{MR_{rig}}{MR_{engine}} \tag{3.4b}$$

$$DR = \frac{\rho_c}{\rho_g} \approx \frac{p_g T_c}{p_c T_g} = \frac{TR}{PR} \tag{3.5a}$$

$$\frac{DR_{rig}}{DR_{engine}} = \frac{TR_{rig}}{TR_{engine}} \cdot \frac{PR_{engine}}{PR_{rig}} \tag{3.5b}$$

$$I = \frac{\rho V_c^2}{\rho V_g^2} = \frac{BR^2}{DR} \tag{3.6a}$$

$$\frac{I_{rig}}{I_{engine}} = \frac{BR_{rig}}{BR_{engine}} \cdot \frac{DR_{engine}}{DR_{rig}} \tag{3.6b}$$

A main-to-coolant temperature ratio of ≈ 2 (close to engine conditions) is achieved by heating the mainflow up to 573 K and keeping the liner cool flow at ambient temperature.

An isothermal point, i.e. with all flows at ambient temperature, was again necessary to be able to use those measurement techniques requiring to be operated at ambient temperature. As already mentioned, no dedicated combustor characterisation was performed out of the measurements on *Plane 40*, while the high pressure *NGV* module is to be deeply investigated.

The assessment of the aerothermal field at the combustor exit was therefore performed with a five hole probe ($5HP$) coupled to a thermocouple and mounted on a traverse system. Such measurements have been performed on *Plane 40* at both the nominal and isothermal points, which showed no particular discrepancy, thus validating the measurements at ambient temperature.

Turbulence intensity was also measured at the combustor and the nozzles exit planes in isothermal conditions by means of hot wire anemometry (*HWA*), which exploited the same traverse system used for the *5HP*.

Eventually, the pressure sensitive paint (PSP) technique have been employed to measure the nozzles film-cooling adiabatic effectiveness in isothermal conditions. *HTC* measurements are yet to be performed at a following stage of the campaign via the

			5HP	HWA	PSP	HTC
Combustor Exit	**Plane 40**	isothermal	x	x		
		nominal	x			
NGV Module	**Plane 41**	isothermal		x		
		nominal				
	Airfoils	isothermal			x	
		transient				f

Table 3.2: *STech* - Experimental campaign test matrix (x: done, f: future measurements)

transient technique, i.e. imposing a temperature step to the mainflow from a stabilised condition, reconstructing the heat flux through *IR* recording of the temperature history of the airfoils and finally reducing the *HTC* via linear regression of heat flux versus temperature over time. The experimental test matrix is summarised in Table 3.2.

Once again, the main goal of this test campaign was to understand the impact of a real swirled, temperature-distorted and turbulent inflow on the aerothermal performance of a film-cooled high-pressure first stage nozzle. This is then to be compared with the industrial standard practice in order to highlight any possible gap or improvement opportunity, which may increase efficiency and/or the durability of gas turbine parts.

3.2 Numerical methodology

3.2.1 Numerical methods for turbomachinery applications

The rapid increase of the available computational power contributes to a fast development of computational fluid dynamics (*CFD*). Nowadays, *CFD* is an essential tool for the industrial everyday work and for the research community. The use of advanced numerical software during the design phase represents one of the main drivers for the improvement of the state of the art of turbomachinery components in the last 40 years. Nevertheless, the application of classical numerical techniques to the combustor-turbine interaction presents major problematics requiring further investigation.

The flow field within a gas turbine is intrinsically unsteady because of the interaction between static and rotating parts (i.e. stator and rotor blades) and because of flow turbulent fluctuations. Turbulent fluctuations are characterized by a wide range of frequencies and are intrinsically present within the Navier-Stokes (NS) equations [93]. Three main numerical approaches exists for their resolution: direct numerical simulation (*DNS*), large-eddy simulation (*LES*) and Reynolds-averaged Navier-Stokes (*RANS*). The part of turbulent spectrum which is resolved and/or modelled by each approach is shown in Fig. 3.11. A brief overview of the methods is presented follows:

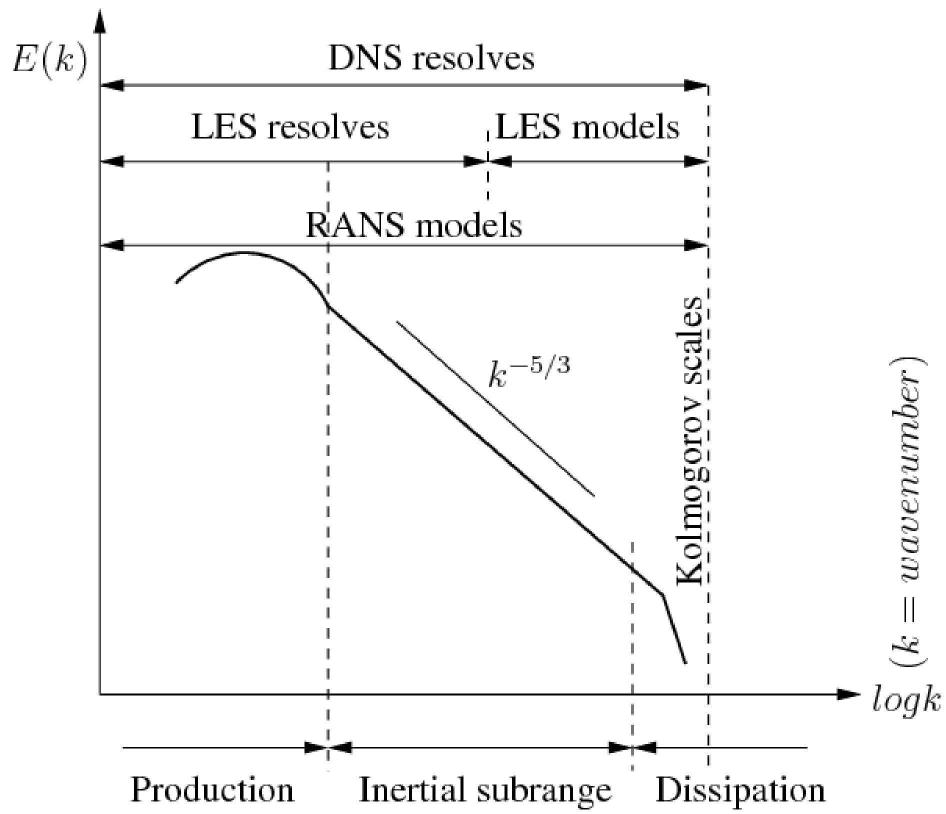

Figure 3.11: Resolved and/or modelled turbulent scales by *DNS*, *LES* and *RANS* [93]

- *DNS* theoretically represents the easiest approach possible, since it basically involves the direct resolution of all turbulent structures generated by the flow field [94]. Historically, this approach has been very useful for the study of the turbulent flow physics. Its main limitation, however, lies in the high-order schemes needed to avoid numerical dissipation and in the required number of grid cells being proportional to $Re^{37/14}$ [95], while the computational cost scales up with Re^3 [96]. As a consequence, the application of *DNS* to engineering-type problems is limited to low-Reynolds cases.

- *LES* resolves the most energetic structures while modelling only the effect of the smallest scales ("Kolmogorov" scales). The smallest turbulent scales drive the energy decay and are more isotropic and universal, which implies only limited adjustments of the turbulence model (subgrid scales models *SGS*) passing from one to another test case. The transition between resolved and modelled scales is obtained by the filtering operation of the NS equation, which is in most cases linked to the mesh size. According to the Pope's criterion [94] (noted as M_P), independently from the SGS model used, the grid must be sufficiently refined as to enable the direct resolution (k_{res}) rather than the modelling (k_{mod}) of at least 80% of the turbulent kinetic energy, as per the following equation:

$$M_P = \frac{k_{res}}{k_{res} + k_{mod}} \geq 0.8 \tag{3.7}$$

An estimate of the computational requirement for wall-bounded *LES* was given by Chapman [97] and recently revised by Choi and Moin [95]. A wall modelled *LES* requires a number of grid points which is proportional to *Re* while it scales up with $Re^{13/7}$ for wall resolved *LES*. Nowadays, the computational cost of *LES* has dropped when not seeking for a detailed wall resolution. This explains the rapid diffusion of the method in combustion chambers [98]. On the contrary, despite the increased popularity of LES applied to high pressure airfoils [99], its computational cost remains prohibitive for the current industrial practice.

- $RANS$ is the least costly approach, as it is based upon the application of time-averaged NS equations to eliminate the unsteady terms. The effect of turbulence on the mean flow field, which explicitly appears into the system because of the non-linear nature of the NS equations, is reproduced by turbulence models [100]. Because of its limited computational cost, $RANS$ is by far the most popular numerical method in use during the design phase, despite the different turbulence models suffering from a lack of universality. A time dependent solution of the flow field using classical $RANS$ models is called unsteady-$RANS$ ($uRANS$).

The $RANS$ methodology is based on a statistical averaging or, in practice, a long-time averaging, sufficiently large in comparison with the turbulence time scale. As a result, it suits best those situations with time variations in the mean flow being of a much lower frequency than the turbulence itself. Due to the inability of $RANS$ of reproducing unsteady flows and the high computational cost of *LES*, new methods of turbulence modelling aiming at combining the advantages of both methods have been recently proposed [101]. These are essentially based on hybrid zonal but also non-zonal schemes [102]. In this framework different hybrid *RANS*-*LES* methods have been developed, e.g. very large-eddy simulation (*VLES*), detached eddy simulation (*DES*), partially integrated transport modeling (*PITM*), partially averaged Navier-Stokes (*PANS*) and scale adaptive simulation (*SAS*).

According to the literature [103], these hybrid methods can be classified into two categories, zonal and non-zonal. The former relies on two different models, a *RANS* and a subgrid-scale one, applied in different domains separated by a sharp or dynamic interface. By contrast, the latter assumes that the governing set of equations be smoothly transitioning from a *RANS* to an *LES* behaviour, based on criteria updated along with computation.

The NS equations, governing the flow physics, are expressed by the conservation laws of mass, momentum and energy and are respectively reported as follows in their differential form (using the Einstein index notation) in case of compressible flow and single species fluid:

$$\frac{\partial \rho}{\partial t} + \frac{\partial}{\partial x_i}\left(\rho u_i\right) = 0 \tag{3.8a}$$

$$\frac{\partial}{\partial t}\left(\rho u_i\right) + \frac{\partial}{\partial x_j}\left(\rho u_j u_i\right) = -\frac{\partial p}{\partial x_i}\delta_{ij} + \frac{\partial \tau_{ij}}{\partial x_i} \tag{3.8b}$$

$$\frac{\partial}{\partial t}\left(\rho E\right) + \frac{\partial}{\partial x_i}\left(\rho u_j E + u_j p\right) = -\frac{\partial q_j}{\partial x_j} + \frac{\partial}{\partial x_i}\left(u_i \tau_{ij}\right) \tag{3.8c}$$

With u_j being the velocity components, p the static pressure, τ_{ij} the viscous shear stress tensor, E the total energy (internal plus kinetic energies), q_i the energy flux components (from the Fourier's law) and δ_{ij} the "Kronecker" symbol (1 if $i = j$ or 0 otherwise), with the following definitions:

$$\tau_{ij} = 2\mu S_{ij} - \frac{2}{3}\mu \frac{\partial u_k}{\partial x_k}\delta_{ij} \tag{3.9a}$$

$$S_{ij} = \frac{1}{2}\left(\frac{\partial u_i}{\partial x_j} + \frac{\partial u_j}{\partial x_i}\right) \tag{3.9b}$$

Note that the above definition for τ_{ij} is valid assuming a Newtonian fluid and using the Stokes' Law for mono-atomic gases.

$$q_j = -\lambda \frac{\partial T}{\partial x_j} \tag{3.10a}$$

$$E = e + \frac{1}{2}u_i u_i \tag{3.10b}$$

The NS equations are to be solved in the framework of *DNS*, more precisely all essential scales of motion of the same order of magnitude and higher with respect to the "Kolmogorov" scale η_K (see Fig. 3.11 for reference). This is the smallest scale in turbulent flows and is estimated via the following expression, with μ being the molecular viscosity and ϵ the dissipation rate:

$$\eta_\kappa = \left(\frac{\mu^3}{\epsilon}\right)^{1/4} \tag{3.11}$$

The above definition derives from the similarity hypotheses by Kolmogorov per which, for turbulent flows with a sufficiently high Reynolds number, the (small) scales at which energy is dissipated depend on both dissipation rate and viscosity (first hypothesis), while the large scales are related more to the macroscopic geometry and depend only on the dissipation rate while being independent of viscosity (second hypothesis) [94]. The "Kolmogorov" scale is thus of fundamental importance, since it divides the scales (eddy sizes) at which energy is transferred from larger to smaller eddies ("energy cascade") against those at which energy is dissipated by smaller eddies into heat.

It is then also possible to relate such length scale with the largest scales, considering that the dissipation rate is equal to the kinetic energy production rate. With the kinetic energy being proportional to the square velocity u^2 and the time scale for large eddies ("turnover" time) estimated through $t_L = L/u$ (with L the integral length scale), it is reasonable to assume that the kinetic energy supply rate be related to the inverse of this time scale, leading to the following relationship:

$$\epsilon \sim \frac{u^2}{t_L} = \frac{u^2}{L/u} = \frac{u^3}{L} \tag{3.12}$$

Therefore, replacing Eq. 3.12 into Eq. 3.11, the following can be written:

$$\eta_\kappa = \left(\frac{\mu^3 L}{u^3}\right)^{1/4} \tag{3.13}$$

Eq. 3.12 and Eq. 3.13 show that the dissipation rate does not depend on viscosity in the production and inertial ranges, as previously mentioned, whereas viscosity serves only to establish at which length scale dissipation takes place. Following Eq. 3.13 the ratio between the largest and the smallest scales can be derived:

$$\frac{L}{\eta_\kappa} \sim \left(\frac{uL}{\mu}\right)^{3/4} = {Re_L}^{3/4} \tag{3.14}$$

Where Re_L is the Reynolds number based on the large length scales. As per such relation, it is to be expected that the separation between largest and smallest scale increases with Re, which means that high Re flows are characterised by large eddies barely affected by viscosity and ultimately decaying to small ones, with little presence of "intermediate" eddies, as exemplified in Fig. 3.12.

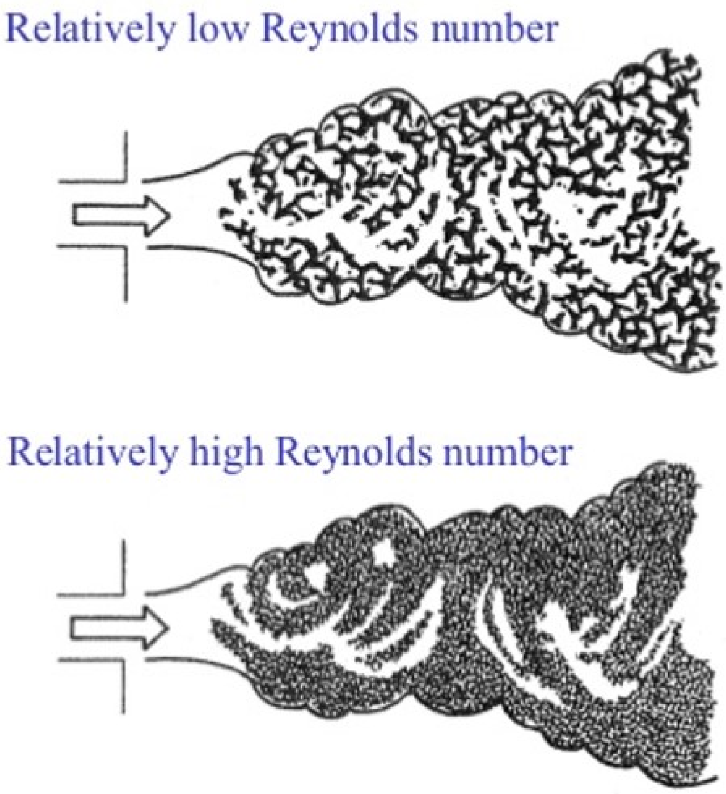

Figure 3.12: Schematic representation of low and high Reynolds flows' eddies [104]

Furthermore, with the time scale for large eddies being t_L (see Eq. 3.12), it is also possible to define the same quantity for small scales as function of viscosity and dissipation rate:

$$t_{\eta_\kappa} = \left(\frac{\mu}{\epsilon}\right)^{1/2} \tag{3.15}$$

Then, replacing Eq. 3.12 into Eq. 3.15, the following is obtained:

$$t_{\eta_\kappa} = \frac{\mu}{u^3/L} \tag{3.16}$$

As a consequence, the ratio between large and small time scales can be derived as:

$$\frac{t_L}{t_{\eta_\kappa}} = \left(\frac{uL}{\mu}\right)^{1/2} = {Re_L}^{1/2} \tag{3.17}$$

The above relationship reveals that the large scale structures in the flow have a much larger time scale (i.e. duration) than the small energy dissipating eddies, with a proportionality to the Reynolds number, which supports the aforementioned statement of separation between largest and smallest scales not only in length but also in time. In addition, it is worth mentioning that appropriate space and time discretisations are therefore required to fully describe the energy spectrum, based on the evaluation of the length and time scales characteristic of the analysed turbulent flow.

Then, it is also interesting to relate the turnover time of a size-l eddy (t_l) to the time necessary to traverse the whole inertial range (τ_l) until its length scale is reduced to η_κ. From a simple dimensional analysis it is possible to write:

$$\frac{dl}{dt} \sim -\frac{l}{t_l} \tag{3.18}$$

Where t_l can be expressed in relation to the integral time scale t_L, by using the "Kolmogorov" scaling applicable to the inertial subrange:

$$t_l \sim \left(\frac{l}{L}\right)^{2/3} t_L \tag{3.19}$$

Now substituting Eq. 3.19 into Eq. 3.18 and integrating from L to η_κ, the following can be obtained:

$$\frac{t_L}{\tau_L} = 1 - \left(\frac{\eta_\kappa}{L}\right)^{2/3} \tag{3.20}$$

Then, recalling Eq. 3.14, Eq. 3.20 becomes:

$$\frac{t_L}{\tau_L} = 1 - \frac{1}{Re^{1/2}} \tag{3.21}$$

Eq. 3.21 therefore illustrates that the ratio between the large eddy turnover time t_L and the time τ_L necessary to reach the dissipation length scale increases with Re, up to the point that for high Reynolds numbers the ratio becomes 1. This further shows that for high Re flows large eddies persist until they rapidly reach the dissipation range, while for low Re the decay is more gradual.

3.2.2 Reynolds averaged Navier-Stokes simulations

In the *RANS* methodology a time average of the *NS* is performed, which results in the unknown turbulent stress appearing in the motion equation and requiring to be modelled to close and solve the set of equations. This is known as the "turbulence closure problem" as extensively described by Schiestel [105] and Hanjalic and Launder [106].

The turbulent stress is defined by the correlation of the fluctuating velocities including all the turbulence scales. The turbulent stress is defined using either eddy viscosity models or second-moment closure models. Usually, the former perform well for shear flows, while the latter account for more physics providing a better prediction of the normal turbulent stresses for flows encountered in aeronautical or turbomachinery applications involving complex physics phenomena, e.g. those induced by streamline curvature such as detachment or reattachment of the boundary layer, separation and recirculation in presence of adverse pressure gradient, as well as rotational effects [107].

For incompressible flows Reynolds Averaged Navier-Stokes (*RANS*) equations are commonly used, whereas compressible flows actually favour the Favre Averaged Navier Stokes (*FANS*) equations, since two kinds of fluctuations are to be considered: in time and density [108]. Fluctuations in time, common for incompressible and low-Mach compressible flows modelling, are handled through the Reynolds decomposition, i.e. the instantaneous value of a variable Φ is split into the temporal mean and a fluctuating part:

$$\Phi = \bar{\Phi} + \Phi' \tag{3.22}$$

With the temporal mean of the fluctuation $\bar{\Phi}' = 0$. However, if all variables in a highly compressible flow were split this way, complex correlations of velocity-density-fluctuations would arise, which are difficult to model or test via experiments. Therefore, Favre's density-weighted averaging may be employed, which is:

$$\tilde{\Phi} = \frac{\overline{\rho\Phi}}{\bar{\rho}} \tag{3.23a}$$
$$\Phi = \tilde{\Phi} + \Phi'' \tag{3.23b}$$

With the temporal mean of the fluctuation $\bar{\Phi}'' \neq 0$, but $\overline{\rho\Phi''} = 0$. Reynolds decomposition is then used for density and pressure, while Favre one for velocity, energy, enthalpy and temperature. Applying such decompositions to Eq. 3.8, these become:

$$\frac{\partial\bar{\rho}}{\partial t} + \frac{\partial}{\partial x_i}\left(\bar{\rho}\tilde{u}_i\right) = 0 \tag{3.24a}$$
$$\frac{\partial}{\partial t}\left(\bar{\rho}\tilde{u}_i\right) + \frac{\partial}{\partial x_j}\left(\bar{\rho}\tilde{u}_j\tilde{u}_i\right) = -\frac{\partial\bar{p}}{\partial x_i}\delta_{ij} + \frac{\partial}{\partial x_i}\left(\bar{\tau}_{ij} - \overline{\rho u_i'' u_j''}\right) \tag{3.24b}$$
$$\frac{\partial}{\partial t}\left(\bar{\rho}\tilde{E}\right) + \frac{\partial}{\partial x_i}\left(\bar{\rho}\tilde{u}_j\tilde{E} + \tilde{u}_j\bar{p}\right) = \frac{\partial}{\partial x_i}\left(-\overline{u_j'' p} - \overline{\rho u_j'' E''} - \bar{q}_j + \overline{u_i\tau_{ij}}\right) \tag{3.24c}$$

With total energy now reading:

$$\tilde{E} = \tilde{e} + \frac{1}{2}\tilde{u}_i\tilde{u}_i + k \tag{3.25a}$$
$$k = \frac{1}{2}\widetilde{u_i' u_i'} \tag{3.25b}$$

Where k is the introduced turbulent kinetic energy, i.e. the kinetic energy due to fluctuations, for which the following transport equation can be derived:

$$\begin{aligned}\bar{\rho}\frac{\partial k}{\partial t} + \rho\tilde{u}_j\frac{\partial k}{\partial x_j} = \tau_{ij,T}\frac{\partial\tilde{u}_i}{\partial x_j} - \mu\overline{\frac{\partial u_i''}{\partial x_j}\frac{\partial u_i''}{\partial x_j}} + \frac{\partial}{\partial x_j}\left(\mu\frac{\partial k}{\partial x_j}\right) + \\ - \frac{\partial}{\partial x_j}\left(\overline{\frac{1}{2}u_j''\rho u_i'' u_i''} - \overline{p' u_j''}\delta_{ij}\right)\end{aligned} \tag{3.26}$$

The tensor $\tau_{ij,T}$ is the so called Favre-averaged turbulent stress tensor, which, as per the “Boussinesq hypothesis” in analogy with the viscous stress tensor τ_{ij}, is defined as:

$$\bar{\tau}_{ij,T} = -\overline{\rho u_i'' u_j''} = 2\mu_T \tilde{S}_{ij} - \frac{2}{3}\mu_T \frac{\partial u_k}{\partial x_k}\delta_{ij} - \frac{2}{3}\bar{\rho} k \delta_{ij} \tag{3.27}$$

It is moreover interesting to notice that the equation for k (Eq. 3.26), other than the two terms on the left-hand side being respectively the “time rate of change” and “advection”, as common for any generic transport equation, presents four terms on the right-hand side:

- “production” - the specific energy gained by an eddy due to the mean flow strain rate;
- “dissipation” - the transfer rate of energy from the turbulent eddies into thermal molecular energy, or also the rate at which work is done by the fluctuating strain rate against fluctuating viscous stresses;
- “molecular diffusion” - turbulent energy diffused by molecular motion, which is equally responsible for diffusing the mean flow momentum;
- “turbulent and pressure transport” - the transport rate of turbulent energy through turbulent plus pressure fluctuations.

It is to be emphasised that the turbulent stress tensor, molecular diffusion and turbulent transport of energy contain correlations of fluctuating quantities, which cannot be directly calculated. For this reason, these correlations need to be modelled, as per the so-called “turbulence closure” problem.

The turbulent viscosity μ_T is the main term in *RANS* and *FANS* to be modelled. There exist several approaches of different kind and order. In general it can be distinguished between Reynolds Stress Modelling (*RSM*), linear eddy viscosity, and non-linear eddy viscosity modelling. In *RSM* the turbulence closure is received one level higher, as for all components of the Reynolds stress tensor τ_{ij} a transport equation is solved [109]. However, although *RSM* models improve the prediction of swirling flows, they require increased computing time due to the additional transport equations and will not be treated herein.

Amongst the eddy viscosity models, 1- or 2-equation models are the most common, with the latter involving one transport equation for the kinetic energy and another for the length or time scale (actually replaced by a dissipation quantity). The most widely used models are the following:

- Spalart-Allmaras (*S-A*) [110] - Based on a single transport equation for the effective viscosity $\hat{\mu}$, it was empirically developed for aerodynamic flows applications and reads as follows.

$$\begin{aligned} \frac{\partial \hat{\mu}}{\partial t} + \frac{\partial}{\partial x_j}\left(\hat{\mu} u_j\right) = C_{b1}\left(1 - f_{t2}\right)\hat{S}\hat{\mu} - \left(C_{w1} f_w - \frac{C_{b1}}{\kappa^2} f_{t2}\right)\left(\frac{\hat{\mu}}{d}\right)^2 + \\ + \frac{1}{\sigma}\left[\frac{\partial}{\partial x_j}\left(\mu + \hat{\mu}\right)\frac{\partial \hat{\mu}}{\partial x_j} + C_{b2}\frac{\partial \hat{\mu}}{\partial x_j}\frac{\partial \hat{\mu}}{\partial x_i}\right] \end{aligned} \tag{3.28a}$$

$$\mu_T = \hat{\mu} f_{v1} \tag{3.28b}$$

Where $\hat{S}$ is the vorticity magnitude, d the wall distance, μ_T the eddy (or turbulent) viscosity, while the remaining parameters are coefficients or blending functions.

- k-ϵ by Jones and Launder [69] - In the framework of high Reynolds flows, eddy viscosity is modelled here by means of the turbulent kinetic energy k and its dissipation rate ϵ, which, being mathematically related, have a transport equation each, as written hereafter.

$$\mu_T = \bar{\rho} c_\mu \frac{k^2}{\epsilon} \tag{3.29}$$

$$\frac{\partial}{\partial t}\left(\bar{\rho} k\right) + \frac{\partial}{\partial x_j}\left(\bar{\rho}\tilde{u}_j k\right) = P - \bar{\rho}\epsilon + J_{k,\epsilon} \tag{3.30a}$$

$$\frac{\partial}{\partial t}\left(\bar{\rho}\epsilon\right) + \frac{\partial}{\partial x_j}\left(\bar{\rho}\tilde{u}_j \epsilon\right) = C_{\epsilon 1}\frac{\epsilon}{k}P - C_{\epsilon 2}\frac{\bar{\rho}\epsilon^2}{k} + J_\epsilon \tag{3.30b}$$

Where P represents production, ϵ dissipation, while J_k and J_ϵ diffusion, defined as per the following expressions:

$$P = \tau_{ij}\frac{\partial \tilde{u}_i}{\partial x_j} \tag{3.31a}$$

$$J_{k,\epsilon} = \frac{\partial}{\partial x_j}\left[\left(\mu + \frac{\mu_T}{\sigma_k}\right)\frac{\partial k}{\partial x_j}\right] \tag{3.31b}$$

$$J_\epsilon = \frac{\partial}{\partial x_j}\left[\left(\mu + \frac{\mu_T}{\sigma_\epsilon}\right)\frac{\partial \epsilon}{\partial x_j}\right] \tag{3.31c}$$

All parameters unspecified are coefficients or blending functions.

- k-ω by Wilcox [108] - Particularly suitable for low Reynolds flows and hence for the resolution of the boundary layer, within this model eddy viscosity is expressed through the turbulent kinetic energy k and its specific dissipation rate (or frequency) ω, similarly to the previous method.

$$\omega = \frac{\epsilon}{c_\mu k} \tag{3.32a}$$

$$\mu_T = \frac{\bar{\rho} k}{\omega} \tag{3.32b}$$

$$\frac{\partial}{\partial t}\left(\bar{\rho} k\right) + \frac{\partial}{\partial x_j}\left(\bar{\rho}\tilde{u}_j k\right) = P - \beta^* \bar{\rho}\omega k + J_{k,\omega} \tag{3.33a}$$

$$\frac{\partial}{\partial t}\left(\bar{\rho}\omega\right) + \frac{\partial}{\partial x_j}\left(\bar{\rho}\tilde{u}_j \omega\right) = \frac{\gamma\omega}{k} P - \beta\bar{\rho}\omega^2 + J_\omega \tag{3.33b}$$

Where the terms on the right-hand side of the transport equations, having the already mentioned characteristics, are defined as:

$$P = \tau_{ij}\frac{\partial \tilde{u}_i}{\partial x_j} \tag{3.34a}$$

$$J_{k,\omega} = \frac{\partial}{\partial x_j}\left[\left(\mu + \sigma_k \frac{\bar{\rho} k}{\omega}\right)\frac{\partial k}{\partial x_j}\right] \tag{3.34b}$$

$$J_\omega = \frac{\partial}{\partial x_j}\left[\left(\mu + \sigma_\omega \frac{\bar{\rho} k}{\omega}\right)\frac{\partial \omega}{\partial x_j}\right] \tag{3.34c}$$

Similarly to previous equations coefficients or blending functions are present.

- k-ω shear-stress transport (*SST*) by Menter [111] - Being an evolution of the standard k-ω model [108], it blends between this and the k-ϵ formulation, as to best fit both low and high Reynolds flow regions within the same computational domain.

$$\frac{\partial}{\partial t}(\bar{\rho}k) + \frac{\partial}{\partial x_j}(\bar{\rho}\tilde{u}_j k) = P - \beta^* \bar{\rho}\omega k + J_{k,\omega} \tag{3.35a}$$

$$\frac{\partial}{\partial t}(\bar{\rho}\omega) + \frac{\partial}{\partial x_j}(\bar{\rho}\tilde{u}_j \omega) = \frac{\gamma\omega}{k}P - \beta\bar{\rho}\omega^2 + J_\omega + \\ + 2(1 - F_1)\frac{\bar{\rho}\sigma_{\omega 2}}{\omega}\frac{\partial k}{\partial x_j}\frac{\partial \omega}{\partial x_j} \tag{3.35b}$$

With F_1 being the specific function blending between the k-ω and the k-ϵ formulations.

3.2.3 Large-eddy simulations

As mentioned, *LES* simulations [94] are a promising route towards the calculation of turbulent flows now largely developed [112], which relies on the spectral filtering of turbulence energy, as already shown in Fig. 3.11. In particular, Fig. 3.13 illustrates how the energy spectrum is decomposed in *LES* into different zones by means of the cut-off wave number κ_c, placed within the inertial range and function of the grid size Δ as $\kappa_c = \frac{\pi}{\Delta}$, and the dissipative wave number κ_d, located at the right far end of the spectrum inertial range.

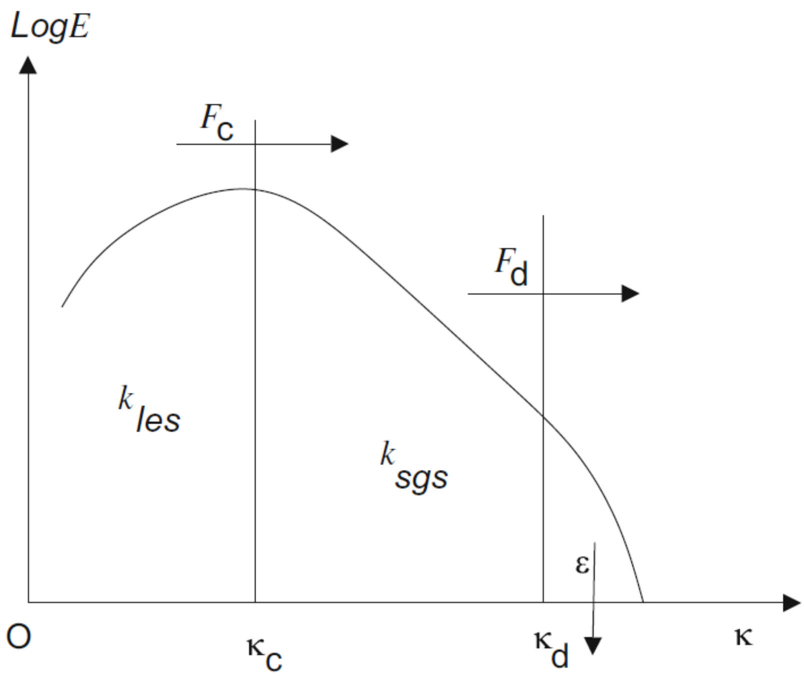

Figure 3.13: Turbulence kinetic energy spectrum splitting in *LES* [113]

Turbulent energy is therefore transferred from the large to the small scales by the turbulence cascade involving non-linear interactions, although backscatter of energy is possible [94]. The *LES* method consists in modelling the more isotropic small scales of the energy spectrum ($\kappa > \kappa_c$), whereas the large scales are explicitly calculated.

By contrast to full statistical modelling, this approach enables to mimic the mechanisms of turbulent interactions, in addition to information on velocity and pressure fluctuations. Applying the filtering process on the instantaneous equations leads to the filtered equations of conservation of mass and momentum of the flow, for which the turbulent subgrid scale stress is to b333e modelled for closure purposes.

In the past, the most widely used subgrid-scale model was a viscosity type model proposed by Smagorinsky [114] (*SM*). It is based on an implicit equilibrium hypothesis which assumes that the viscosity can be calculated using the resolved scales as a characteristic velocity and the grid size as a characteristic length. Many flow studies can be found in the scientific literature that have used this model. However, it soon appeared that the "Smagorinsky" constant is not universal and shall be varied from one flow field to another, as suggested for instance by the dynamic Smagorinsky model (*DSM*) [115]. Eddy viscosity models based on the transport equation of the subgrid scale turbulent energy [116] or second moment closure models based on the transport equation of the subgrid scale stresses [117], both levels of closure using an algebraic relation for length-scale, have been also proposed to overcome the limitations of the Smagorinsky model.

However, accurately resolving the viscous region of wall-bounded flows as well as high Reynolds flows via *LES* is very costly in computational time, due to the very refined mesh required, which increases the number of grid points together with the need for reducing the Courant-Friedrichs-Lewy (*CFL*) number selected in the simulation and hence the time step.

As a consequence, the extension of *LES* to practical applications is not always feasible, which has called for the development of several techniques to model the wall flow region instead of solving all the turbulent scales [118]. *LES* is then performed in the core flow accounting for a wall modeling (*WM*) for reproducing the boundary layer. The first technique is based on the equilibrium laws [116] assuming a relation between the shear stress at the wall and the velocity of the core flow. The second technique relies on a zonal approach based on the explicit solution of a different set of equations in the inner layer, by means of either different or single calculation grids as in *DES*.

The filtering operation of a certain variable ϕ for incompressible flows is performed as follows:

$$\bar{\phi}(x,t) = \int F_{\Delta}\left[x-\xi, \Delta(x,t)\right]\phi(\xi,t)d\xi \tag{3.36}$$

Where F_{Δ} is the filter kernel with Δ width. Therefore the unresolved (subgrid scale SGS) contribution is defined by the following expression:

$$\phi'(x,t) = \phi(x,t) - \bar{\phi}(x,t) \tag{3.37}$$

For compressible flows the Favre-filtering operation (density-weighted) is performed, for which Eq. 3.36 modifies to:

$$\bar{\rho}\tilde{\phi}(x,t) = \int \rho F_{\Delta}\left[x-\xi, \Delta(x,t)\right]\phi(\xi,t)d\xi = \overline{\rho\phi} \tag{3.38}$$

Then, applying such filtering procedure to Eq. 3.8, the filtered NS equations read as reported hereafter:

$$\frac{\partial\bar{\rho}}{\partial t} + \frac{\partial}{\partial x_i}\left(\bar{\rho}\tilde{u}_i\right) = 0 \tag{3.39a}$$

$$\frac{\partial}{\partial t}\left(\bar{\rho}\tilde{u}_i\right) + \frac{\partial}{\partial x_j}\left(\bar{\rho}\tilde{u}_j\tilde{u}_i\right) = -\frac{\partial\bar{p}}{\partial x_i}\delta_{ij} + \frac{\partial}{\partial x_i}\left[\bar{\tau}_{ij} - \bar{\rho}\left(\widetilde{u_i u_j} - \tilde{u}_i\tilde{u}_j\right)\right] \tag{3.39b}$$

$$\begin{aligned}\frac{\partial}{\partial t}\left(\bar{\rho}\tilde{E}\right) + \frac{\partial}{\partial x_i}\left(\bar{\rho}\tilde{u}_j\tilde{E} + \tilde{u}_j\bar{p}\right) &= \\ = \frac{\partial}{\partial x_i}\left[-\left(\widetilde{u_j p} - \tilde{u}_j\bar{p}\right) - \bar{\rho}\left(\widetilde{u_j E} - \tilde{u}_j\tilde{E}\right) - \bar{q}_j + \overline{u_i\tau_{ij}}\right]\end{aligned} \tag{3.39c}$$

Many analogies lay in Eq. 3.39 with respect to Eq. 3.24. In fact, in a similar manner, unresolved scales effect on the filtered quantities can be modelled. Models based on the transport equation of subgrid turbulent energy exist, in analogy with the aforementioned Reynolds stress models. However, the eddy-viscosity based models are the simplest and easiest to adopt and will be briefly mentioned here.

The unresolved subgrid-scale tensor $\tau_{ij,sgs}$, analogous of the turbulent stress tensor of Eq. 3.9 is therefore definable as:

$$\bar{\tau}_{ij,sgs} = 2\mu_{sgs}\tilde{S}_{ij} - \frac{2}{3}\mu_{sgs}\frac{\partial u_k}{\partial x_k}\delta_{ij} \tag{3.40}$$

Similarly, the unresolved subgrid-scale energy flux $\bar{q}_{j,sgs}$ is modelled by means of a turbulent thermal conductivity λ_{sgs} and Prandtl number Pr_{sgs} (commonly set equal to 0.7):

$$\bar{q}_{j,sgs} = -\bar{\rho}\left(\widetilde{u_j E} - \tilde{u}_j \tilde{E}\right) = -\lambda_{sgs}\frac{\partial \tilde{T}}{\partial x_i} \tag{3.41a}$$

$$\lambda_{sgs} = \frac{\mu_{sgs}\bar{c}_p}{Pr_{sgs}} \tag{3.41b}$$

The subgrid scales are assumed to have a universal behavior. Following the Kolmogorov cascade theory [119], their contribution is generally represented as purely dissipative. Under this hypothesis the energy is transferred only from the filtered motions to the residual motions, with no backscatter [94]. The main subgrid models based on eddy viscosity are the following:

- Smagorinksy - Initially proposed by Smagorinsky [114], the expression of turbulent viscosity in this model, based on a mixing-length analogy, reads:

  $$\mu_{sgs} = (C_S \Delta)^2 \sqrt{2\tilde{S}_{ij}\tilde{S}_{ij}} \tag{3.42}$$

  Where Δ is the characteristic filter width (linked to the cube-root of the cell volume) and C_S is the model constant, with a typical value of 0.17 estimated from the Kolmogorov spectrum [120]. This model is able to correctly predict the decay of turbulence in homogeneous isotropic turbulence. However, the model is non-vanishing in pure shear. It is therefore generally not suitable for wall-bounded flows when using no-slip walls and is generally too dissipative.
  In the case of one transport equation for the subgrid turbulent energy, the following equations apply:

  $$k_{sgs} = \frac{\tau_{ij,sgs}}{2} \tag{3.43a}$$

  $$\mu_{T,sgs} = c_\mu k_{sgs}^{1/2}\Delta \tag{3.43b}$$

  Where Δ is the mesh grid size. In first moment closure, the subfilter energy k_{sgs} is computed by means of its transport equation. The modelling of the subgrid energy equation has been worked out by several authors, among which Schumann [116] and Yoshizawa and Horiuti [121]. The following is inspired by its corresponding *RANS* modelling, but assumes that the turbulence length-scale is of the same order of the grid-size Δ leading to:

$$\frac{\partial}{\partial t}\left(\rho k_{sgs}\right) + \frac{\partial}{\partial x_j}\left(\rho u_j k_{sgs}\right) = P_{sgs} - \rho\epsilon_{sgs} + J_{k,sgs} \tag{3.44}$$

With P_{sgs}, ϵ_{sgs} and $J_{k,sgs}$ being respectively once more the production, dissipation and diffusion terms. Noting that the dissipation is not expressed via a transport equation but explicitly through the grid size Δ, these read as follows:

$$P_{sgs} = -\tau_{ij,sgs}\frac{\partial \tilde{u}_j}{\partial x_i} \tag{3.45a}$$

$$\epsilon_{sgs} = C_\epsilon \frac{k_{sgs}^{3/2}}{\Delta} \tag{3.45b}$$

$$J_{k,sgs} = \frac{\partial}{\partial x_j}\left[\left(\mu + \frac{\mu_{T,sgs}}{\sigma_k}\right)\frac{\partial k_{sgs}}{\partial x_j}\right] \tag{3.45c}$$

With σ_k being a constant coefficient.

- Dynamic Smagorinsky - In this approach, the constant C_S is no longer a user-defined constant. By contrast, it is evaluated dynamically in the simulation on the basis of the Germano identity, as done by Lilly [122] using a test-filter scale.
- Wall-Adaptive Local Eddy viscosity (*WALE*) - Initially proposed by Ducros et al. [123], it models the eddy viscosity with the following formula:

$$\mu_{sgs} = \left(C_w\Delta\right)^2 \frac{\left(s_{ij}^d s_{ij}^d\right)^{3/2}}{\left(\tilde{S}_{ij}\tilde{S}_{ij}\right)^{5/2} + \left(s_{ij}^d s_{ij}^d\right)^{5/4}} \tag{3.46a}$$

$$s_{ij}^d = \frac{1}{2}\left(\tilde{g}_{ij}^2 + \tilde{g}_{ji}^2\right) - \frac{1}{3}\tilde{g}_{kk}^2\delta_{ij} \tag{3.46b}$$

With $C_w = 0.4929$ being the model constant and $\tilde{g}_{ij}$ denoting the resolved velocity gradient, the model was developed to obtain correct scaling laws in near wall regions for wall bounded flows.

3.2.4 Hybrid RANS-LES methods

Hybrid *RANS-LES* methods capable of reproducing a *RANS*-type behaviour in the vicinity of a solid boundary and an *LES*-type one far away from the wall boundary have been developed in the past two decades for improving the numerical prediction of complex flows encountered in engineering applications with affordable computational resources. In particular, depending on the physical problem to be studied, some regions of the flow may require a more refined description of the turbulent eddy interactions using finer grids with *LES* simulations whereas other regions that are of less complex physics can be calculated satisfactorily from *RANS* models.

As statistical and filtered equations can be written formally in the same mathematical form at a first sight, *RANS* and *LES* can be combined by using turbulence models based on different type of closure to build composite methods.

Usually, hybrid *RANS-LES* methods are inspired by *RANS* modelling, which constitutes a convenient framework. According to the literature [103], hybrid methods can be broadly classified into two main categories: "zonal" and "non-zonal". The former relies on two different models, a *RANS* model and a subgrid-scale model, which are applied to different domains separated by a sharp or dynamic interface, whereas the latter assumes that the governing set of equations is smoothly converting from a *RANS* to an *LES* behaviour, based on criteria updated during the computation. However, some authors [102] prefer to name these two categories as "segregated" and "unified".

"Segregated" methods have a discontinuous flow solution (including velocity) at the interface but were the first hybrid *RANS-LES* models to be developed [124]. However, more recently, new models based on a "unified" approach are becoming of growing interest for simulations of complex turbulent flows encountered in engineering applications.

Noticeably, the main shortcoming of "zonal" methods lies in the connection interface between *RANS* and *LES* regions. Other drawbacks of the method are [125]:

- the interface being empirically set inside the computational domain;
- the turbulence closure changes from one model to the other, without continuity when crossing the interface;
- an internal forcing produced by artificial instantaneous random fluctuations necessary for restoring continuity at the crossflow between these domains;
- extra terms introduced in the equations needed to get the correct velocity and stress profiles in the boundary layer.

Among these hybrid *RANS-LES* methods, one of the most popular is the Detached Eddy Simulation (*DES*) developed by Spalart et al. [124], which switches from a *RANS* to an *LES* behavior depending on a criteria based on the turbulent length-scale.

It is often used for the simulation of high Reynolds number flows with massive separation around obstacles, with the purpose of calculating global coefficients such as drag, lift and pressure coefficients, useful in the aerodynamic design optimization of aircraft wings. This approach is zonal, but, considering that the same basic model is used both in *RANS* and *LES* zones, the transition between the two occurs without true discontinuity. As *DES* is based on the Spalart-Allmaras model, the wall distance d_w is herewith replaced by $\tilde{d}$ involving also the grid-size Δ:

$$\tilde{d} = \min(d_w, C_{DES}\Delta) \tag{3.47a}$$

$$\Delta = \max(\Delta_1, \Delta_2, \Delta_3) \tag{3.47b}$$

With C_{DES} a coefficient set to 0.65 as calibrated with decaying homogeneous turbulence. In the near wall region $\tilde{d} = d_w$, reducing to the *S-A* model, while far away from the wall $\tilde{d} = C_{DES}\Delta$ making the model acting as a sub-grid scale model.

However, *DES* is very sensitive to the grid-size. In particular, the gray area where the model varies from *uRANS* to *LES* mode may be problematic unless the separation is abrupt and determined by the geometry [126]. The second problem of *DES* consists in a possible delay in the formation of instabilities in mixing layers, although a new version of the detached-eddy simulation, referred to as *DDES* [127] (i.e. delayed-*DES*), resistant to ambiguous grid densities, has been developed recently. From a practical perspective, the *DES* technique was afterwards applied on two-equation models, such as the *k-ω SST*.

One of the first “non-zonal” hybrid *RANS-LES* method was derived by Speziale [128], who performed very-large eddy simulation (*VLES*). In this method, the turbulent stresses are computed by damping the Reynolds stresses in regions where the grid spacing is of the order of the Kolmogorov length-scale. This method presents the advantage of continuously varying between *DNS* and *RANS* computation. The partially-integrated transport modelling (*PITM*) is a promising method in turbulence modelling (developed by Schiestel and Dejoan [129] and Chaouat and Schiestel [113]), since it allows numerical simulation of turbulent flows out of spectral equilibrium performed on relatively coarse grids. The subfilter models herewith derived have the property of working on *LES* mode and smoothly change from *RANS* to *DNS* if the grid-size is enough refined in the flow region with seamless coupling, thanks to a new dissipation-rate equation, used in conjunction with the equation of the subfilter scale energy or the equations of the subfilter scale stresses, whether the first or second level of closure is adopted. The partially averaged Navier-Stokes (*PANS*) method developed by Girimaji and Abdol-Hamid [130] is also similar to the *PITM* equations.

One further method is scale adaptive simulation (*SAS*), which uses a two-equation model proposed by Menter and Egorov [131] to simulate unsteady turbulent flows. This method is based on the introduction of the "von Karman" length-scale into the turbulence scale equation. However, *SAS* and *PANS* shall be considered closer to *uRANS* methods, since no explicit filter or grid size appears in the formulation of their basic equations.

One last "non-zonal" method worth mentioning is the stress-blended eddy simulation *SBES*, in which turbulence models are blended using a weighted sum of *RANS* and *LES* models.

3.2.5 Scale-adaptive simulations

The method of scale adaptive simulation (*SAS*) has been proposed by Menter and Egorov [131] to simulate unsteady turbulent flows by using two-equation models. As mentioned earlier *SAS* is essentially a *uRANS* model able of adjusting to resolved structures in a flowfield through its source term equilibrium. As classical *RANS* adjusts the length scale to the shear layer thickness, independent of any resolved scales, it is believed that suppressing the formation of turbulent structures is a necessary consequence of Reynolds averaging and an inevitable feature of the method. On the contrary Menter and Egorov [131] state that the fact that the equations have been Reynolds averaged is only known by the human observer, rather the information handed to the momentum equations is only the eddy viscosity (or the Reynolds stresses). If the eddy viscosity is small enough, the model allows the formation of a turbulent spectrum, provided that the flow is sufficiently unstable. In fact, it is important to note that the momentum equations for *LES* and *RANS* are identical even though their derivation is entirely different (assuming an eddy viscosity model is used in both concepts). In other words, it is not the averaging concept which defines the equations, but the details of the turbulence model formulation.

SAS modelling, in fact, is based on the use of a second mechanical scale in the source-sink terms of the underlying high-Reynolds number turbulence model. In addition to the standard input from the momentum equations in the form of first velocity derivatives (strain rate tensor, vorticity tensor, etc.) *SAS* models rely on a second scale, typically in the form of higher velocity derivatives (here a second derivative), which allows the model to adjust its length scale to resolved structures in the flow.

This is achieved by means of the introduction of the generalised "von Karman" length-scale L_{vK} defined as per Rotta [132] into the turbulence scale equation:

$$L_{vK} = K_{vK} \sqrt{\frac{2\bar{S}_{ij}\bar{S}_{ij}}{\frac{\partial^2 \bar{u}_i}{\partial x_k^2}\frac{\partial^2 \bar{u}_i}{\partial x_j^2}}} \tag{3.48}$$

With K_{vK} being the "von Karman" constant, the meaning of this turbulence length-scale is simple: for a boundary layer, the L_{vK} length-scale is the distance normal to the wall x_n in the logarithmic layer region, assuming that the velocity gradient is given by the following expression:

$$\frac{\partial \bar{u}_{\perp x_n}}{\partial x_n} = \frac{u_\tau}{K_{vK} x_n} \tag{3.49}$$

Where u_τ is the friction velocity. Menter and Egorov [131] indicated in their paper that it is by accounting for the "von Karman" length-scale into *RANS* that allows for the corresponding *SAS* model to dynamically adjust to resolved structures in a *uRANS* simulation, which results in a *LES*-like behaviour in unsteady regions of the flow field, while acting like standard *RANS* models in stable regions. This occurs since eddy viscosity is small enough to allow a break-up of large scales into smaller ones under unsteady flow situations, even though there is no theoretical criterion with respect to when a flow is sufficiently unstable to induce such a mode.

This argument is supported by the test case of turbulent shear flow: in the case of homogeneous shear flow, frequency (ω) is proportional to the mean strain rate, while the length-scale L goes to infinity; by contrast, in the case of non-homogeneous flows, frequency is proportional to the local strain rate but the spatial variation of the length-scale L is then limited by L_{vK}.

For unsteady flows, the model has the feature to work in a *LES* mode because the turbulence length-scale is reduced, which yields a lower eddy viscosity allowing for the development of turbulent fluctuations. Moreover, *SAS* relies on local flow physics rather than the grid-size to make the transition from *RANS* to *LES*-like behaviour. In this sense, the method has been derived from the RANS formalism, i.e. without referring to filtering or to the grid-size Δ (or alternatively the cutoff wave number κ_c), which makes it more similar to an unsteady *RANS* than a real hybrid *RANS-LES* method. This also means that, unlike other more properly regarded hybrid methods, *SAS* does not revert to *DNS* in the limiting condition where the grid-size Δ is reduced to the "Kolmogorov" length-scale η_K.

Initially Menter and Egorov [131] have derived the transport equation for the variable $\Psi = kL$ inspired by the work of Rotta [132], then they have introduced the variable $\Phi = \sqrt{k}L$ with a simple transformation of variables, since this one is directly proportional to the turbulent eddy viscosity $\mu_T = c_\mu^{1/4}\Phi$. As a result, they proposed the K-square-root K-L (*KSKL*) model, formally reading:

$$\frac{\partial}{\partial t}(\rho k) + \frac{\partial}{\partial x_j}(\rho u_j k) = P - \rho c_\mu^{3/4}\frac{k^2}{\Phi} + J_{k,\Phi} \tag{3.50a}$$

$$\frac{\partial}{\partial t}(\rho \Phi) + \frac{\partial}{\partial x_j}(\rho u_j \Phi) = \frac{\Phi}{k}P\left[\zeta_1 - \zeta_2\left(\frac{L}{L_{vK}}\right)^2\right] - \rho\zeta_3 k + J_\Phi \tag{3.50b}$$

Where J_Φ denotes the diffusion process associated with Φ, whereas ζ_1, ζ_2 and ζ_3 are numerical coefficients. In comparison with the *k*-ω *SST* model, which returns only large scale fluctuations, it has been found that the *KSKL* model is capable of capturing the formation of turbulent structures in the separated zone of a flow past a cylinder ("vortex shedding instability"). Subsequently, the *KSKL* was transformed into the *k*-ω *SST* model using the relation:

$$\Phi = \frac{1}{c_\mu^{1/4}}\frac{k}{\omega} \tag{3.51}$$

With such intent, the additional term involving the $\left(\frac{L}{L_{vK}}\right)^2$ ratio of Eq. 3.50 was included as a source term in the ω equation, which reads:

$$Q_{SAS} = \max\left[\zeta_2 S^2\left(\frac{L}{L_{vK}}\right)^2 - C_{SAS}\frac{2k}{\sigma_\Phi}\max\left(\frac{1}{k^2}\frac{\partial k}{\partial x_j}\frac{\partial k}{\partial x_j}, \frac{1}{\omega^2}\frac{\partial \omega}{\partial x_j}\frac{\partial \omega}{\partial x_j}\right), 0\right] \tag{3.52}$$

Where $C_{SAS} = 2$, $\sigma_\Phi = \sigma_k$ in the diffusion term $J_{k,\Phi}$, while the length-scale L is given by:

$$L = \frac{\sqrt{k}}{C_\mu^{1/4}\omega} \tag{3.53}$$

Q_{SAS} is the dominant term in the ω transport equation in situations of unsteady flows, implying an increase of ω that leads to a decrease of the turbulent eddy viscosity ($\mu_T = k/\omega$). In addition, it is to be noted that *SAS* provides a continuous variation of solution ranging from *LES*- to *RANS*-mode with respect to the time step Δt corresponding to the *CFL* number selected in the simulation.

Chapter 4

Combustor-turbine interaction in an aero-engine

Contents

4.1 Numerical setup

The calculations reported hereafter were carried out with the *CFD* solver ANSYS® Fluent release 18.0. The working fluid (air) was treated as a compressible ideal gas with variable thermophysical properties. Two computational domains were considered, i.e. a smaller domain, analysed with *RANS* and consisting of just the *NGVs*, and a more extended domain that integrates combustor simulator and *NGVs*. *RANS* simulations were performed with the k-ω *SST* model, whereas *SAS* was exploited for the integrated case, as to assess the capabilities of scale-resolving simulations to better predict the turbulent mixing. *RANS* simulations were performed with a standard value of 0.85 for the turbulent Prandtl number, whereas *SAS* was performed using a value of 0.50 as suggested in [133]. There are conflicting reports in literature about the most appropriate choice, however it is reasonable to state that its impact in a *SAS-LES* framework is modest if compared to *RANS*.

Turbulence equations are integrated up to the wall for both k-ω *SST* and *SAS* runs. All equations were discretised in space with a 2*nd* order upwind scheme, whereas for the scale-adaptive simulation a bounded central differencing scheme was used for the momentum equation, in agreement with the best practices specified by the software developers [134]. A bounded 2*nd* order implicit scheme for time discretisation was used for the unsteady simulations.

The time step to advance in time for *SAS* is $5 \cdot 10^{-7}$ s, chosen in order to ensure a Courant number < 1 in the zones of interest. The data sampling for statistical averaging was made on a time frame of 0.0089 s, corresponding to 39 flow-through times across the *Plane 40*-Plane *41* distance, which proved to be capable of collecting representative statistics, as confirmed by monitoring velocity and temperature values in representative locations converging within a $\pm 1\%$ range.

A sketch of the computational domain for the integrated combustor-turbine simulations is reported in Fig. 4.1. It is to be noted that the *NGVs*-only simulations considered only a portion of this domain, i.e. from the *Plane 40* section to the outlet one. The boundary conditions at the inlet were assigned in this case by prescribing previously calculated 2D maps obtained at the *Plane 40* of the hot streak generator domain with *RANS* and *SAS* [135]. Conditions were defined in terms of total pressure and temperature, velocity components and turbulence quantities like k and ω. At the outlet of both simulations, a radial equilibrium profile of static pressure was imposed, adjusting its value to match the experimental mass flow rate at *Plane 40*. Walls were treated as no slip, smooth and adiabatic. A periodic condition was assumed on the lateral interfaces to consider only one sector. To trace the evolution of film cooling a passive scalar was transported, assigning a boundary condition of 1 to the inlets of the internal channels and 0 at either the swirler inlet or *Plane 40*.

The computational grid was generated with the commercial software ANSYS® Meshing. The hybrid unstructured mesh is composed by tetrahedra and prisms, includes 10 prismatic layers for the near-wall discretisation and counts about $26.3 \cdot 10^6$ elements and $8.8 \cdot 10^6$ nodes for the *NGVs*-only domain. For the integrated simulation including both combustor and *NGVs* a size of 1 mm was used in the region of the swirling flow, as done by Andreini et al. [135]. This increases the mesh size to $43.5 \cdot 10^6$ elements and

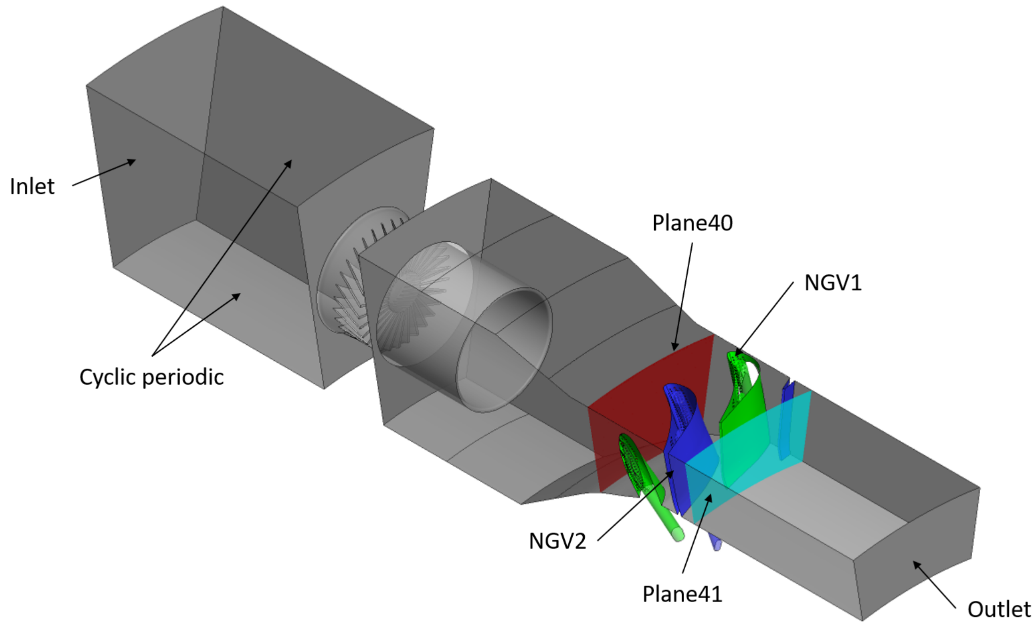

Figure 4.1: *FACTOR* - Computational domain for the integrated combustor-turbine simulations

$12.7{\cdot}10^6$ nodes. In both cases nozzles film-cooling holes have been discretised with 7 tetrahedra along the 7-mm diameter in addition to the 10 prisms. An overview of the mesh grid for the integrated simulation is given in Fig. 4.2.

The quality of the mesh for scale-resolving simulations was then evaluated *a posteriori* calculating the criterion proposed by Pope [136] (recalling Eq. 3.7) and checking that more than 80% of the turbulence kinetic energy was resolved in most of the domain, as illustrated in Fig. 4.3.

For the integrated case, where the combustor simulator is included, the presence of a huge number of effusion cooling holes (more than 5000 holes per sector) demands for an appropriate modelling strategy in order to reduce the computational cost. At this purpose, the Adiabatic Homogeneous Model (*AHM*) proposed by Mendez and Nicoud [137] was employed to account for multiperforated liners in combustor flow simulation. Mendez and Nicoud [137] developed a coupled suction/injection model to reproduce the average effect of coolant injection on the mainstream. The perforation is replaced by a uniform boundary condition, thus distributing the coolant mass flow over the whole liner, rather than extracted/injected at each entrance/exit of the holes. The exploitation of this method allows to employ coarse grids in the near-wall region of the liners, making feasible the reproduction of the global flow field structures even with a simplified effusion cooling modelling.

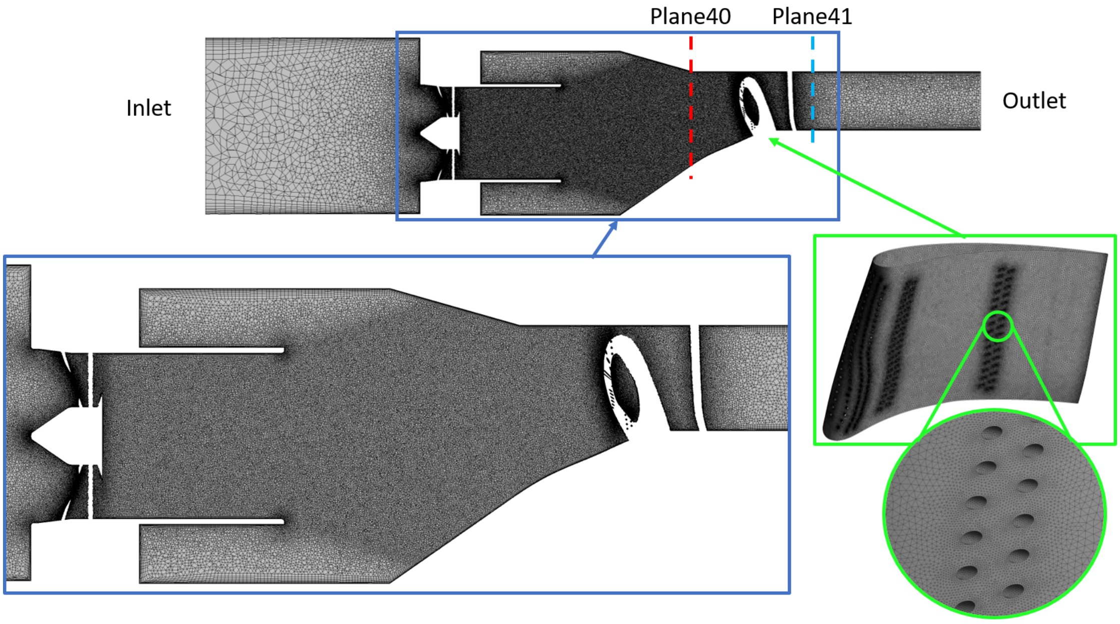

Figure 4.2: *FACTOR* - Computational mesh grid for the integrated combustor-turbine simulations

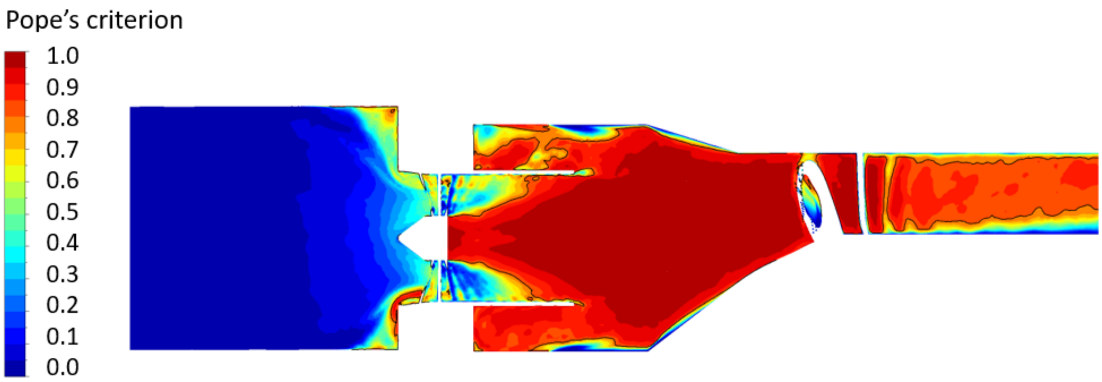

Figure 4.3: *FACTOR* - Pope's criterion on the integrated combustor-turbine domain

4.2 First stage nozzles aerothermal performance

4.2.1 Combustor and conditions at Plane 40

To better understand the flow physics that leads to the formation of the hot streak on *Plane 40*, a brief summary of some previously obtained results on the combustor-only domain (see for example Andreini et al. [138] and Andreini et al. [135]) is hereafter reported.

The velocity field on the meridional plane is reported in Fig.4.4 for the isothermal test point and with no ducts installed on the swirlers. As it can be noted, the experimental data is available only in a restricted area due to the limited optical access. Moreover, the region of the upper part of the swirling flow, significantly reduced if compared to the lower one, is to be ascribed to a light reflection that alters the *PIV* measurements. Experiments are compared against numerical results obtained with ANSYS® *CFX* using the steady *RANS* approach and with ANSYS® Fluent using both *RANS* and *SAS* approaches. Numerical simulations were performed using a single sector domain with circumferential periodicity.

Within the *RANS* framework both solvers over-predict the opening of the jets exiting from the swirler (as shown in Fig.4.4, which actually reports only the ANSYS® Fluent results). The central recirculation zone generated from the vortex breakdown mechanism results larger than in experiments and the high-speed flow coming from the swirler impacts on the endwalls interacting with the cooling flow near the effusion cooled liners. The *SAS* case shows a very different behaviour with respect to *RANS*, predicting an asymmetric shape of the high-speed jets. In addition this is radially more confined with a closer resemblance to *PIV* measurements. Moreover, a similar asymmetric behaviour has been found also with large-eddy simulations performed by a partner of the *FACTOR* project [22], shown in Fig.4.5.

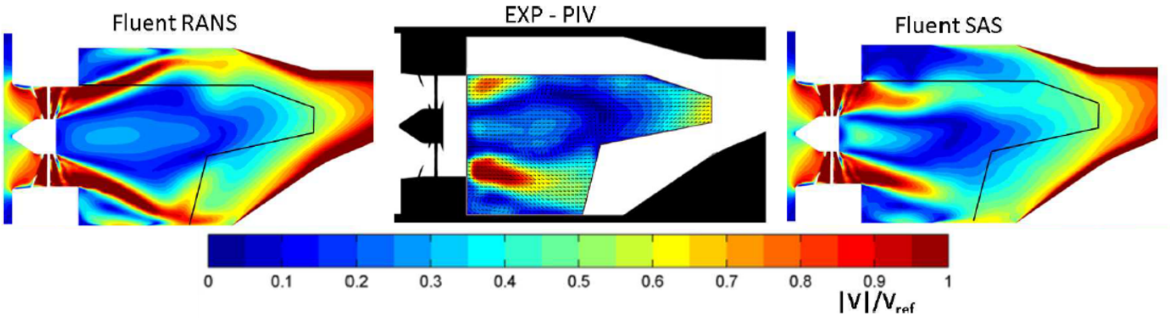

Figure 4.4: *FACTOR* - Comparison of velocity field on the meridional plane between experiments and *CFD* (without ducts) at isothermal point [138]

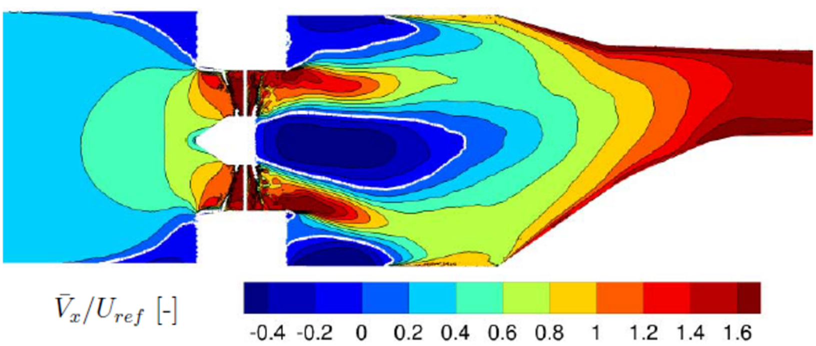

Figure 4.5: *FACTOR* - Time-averaged velocity field and reversed flow contours on the meridional plane by *LES* at isothermal point [22]

In a following stage of the project, when ducts were installed immediately downstream of the swirlers, *PIV* measurements were repeated and once more compared against *CFD* with cyclic periodicity, as shown in Fig. 4.6. Unfortunately in this case *PIV* allows for an even more limited view of the combustor meridional plane with respect to the case without ducts installed. Nevertheless *SAS* proves to better predict the velocity field if compared to *RANS* models.

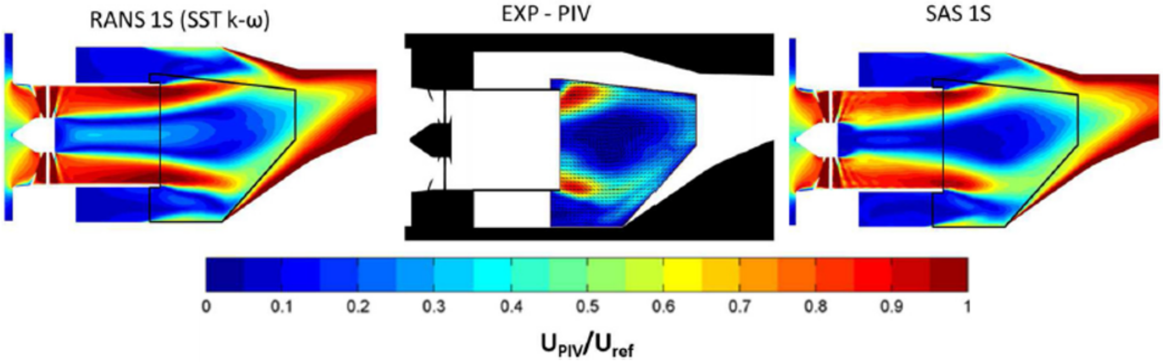

Figure 4.6: *FACTOR* - Comparison of velocity field on the meridional plane between experiments and *CFD* (with ducts) at design point [135]

As a general comment, it can be noted how the velocity field is characterised by the presence of a strong recirculation region (coloured in dark blue) extending down to the chamber exit, while the swirling flow interacts with the cold streams injected through the liners, especially nearby the inclined walls. For this sake Fig.4.7 reports the vortices generated by the swirlers, highlighting the structures categorisation recalled in Section 2.1.1 by means of isosurfaces of instantaneous lower-than-mean static pressure and lambda2 criterion.

Furthermore, downstream of the duct such an interaction leads to a significant and progressive turbulent mixing that promotes the formation of the hot streak at the combustor outlet section. However, if the aerodynamic field at the combustor outlet section (*Plane 40*) is to be compared between experiments (*5HP*) and numerical predictions, swirl (or yaw) and pitch angles can be drawn, as illustrated in Figs.4.8 and 4.9 and as expressed by the following definitions:

$$Swirl\ (Yaw) = atan\left(\frac{V_{tan}}{V_{ax}}\right)\frac{180}{\pi} \tag{4.1a}$$

$$Pitch = atan\left(\frac{V_{rad}}{V_{ax}}\right)\frac{180}{\pi} \tag{4.1b}$$

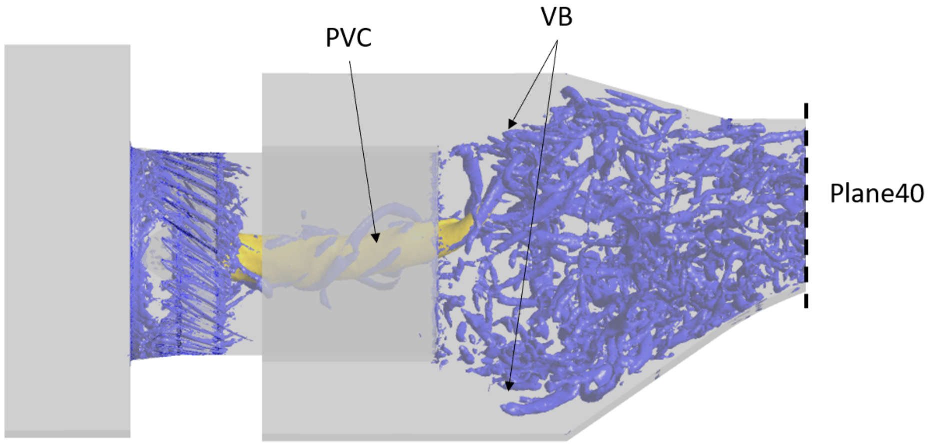

Figure 4.7: *FACTOR* - Precessing vortex core (orange, *PVC*) and vortical structures (blue, including vortex breakdown *VB*) highlighted by isosurfaces of respectively instantaneous static pressure and lambda2 criterion

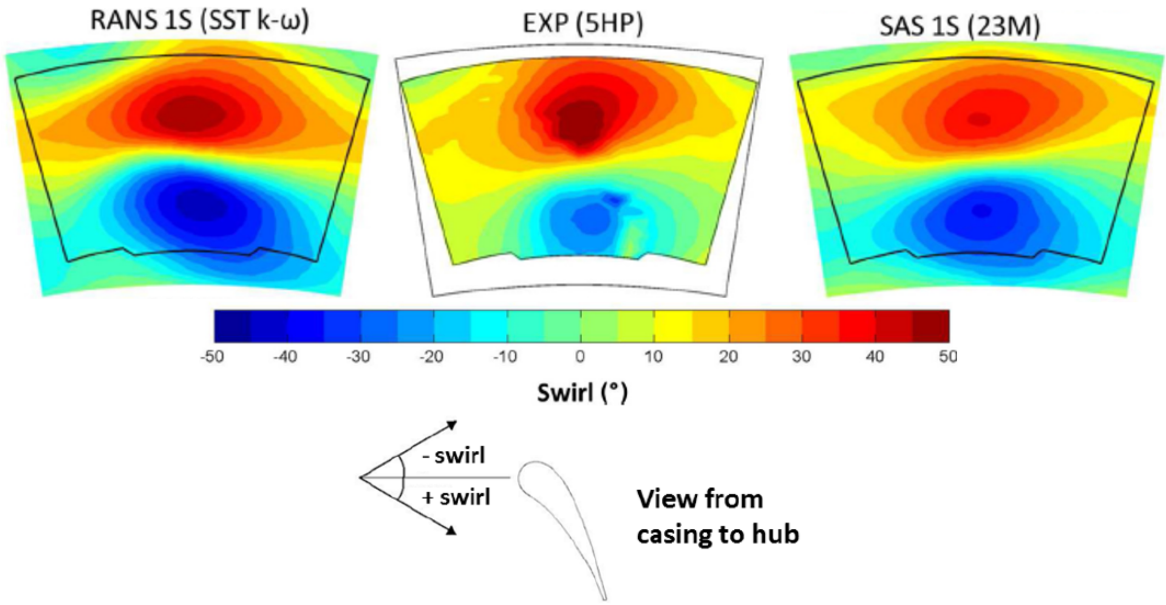

Figure 4.8: *FACTOR* - Comparison of swirl (or yaw) angle at Plane40 between experiments and *CFD* (with ducts) at design point [135]

Although at a first sight *RANS* may seem to fairly replicate experiments, it is fundamental not to compare only the velocity related quantities, but also temperature. To really understand the final impact of the different modelling strategies on turbulent mixing, it is therefore necessary to evaluate the thermal field at the combustor outlet. Among the different definitions usually employed to quantify temperature distortions,

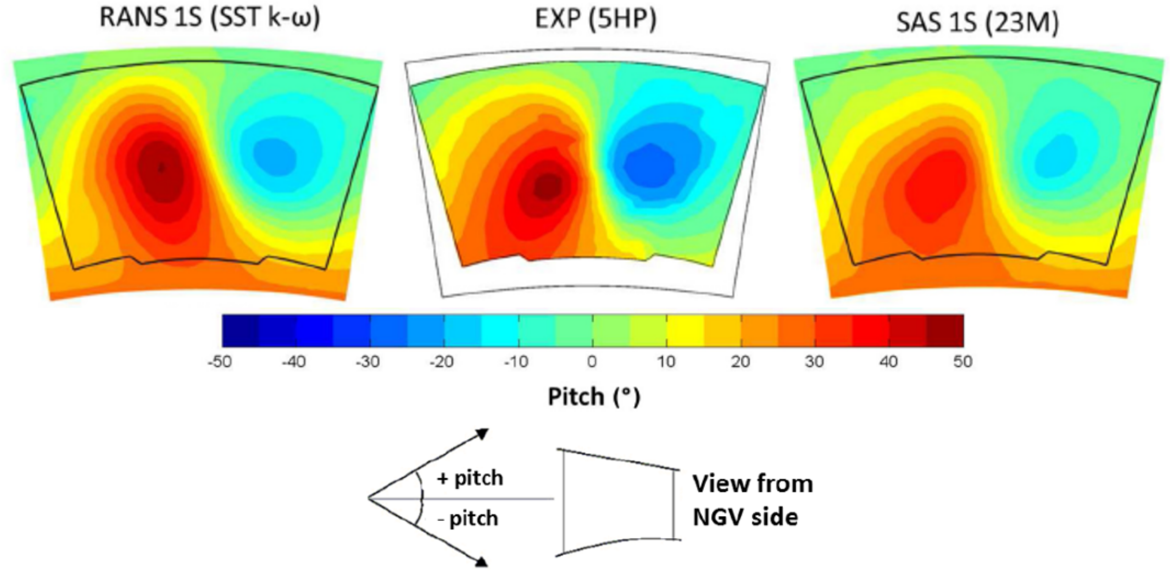

Figure 4.9: *FACTOR* - Comparison of pitch angle at Plane40 between experiments and *CFD* (with ducts) at design point [135]

the $LOTDF_{rig}$ quantity is used here, as recalled from Eq. 2.3a:

$$LOTDF_{rig} = \frac{T\left(r,\theta\right)_{40} - \bar{T}_{40}}{\bar{T}_{40} - T_{cool}} \tag{4.2}$$

The choice between different modelling strategies (*SAS* and *RANS* in this case) leads as expected to huge differences in such reference parameter, as depicted in Fig. 4.10, which also shows the circumferentially-averaged *LOTDF* (*LRTDF*, i.e. Local Radial Temperature Distortion Factor, see Eq. 2.3b) plotted as a function of the radial span. This highlights how a more accurate reproduction of the pattern can be obtained only exploiting *SAS* (or, more generally, scale-resolving simulations), whereas *RANS* strongly underestimates the turbulent mixing, which results in a more confined hot spot, with significantly higher non-uniformities in both radial and tangential directions.

4.2.2 Conditions at Plane 41

As explained in [139], one of the primary objectives of this work consists in analysing the impact of the turbine inlet conditions on the *NGVs* in both uncooled and cooled configurations due to the flow field generated by the combustor with particular focus on the hot streak. As described earlier, the difference in the prediction consists in the approach used to obtain the inlet conditions at *Plane 40*, i.e. *RANS* and *SAS*.

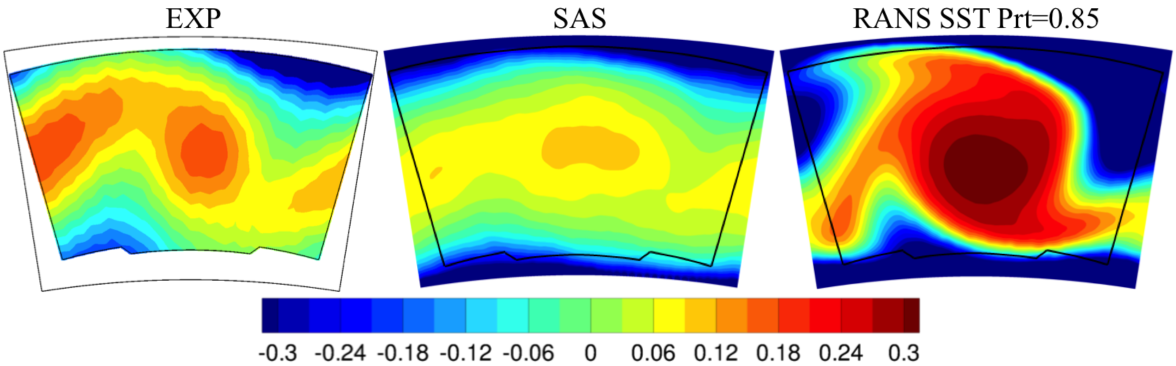

(a)

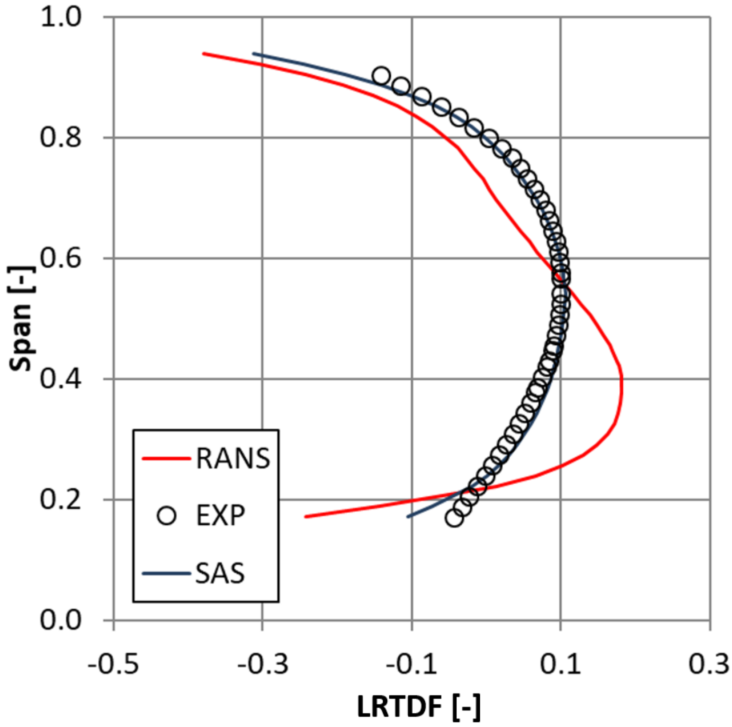

(b)

Figure 4.10: *FACTOR - LOTDF* (a) and *LRTDF* (b) at the combustor outlet section (Plane40) [135]

Indeed the tags 'Inlet RANS' and 'Inlet SAS', mentioned hereafter, indicate analyses performed on the *NGVs*-only domain applying:

- 'Inlet RANS' - Inlet boundary conditions derived from a *RANS* simulation of the combustor-only domain;
- 'Inlet SAS' - Inlet boundary conditions derived from a *SAS* simulation of the combustor-only domain.

Fig. 4.11 compares the temperature fields at the combustor-turbine interface section as predicted by *SAS* and *RANS*, with the left-hand side contours reporting *Plane 40*, while the right-hand ones a 3D view of the uncooled nozzles invested by an isovolume of total temperature higher than 485 K.

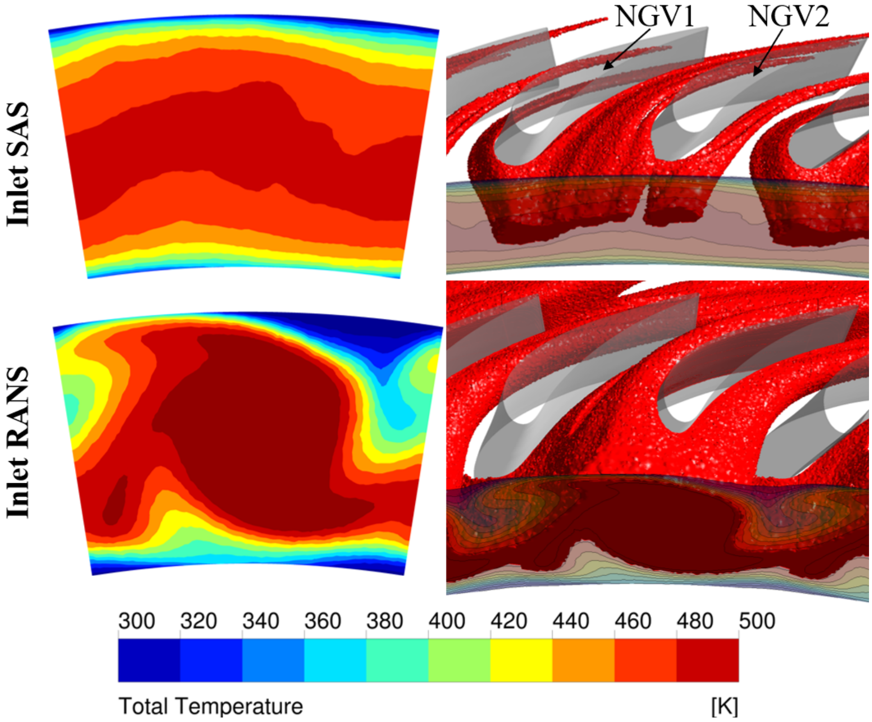

Figure 4.11: *FACTOR* - Comparison of temperature inlet and isovolume with total temperature above 485K between 'Inlet RANS' and 'Inlet SAS' cases

It is also worth pointing out that at this stage only a *RANS* approach was applied for the simulation of the *NGVs*, as the use of an unsteady approach in absence of time-varying inlet boundary conditions would be useless or even not physical. Furthermore, this process is similar to the procedure usually employed in industrial applications to design high-pressure *NGVs* and lays the foundation for a comparison with the following integrated combustor-*NGVs* approach.

The first assessment is focused on pure aerodynamics aspects, i.e. the pressure coefficient, which, recalling Eq. 2.5a, quantifies the level of non-uniformity of total pressure at a certain location, in this case at *Plane 41*:

$$C_p = \frac{\bar{P}_{t,40} - P_t}{\bar{P}_{t,40} - P_s} \tag{4.3}$$

As depicted in Fig. 4.12 and described in greater detail by Bacci et al. [140], despite swirler and *NGV2* leading edge are nominally aligned, the swirling flow is mainly convected on the PS of *NGV2*. Part of the swirl component is preserved up to *Plane 41*, resulting in a total pressure non-uniformity in the right-hand passage whereas the left-hand one is barely affected. Considering the corresponding numerical predictions, it is possible to observe that *CFD* is capable of reproducing the overall pattern even though the intensity of some flow structures are somewhat over-preserved. This greater coherency can be reasonably ascribed to the exploitation of the *RANS* approach that could underestimate the mixing nature of flow due to turbulent fluctuations.

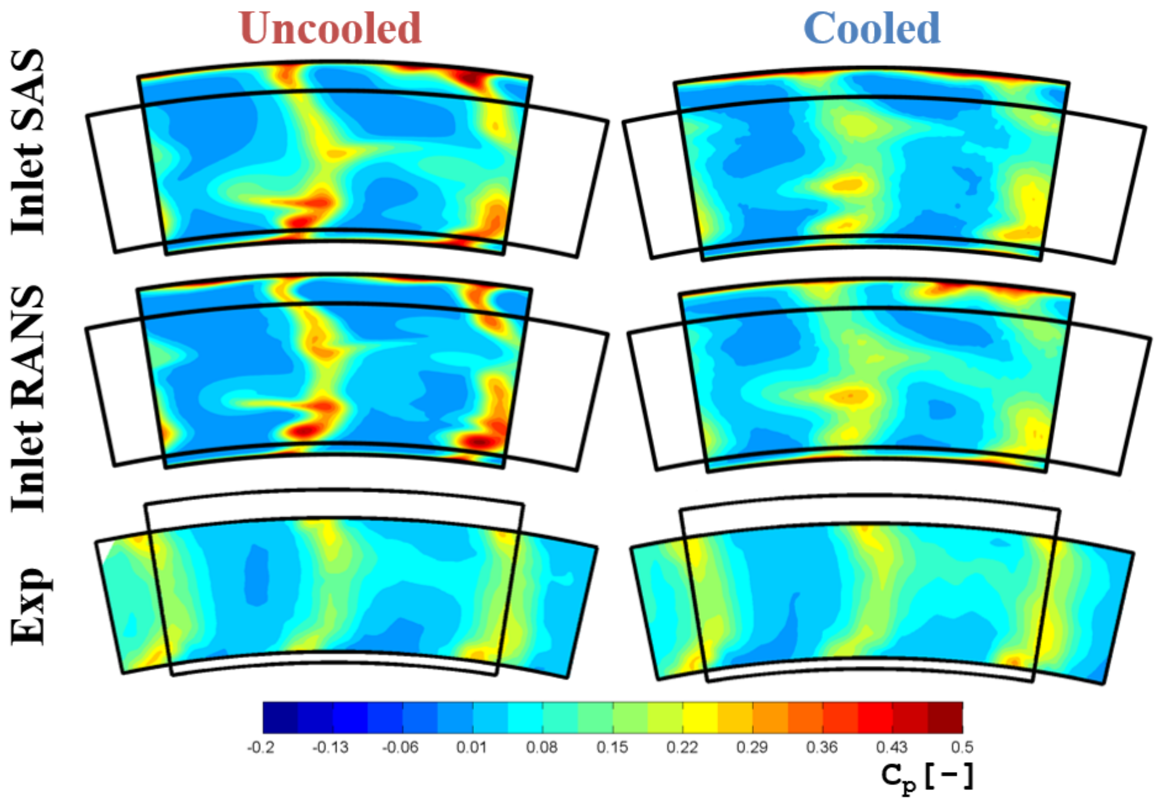

Figure 4.12: *FACTOR* - Comparison of pressure coefficient C_p at *Plane 41* between experiments and ‘Inlet SAS’ and ‘Inlet RANS’ simulations of the *NGVs*

Some additional differences can be noted comparing uncooled versus cooled nozzles. To further investigate the aerodynamic field, it can be helpful to plot the airfoil pressure loading, defined as the ratio between local static pressure and total pressure at *Plane 40*. Fig. 4.13 reports a comparison between the ‘Inlet SAS’ simulation of the *NGVs* against measurements taken with the *PSP* technique. Although the two graphs show different operating points, since *PSP* measurements were conducted in isothermal conditions, the trend is successfully captured also with *CFD*. Moreover, it should be pointed out that also the test of the uncooled configuration was carried out using perforated nozzles.

This justifies the presence of spikes in the proximity of the holes also in absence of coolant injection.

In particular small discrepancies exist between the two *NGVs*, due to the difference in pitch and swirl angles of the flow approaching the two nozzles. More clearly, while for low axial chords Ch_{ax} the uncooled and cooled cases profiles have negligible differences, downstream the throat section the cooled case profiles show an evidently lower pressure. This can be attributed to a higher Mach in the throat section of the cooled nozzles due to the higher flow rate, which necessarily leads to a higher pressure ratio across the nozzles.

However, it is well known that reproducing the turbulent energy transport represents a tougher challenge compared to the flow field, therefore greater differences can be reasonably expected in terms of temperature non-uniformity, which is reported in Fig. 4.14. Again, *CFD* correctly reproduces the presence of two separate hot spots at the exit of the nozzles, however the temperature gradients are significantly overestimated regardless of the way the inlet conditions are obtained. This should come at no surprise, since the exploitation of *RANS* (at least with standard models) tends to underpredict turbulent mixing. This is a well-known effect and was highlighted also when the upstream hot streak generator was simulated alone (see Fig. 4.10).

4.2.3 Hot streak propagation

Since *CFD* demonstrated its ability to adequately reproduce the aerodynamic field, it is worth exploiting such tool to better understand the hot streak evolution and support the experimental data acquired on *Plane 40* and *41*.

First of all, since a huge difference was highlighted in the temperature distribution at *Plane 40*, it is interesting to investigate how the hot streak propagates throughout the nozzles as estimated via the two approaches. Fig. 4.15 and 4.16 show a comparison of static temperature for the uncooled and the cooled *NGVs* respectively in consecutive sections normal to the axis from the bottom (*Plane 40*) to the top (*Plane 41*). A midspan view of the total temperature field is superimposed at the top as to highlight the hot streak alignment with respect to the airfoils.

In fact *NGV2* is directly impacted by the hot streak in the *LE* region, while *NGV1* is hardly getting in contact with the hot gas, especially for the 'Inlet RANS' case. For what concerns the comparison between uncooled and cooled *NGVs*, as expected, no huge differences are found in the mainstream, whereas the presence of the coolant film is more evident close to the airfoils. What can be further observed on the midspan section in the cooled configuration is the coolant penetration inside the main flowpath in the *LE-PS* region of *NGV2*. This can be ascribed to the low velocity of the main-

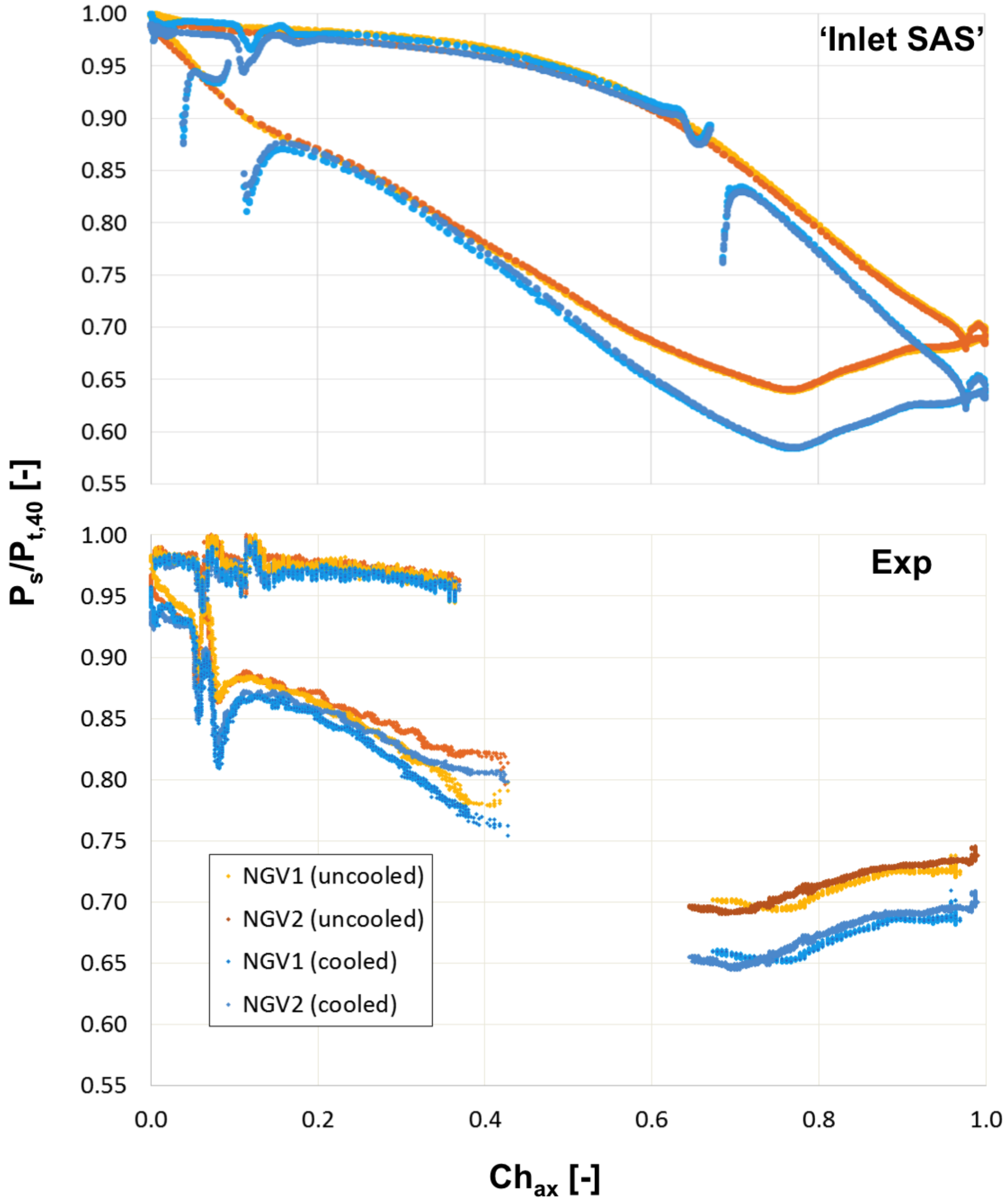

Figure 4.13: *FACTOR* - Comparison of pressure loading along axial chord Ch_{ax} at the airfoils midspan of uncooled/cooled *NGVs* between experiments and 'Inlet SAS' simulations of the *NGVs*

stream in the proximity of the stagnation region, resulting in a high blowing ratio of the cooling jets. As a consequence, no film is generated in that zone, somehow failing the design intent of protecting the airfoil against the hot gas.

Another interesting way to visualise the hot streak propagation is by analysing

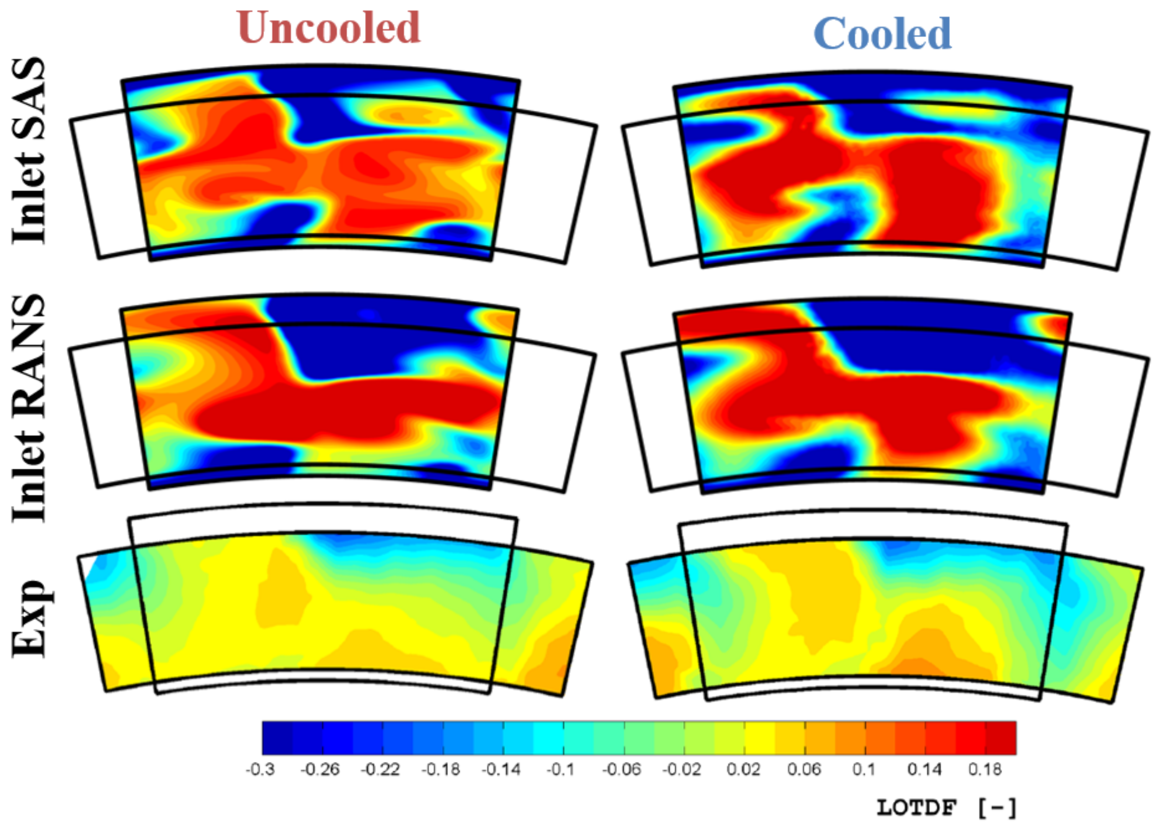

Figure 4.14: *FACTOR* - Comparison of non-dimensional temperature field (*LOTDF*) at *Plane 41* between experiments and 'Inlet SAS' and 'Inlet RANS' simulations of the *NGVs*

the temperature contours taken in the fluid domain along the axial direction (bottom part of Fig. 4.15 and 4.16). Initially the presence of coolant can be noticed only in the proximity of the walls, while the mainstream appears roughly unaffected. Moving downstream the discrepancies arise due to the presence of secondary flows that increase the coolant transport. Then, turbulent mixing is maximised downstream of the trailing edge. In addition, the over-intense hot streak of the 'Inlet RANS' case is somehow maintained from *Plane 40* down to *Plane 41*, showing that mixing with *RANS* modelling is not satisfactorily achievable.

4.2.4 Impacts on the airfoils thermal performance

It is clear that the different hot streak propagation modes will have a direct impact on the airfoils temperature. This is well illustrated in Fig. 4.17, which shows the predicted airfoils adiabatic temperature: the uncooled case is the most appropriate configuration for such purpose, since it gives the possibility to exclude the influence of film cooling, on the contrary to what occurs on the cooled vanes. As previously

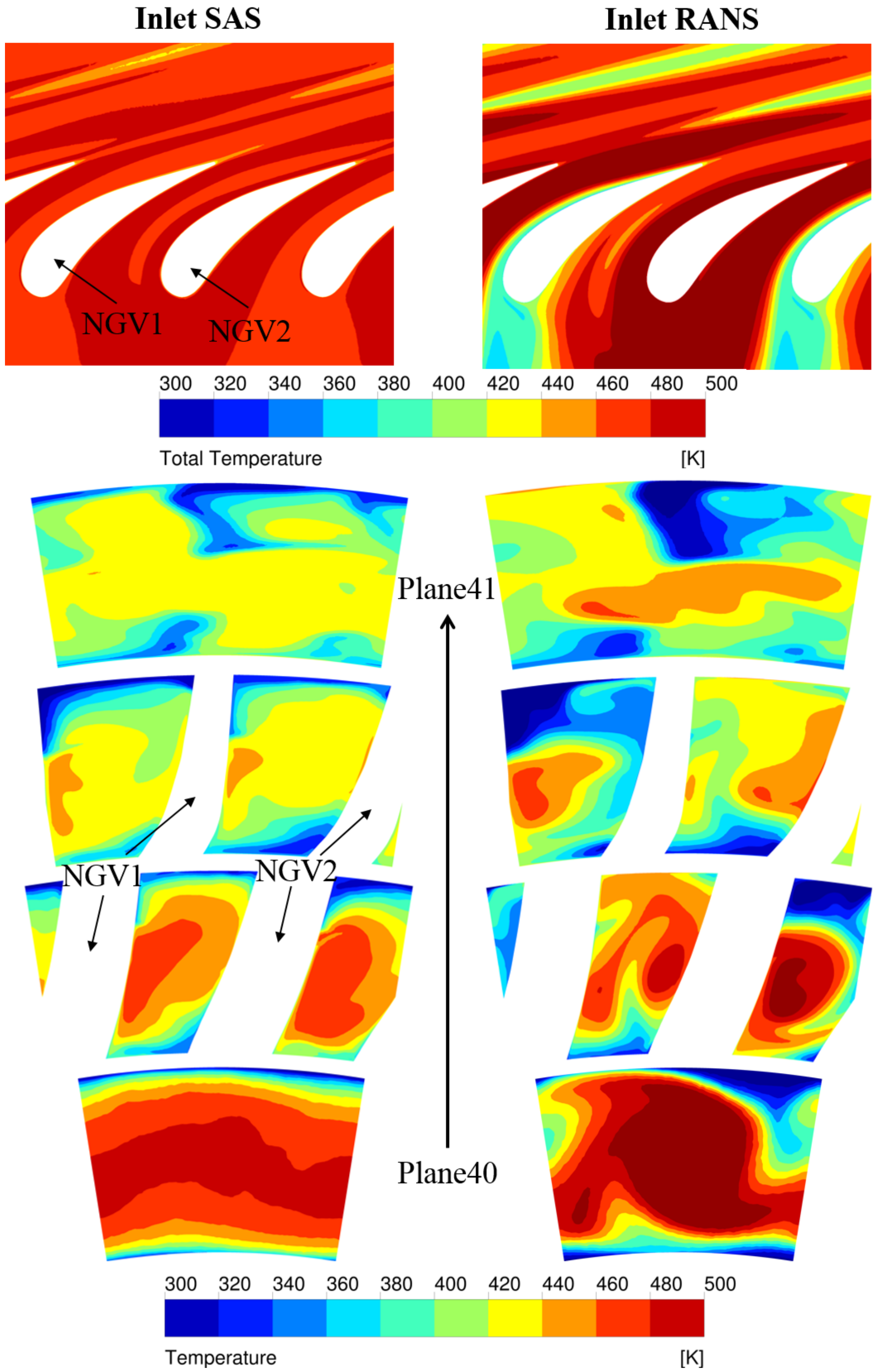

Figure 4.15: *FACTOR* - Midspan total temperature and temperature field on planes normal to the axis throughout the nozzle (uncooled *NGVs*): comparison between 'Inlet SAS' and 'Inlet RANS' simulations of the *NGVs*

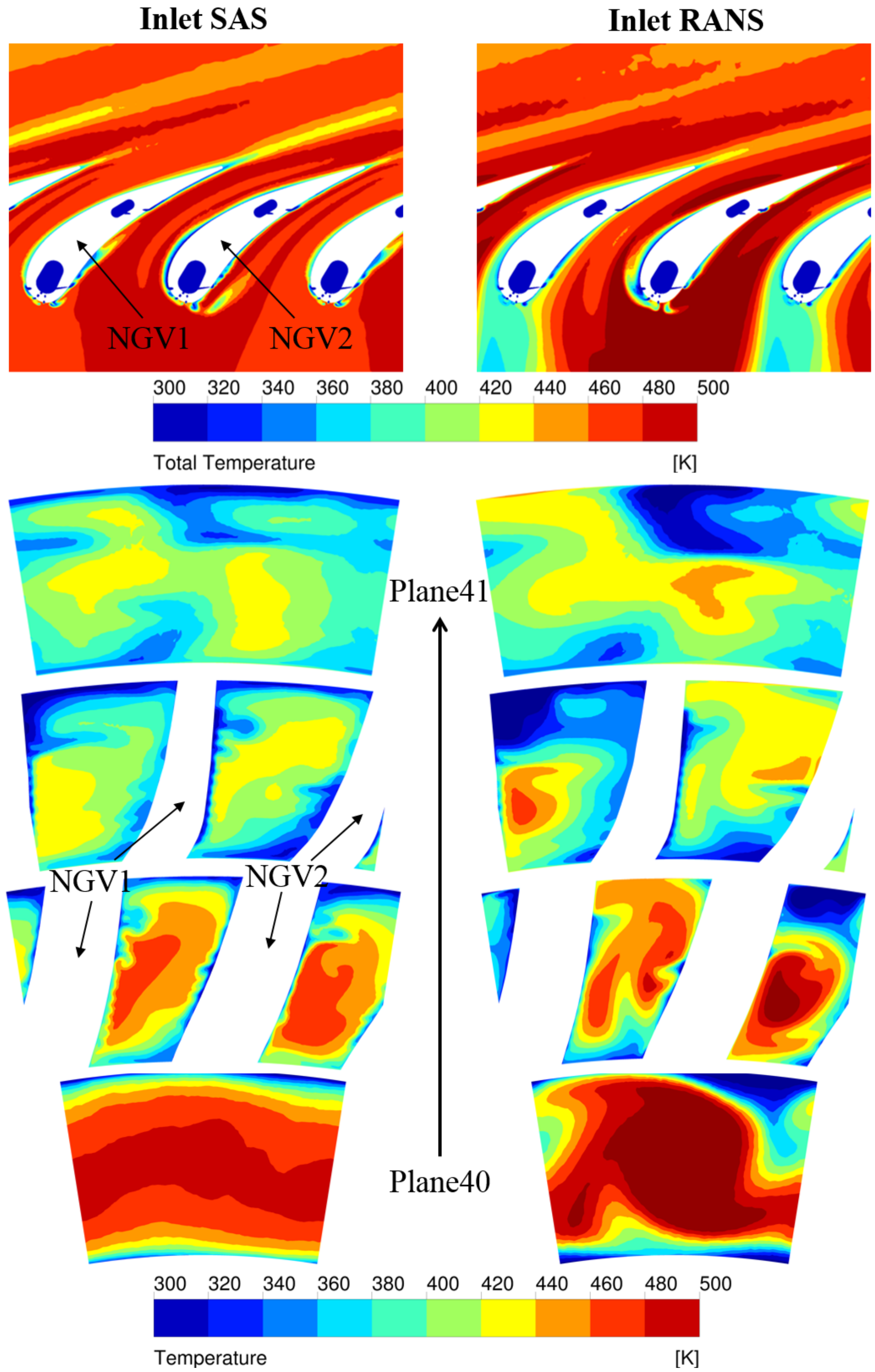

Figure 4.16: *FACTOR* - Midspan total temperature and temperature field on planes normal to the axis throughout the nozzle (cooled *NGVs*): comparison between 'Inlet SAS' and 'Inlet RANS' simulations of the *NGVs*

anticipated in Fig. 4.15 and 4.16, the 'Inlet RANS' case should penalise *NGV2* more than *NGV1*, since the hot streak is less uniformly spread in the circumferential direction as compared to the 'Inlet SAS' case.

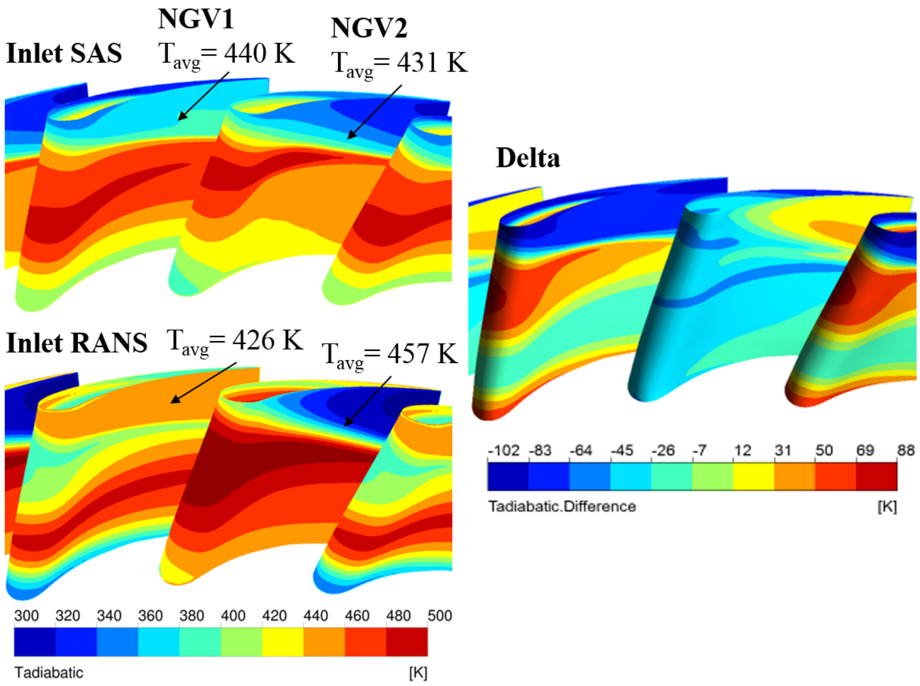

Figure 4.17: *FACTOR* - Airfoil wall adiabatic temperature (uncooled *NGVs*): comparison between 'Inlet SAS' and 'Inlet RANS' simulations of the *NGVs*

As shown in the delta contour on the right-hand side of Fig. 4.17, *NGV2* in the 'Inlet SAS' case has a wide region colder than in the 'Inlet RANS' case by ≈ 25-45 K. *NGV1* has a large hotter zone at the midspan by even 50-70 K and is considerably colder close to the tip by up to 100 K. This is particularly interesting from a design perspective, since such a result would supposedly wrongly suggest the adoption of different cooling schemes for the two nozzles or even the overdesign of the same. By contrast, this could be contradicted by a more accurate estimation carried out with inlet conditions obtained via *SAS*.

As a further indication, also the airfoils average-temperature prediction is different in the two cases and may lead to an excessively conservative design with *RANS*-derived boundary conditions. In fact in the 'Inlet RANS' case the average adiabatic-wall temperature not only has a significant spread between the two airfoils but also has the hottest *NGV2* (457 and 426 K for *NGV2* and *NGV1* respectively), whereas the opposite is true for the 'Inlet SAS' case (431 and 440 K).

Fig. 4.18 includes the effect of film cooling on the airfoils, which overall reduces significantly the surface adiabatic temperature, although there are regions where film cooling looks clearly not effective, leaving portions of the airfoils unprotected. This is more evident in the 'Inlet RANS' case, where these are more extended, whereas in the 'Inlet SAS' simulation this occurs mainly in the *LE* region, which shows the greatest differences especially at the stagnation line. It is worth underlining that in addition to the already mentioned differences in temperature distribution, also the flow angles (swirl and pitch), which play a key role in this region, are extremely affected by the used approach (see Section 4.2.1).

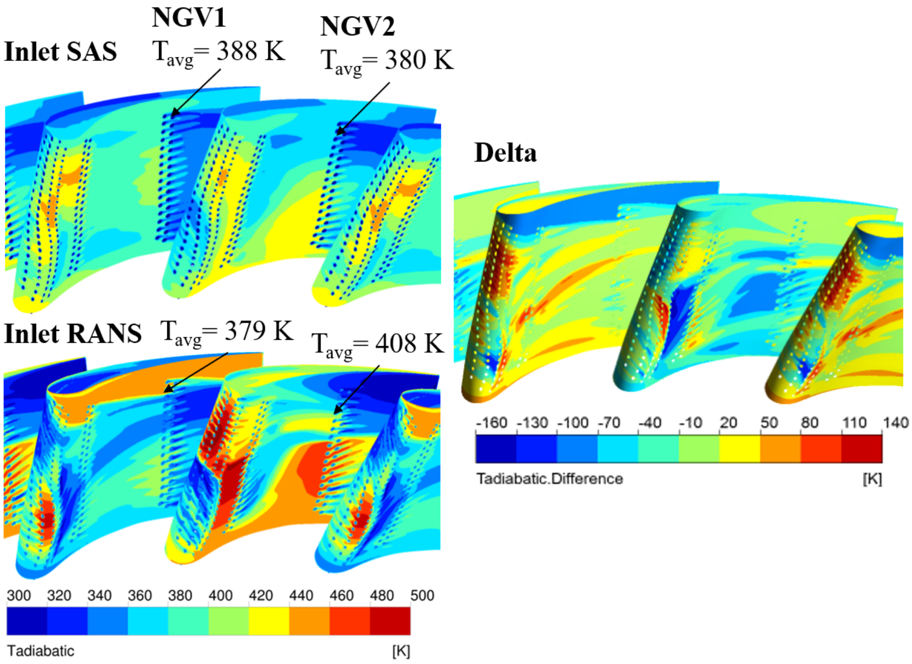

Figure 4.18: *FACTOR* - Airfoil wall adiabatic temperature (cooled *NGVs*): comparison between 'Inlet SAS' and 'Inlet RANS' simulations of the *NGVs*

The delta contour in Fig.4.18 shows, as a whole, that the 'Inlet SAS' case estimates a better protection of the airfoils surface than the 'Inlet RANS' one. It is also interesting to observe that the presence of film cooling magnifies the detrimental effect of the misprediction associated to inlet boundary conditions obtained from *RANS*. In fact, in such conditions the difference increases locally up to -180 K and +140 K, further stressing the importance of an accurate prediction of the combustor outlet conditions. Again, as in the uncooled configuration, the average temperature estimation differs: 408 and 379 K for *NGV2* and *NGV1* respectively in the 'Inlet RANS' versus 380 and 388 K in the 'Inlet SAS' case.

4.2.5 Effect of flow unsteadiness

After discussing the dissimilarities in the thermal behaviour of the airfoils as subject to differently obtained inlet conditions at *Plane 40*, the results obtained with the *SAS* approach of the integrated combustor-turbine model ('All SAS' tag in figures) will be now presented. It is furthermore to be noted that all contours relative to the *SAS* model show time-averaged values, which are presented in comparison only to the *RANS* model of the *NGVs* with *SAS* inlet conditions, as to isolate the effect of flow unsteadiness over results.

To start with, as previously done for the *RANS* models, the pressure coefficient obtained within the *SAS* integrated domain is shown in Fig. 4.19 next to the experimental results. The comparison highlights how the adopted methodology is capable of reproducing the intensity of the flow structures in addition to the pattern, which, in spite of some small differences, indicates how the swirling flow is predominant on the right-hand vane passage. This feature is typically referred to as "hot streak migration", i.e. the convection of the hot streak from the combustor into one specific vane passage, due to the high swirl component of velocity and the consequent distinct rotating motion.

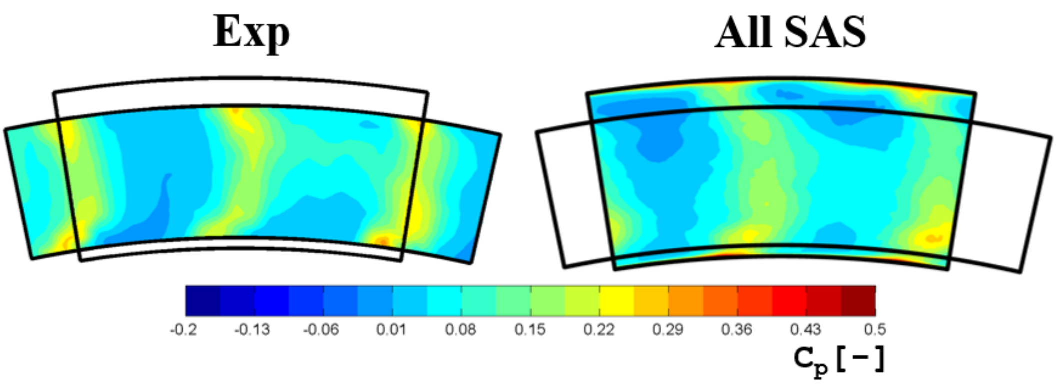

Figure 4.19: *FACTOR* - Comparison of pressure coefficient C_p at *Plane 41* (cooled *NGVs*) between experiments and the integrated combustor-*NGVs SAS* simulation

A further comparison against experiments is performed on the basis of temperature distribution at *Plane 41*, which is illustrated in Fig. 4.20, where the *LOTDF* is plotted. Although the *SAS* model shows a higher degree of temperature distortion than what captured by measurements, the gain with respect to the *RANS* cases (see Fig. 4.14) can be clearly appreciated. Even though turbulent mixing still looks underestimated by *CFD*, the achieved improvement is evident.

To understand what would be the impact of such temperature field on the rotor stage, it can be beneficial to extend the comparison also in terms of radial temperature

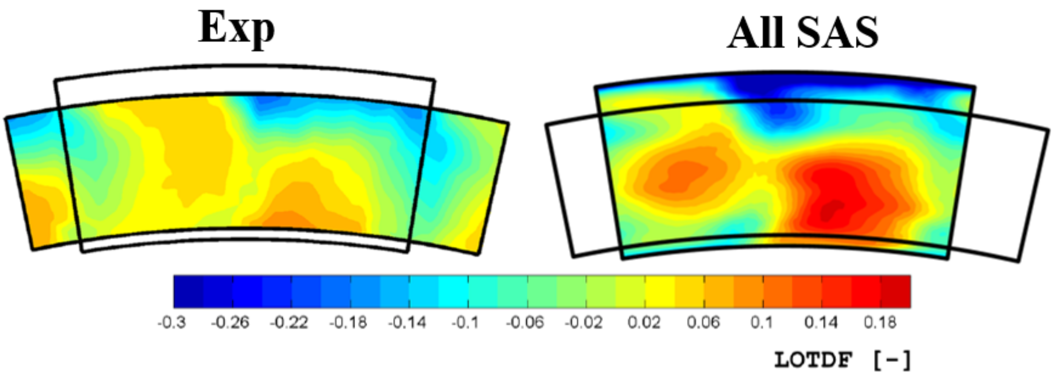

Figure 4.20: *FACTOR* - Comparison of *LOTDF* at *Plane 41* (cooled *NGVs*) between experiments and the integrated combustor-*NGVs SAS* simulation

profile. For this reason the *LRTDF* at *Plane 41* for all the cases analysed so far is reported in Fig. 4.21, considering only the cooled nozzles configuration. The 'All SAS' profile places the closest to measurements, proving once more the higher level of adequacy of the method. Within the experimentally investigated span range, the 'All SAS' profile is roughly as flat as the test one, while *RANS* shows larger discrepancies. A pronounced temperature peak is clear at midspan, as induced by the hot streak on the right-hand passage, in addition to a valley at around 0.7 radial span fraction. This is due to the excessive entrainment of coolant in the mainstream shown at the top right corner of *Plane 40* (see Fig. 4.10 for reference). Even if the 'Inlet SAS' case succeeds in mitigating such an effect, the *RANS* approach tends to maintain the coherence of this flow structure down to *Plane 41*.

Evaluating the error of each profile against measurements within the experimental span range, the *RANS* cases present an average absolute error of 0.08 and 0.13 for the 'Inlet SAS' and 'Inlet RANS' cases respectively. On the contrary, the 'All SAS' has an average absolute error of 0.04, which represents a reduction of respectively 50% and 70% as compared to *RANS*.

Then, as done for the previous results, the hot streak propagation is investigated. It is interesting to emphasise how the hot streak is directly impacting one of the two airfoils (*NGV2*), which is clearly shown in 4.22 by an isosurface of total temperature.

The hot streak propagation through the channels is then presented in Fig. 4.23. Some differences can be observed with respect to the *RANS* simulations of the *NGVs* alone, even though the conditions at *Plane 40* are nominally the same, at least in time-averaged terms. In particular, the hot streak at midspan shows a lower extension in the 'All SAS' case if compared to the 'Inlet SAS', which could be ascribed to potential effects of the *NGVs* that were not accounted for in the simulation of the combustor

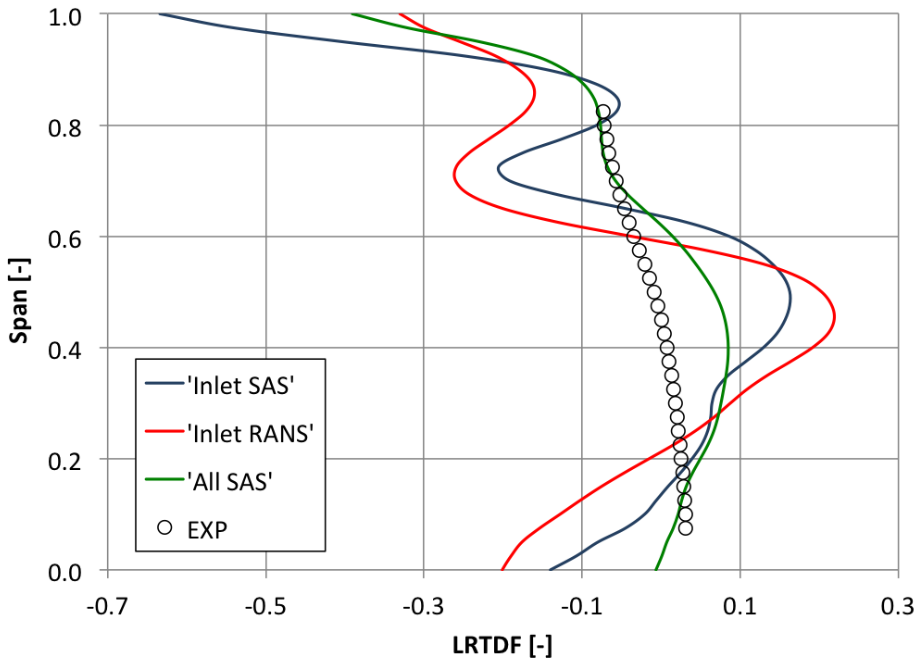

Figure 4.21: *FACTOR* - Comparison of *LRTDF* vs radial span at *Plane 41* (cooled *NGVs*) between experiments and all the investigated CFD simulation cases

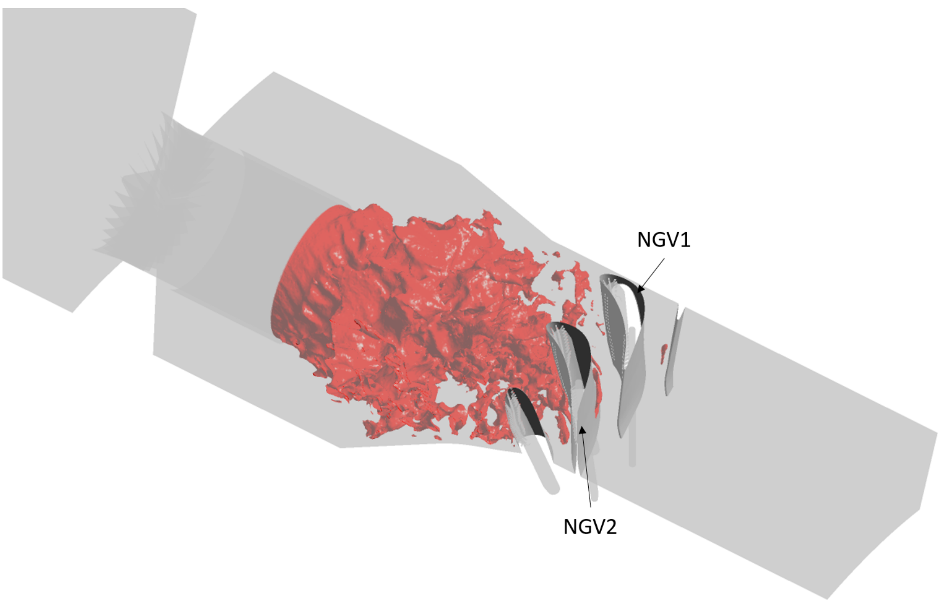

Figure 4.22: *FACTOR* - Isosurface of total temperature showing the hot streak impacting *NGV2* leading edge

alone. In addition, the *SAS* methodology promotes a higher level of turbulent mixing between coolant and mainstream, which further dampens the hot streaks transport throughout the nozzles and hence flow temperature decreases at a larger rate moving downstream from *Plane 40* to *Plane 41*.

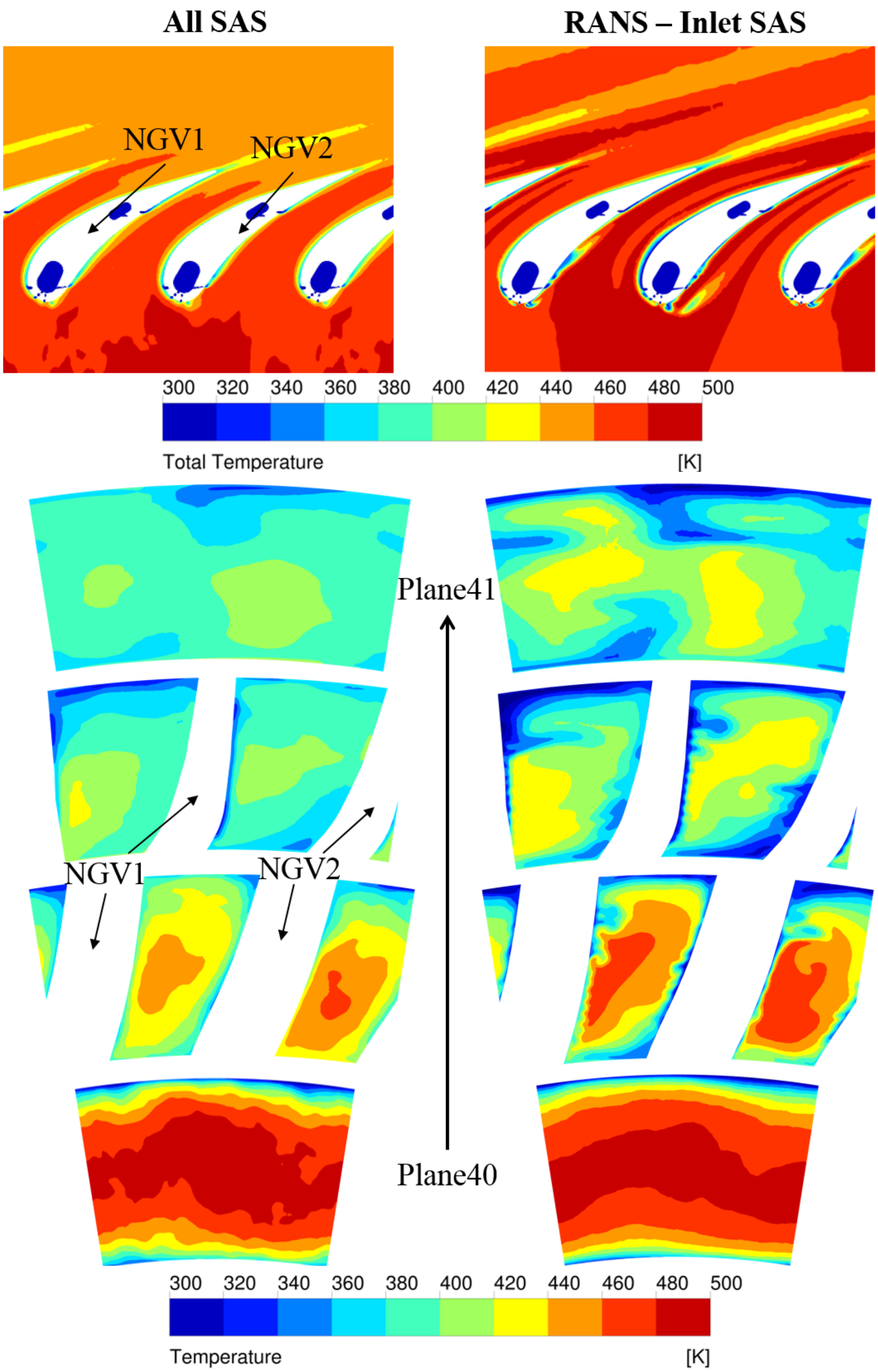

Figure 4.23: *FACTOR* - Midspan total temperature and temperature field on planes normal to the axis throughout the nozzle (cooled *NGVs*): comparison between 'All SAS' and 'Inlet SAS' cases

The adiabatic temperature on the airfoil surface is then illustrated in Fig. 4.24. The 'All SAS' case presents a smoother contour and does not show the temperature peaks on the nozzles *LE*, visible in the 'Inlet SAS' case. This supports the assertion of a way higher mixing obtained with the scale-resolving technique, which is to some extent validated by the predicted airfoils average-temperature: *NGV2* and *NGV1* present indeed almost the same average adiabatic-wall temperature (382 and 380 K respectively). However, in spite of a slightly lower average temperature than the 'Inlet SAS' case (380 and 388 K), the delta contour highlights regions with higher thermal load, especially on the *NGV2 PS*, where deltas of about 50 K exist. This suggests that, although average temperature is somehow captured even by the *NGVs*-only simulation with *SAS*-derived inlet conditions, scale-resolving methodologies may be able to better reproduce flow structures, mixing and ultimately the interaction between coolant and main flow.

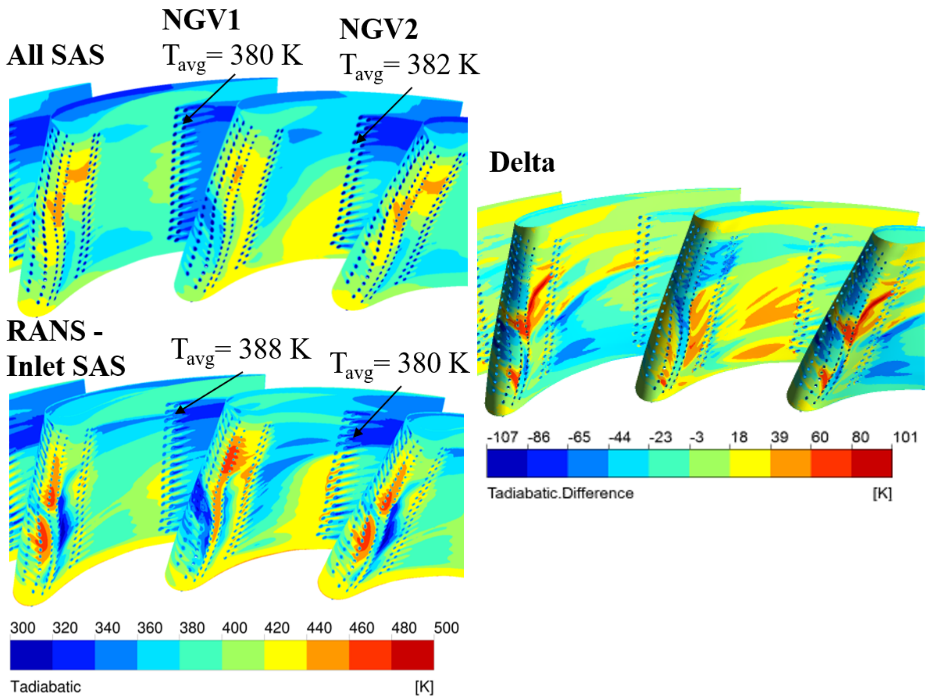

Figure 4.24: *FACTOR* - Airfoil wall adiabatic temperature (cooled *NGVs*): comparison between 'All SAS' and 'Inlet SAS' cases

To support this statement and assign a degree of validation to the methodology used to carry out the present work, numerical results are finally compared against *PSP* measurements. In particular, since this is one of the first attempts to compare numerical simulations and experiments on film cooled *NGVs* with realistic upstream conditions, it is of fundamental interest to focus on film cooling effectiveness. To this extent, Fig. 4.25 shows the contours of coolant concentration and hence, via the heat and mass transfer analogy, of film cooling effectiveness (see Section 3.1.1 for reference). Only limited portions of the airfoils are shown on pressure and suction sides, due to the limits imposed by camera accessibility in the test rig.

The results obtained with the *SAS* integrated model are worthy of attention, as experimental measurements are satisfactorily replicated. In particular, even though the intensity of coolant concentration is generally lower than that captured with the *PSP*, the coolant flow patterns are caught with high accuracy. Reasonably this means that the overall characteristics of the main flow and its interaction with the cooling system are predicted adequately, even though some differences still persist. Among the possible causes is a wrong prediction of the coolant flow split between *LE* and *TE* channels and/or among the three film-cooled *NGVs*, as well as a mismatch between the CAD model and the actual geometry, potentially affecting the hole diameter and the discharge coefficient. This could alter the actual blowing ratio and thus the jet flow regime.

Despite all of this, the improvement is remarkable with respect to the *RANS* case, which has too marked streaks of coolant concentration, not captured at all by measurements. This brings to light the potential capability of the *SAS* technique and, although it may be sufficient for the study of aerodynamic aspects, the necessity of studying combustor and turbine no longer as separate entities, but as one single component, provided that high-fidelity predictions are sought in the design phase, with special focus on the *NGVs* thermal management.

4.3 External heat transfer under swirled inflow

4.3.1 Redefinition of inlet boundary conditions

At this stage, scale-resolving methods have been shown to be the adequate means for a proper reproduction of not only the aerodynamic but also the thermal field through first stage nozzles, which has been validated to some extent against measurements. The match at the combustor-turbine interface of aerothermal quantities and the hot streak propagation through the *NGVs* has been studied to prove the methodology with respect to experimental results. Based on this, it may be therefore convenient to further expand the discussion and investigate with a broader perspective the impacts of highly swirled inflow over the *NGVs* as generated by a modern lean burn combustor, as reported also in [141].

With this intent, in addition to discarding the *RANS* simulation with *RANS*-derived *BCs*, a further set of simulations was analysed, characterised by a more uniform

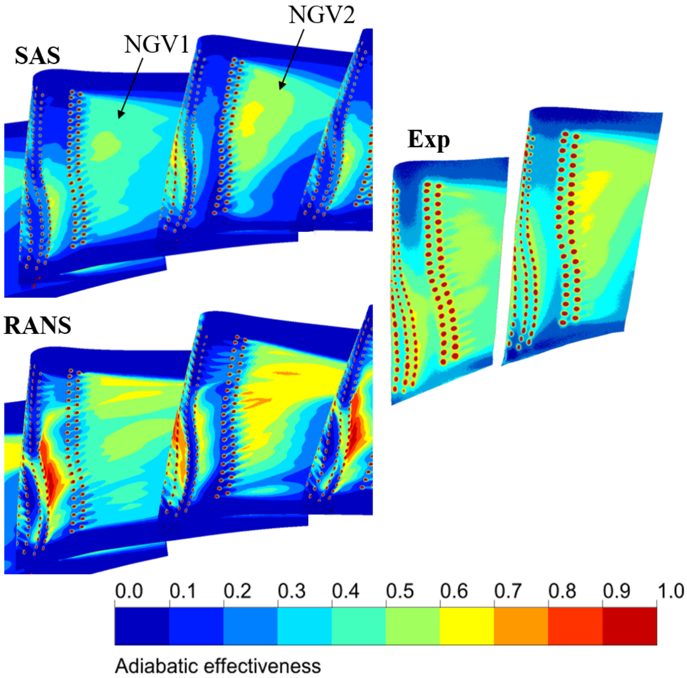

(a)

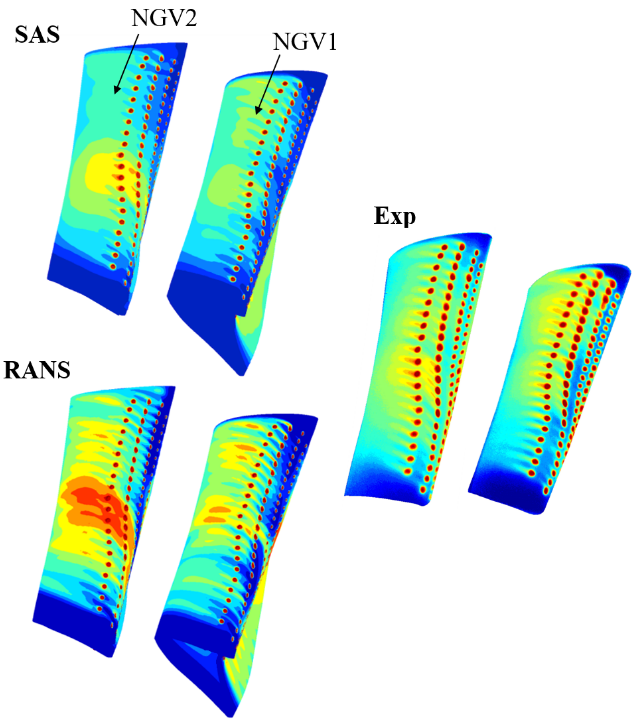

(b)

Figure 4.25: *FACTOR* - Film-cooling adiabatic effectiveness on *PS* (a) and *SS* (b): comparison between experiments against ‘All SAS’ and ‘Inlet SAS’ cases

flow field at the turbine inlet section. More specifically two sets of runs were added, based on the *NGVs*-only domain and hence simulated via *RANS*:

- 'Uniform T-V' - A purely ideal uniform velocity and temperature field, similarly to what reported by Qureshi et al. [142], were imposed at *Plane 40* as to appreciate any differences related to coolant flow distribution within the flowpath and over the airfoils;

- 'Uniform V' - A quasi-uniform velocity field with a temperature profile at *Plane 40* resulting from the mixing of the mainstream and effusion cooling flows, which builds up a 1D profile, fairly resembling the flow characteristics out of an *RQL* combustor, where dilution air abates the mainstream swirling motion.

Fig. 4.26 illustrates the contours of temperature and swirl at *Plane 40* used in the aforementioned 'Uniform' cases and as obtained with *SAS*. In addition, for comparison purposes, also the circumferentially averaged values are reported in the right-hand graphs.

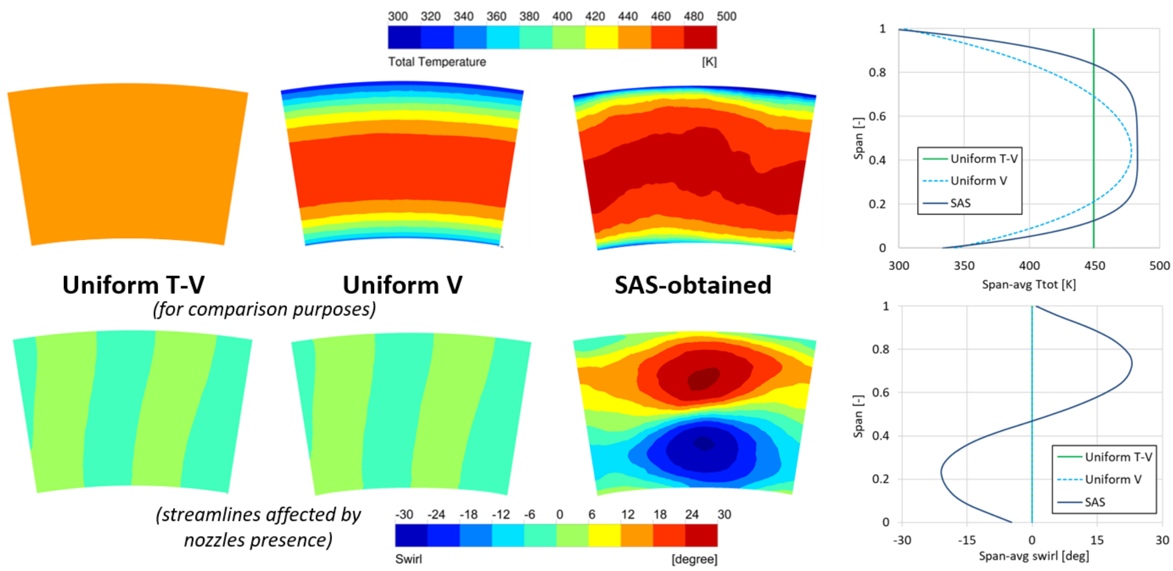

Figure 4.26: *FACTOR* - *Plane 40* temperature and swirl fields for studying the impact of highly-swirled turbine inflow

4.3.2 Film-cooling adiabatic effectiveness

Recalling Fig. 4.25, it is interesting to widen the comparison to the 'Uniform' cases in order to further emphasise the effect of swirling flow on the coolant distribution over the airfoils. In fact, only by including the effect of flow unsteadiness on turbulent mixing, it is possible to reduce the gap with the experimental measurements, as highlighted in Figs. 4.27 and 4.28.

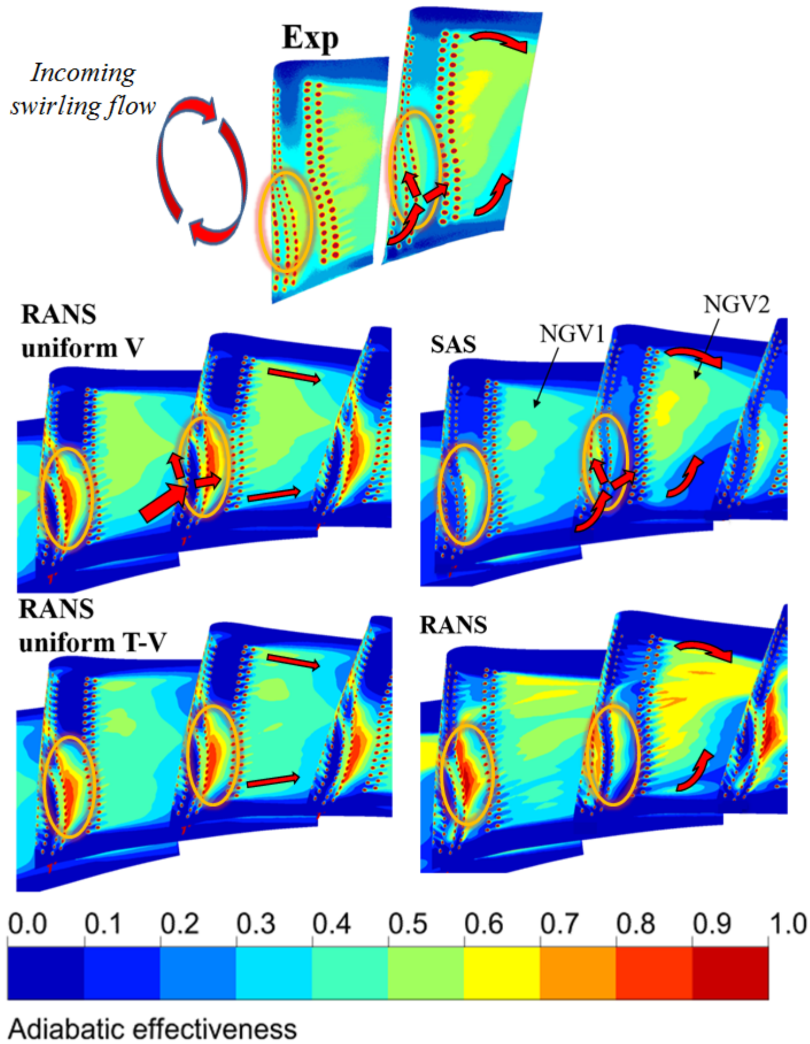

Figure 4.27: *FACTOR* - Film-cooling adiabatic effectiveness on the airfoils *PS* (a) and *SS* (b): comparison between experiments against 'Uniform', 'SAS' and 'RANS' cases

Note that the following notations apply:

- 'RANS uniform V' is the 'Uniform V' case just introduced in Section 4.3.1 and somehow representative of an *RQL* combustor configuration;
- 'RANS uniform T-V' is the purely ideal 'Uniform T-V' case as well introduced in Section 4.3.1;
- 'SAS' indicates the *SAS* integrated simulation;

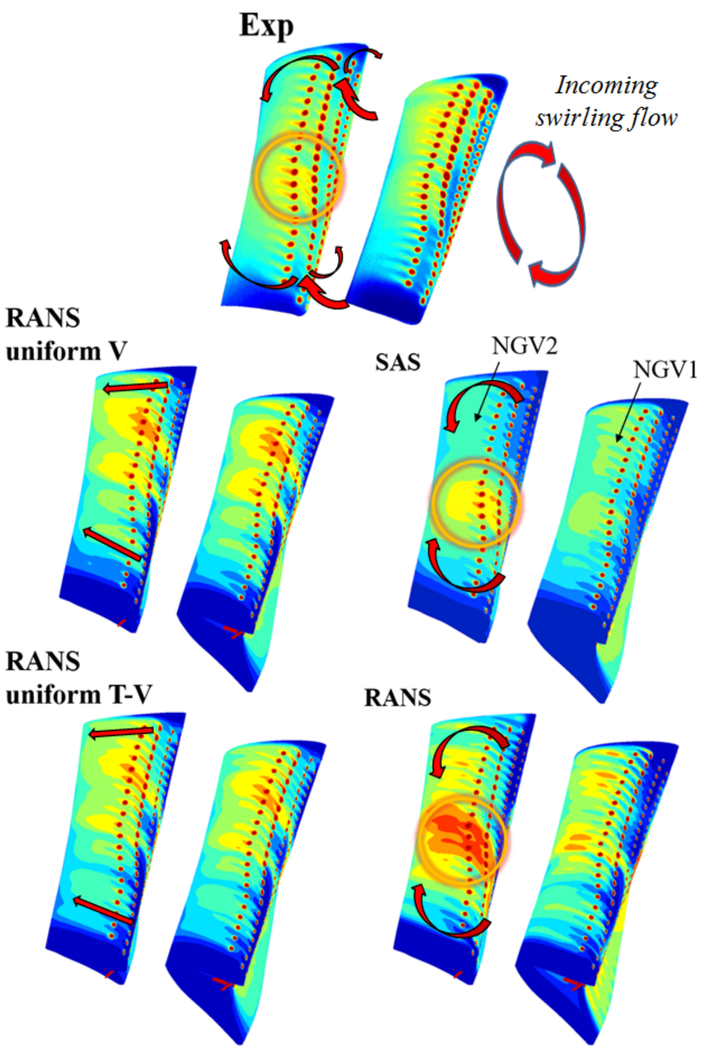

Figure 4.28: *FACTOR* - Film-cooling adiabatic effectiveness on the airfoils *SS*: comparison between experiments against 'Uniform', 'SAS' and 'RANS' cases

- 'RANS' is relative to the *RANS* simulation with *SAS*-derived inlet boundary conditions.

It is of paramount importance to notice how flow structures, visible on the airfoils surface, are intrinsically different between all the compared cases. In fact, the experimental map of Fig. 4.27 shows how the coolant on the *PS* is slightly forced towards the upper region of *NGV1* and, at an even higher extent, of *NGV2*. This is not captured by the 'Uniform' cases, since inlet swirl is not present at all. Furthermore, the two non-swirled *RANS* cases predict a way too high effectiveness close to the *LE* region, in addition to a distinct separation between coolant flows directed either towards the *PS* or the *SS* surfaces. This is replicated by the swirled *RANS* case, even if *NGV2* shows a less intense coolant spot than *NGV1*, due to the impacting hot streak, which, on the contrary, is not predictable with a uniform inlet velocity field. By contrast, *SAS* gives both non-equal effectiveness at the airfoils *LE* and smoother contours, which match experiments closer.

Similarly, Fig. 4.28 shows part of the airfoils *SS*, as visible by the *IR* camera. The high intensity spot of coolant at the centre of the *NGV2* leading edge is a direct effect of the highly swirled inlet flow. In fact, the portion of coolant that is convected towards the suction side surface keeps undisturbed only close to the 50% span, i.e. where mainflow swirl is close to zero. This is captured by measurements and the two swirled numerical cases, with *SAS* delivering a smoother contour plot and hence a closer match, which cannot be captured by the ‘Uniform’ cases.

4.3.3 Secondary flows and vortical structures

In order to even better visualise all these considerations, it can be convenient to plot the contours of wall shear over the airfoils surface for the different simulated cases, which is given in Fig. 4.29. The ‘Uniform’ cases, as characterised by uniform inlet velocity, present almost straight traces of wall shear in correspondence of film cooling, since there are no velocity gradients to alter its distribution. On the *SS* surface the presence of the corner vortices is indicated by the whiter streaks close to the endwalls, representing regions of high wall shear, being the greyscale inverse.

The ‘RANS’ case, on the other hand, shows some little disturbance of the film-cooling flow over the pressure side, especially on *NGV2*, that is directly impacted by the hot streak (see Fig. 4.22 for reference). By contrast, the suction side surface has a barely different wall shear contour than the ‘Uniform’ cases. Lastly, noting that an instantaneous contour is herein presented, the ‘SAS’ model returns heavier traces of impacting main flow over the airfoils *PS* surfaces, significantly altering the film cooling spreading. Moreover, on the *SS* the corner vortices are modified with respect to the previous maps, while additional vortices seem to be present at about the 50% span, which can be ascribed to the main-flow vortical structures being transported by the scale resolving technique through the nozzles, affecting also the pressure losses prediction, as already shown in Section 4.2.5.

An interesting method to further highlight such secondary flow structures is to plot an isosurface of the lambda2 criterion, which defines the vortical structures. Fig. 4.30 shows, for the ‘SAS’ case, the front and rear views of the airfoils with an isosurface of lambda2 criterion coloured as per the vortex helicity, i.e. indicating the sense of rotation. The horseshoe vortices at the root of the airfoils are visible together with the passage vortices, moving across the channels from the pressure to the suction side of

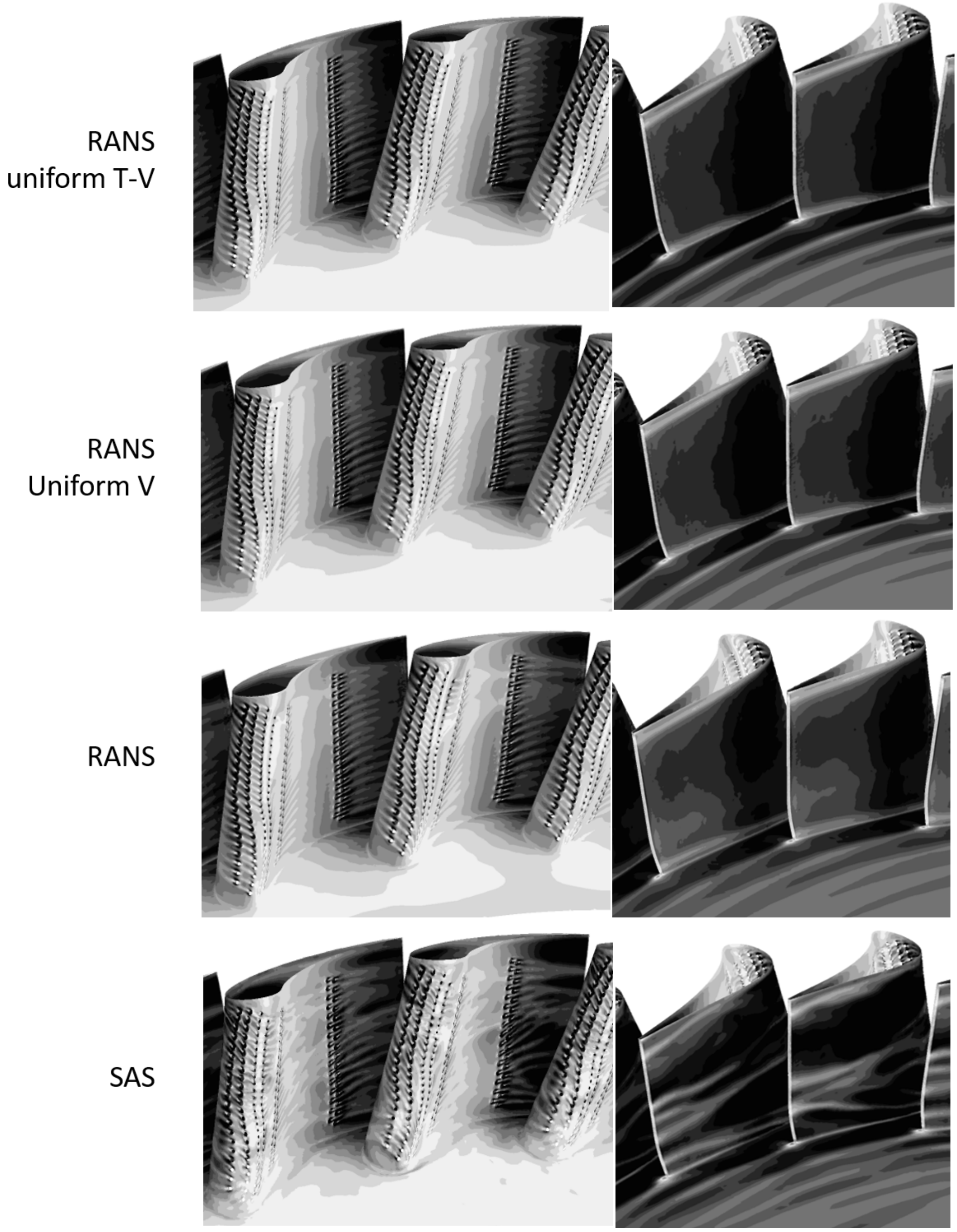

Figure 4.29: *FACTOR* - Wall shear over the airfoils *PS* and *SS* surfaces: comparison between 'Uniform', 'RANS' and 'SAS' cases

the adjacent airfoil, and the corner vortices, clearly shown by the rear view. In addition to a simpler case with uniform inlet flow field, some midspan horseshoe vortices are created by the incoming highly swirled flow, which are therefore broken down into a *PS* (passage vortex) and a *SS* legs, with the latter being responsible for the wall shear "streaks" of Fig. 4.29.

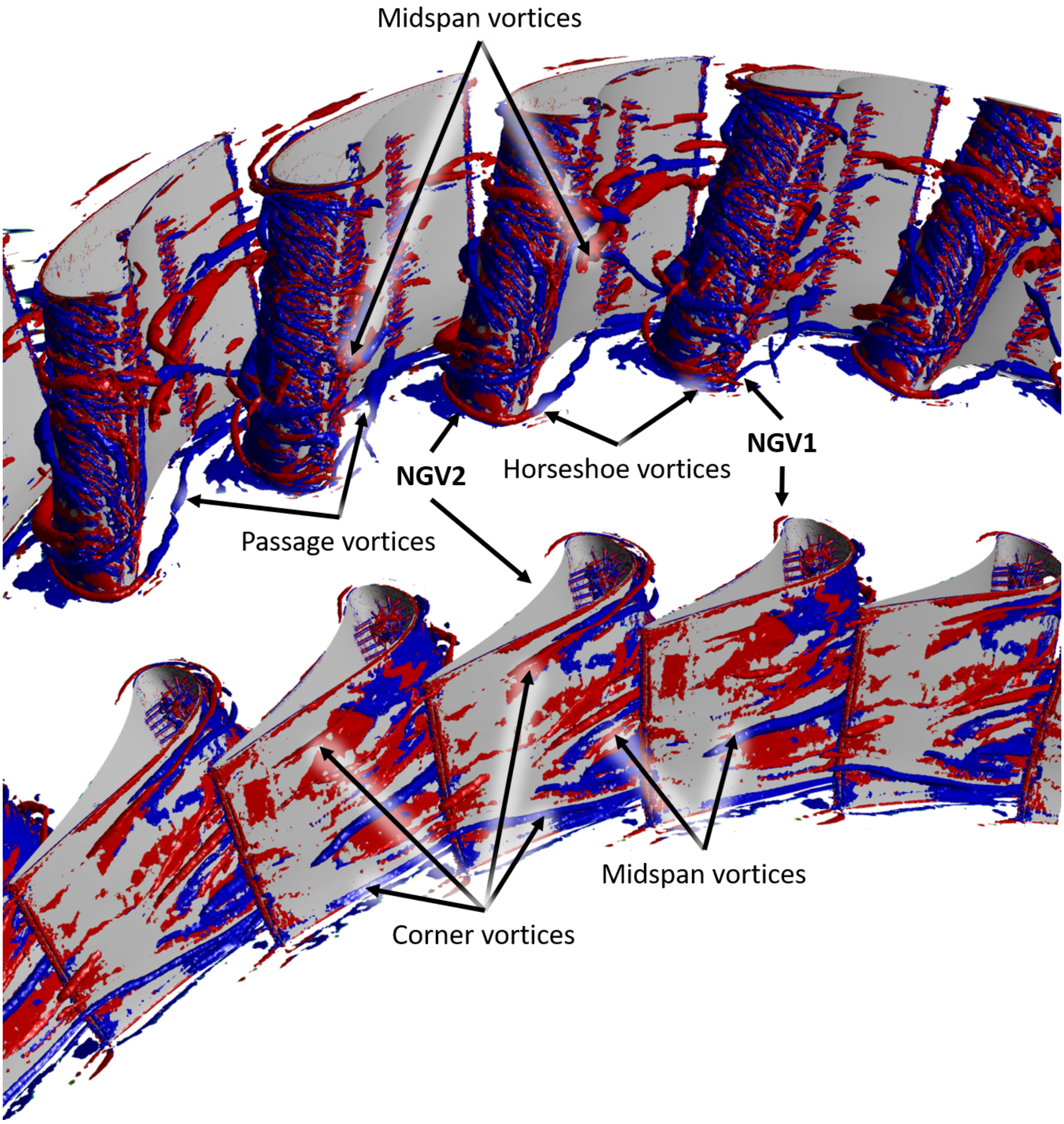

Figure 4.30: *FACTOR* - Secondary-flow vortical structures of the 'SAS' case highlighted by an iso-surface of lambda2 criterion and colored as per helicity

4.3.4 External heat transfer

The heat transfer mechanism taking place on the external surface of the airfoils was studied for both uncooled and cooled nozzles only within the *NGVs* domain. The combined combustor-nozzles domain was instead simulated only in the presence of film cooling, since the specific purpose was indeed oriented to better appreciate the effect of flow unsteadiness on the mixing process between all coolant sources and main flow. It is worth reaffirming that no results are herein being shown relatively to the *RANS* case with *RANS*-derived combustor outlet conditons, since, as largely discussed in Section 4.2, it gives similar though less accurate results than employing *SAS*-obtained inlet conditions.

The heat transfer coefficient, as common for compressible fluids, can be expressed in conjunction with the adiabatic wall temperature by performing two runs in series:

- *Adiabatic* - First an adiabatic run, from which the adiabatic wall temperature T_{aw} at the vanes surface is retrieved;
- *Imposed temperature* - Then a second run imposing a given temperature at the airfoils walls, i.e. the just evaluated T_{aw} detracted by an arbitrary ΔT (100 K), which determines a wall heat flux q_w.

The heat transfer coefficient HTC can be therefore defined at any location as per the following expression:

$$HTC = \frac{q_w}{T_{aw} - T} = \frac{q_w}{\Delta T} \tag{4.4}$$

Fig. 4.31 thus compares T_{aw} and HTC between the so far considered cases, even if no experimental measurements are available for validation purposes. The HTC maps are quite similar for all cases, although the swirled-inlet cases are those showing more evident traces of the impacting flow, especially on the airfoils *PS*. In addition, the *SAS* simulation estimates a higher HTC on part of both *PS* and *SS* in the vicinity of the leading edge region.

By contrast, the temperature maps disclose the major differences. In fact, the *RANS* simulation (with *SAS*-derived boundary conditions) locally presents even 100 K higher temperature on the LE of both nozzles with respect to *SAS*, although on average it looks colder. For what regards the non-swirled cases, the run with uniform inlet velocity has on average a lower T_{aw}, since there is no hot streak to affect the film cooling distribution. Moreover, the 'Uniform T-V' case shows at a larger extent the areas where film cooling is not working properly or where is totally absent, such as the hub and tip regions, where protection was rather designed to be provided by the upstream effusion cooling system.

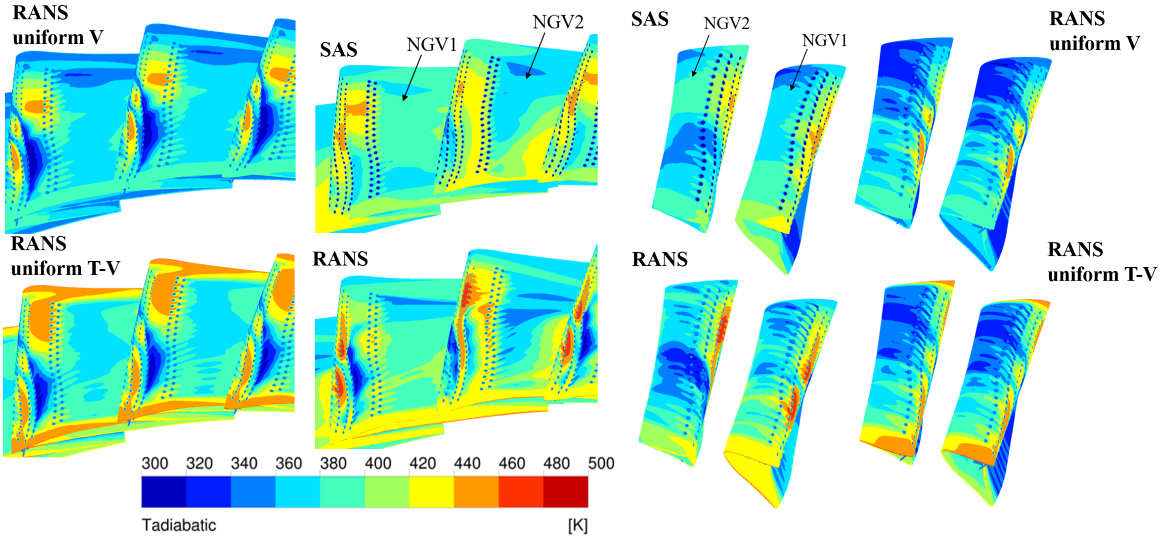

(a)

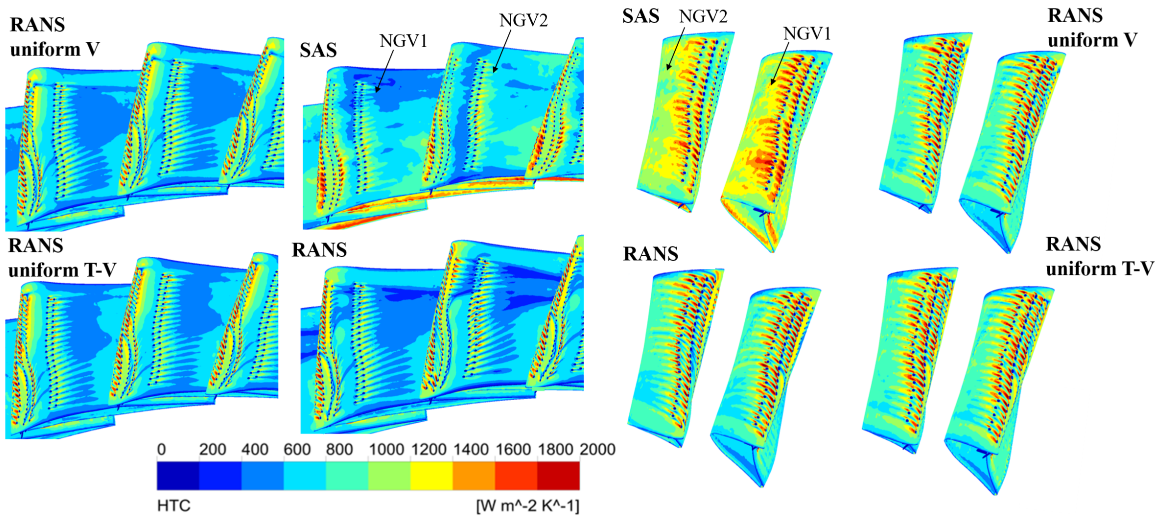

(b)

Figure 4.31: *FACTOR* - Adiabatic wall temperature (a) and heat transfer coefficient (b) on the airfoils *PS* and *SS*

To have a deeper insight into T_{aw} and HTC over the airfoils from the leading to the trailing edge, it can be convenient to extract the 50% span profiles. These are indeed plotted in Fig. 4.32 for *NGV1* and *NGV2*, with T_{aw} displayed on the left and HTC on the right. Note that such profiles are plotted as function of the non-dimensional curvilinear abscissa, i.e. the distance relative to the minimum axial-coordinate point (on the *LE)*, with negative abscissae indicating the pressure side, while positive ones the suction side.

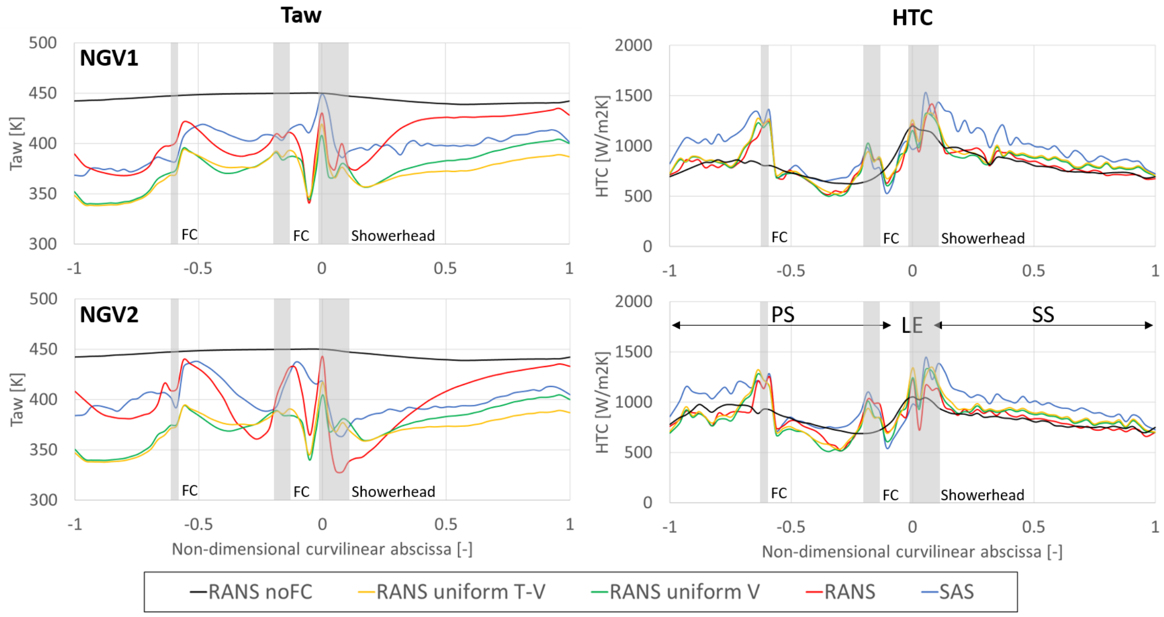

Figure 4.32: *FACTOR* - Adiabatic wall temperature and heat transfer coefficient vs. curvilinear abscissa at the nozzles 50% span

The uncooled-nozzles configuration with *SAS*-derived inlet conditions is picked as baseline case, also because there is no experimental term of comparison. As common to this kind of geometry, this case presents a *HTC* peak on the *LE* of both nozzles, up to about 1200 W/m^{2}K on *NGV1*, while the highest value of *NGV2* does not overcome 1050 W/m^{2}K. This is because *NGV2* is directly hit by the hot streak, which has a core of low or even null velocity. At 0 to -1 abscissae, the *HTC* rapidly drops and then smoothly increases moving downstream in accordance with the increasing velocity. On the contrary, on the *SS* surface the *HTC* is slowly reduced to around 800 W/m^{2}K, without showing any transitional behaviour. This, regardless of the high Reynolds number and turbulence level generated by the mainstream conditions, may be ascribed to the specific swirl direction of the main flow, which tends to keep the flow attached to the *SS* surface of the airfoils.

Comparing the *RANS* cases, the presence of shower heads on the *LE* surface and the film cooling (*FC*) rows is identifiable in locally augmented *HTC*, in addition to the grey bands laid over the graphs. This is evident for instance on the leading edge, with spikes of about 1500 W/m^{2}K rapidly decreasing afterwards. Moreover, the *RANS* simulations deliver very similar results despite the inlet boundary conditions, while *SAS* gives a consistently enhanced *HTC* after the second *FC* row on the *PS* and everywhere on the *SS*, with the gap against *RANS* profiles being proportional to the *HTC* value itself.

Also the T_{aw} profiles give an interesting picture. In fact, with the uncooled case setting the supposedly worst-condition surface temperature, the other cases show the degree of cooling performance at given boundary conditions. The two non-swirled simulations return a quite uniform temperature distribution, with maximum and minimum values ranging between 350 and 400 K. On the contrary, the *RANS* simulation with *SAS*-derived combustor outlet conditions shows a very non-uniform profile, especially for *NGV2*: here the impact of the hot streak and the consequent distribution of coolant result in a very cold region (with a minimum of about 330 K close to the LE). This contrasts with a very hot SS, very close to the 440 K of the uncooled nozzles.

The combustor-turbine integrated simulation, solved via *SAS*, instead, estimates a more uniform temperature pattern, but hotter than the unswirled cases. The *SAS* temperature profile almost overlaps with the *RANS* swirled results in some regions, but it is accompanied by higher *HTC*, which would imply higher metal temperatures. Moreover, whereas the wall temperature is higher for the *SAS* case on the *PS* and at the initial stage of the *SS* (with few peaks of even 430 K), further towards the trailing edge its trend remains almost flat at about 400 K.

4.4 Concluding remarks

An overall comparison among the adopted modelling strategies can at last be made, focusing on the potential improvement in the prediction of hot streak propagation and impact on the turbine nozzles, with attention to the related computational cost. With reference to Table 4.1, it is possible to conclude this assessment by drawing some considerations on the computational effort associated to the exploitation of scale-resolving methodologies. The comparison was performed running the simulations on four Intel(R) Xeon(R) E5-2630 v3 processors (64 cores), equipped with 64 GB of RAM per node.

Case	**N. of cells**	Δt **[s]**	**Simulated time [s]**	**N. of time steps**	**Wall-clock time for time step [s]**	**Tot. wall-clock time [h]**
RANS comb	$17.2 \cdot 10^6$	–	–	–	–	few
SAS comb	$17.2 \cdot 10^6$	$1 \cdot 10^{-5}$	0.1	10000	22	70
RANS turb	$26.3 \cdot 10^6$	–	–	–	–	few
SAS comb+turb	$43.4 \cdot 10^6$	$5 \cdot 10^{-7}$	0.01	20000	56	389

Table 4.1: *FACTOR* - Effect of modelling strategy on computational cost

Data relative to the combustor simulation are reported just to highlight the cost associated to the generation of more accurate boundary conditions for the *RANS* simulations of the *NGVs*. It is possible to notice that the cost of *RANS* simulations is negligible if compared to *SAS*, for which only the computational time required by data sampling is reported (i.e. neglecting the time necessary to flush the initialisation).

The huge improvement obtained with the exploitation of *SAS* for the integrated approach comes at the cost of a significant increase in computational effort. Such increase is to be ascribed to the higher number of mesh elements as well as to the significant reduction in time step to ensure an adequate Courant number in the proximity of the *NGVs*.

Bearing this in mind, it is evident that the undeniable benefits provided by *SAS* are to be evaluated on the basis of the available computational resources. However it is also worth pointing out that potentially more efficient approaches are possible, e.g. collecting the time-dependent solution on *Plane 40* and applying it on a separate transient simulation of the *NGVs* alone, or coupling different codes/approaches for the two domains (as also presented in Section 2.4.2). This is realisable and can shorten the overall computational expenses at the cost of a longer set-up phase, which shall be taken into account.

Moreover, it is to be emphasised how *RANS* seems sufficient for predicting the turbine aerodynamics, while Scale-Resolving methods are needed to assess the thermal behaviour of the nozzles in a more accurate way. In fact, only the combined domain solved via *SAS* can successfully account for the effect of flow unsteadiness on turbulent mixing, as such approach showed a better match with experimentally measured coolant distribution on the airfoils. Consequently also adiabatic wall temperature and heat transfer coefficient appear more reliable, even if an experimental validation would give a higher degree of confidence.

When *SAS* is considered, wall temperature is more uniform than in *RANS* simulations, while heat transfer coefficient is generally higher, suggesting an exploitation of *RANS* with particular care. An additional comparison against uniform velocity/temperature conditions at the inlet was provided, confirming that the presence of a non-uniform swirl/temperature pattern exacerbates the intensity of the heat loads, both in terms of adiabatic wall temperature and heat transfer coefficient. This indicates once again that integrated approaches based on high-fidelity *CFD* are mandatory for a more sophisticated estimation of thermal conditions.

Chapter 5

Combustor-turbine interaction in an industrial turbine

Contents

5.1 Design of the combustor module

5.1.1 Target parameters

As anticipated in the earlier chapters of this manuscript, a warm rig including a real lean-premix combustor and a real high-pressure first-stage nozzle sector has been designed to operate in non-reactive conditions. In the early design phase it was established to study one of the industrial gas turbines in the *Baker Hughes* (formerly *GE Oil & Gas*) portfolio in order to verify the goodness of the original design and to find possible improvements eligible for future versions of the same engine or, in general, for new products.

The warm rig design was based on the objective of replicating the main flow features of the selected combustor, which led to the identification of the following non-dimensionalised parameters of interest, to be matched at the combustor/turbine interface plane:

- Temperature;
- Velocity components (axial, tangential, radial);
- Turbulence intensity.

The targets for the proposed study were set on the basis of a Large-Eddy Simulation of a periodic sector of the annular combustion chamber in nominal conditions, i.e. the engine (reactive) design point, representative of the gas turbine full load and already available at *Baker Hughes*. These are reported in Figs. 5.1, 5.2 and 5.3, noting that temperature has been non-dimensionalised based on the *LOTDF* definition of Eq. 2.2a, the velocity components by the average axial velocity at the combustor exit and turbulence intensity by its average value at the combustor exit:

$$LOTDF = \frac{T - \bar{T}_{40}}{\bar{T}_{40} - \bar{T}_{30}} \tag{5.1a}$$

$$u_{ax,nd} = \frac{u_{ax}}{\bar{u}_{ax,40}} \tag{5.1b}$$

$$u_{tan,nd} = \frac{u_{tan}}{\bar{u}_{ax,40}} \tag{5.1c}$$

$$u_{rad,nd} = \frac{u_{rad}}{\bar{u}_{ax,40}} \tag{5.1d}$$

$$Tu_{nd} = \frac{Tu}{\overline{Tu}_{40}} \tag{5.1e}$$

The definition of turbulence intensity is also recalled hereafter:

$$Tu = \sqrt{\frac{1}{3}\frac{\sum u_j'^2}{u^2}} \tag{5.2}$$

It is also to be noted that the swirler's cross section has been removed to protect the *Baker Hughes*' intellectual property.

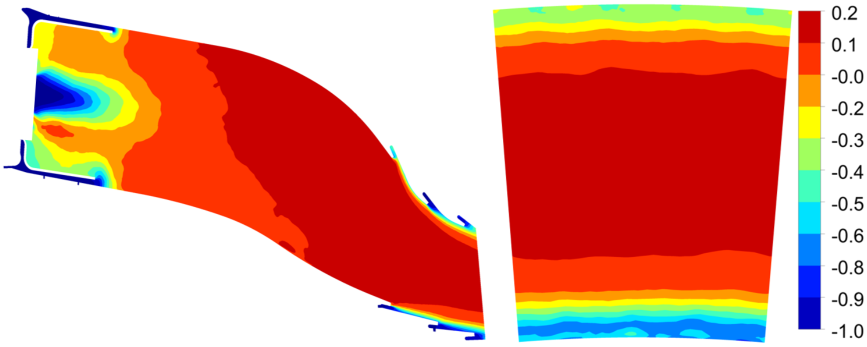

Figure 5.1: *STech* - Non-dimensionalised target temperature (*LOTDF*) on the meridional plane and at the combustor exit

For what concerns the scaling of the nominal into the rig operating conditions, these are somehow limited by the capability of the testing facility, as summarised as follows:

- $T_{max} \leq 600$ K;
- $\dot{m}_{tot} \leq 0.95$ kg/s;
- $P_{max} \leq 2.5$ barA.

With this in mind, the scaling process was performed by considering the main flow Reynolds number Re_g, Mach number Ma_g and the temperature ratio between main and coolant flows. As already mentioned, however, it was not possible to match both Re_g and Ma_g at the same time, since this would have needed to increase mass flow rate and pressure over the test bench capabilities. Temperature ratio, on the other end, could be set to ≈ 2, versus the 2.3 value present in the real engine, due to the maximum temperature rig constraint. In spite of this, the rig operating conditions were set in Mach similitude, which enabled the accurate reproduction of the airfoils expansion ratio and hence pressure profile, with a direct impact on film-cooling distribution. Reynolds number at *Plane 40* is therefore set at around 50% of the engine value, which, in spite of reducing heat transfer, is still representative for secondary flows and pressure loss mechanisms.

The cited necessary variations to the engine parameters have therefore been highlighted and a trade-off between similitude requirements and rig limitations has been set. The largest difference lays in the Reynolds number, affecting the heat transfer on the airfoils.

Based on this preamble, the test bench could accommodate three swirlers and a nozzle doublet (or, equivalently, three passages). However it is to be noted that the ratio between the total number of swirlers and that of airfoils in the real engine is not

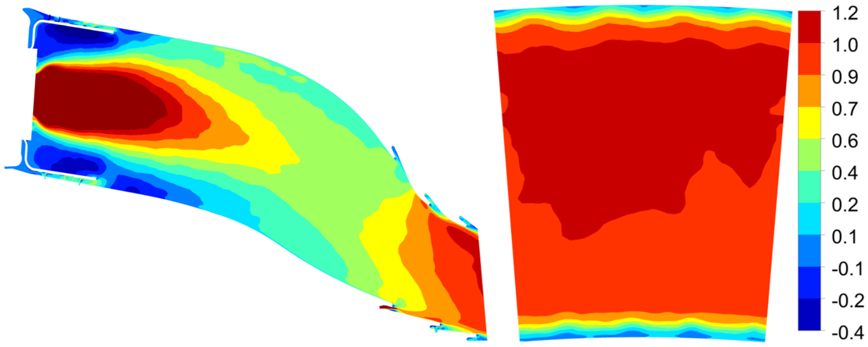

(a)

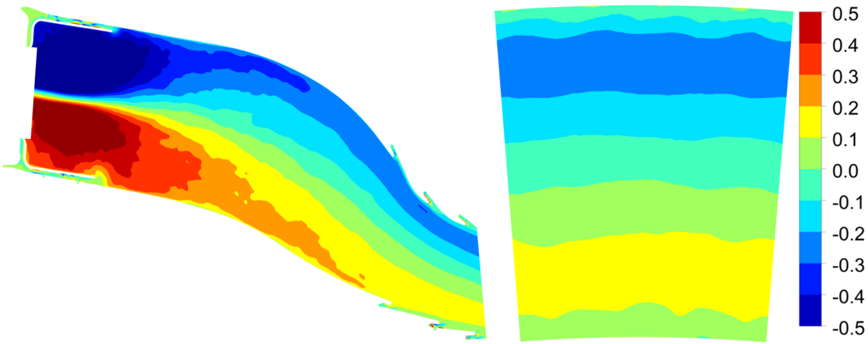

(b)

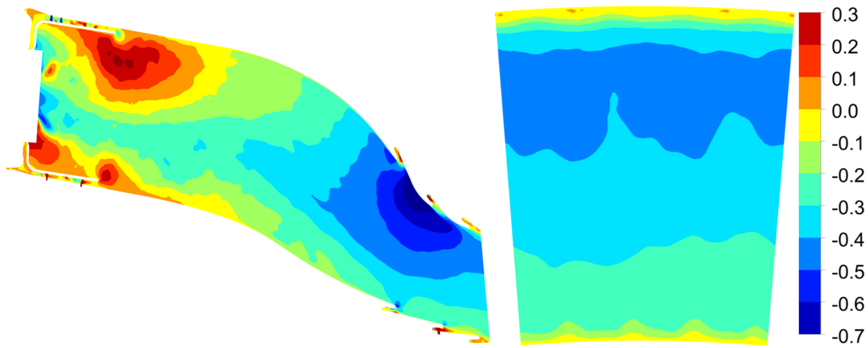

(c)

Figure 5.2: *STech* - Non-dimensionalised target velocity components (axial (a), tangential (b) and radial (c)) on the meridional plane and at the combustor exit

exactly 1, which required a dedicated analysis to design the *NGV* tailboards, which could be non-equally spaced from the central vanes. To do so, in the early design phase and due to the tight time schedule, a *uRANS* simulation of the non-reactive trisector combustion chamber was performed. Reminding how during the *FACTOR* project *RANS* was found acceptable to provide satisfactory information at the combustor/turbine interface plane to study the aerodynamics through the nozzles, this was herein replicated. This was thus used as inlet boundary conditions to a *RANS*-based

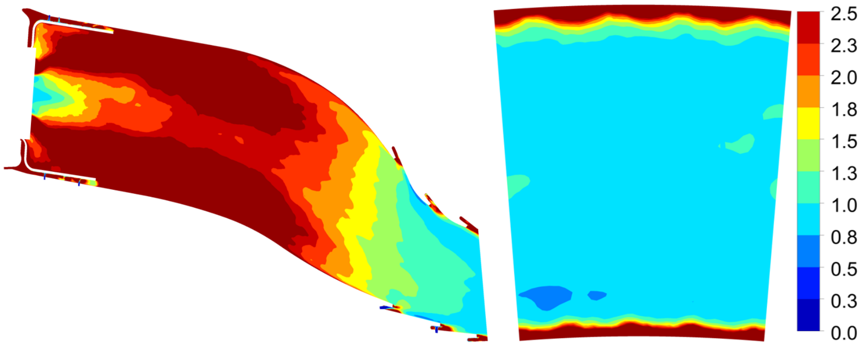

Figure 5.3: *STech* - Non-dimensionalised target turbulence intensity on the meridional plane and at the combustor exit

DOE campaign of the *NGV* module for the tailboards design. It is worth mentioning that, other than for purposes related to the rig design, numerical simulations could not be run on a limited domain (e.g. periodic), also because having just two film-cooled nozzles implies that each airfoil has either its pressure or suction side exposed to a lateral passage, where main flow split could be different and hence alter the film-cooling distribution if not accounted for.

Furthermore, two geometry modifications were to be implemented to the original combustion chamber layout:

- Heat shields - Installed right downstream of the swirlers exit to protect the liners from the high temperature mixture of fuel and air, these were eliminated in the rig layout since not necessary;

- 3rd nugget rows - Present at both inner and outer radius, these had to be removed to enable the installation of the traverse system and hence the measurements at *Plane 40* with the *5HP* and *HWA*.

It is also worth mentioning that it was necessary to select the appropriate software for this study, since within the industrial partner different tools are used by the combustion and the turbine teams. In fact, the former uses ANSYS®Fluent, which works best within the combustion environment and has the capability to handle different fuel species. The latter, on the other hand, utilises ANSYS®CFX, which is robust and best manages complicated geometries such as film-cooled airfoils. However, with in mind the need for simulating the integrated combustor and turbine modules at a later stage, one single tool had to be chosen.

Therefore, recalling that the present investigation is especially focused on the turbine module and that the swirlers are operated in the absence of combustion, it was decided to make use of the ANSYS®CFX v.19.2 tool for all the simulations involved in this work.

5.1.2 Numerical setup

The combustor simulator was therefore run with rig representative boundary conditions, which are basically the following:

- Inlets (main and coolant) - Mass flow rate;
- Outlet - Average static pressure;
- Walls - Adiabatic, no slip, smooth.

For what regards turbulence modelling, as said, unsteady *RANS* was adopted based on the *k-ω SST* model, with a time step of $2.5 \cdot 10^{-6}$. In agreement with the best practices specified by the software developers [143], all equations are discretised in "high resolution", as available in the tool, corresponding to a 2nd order upwind scheme (for *RANS*, while it would blend to a central difference scheme with *SAS* when the solution turns to *LES*-like). An automatic near-wall treatment approach is employed, blending between wall-function and wall-integration application on the basis of the y^+ value, which is not always lower than 1 in this case needing a blending between the low and the high Reynolds formulations of the boundary layer. Moreover, the solution algorithm is pressure based, with "Rhie-Chow" pressure-velocity coupling, while time marching is based upon the second order backward Euler scheme.

The considered computational domain is the one shown in Fig. 5.4, with *Plane 40* representing the combustor-turbine interface plane. As noticeable, ducts were installed at the swirlers exit, for reasons that are going to be better explained in the following Section. The grid, reported in Fig. 5.5, was generated with ANSYS® Meshing and is hybrid unstructured, as it is composed by tetrahedra and prisms, including 3 prismatic layers. The mesh therefore counts $65.5 \cdot 10^6$ elements and $13.6 \cdot 10^6$ nodes, with a 1 mm size within the injectors as well as in the refinement region immediately downstream of the swirlers.

5.1.3 Combustor simulations and conditions at Plane 40

A non-reactive simulation of the combustor was therefore performed (with the very same geometry) in order to compare the behaviour of the same with respect to the engine-like case, thus bearing in mind the expected distribution of the target parameters previously shown in Figs. 5.1, 5.2 and 5.3. The resulting temperature, velocity components and turbulence distribution on the meridional plane and at the combustor exit are illustrated in the contour plots of respectively Figs. 5.6, 5.7 and 5.8.

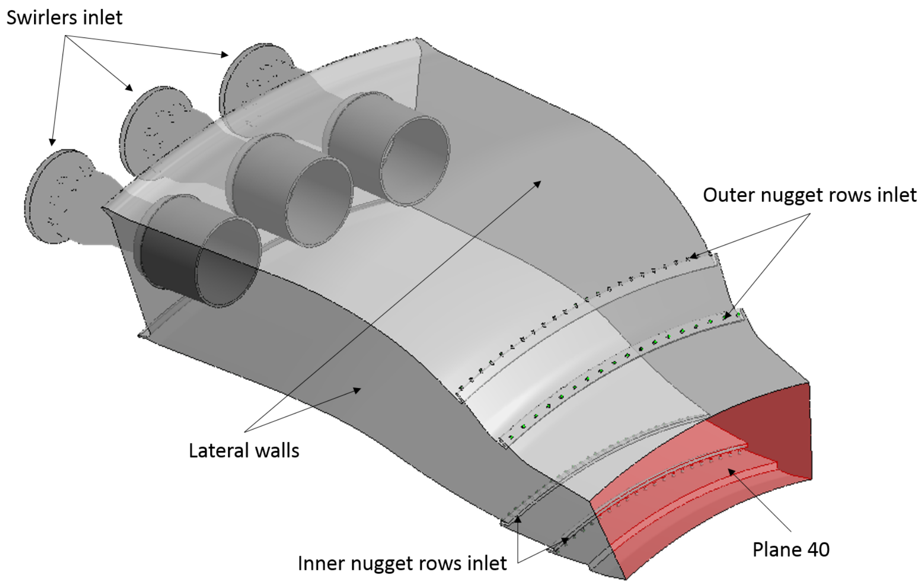

Figure 5.4: *STech* - Combustor computational domain

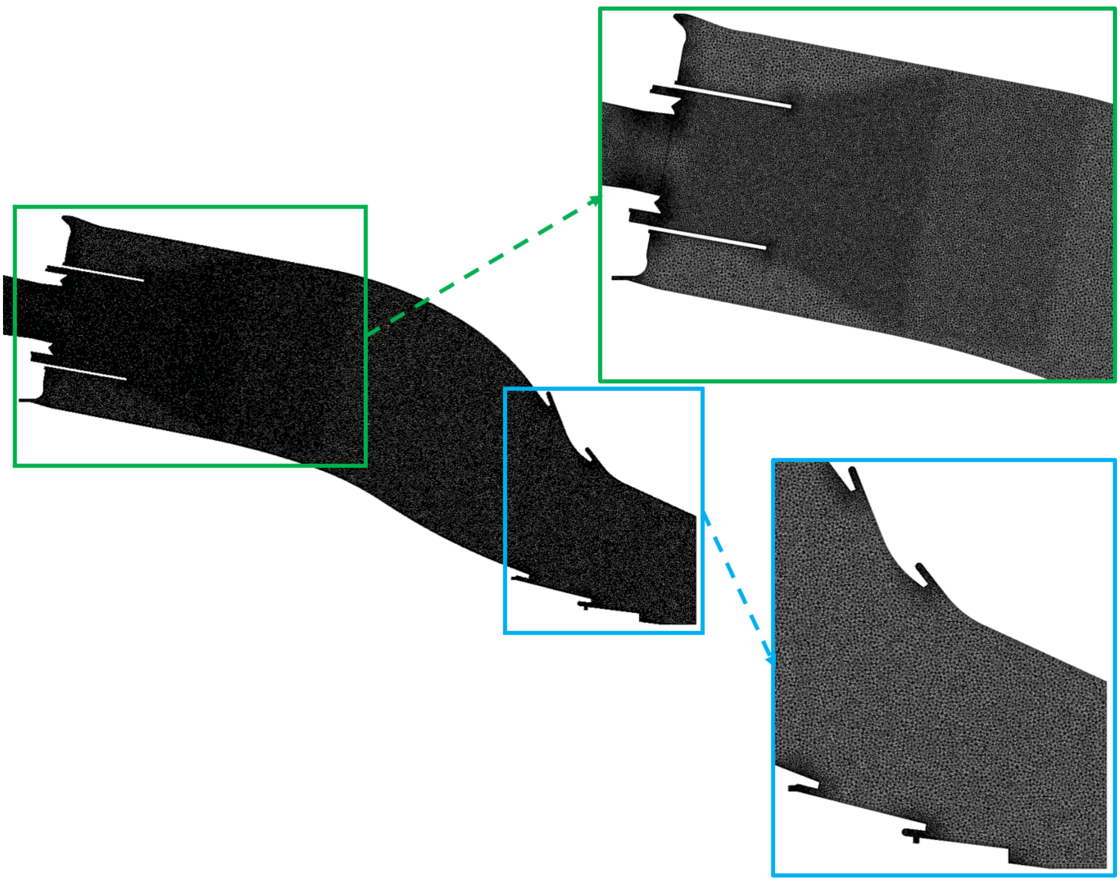

Figure 5.5: *STech* - Combustor computational grid

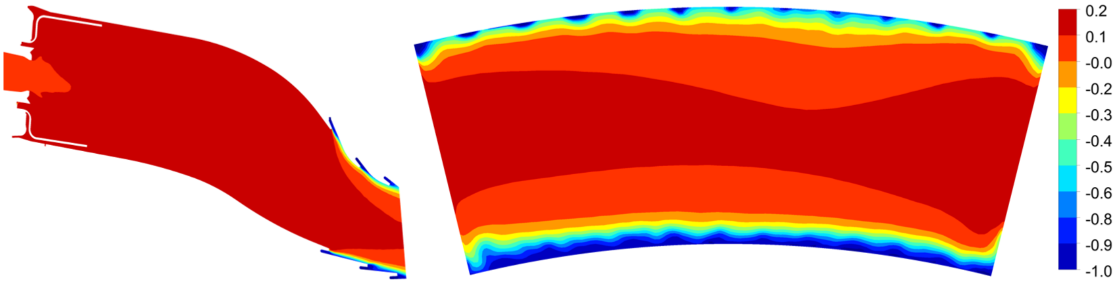

Figure 5.6: *STech* - Non-dimensionalised temperature ($LOTDF$) on the meridional plane and at the combustor exit

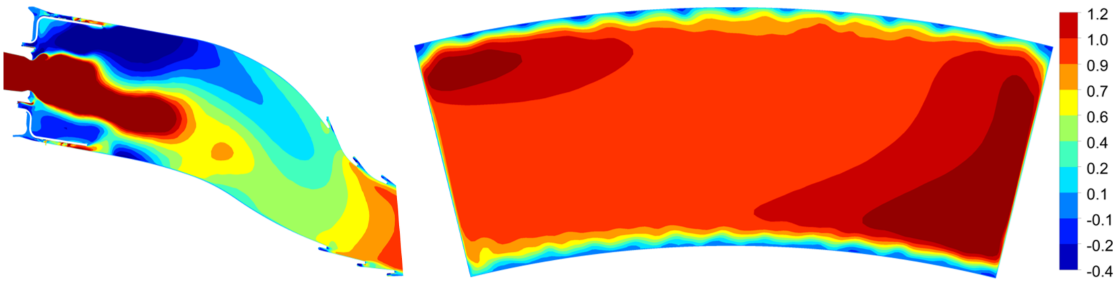

(a)

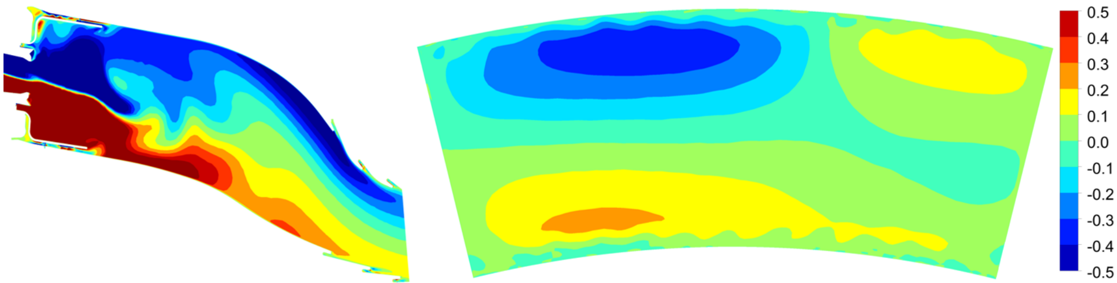

(b)

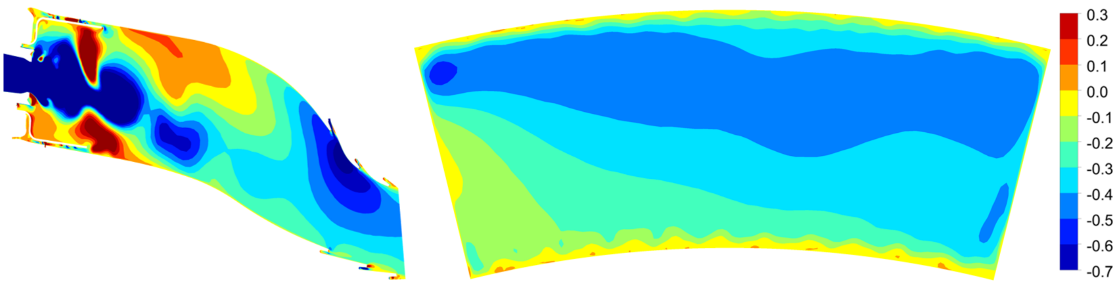

(c)

Figure 5.7: *STech* - Non-dimensionalised velocity components (axial (a), tangential (b) and radial (c)) on the meridional plane and at the combustor exit

Unfortunately, a sufficiently accurate reproduction of the target parameters is not achieved with the proposed features. Although the monitored parameters' intensity is

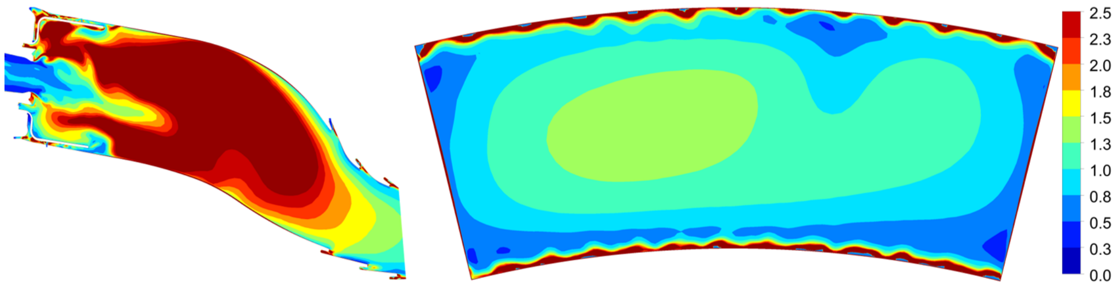

Figure 5.8: *STech* - Non-dimensionalised turbulence intensity on the meridional plane and at the combustor exit

somehow similar to the expected values, there is a misalignment particularly highlighted by the contour of tangential velocity (Fig. 5.2b). In fact, this shows that the main swirling structure is confined to the left-hand side of the sector (aft-looking-forward view), with a counter-rotating structure to balance momentum on the right-hand side. This is ascribable to the long chamber length, which makes the lateral walls heavily interact with the swirling structures. As a consequence, this would bring the risk to have an uncertain tangential flow field at the nozzles inlet, which could jeopardise the testing intents. Another evident discrepancy is related to the predicted turbulence intensity at the outlet plane, which, however, can be ascribed to the adoption of the *RANS* methodology, which is known to over preserve turbulence, being fully modelled.

For these reasons, and based also on the experience gained during the *FACTOR* project, it was decided to install circular ducts right downstream of the swirlers exit in order to align the swirling flow to the central vane passage. After a few trials, a duct as long as roughly the swirler outer diameter ("L1D") was selected, with the correspondent updated key parameters contours being reported in Figs. 5.9, 5.10 and 5.11.

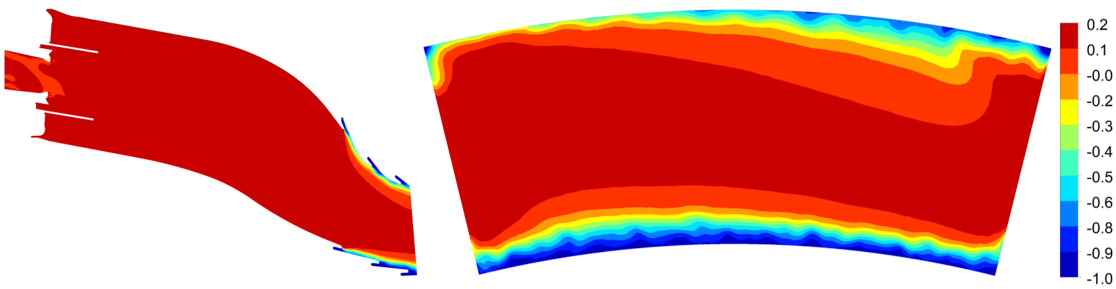

Figure 5.9: *STech* - Non-dimensionalised temperature (*LOTDF*) on the meridional plane and at the combustor exit with the "L1D" duct installed

To appreciate the differences between the two rig cases and the target parameters with a more quantitative measure, it can be convenient to report the circumferential average (on the central sector only) of each quantity on a graph, as shown in Figs. 5.12,

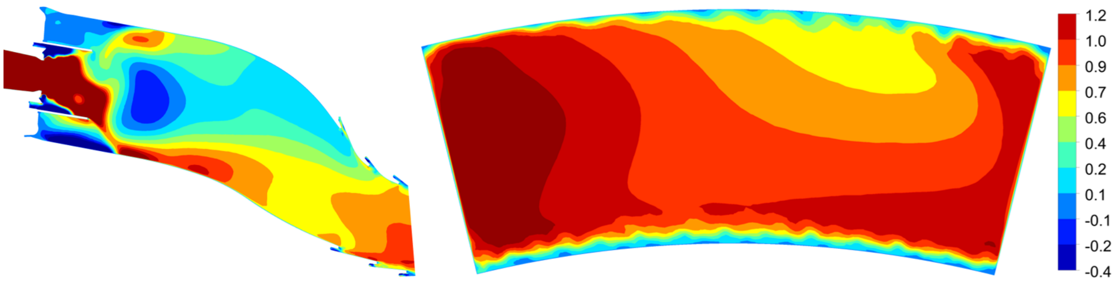

(a)

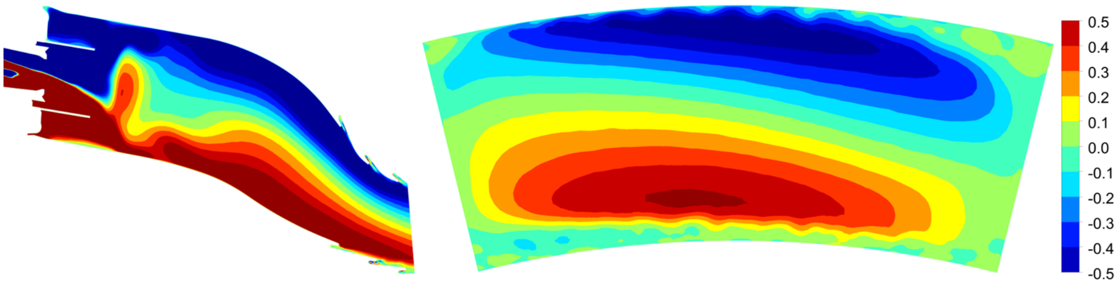

(b)

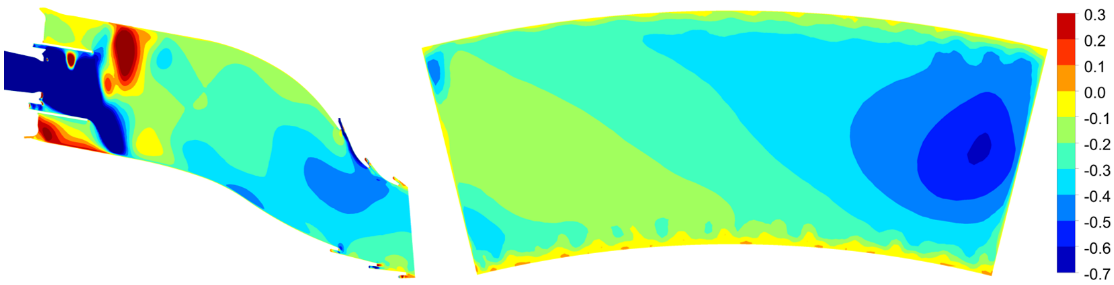

(c)

Figure 5.10: *STech* - Non-dimensionalised velocity components (axial (a), tangential (b) and radial (c)) on the meridional plane and at the combustor exit with the "L1D" duct installed

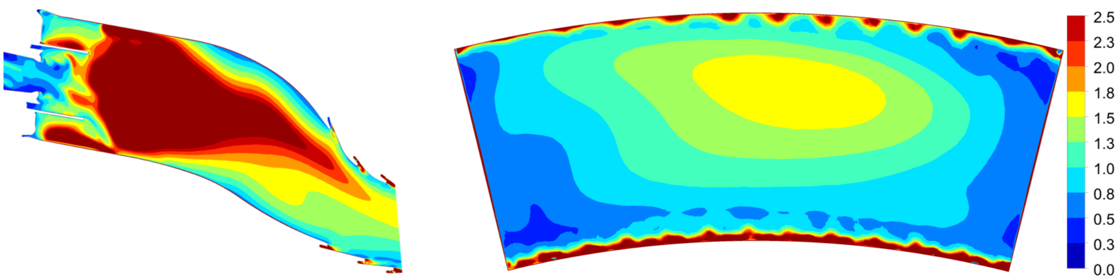

Figure 5.11: *STech* - Non-dimensionalised turbulence intensity on the meridional plane and at the combustor exit with the "L1D" duct installed

5.13 and 5.14.

Looking at all these contour plots and comparative graphs, it could be argued that the duct installation has significantly altered the flow field at the combustor outlet.

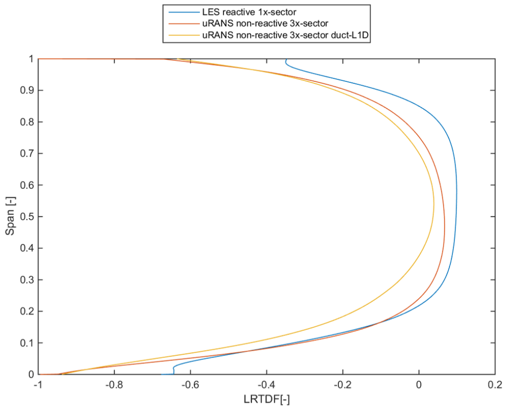

Figure 5.12: *STech* - Comparison of circumferentially averaged non-dimensionalised temperature ($LRTDF$)

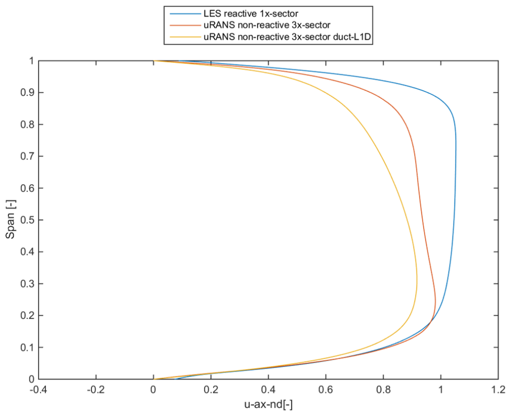

(a)

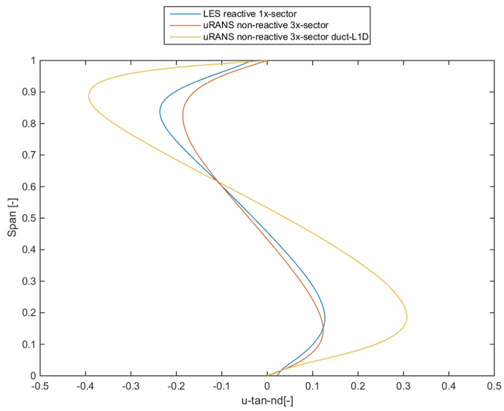

(b)

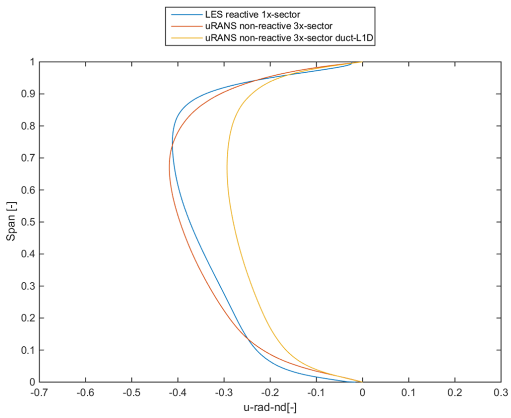

(c)

Figure 5.13: *STech* - Comparison of circumferentially averaged non-dimensionalised velocity components (axial (a), tangential (b) and radial (c))

Also looking at the circumferentially averaged quantities, it looks like the configura-

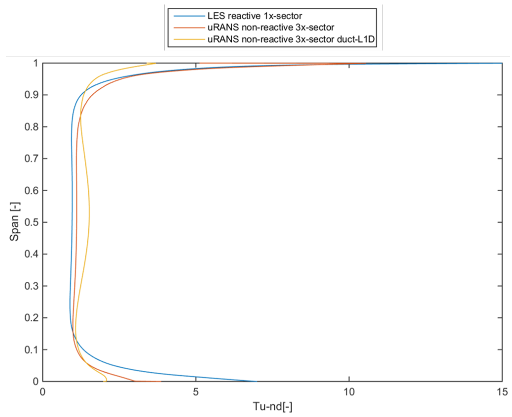

Figure 5.14: *STech* - Comparison of circumferentially averaged non-dimensionalised turbulence intensity

tion without duct better matches the target parameters. However, this can bring to misleading considerations, since the circumferential averaging process balances out any tangential deviation. It is more appropriate to state that, even though the duct presence brings to more intense tangential velocity, which is key in the replication of a representative turbine inflow, this is at the same time more uniformly distributed over the full sector.

5.2 Design of the nozzles module

5.2.1 Target parameters

For what regards the nozzles module, it is to be reminded that only one sector composed of two airfoils could be fit into the rig, due to the imposed limitations to flow rate. For this reason the full turbine module comprehensive of the tailboard walls had to be studied. The discharge duct is included in the simulation until the flange section, which is enough far away from the regions of interest for measurement purposes.

The main target for the nozzles study is the exit Mach number, that is on average 0.74 at *Plane 41*, which is located about 15 mm downstream of the nozzles' trailing edge. As already mentioned in Section 3.1.2, the film cooling flow was replicated in terms of blowing and momentum flux ratios by controlling *MR*, *TR* and *PR*. The third one is satisfied by appropriately setting the flowpath pressure, which is achieved via the Mach similitude, and mass flow rate, since, with a fixed geometry, pressure ratio and mass flow rate are proportional. The second one is almost matched (2 against 2.3), while the first one is respected by arbitrarily adjusting the coolant inlet pressure.

However, it is to be acknowledged that, due to the non periodicity on the lateral vane passages, the just mentioned parameters may not be matched on the airfoils' surfaces exposed to the lateral sides, where the pressure profile can differ from the target distribution. The target pressure profile, i.e. the one for the periodic airfoil, is reported in the following Section, for sake of direct comparison with the test rig values. It is further to be mentioned that the periodic configuration run in rig conditions, rather than in engine ones, was assigned to be the reference case, because the turbine inlet *BCs* have necessarily changed as per the assumptions made during the rig design phase.

5.2.2 Numerical setup

The turbine module was simulated based on rig representative boundary conditions, as previously done for the combustor, and consecutively to the combustor itself in the following way:

- Main inlet - 2D map of boundary conditions obtained from the combustor simulation in terms of total pressure, total temperature, normalised velocity components, turbulence kinetic energy and specific dissipation rate;
- Secondary inlets (cooling) - Mass flow rate;
- Outlet - Average static pressure (iterated as to get measured outlet mass flow rate);
- Walls - Adiabatic, no slip, smooth.

For what regards turbulence modelling, the *k*-ω *SST RANS* model was utilised. Once more, in agreement with the best practices specified by the software developers [143], all equations are discretised in "high resolution", as available in the tool, corresponding to a 2nd order upwind scheme. An automatic near-wall treatment approach is employed, blending between wall-function and wall-integration application on the basis of the y^+ value, which is always lower than 1, i.e. ensuring the wall boundary layer resolution and the effective application of the low-Re model, fundamental for a correct evaluation of heat transfer in a following stage of the programme. Moreover, the solution algorithm is pressure based, with "Rhie-Chow" pressure-velocity coupling.

The considered computational domain is the one shown in Fig. 5.15, with *Plane 40* representing the inlet section, while *Plane 41* a plane at about 15 mm axial distance from the airfoils' trailing edge. This is going to be the monitor plane downstream of the nozzles, since it is the axial location at which the traverse system for *5HP* and

HWA measurements is placed. The grid, reported in Fig. 5.16, was generated with ANSYS® Meshing and is hybrid unstructured, as it is composed by tetrahedra and prisms, including 15 prismatic layers. The mesh therefore counts $95.2{\cdot}10^6$ elements and $23.2{\cdot}10^6$ nodes, with a 0.5 mm size on the airfoils surface and 0.1 mm in the film cooling holes, which are the smallest feature of the domain. It is also to be noted that the airfoils' internal core has been removed to protect the *Baker Hughes*' intellectual property. Walls were treated as no slip, smooth and adiabatic. In addition, a passive scalar was transported as to trace the evolution of film cooling, assigning a boundary condition of 1 to the inlets of the nozzles' internal channels and 0 at the main inlet.

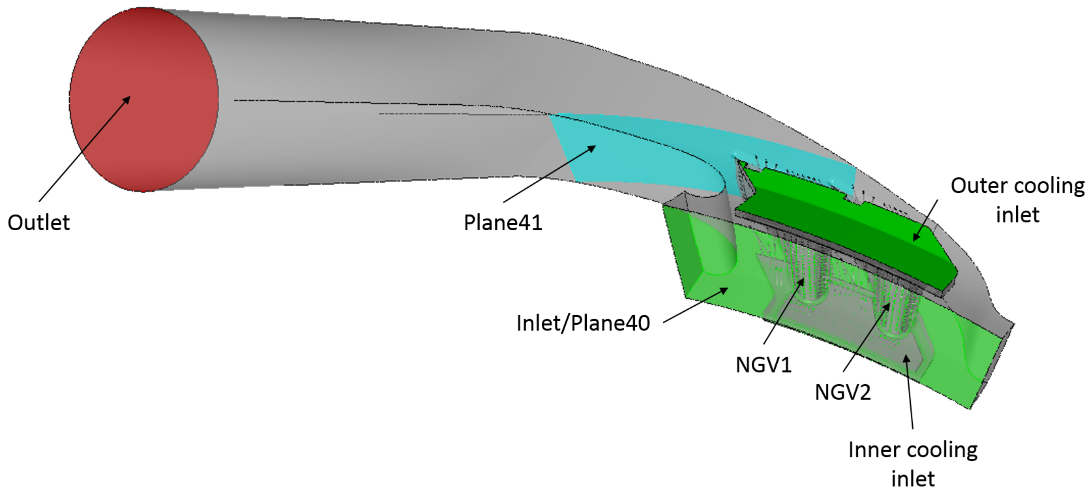

Figure 5.15: *STech* - Nozzles module computational domain

5.2.3 Tailboards design and simulations

Based on the analysis performed on the combustor simulator, the nozzle module design could be performed with the main intent of defining the lateral walls geometry. As the ratio between the number of airfoils and that of burners in the engine is slightly higher than 1 and since modifying the burners flow rate was regarded improper, it was decided to have different width vane passages by adjusting the pitches (p_1 and p_2 of Fig. 5.17) between the airfoils and the lateral walls. By contrast, reducing the tangential length of the combustion chamber could have generated the risk of enhanced interaction between the swirlers and the lateral walls leading to a further alteration of the outlet flow field. An additional geometrical parameter to be defined were the aperture angles (ϕ_1 and ϕ_2 of Fig. 5.17) of the discharge duct, right downstream of the nozzles, which can have an impact on the airfoils pressure distribution. As anticipated,

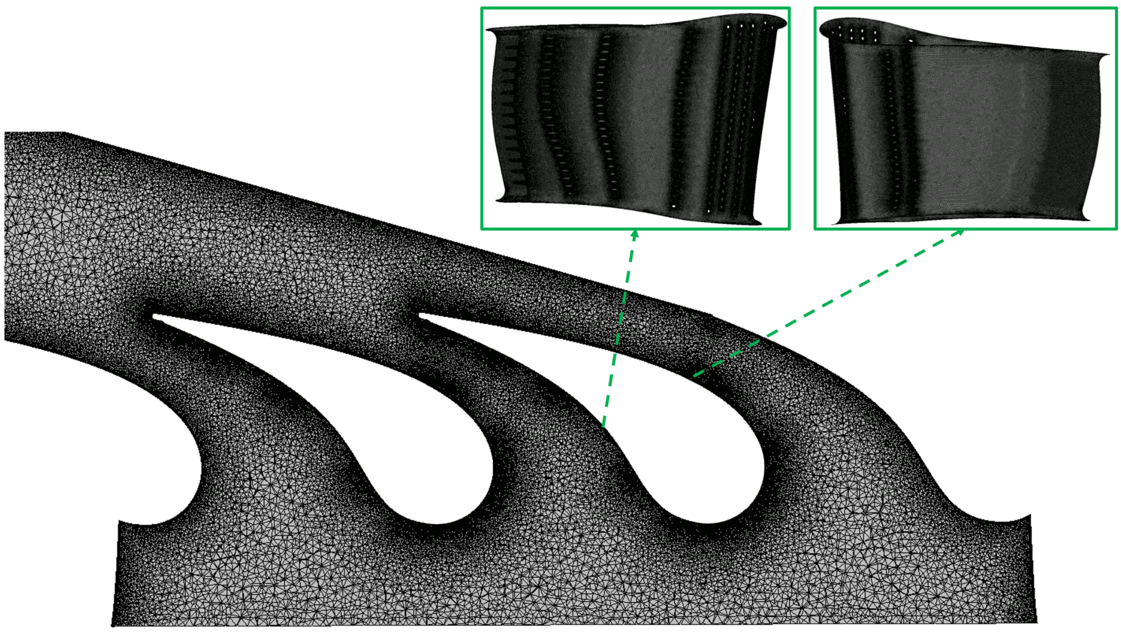

Figure 5.16: *STech* - Nozzles module computational grid

Fig. 5.17 reports these parameters on the *NGV* module geometry for sake of a graphical illustration.

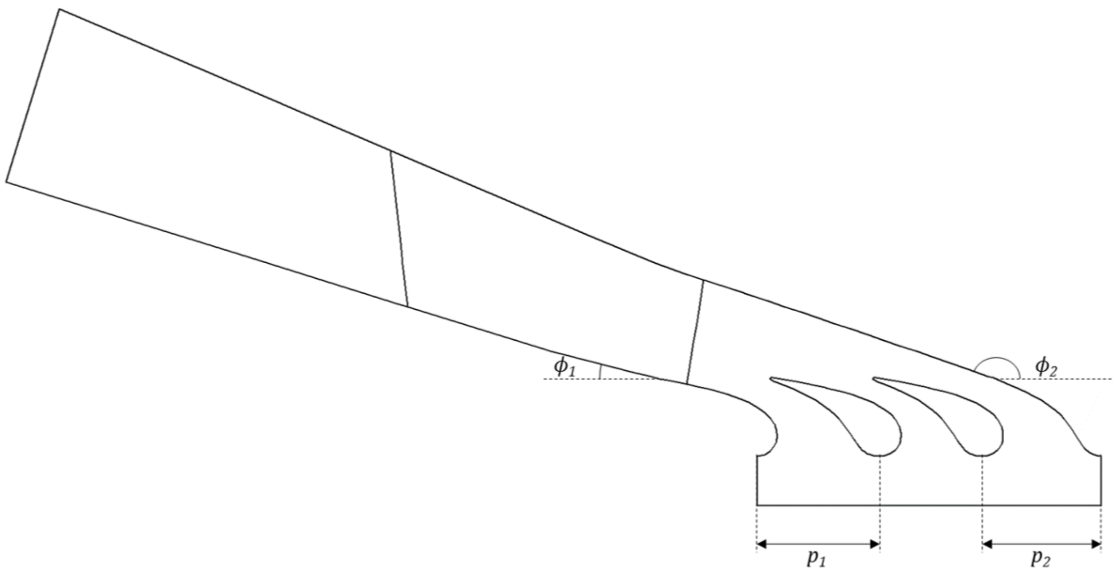

Figure 5.17: *STech* - Tailboards design parameters

Therefore a *DOE* campaign was necessary to determine the best configuration to be implemented in the warm rig. The best combination of the aforementioned parameters was set as the one providing the closest match in terms of static pressure field to an equivalent periodic nozzle. Noting that for this study no film-cooling was considered on the airfoils in order to limit the costs of such analysis, four monitor regions were individuated to perform the comparison:

- Midspan passage plane,
- Airfoils surface,
- Midspan airfoils section,
- Outlet plane.

In addition to this, also the flow split among the three vane passages was monitored to keep within a ± 1% range, as to have a roughly uniform distribution of flow over the entire domain. A comparison of the static pressure field at the monitor regions is shown in Figs. 5.18, 5.19, 5.20 and 5.21 as non-dimensionalised with respect to the *Plane 40* static pressure value.

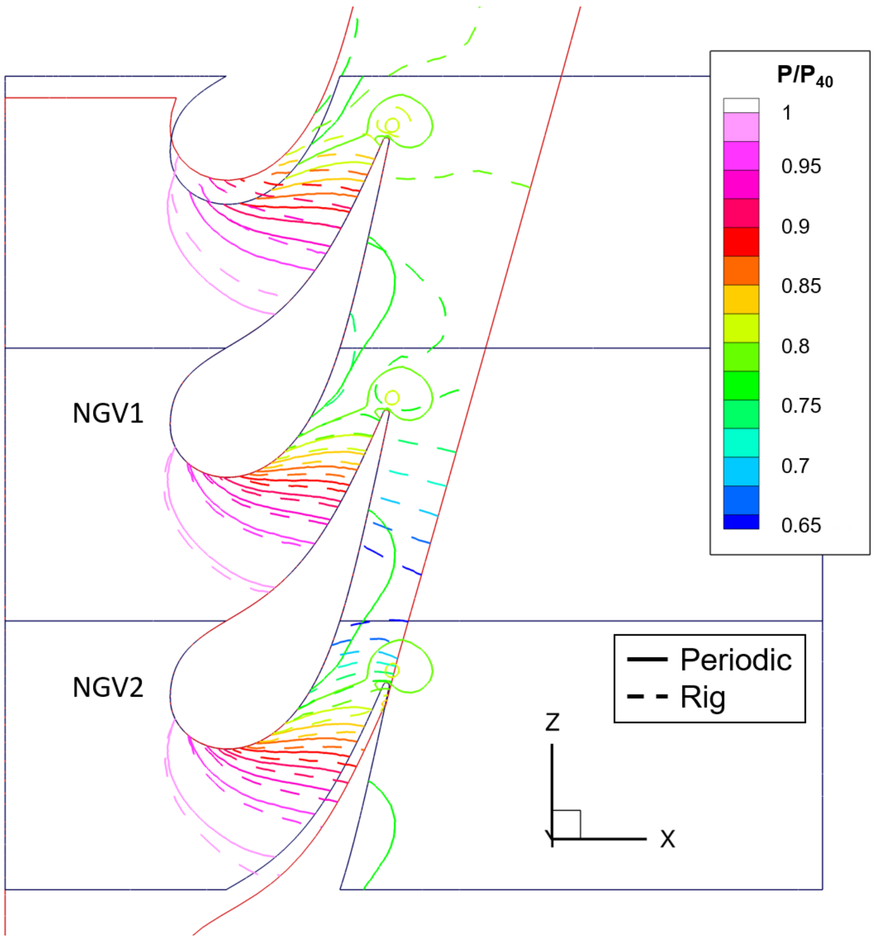

Figure 5.18: *STech* - Pressure field comparison at the midspan passage plane against the periodic uncooled case

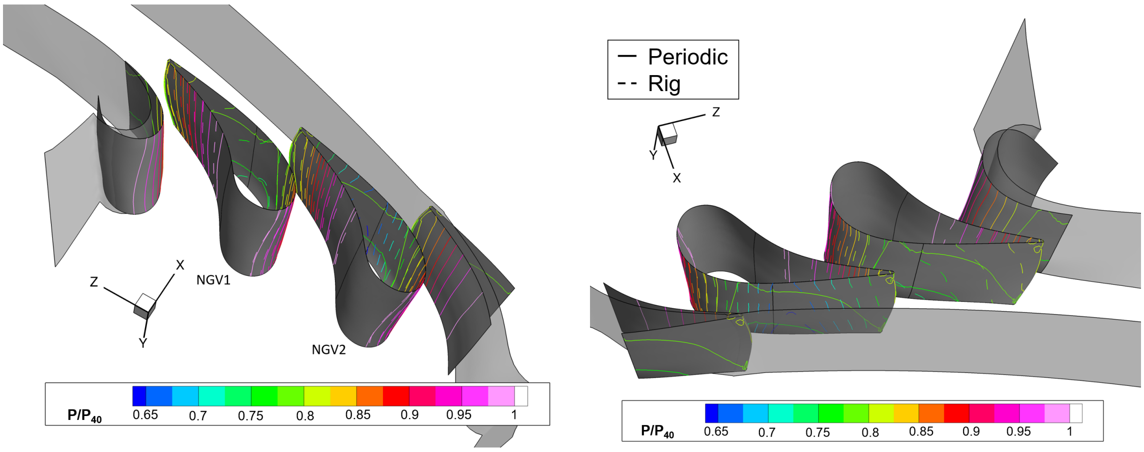

(a) (b)

Figure 5.19: *STech* - Pressure field comparison on the airfoils surface against the periodic uncooled case

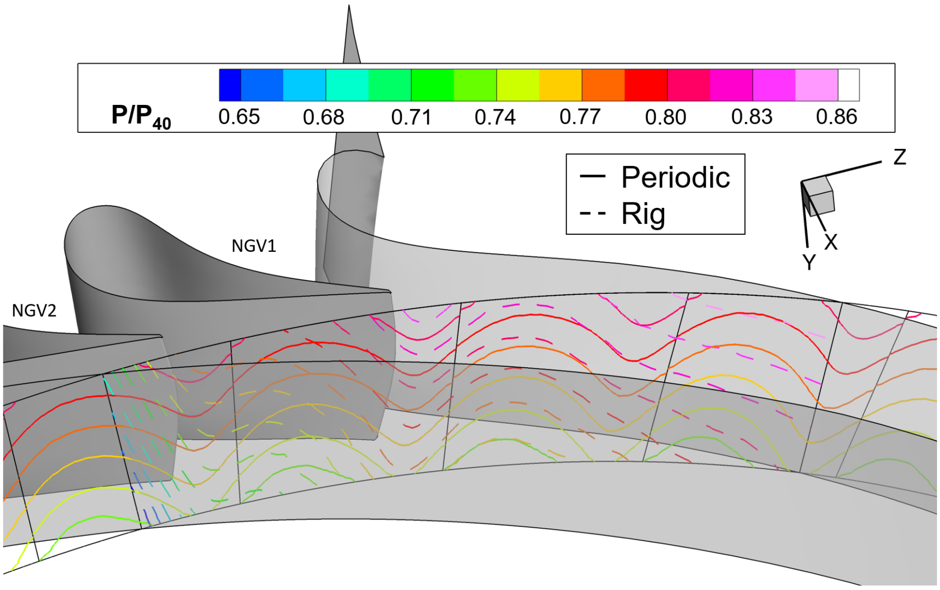

Figure 5.20: *STech* - Pressure field comparison at the outlet plane (*Plane 41*) against the periodic uncooled case

With reference to Fig. 5.18, the black geometry profiles are those pertaining to the periodic case, while red ones are relative to the rig configuration. Focus should be directed towards the central vane passage, where continuous lines (periodic) almost overlap with the dotted lines (rig) over the whole pressure side, whereas some discrepancy is present downstream of the throat section on the suction side. The lateral passages have slightly different pressure contours, since, as visible, are larger than the central one. These considerations are applicable also when looking at Fig. 5.19, which presents the comparison over the airfoils surface.

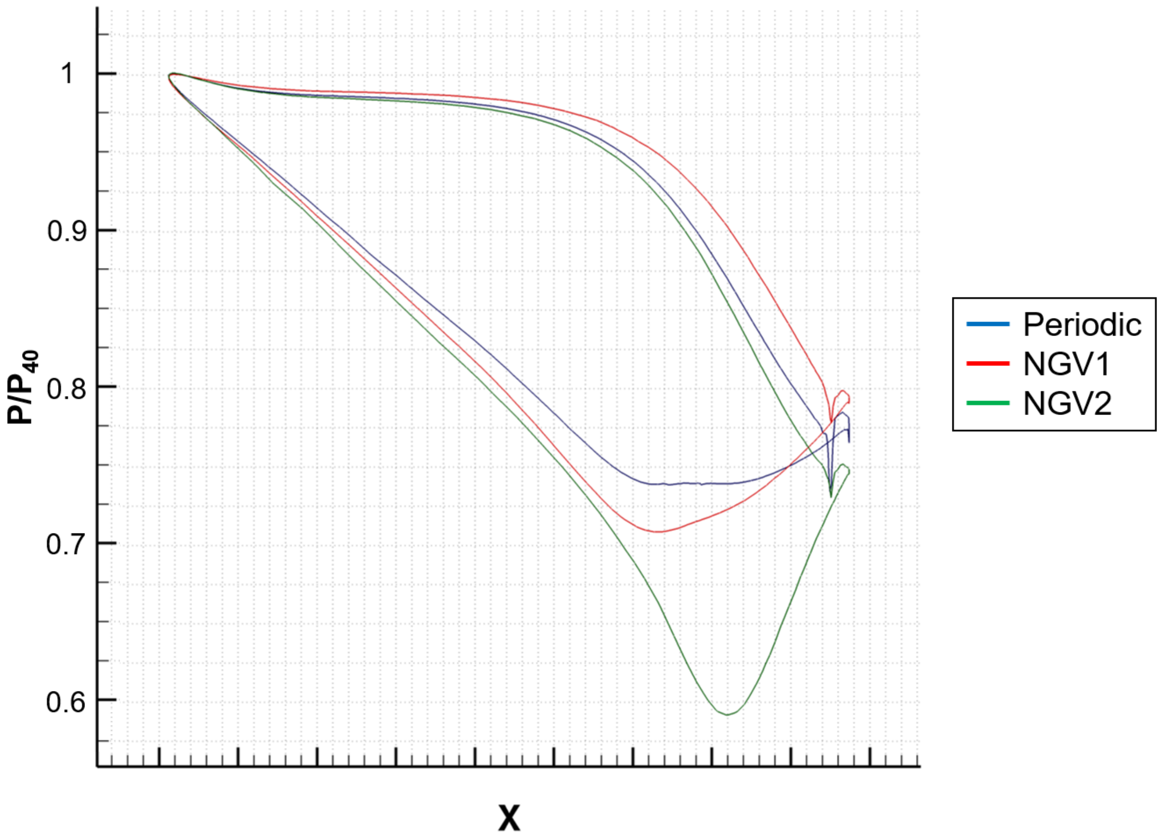

Figure 5.21: *STech* - Pressure field comparison at the midspan airfoils section against the periodic uncooled case

Fig. 5.20, on the other hand, shows the static pressure field on a plane at a given distance from the airfoils trailing edge and highlighting how this is similarly reproduced on the central portion of the rig case, while it is deviating from the periodic results in the lateral regions.

However, the most relevant comparison is based on the airfols load, since this has a direct impact on the film-cooling system. With reference to Fig. 5.21 the blue profile is relative to the periodic case, while the red and the green ones respectively to the left- and the right-hand side airfoils in the rig configuration with an aft-looking-forward view. Although there is a considerably low pressure on the suction side of the right-hand airfoil, there is also a satisfactory match of the pressure side profile of the same and of the suction side of the left-hand airfoil with respect to the periodic case.

Once the tailboards geometry definition had been completed, the so found domain was simulated in cooled conditions, i.e. activating the film-cooling presence. It was therefore possible to compare the rig configuration against the periodic domain in terms of pressure distribution along the vane channels and around the airfoils. A comparison on the midspan plane is given in Fig. 5.22, while Fig. 5.23 shows the comparison at

Plane 41 and Fig. 5.24 the airfoils' load at the midspan section.

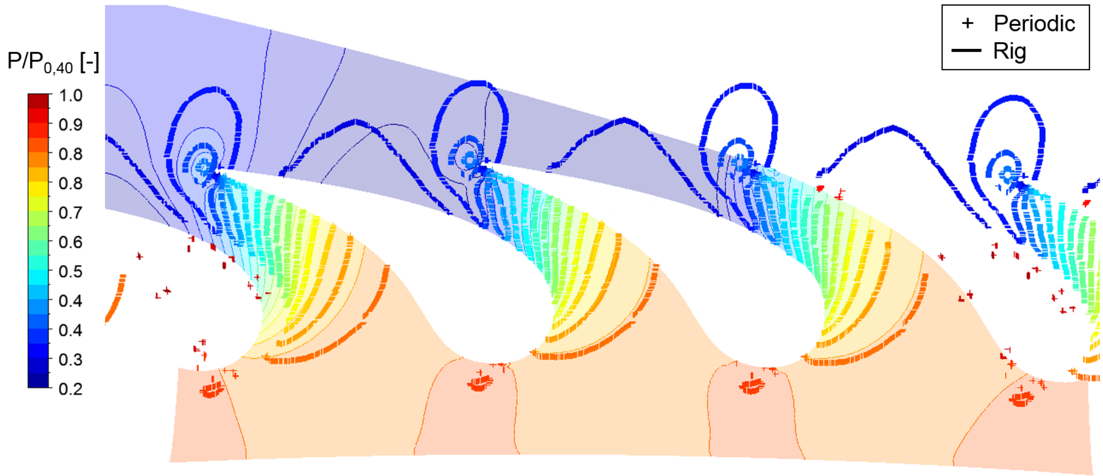

Figure 5.22: *STech* - Pressure field comparison at the midspan passage plane against the periodic cooled case

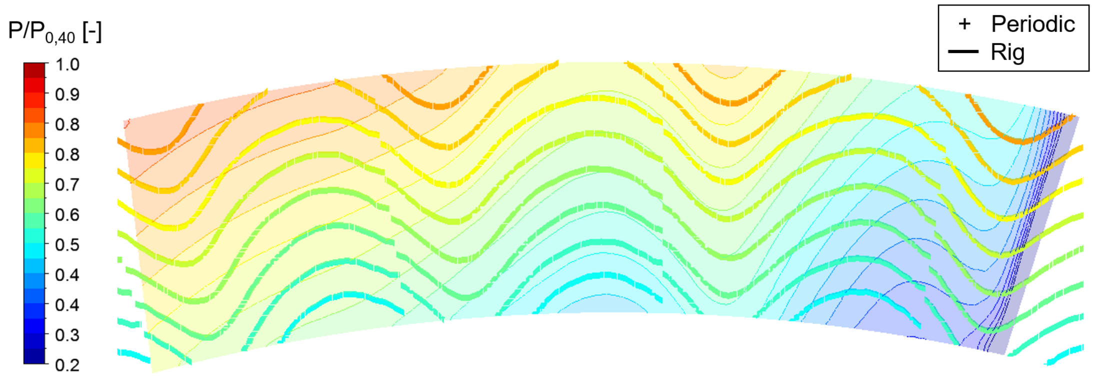

Figure 5.23: *STech* - Pressure field comparison at the outlet plane (*Plane 41*) against the periodic cooled case

There is acceptable agreement between the periodic and the rig cases on the central vane passage, while a reduced discrepancy is present on the left-hand side channel and non negligible differences, instead, are evident on the right-hand side channel. These are partly shown in the midspan passage plane of Fig. 5.22, but are especially higlighted by the airfoils' pressure load at the midspan section of Fig. 5.24. A fair comparison is between the suction side of *NGV1* and the periodic nozzle, which are overlaid for most of the surface with some difference at axial chord lengths of 0.7-0.9, and between the pressure side of *NGV2* and the periodic nozzle, where is a very good match except at the very proximity of the airfoil's trailing edge. By contrast, Fig. 5.23 illustrates a "wavy" pressure profile at the outlet section that overlays with the periodic nozzle pattern in the central region, while reveals a steep drop in static pressure moving towards the walls of the right-hand passage.

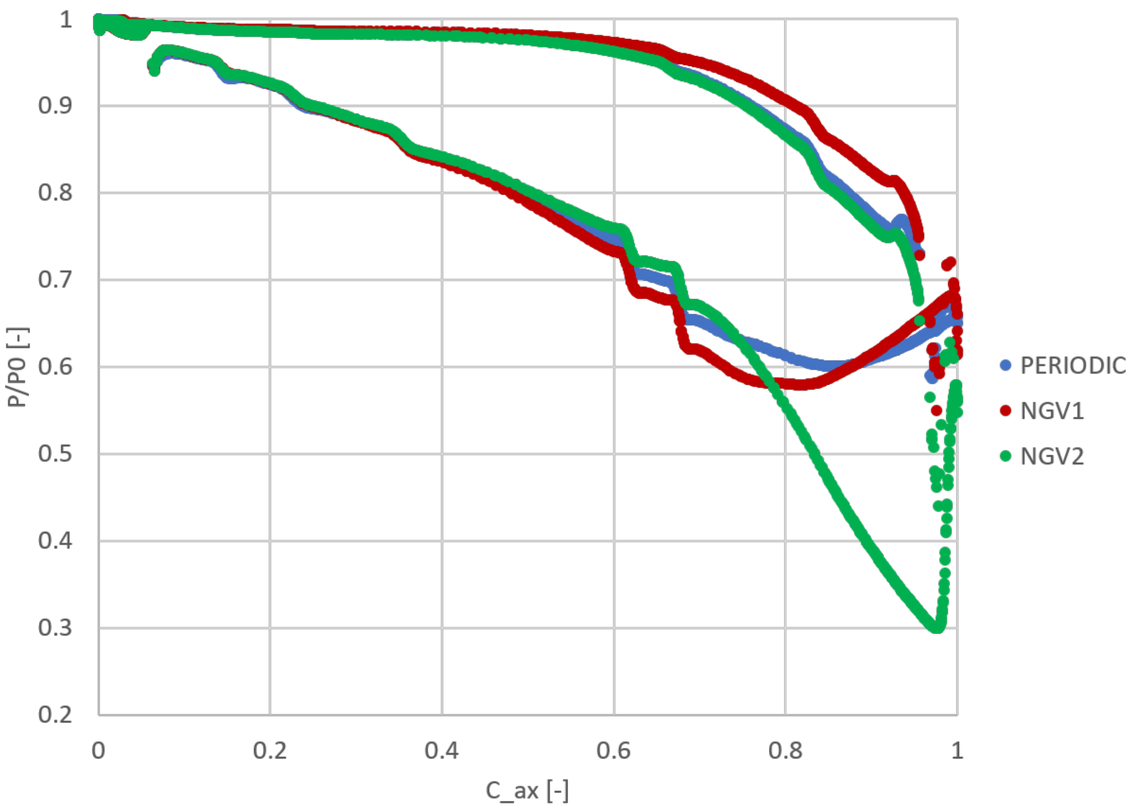

Figure 5.24: *STech* - Pressure field comparison at the midspan airfoils section against the periodic cooled case

5.3 Preliminary results and comparisons

5.3.1 Measurements and comparisons at Plane 40

At the very beginning of the test campaign, the rig was commissioned through the following procedure:

1. The desired mass flow rates through each cooled component was achieved by varying pressure at the cooling plena at room temperature (components flow check);

2. An overall satisfying pressure ratio through the nozzles was achieved in order to fulfil both the Mach similitude and the characteristic ratios across the cooling holes;

3. The rig reference running conditions were established based on the pressure probes reading localised in the main sections of interest (*Plane 40* and *Plane 41*).

This enabled to quickly set the operating conditions at any following test run and was repeated for the nominal and the isothermal points.

As already mentioned in Section 5.1 a duct was designed to be installed at the swirlers outlet section in order to ensure the periodicity condition on the central sector and to preserve the swirling flow in non reactive conditions. Therefore, with the intent of verifying the goodness of the design, the first performed measurements aimed at validating such configuration, by selecting the most appropriate among three geometries, i.e.:

- "L0" - No duct installed;
- "L075" - A duct with roughly $L = 0.75 \cdot D$;
- "L1" - A duct with about $L = 1 \cdot D$.

Where D is the swirlers' exit outer diameter. The three configurations were investigated with *5HP* and *HWA* and then compared against the expected figures, based on the distribution of the target parameters presented in Section 5.1.1 at *Plane 40*. Fig. 5.25 therefore reports the comparison of normalised turbulence intensity (from *HWA*), temperature, swirl and pitch angles, Mach number and total pressure (from *5HP*). Note that on the x-axis of the plots is the t/p_{NGV}, i.e. the tangential-angle to the NGV-pitch ratio, whereas on the y-axis is the normalised NGV height h/H. It is also interesting to add the *uRANS* predictions, which are provided at the far right-hand side of Fig. 5.25. Furthermore, tangentially averaged quantities are given in the graphs of Fig. 5.26.

The comparison on overall shows a fair agreement of experimental with respect to target results. In particular, although the "L0" configuration is the one better replicating the intensity of the considered quantities, it doesn't provide a periodic distribution of especially the swirl angle and hence needs to be discarded. By contrast, the "L1" configuration gives quasi-periodic contour plots, even if with enhanced intensity. In conclusion, it is convenient to adopt the "L1" configuration, since it is the only one ensuring an appropriate flow pattern on the central vane passage, object of the performed investigations. Moreover, even though *uRANS* proves to be able to capture the macroscopic flow features from a qualitative perspective, it fails in providing an accurate reproduction of the same, which could have possibly been achieved with scale resolving techniques. In fact, flow features look over preserved by *uRANS*, while some more mixing is actually occurring and should be accounted for. In a future phase, it is intended to simulate the whole rig via *SAS*, which will supposedly provide better results

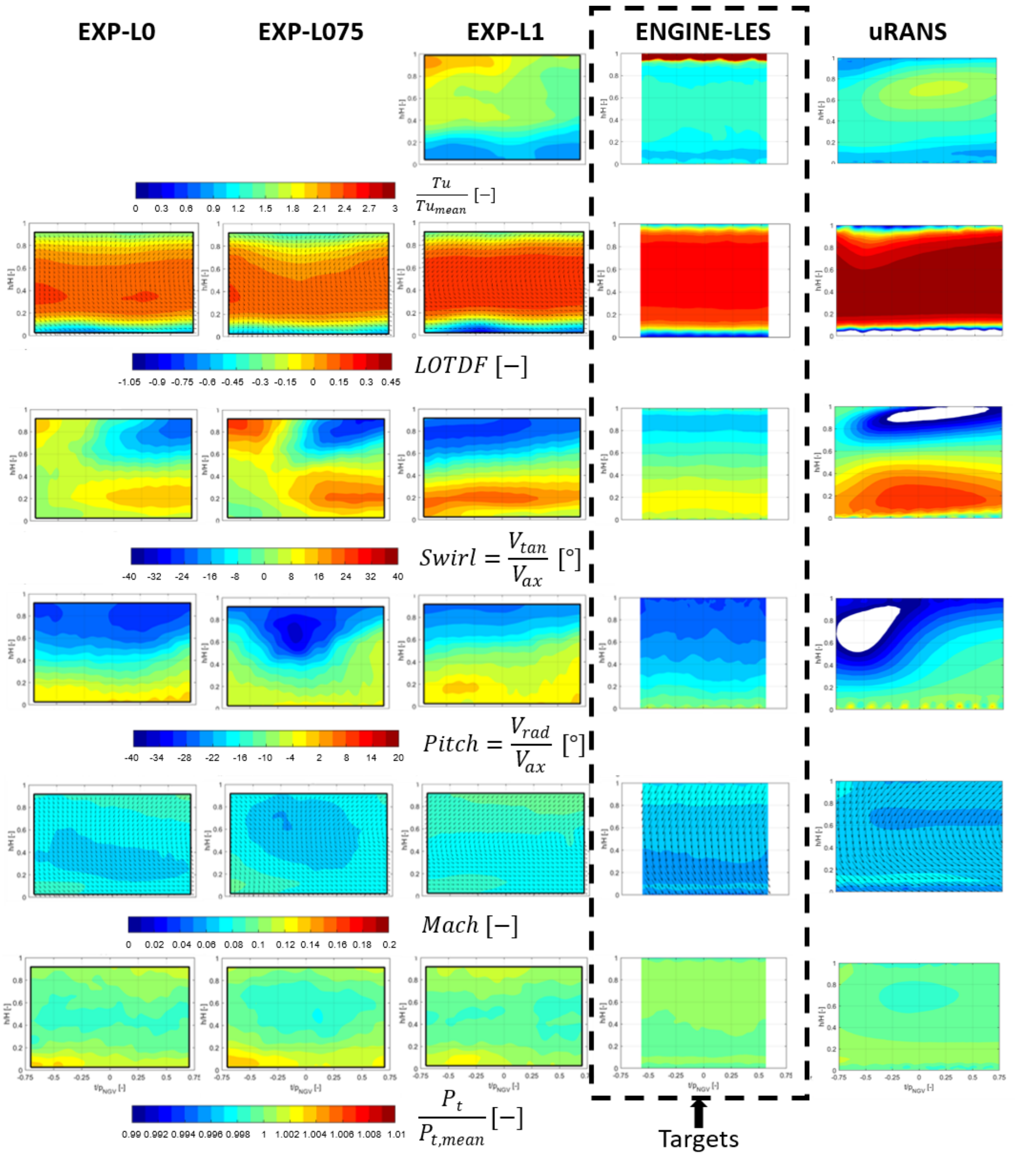

Figure 5.25: *STech* - Comparison of target *ENGINE-LES* vs. *uRANS* vs. experimental Tu/Tu_{mean} *LOTDF*, *Swirl*, *Pitch*, *Mach* and $P_t/P_{t,mean}$ ("L0", "L075", "L1" configurations) at *Plane 40*

to be compared against experiments, although no impact is expected on the definition of macro aerodynamic quantities, as largely shown within the *FACTOR* project.

In addition, the isothermal operating condition was also tested and measurements were taken at *Plane 40* with the five hole probe. This was done in order to verify the actual difference between the two conditions and their related impact on those measure-

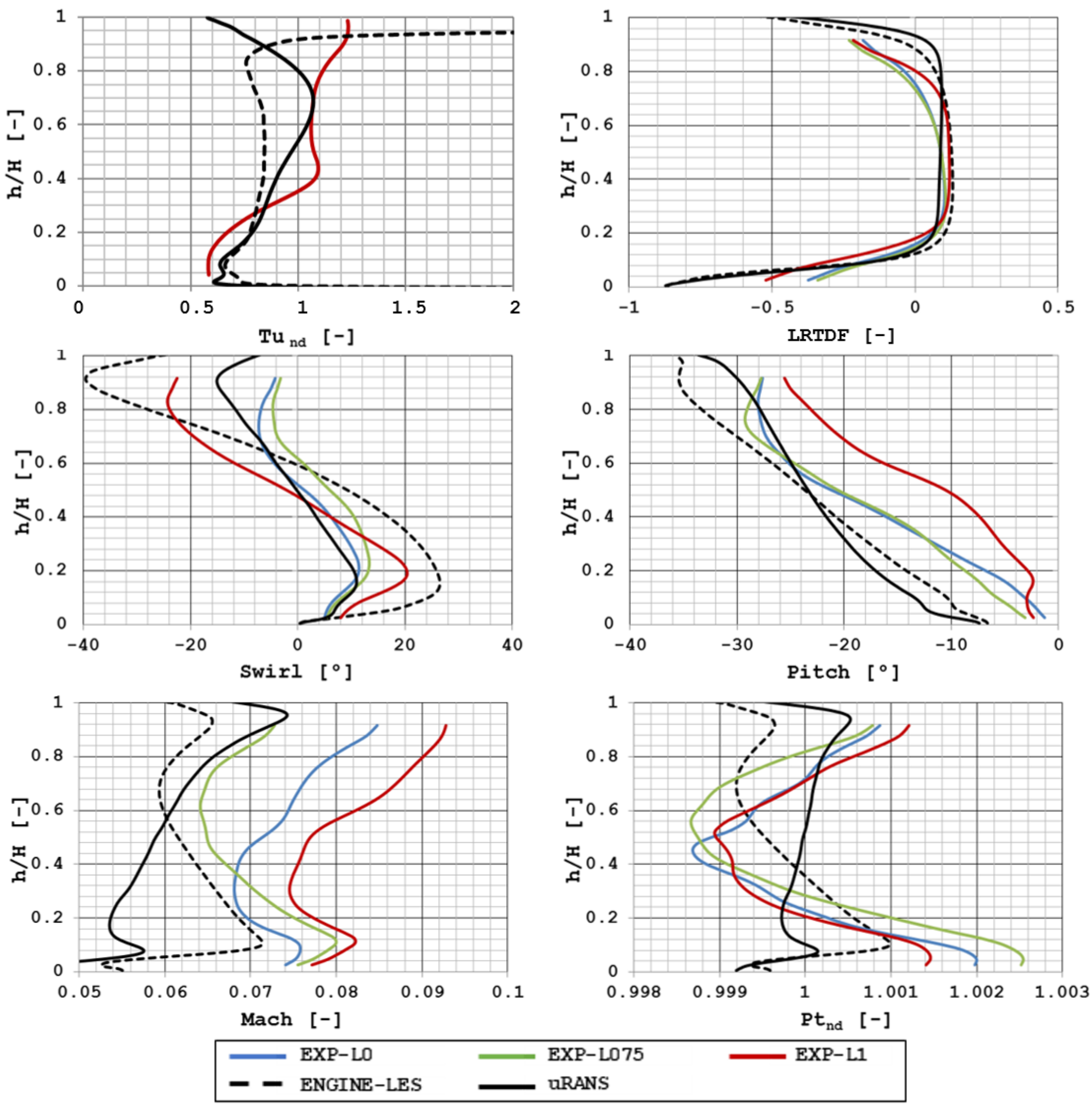

Figure 5.26: *STech* - Comparison of tangentially-averaged target *ENGINE-LES* vs. *uRANS* vs. experimental Tu/Tu_{mean}, *LRTDF*, *Swirl*, *Pitch*, *Mach* and $P_t/P_{t,mean}$ ("L0", "L075", "L1" configurations) at *Plane 40*

ments realisable only at ambient temperature. Fig. 5.27 illustrates the contours of swirl and pitch angles, Mach number and total pressure together with the correspondent tangentially averaged profiles. The plots show some non-negligible difference between the two cases, although they are qualitatively very similar. This enables the treatment of isothermal conditions in place of the nominal configuration without loosing the main flow characteristics.

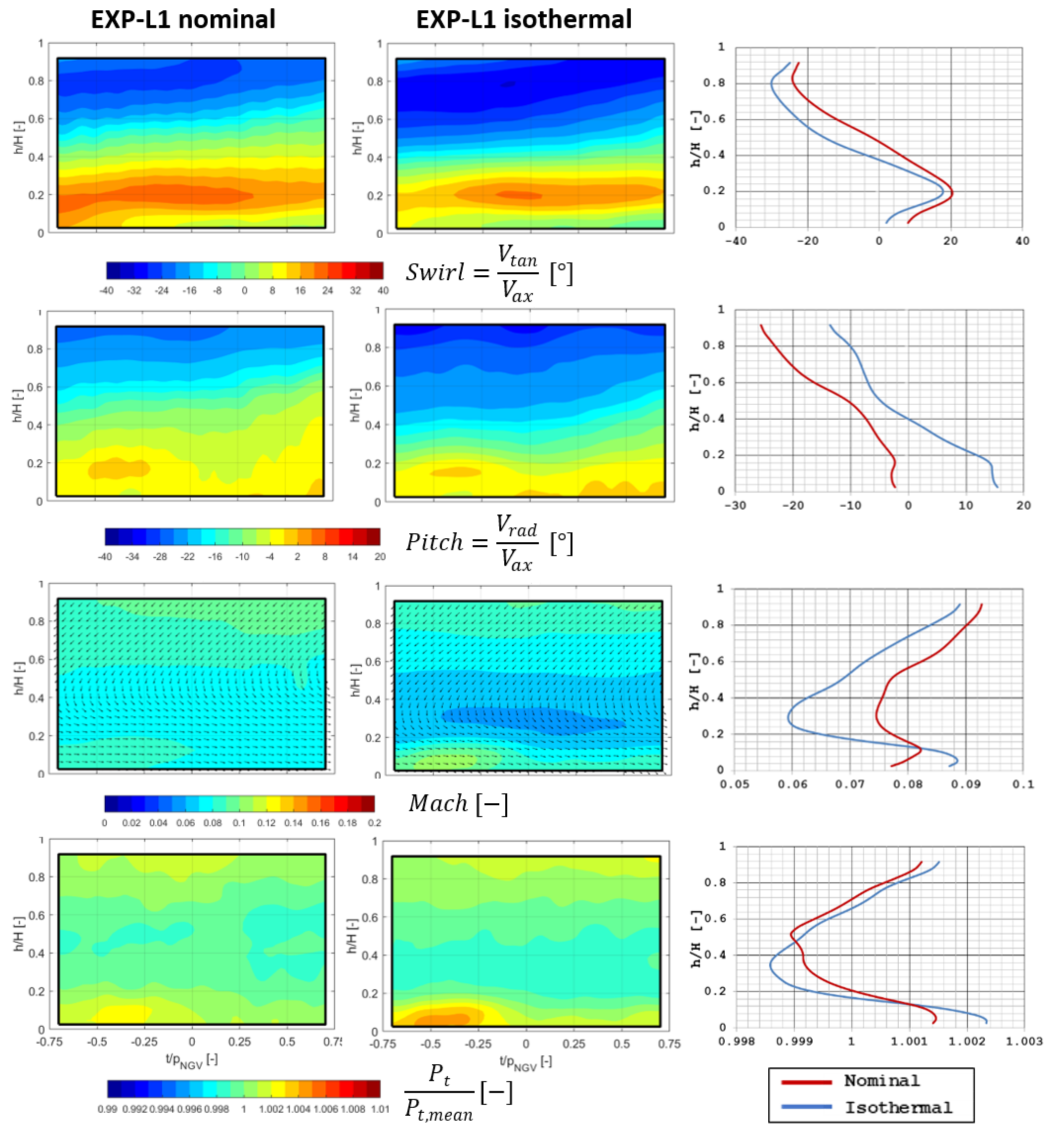

Figure 5.27: *STech* - Comparison of experimental *Swirl*, *Pitch*, *Mach* and $P_t/P_{t,mean}$ at *Plane 40* in nominal and isothermal conditions

5.3.2 Measurements and comparisons at Plane 41

The first measurement to be performed at *Plane 41* was punctual, i.e. a number (5) of local points were picked on the outer endwall of the nozzles module in correspondence of *Plane 41*. This was done with the major purpose of setting up appropriate running conditions to be targeted at any test attempt of the overall campaign, as already mentioned in Section 5.3.1. The measurements at *Plane 41* were of fundamental importance as reference for the actual expansion ratio through the nozzles.

Fig. 5.28 shows the non-dimensionalised values of static pressure as expected by the periodic and the rig *CFD* cases with respect to the measurements on the real hardware in both the nominal and the isothermal (ambient) operating points. Experimental data reveals to be sufficiently close to the periodic conditions also within the lateral passages for the isothermal conditions. The *RANS* model of the nozzles module, on the other hand, is able to roughly catch 4 out of 5 pressure probe readings, although the discrepancy at the 5th probe location is significant, which may be due to a somehow wrong prediction of quasi-sonic flow through the right-hand passage.

Then *Plane 41* was investigated via *HWA* in order to characterise the exit velocity components. Fig. 5.29 shows the comparison between experimental, periodic and rig numerical calculations in terms of swirl and pitch angles in addition to momentum and in isothermal conditions. Experimental results are available for three configurations based on the film-cooling flow rate through the nozzles, i.e.:

- "0x m_{FC}" - No coolant is provided to the nozzles;
- "0.5x m_{FC}" - Half of the nominal coolant flow rate is supplied to the nozzles;
- "1x m_{FC}" - The nozzles' film-cooling flow rate is nominal.

Comparing the related contours, no significant difference is highlighted on the aerodynamic quantities of swirl and pitch angles. On the contrary, some difference is present on the momentum plot, which is directly proportional to flow rate. In fact, for lower or null film-cooling flow rate, the streaks generated by separation at the airfoils' trailing edge are more visible. It is also interesting to notice, thanks to the superimposed vector field, the evolution of the secondary flows, which were isolated by subtracting the average swirl field to the local one, according to the following formula:

$$V_{tan}^{sf} = V_{ax} \cdot (swirl - swirl_{mean}) \tag{5.3}$$

Then, by looking also at the numerical plots, although the same pattern can be observed for each quantity, significant differences are shown, especially on the pitch angle. On the swirl contour the two low angle regions corresponding to the vane passages are identified by the pale blue spots. For what regards the momentum plot, although streaks are less pronounced than in the experimental maps, the secondary flows structures represented by the vector field are well reproduced by *CFD*, clearly showing how the recirculating flow at the nozzles' inlet is to some extent preserved even downstream of the airfoils.

Furthermore, by zooming in the experimental map of momentum for the film-cooling nominal case (see Fig. 5.30), it is possible to identify the inclined streaks

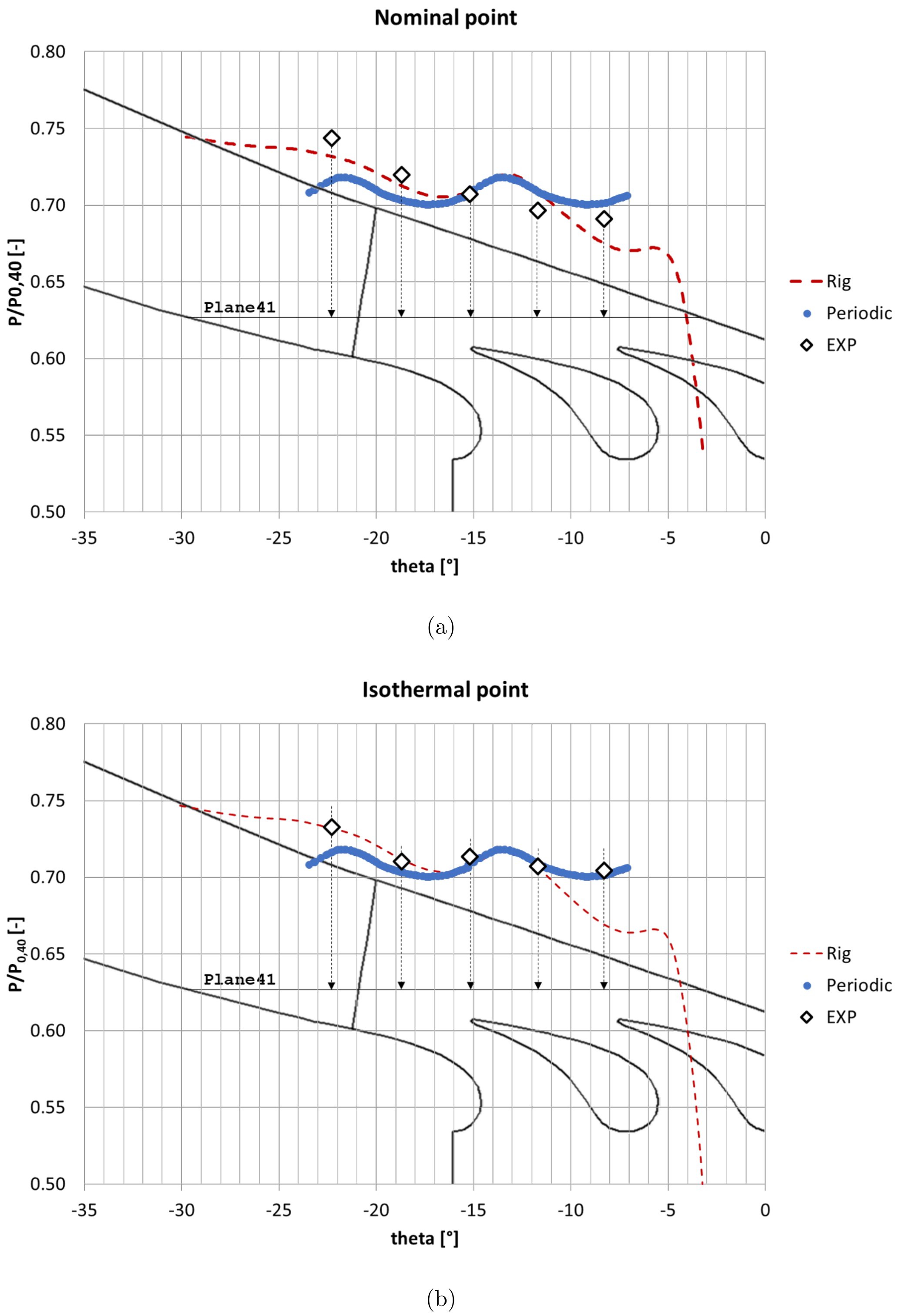

Figure 5.28: *STech* - Static pressure comparison at 5 locations at the *Plane 41* outer endwall for the nominal (a) and the isothermal (b) operating points

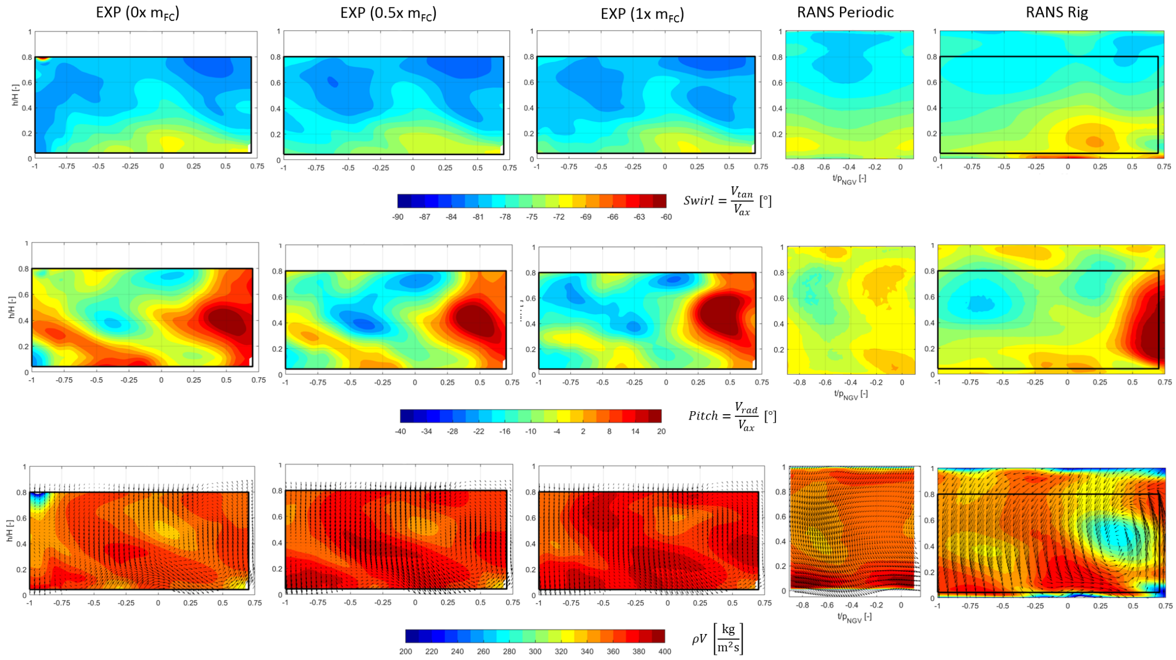

Figure 5.29: *STech* - Comparison of experimental vs. numerical *Swirl*, *Pitch* and ρV at *Plane 41* in isothermal conditions

splitting pressure and suction sides, which are generated by the separation of main flow in correspondence of the airfoils' trailing edge. In addition, it is to be mentioned that one portion of the central sector (top, left-hand side) could not be fully measured due to probe's accessibility issues, which, however, did not compromise the capturing of the swirled secondary flow structures arriving from the combustor. It is also important to notice that some non-physical ascending motion was detected in the upper part of the map, ascribable to the presence of the buttonhole where the probe is inserted, which was therefore removed from the image.

5.3.3 Measurements and comparisons on the airfoils

Film-cooling adiabatic effectiveness measurements were performed via the *PSP* technique, recalling the heat and mass transfer analogy (see Section 3.1.1 for reference). Acquisitions were made through the three optical accesses shown in Fig. 5.31, which also reports a sample of the image dewarping process that allows to link the coordinates associated to every pixel and build the investigated geometry with the contour of film-cooling adiabatic effectiveness.

As mentioned, the first available result out of the *PSP* measure is relative to the pressure distribution over the airfoils surfaces, which is indeed shown in Fig. 5.32, comparing experiments against the numerical predictions relatively to the rig config-

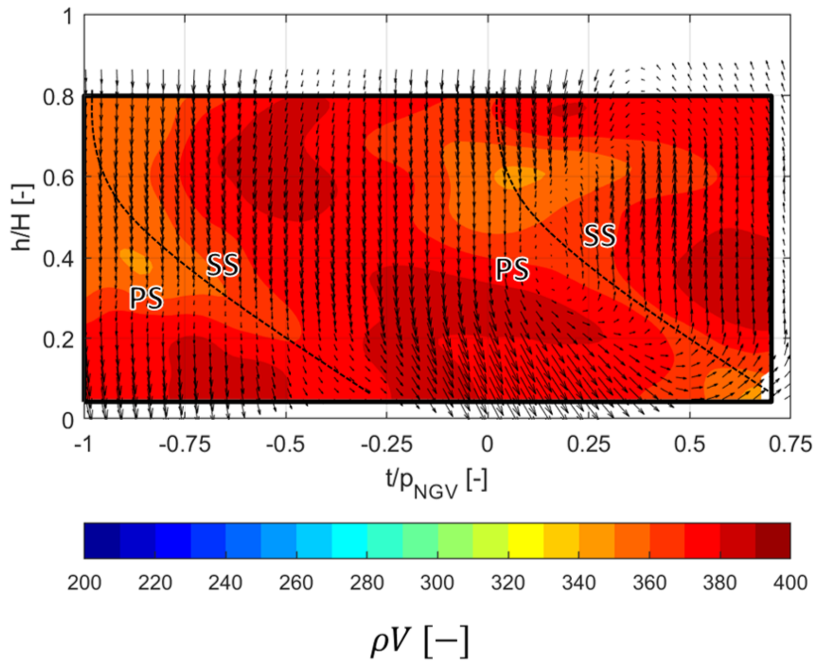

Figure 5.30: *STech* - Momentum contour with superimposed local swirl vectors field at *Plane 41*

uration. It is possible to notice how pressure is predominantly uniform on the initial part of *PS* surface, especially close to the *LE* region (Frame 1), while a lower pressure with a radial-equilibrium induced distribution is present on the *SS* (Frame 3), i.e. an increasing pressure level from low to high radii. The numerically estimated pressure distribution shows some discrepancies with respect to measurements, e.g. lower pressure is predicted at the throat section, yet capturing the proper trend.

The pressure distribution comparison is then extended to the airfoils load, in analogy to what already shown in Fig. 5.21, as illustrated in Fig. 5.33. The *CFD* results relative to the rig configuration satisfactorily match the pressure profiles of both periodic and experimental cases on the *PS* of *NGV2* and the *SS* of *NGV1*. On the contrary a large discrepancy still exists on the *SS* profile of *NGV2*, which needs further investigations.

However, the lack of accuracy of the rig *CFD* can be reasonably ascribed to the imposed inlet boundary conditions, which were derived from a *uRANS* simulation of the combustor domain. These may be inaccurate in estimating the flow split among the three vane passages thus affecting the pressure distribution, since experimental results reveal to be closer to the periodic *CFD* predictions, which nevertheless shows how the rig design fulfills the design requirements.

It is also to be noted how the *PSP* profiles present a non negligible noise value, which is due to the high sensitivity of the measurement technique to the tested con-

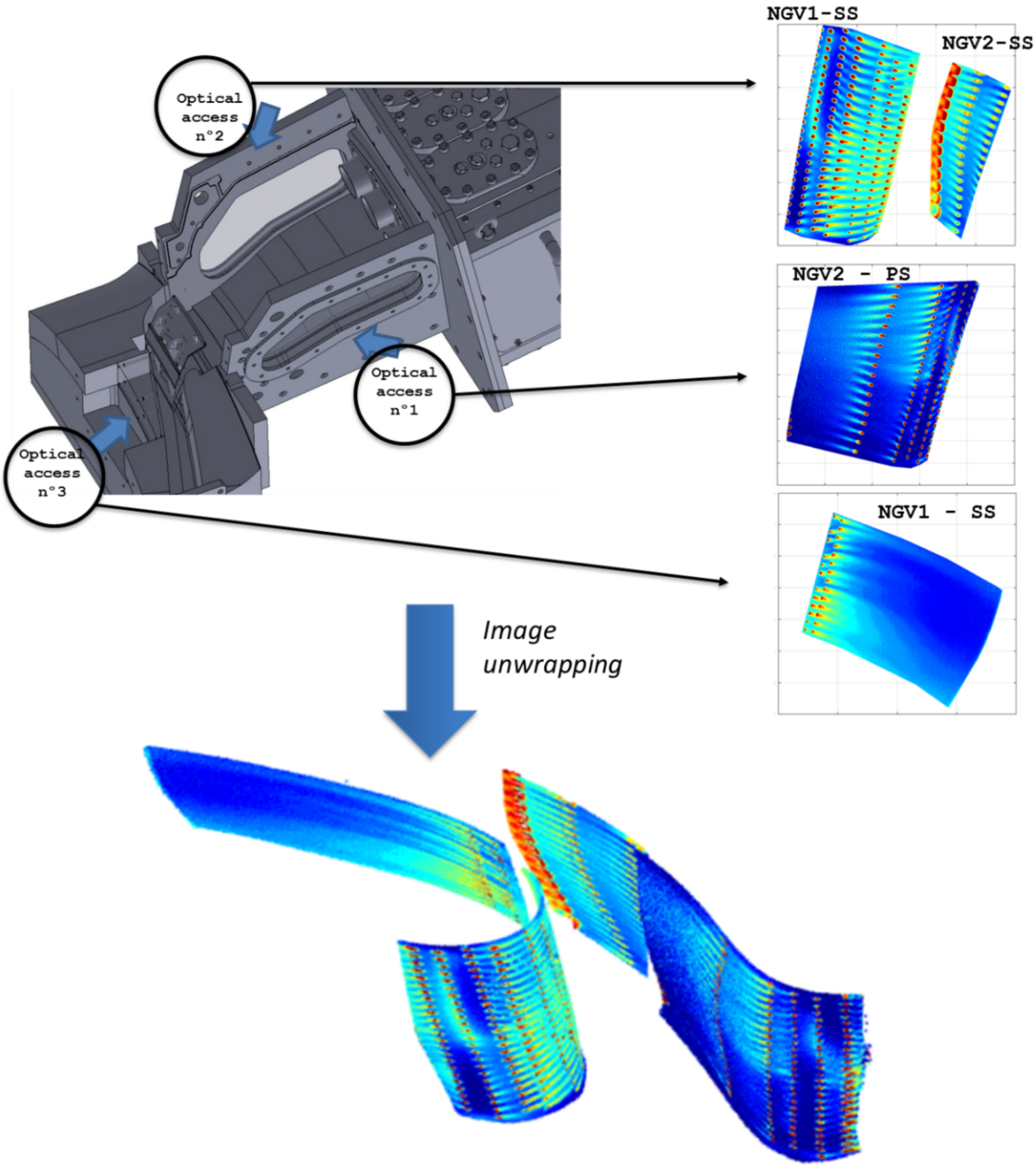

Figure 5.31: *STech* - Test rig optical accesses and *PSP*-obtained adiabatic effectiveness sample results

ditions. Nevertheless, they allow a good estimate of the pressure distribution over the central vane and, in particular, prove that a uniform flow split has been realistically achieved among the passages. This validates the rig design to some extent, as also emphasised by the comparison against the periodic *CFD* run.

Following the pressure distribution, as mentioned, it was also possible to measure the film-cooling adiabatic effectiveness. Therefore the *PSP*-obtained adiabatic effectiveness contours are reported in Fig. 5.34, with three different coolant flow rates. One

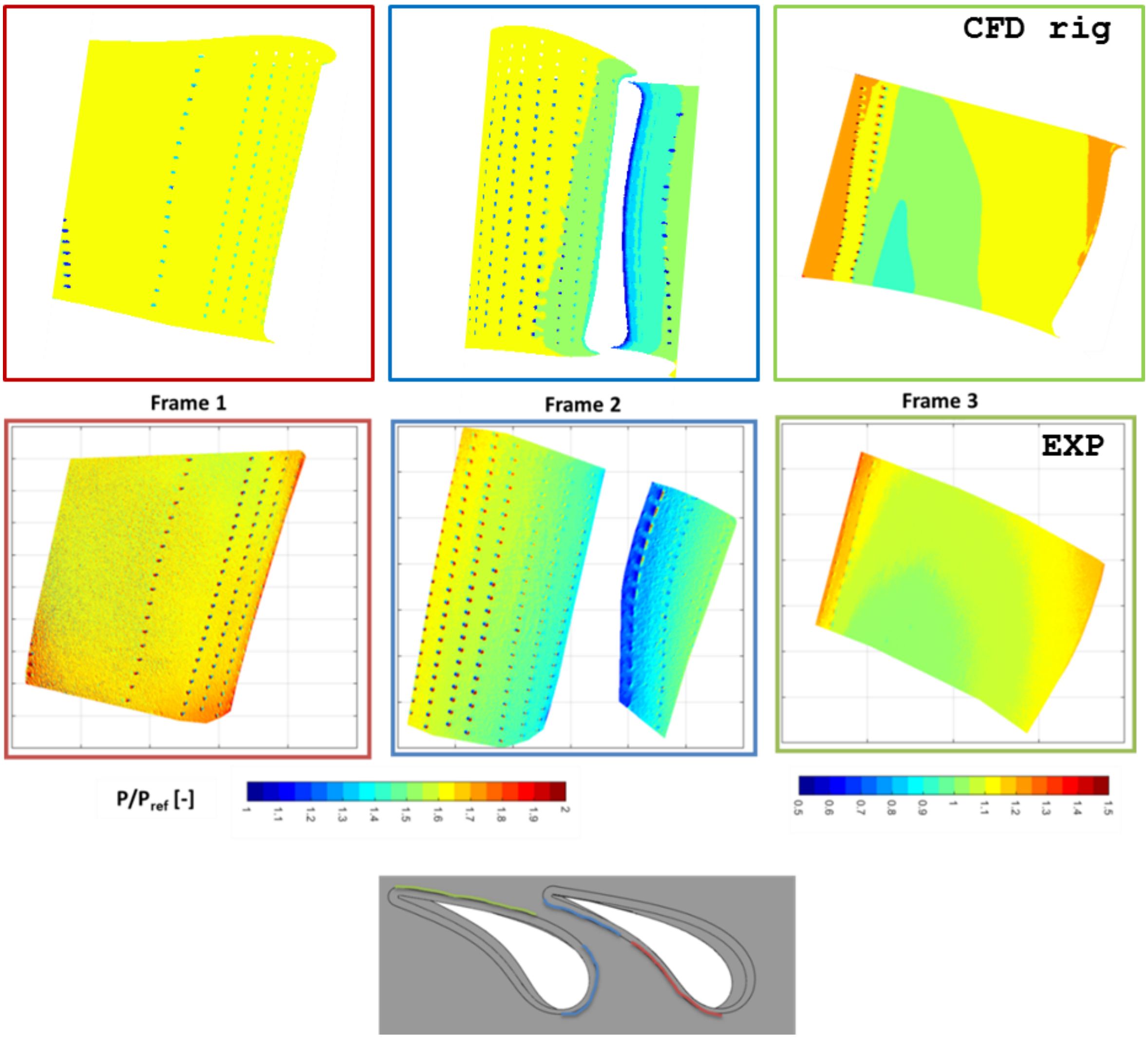

Figure 5.32: *STech* - Comparison of experimental vs. numerical pressure field on the airfoils surfaces

of these represents the nominal case ("1x m_c"), while the other two have lower coolant flows ("0.75x m_c" and "0.5x m_c") as to investigate over different film-cooling regimes (see Section 2.2.2 for reference).

It is to be noted that, in order to protect the *Baker Hughes*' intellectual property, the film-cooling adiabatic effectiveness has been further normalised by a reference value, leading therefore to the quantity η_{ad}/η_{ref}.

It is possible to notice how the coolant flow increase is associated with reduced coolant 'streaks' but also with a larger surface coverage. This is in fact dictated by the film-cooling behaviour that moves towards the penetration regime, i.e. more coolant penetrates the main stream and hence looses its ability to build a film in the vicinity of the hole, yet covering a larger overall region.

Furthermore, the coolant jets on the *PS* surface (see Frame 1) are conveyed to-

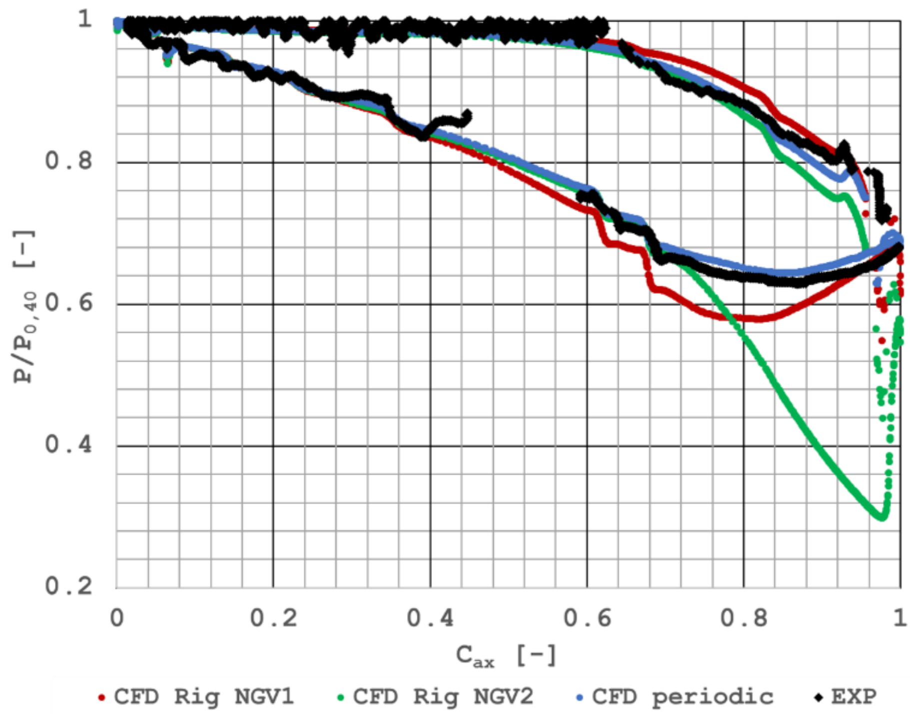

Figure 5.33: *STech* - Comparison of experimental vs. numerical pressure field at the midspan airfoils section

wards the airfoil's midspan, while the regions close to the endwalls are somehow left uncovered, also due to the secondary vortices developing over the airfoil (see Section 2.2.1 for reference). The same behaviour is observed on the *PS* region closer to the *TE* in Frame 2, where also the stagnation line is shown to be deflected on the *LE* from one to another film-cooling row as per the incoming main flow angles, thus leaving some uncovered local regions. Moreover, the *SS* upper half is shown to be barely protected by film-cooling due to the swirled main flow, while coolant is predominantly convected on the lower half (Frame 3).

It is then fundamental to extend the comparison to the periodic and the rig *CFD* simulations, as reported in Fig. 5.35, with reference again to the isothermal condition. Fig. 5.35 also includes the so-called "standard" case ("std"), which represents the commonly adopted industrial design procedure run in engine representative conditions. Similarly to the periodic configuration, the "std" case considers the turbine-only domain with imposed boundary conditions at the inlet: namely uniform average characteristic quantities (total pressure and flow angles) except for temperature, which is the circumferentially-averaged temperature field at the combustor outlet.

It was decided not to include any "std" case results in the previous analyses, since the periodic *CFD* simulation was regarded more appropriate to validate the rig nozzles-

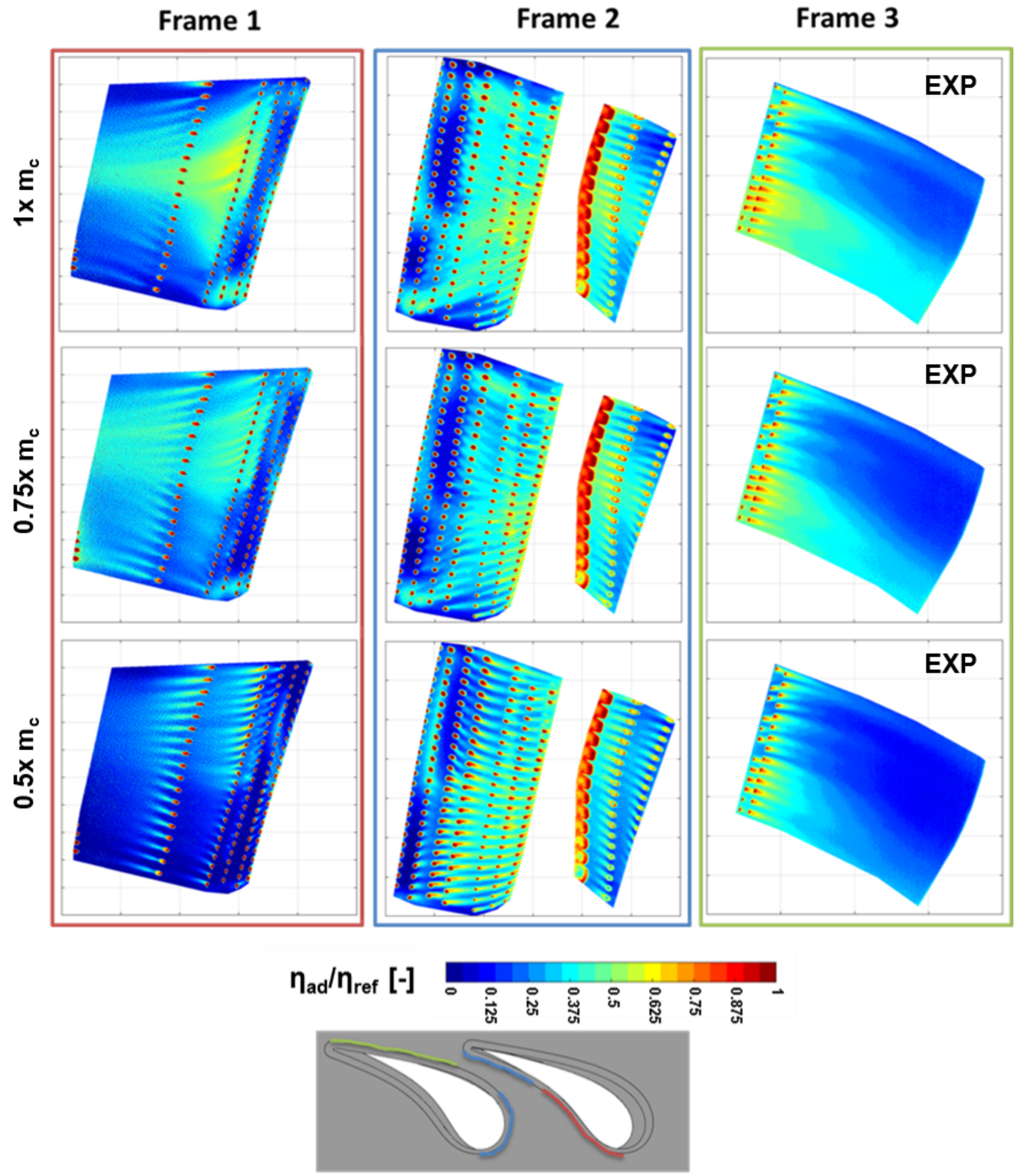

Figure 5.34: *STech* - Experimental film-cooling adiabatic effectiveness on the airfoils surfaces as per different coolant flow rates

module design. This, by contrast to the combustor module, was necessarily affected by the adopted assumptions previously illustrated in this Section. On the contrary, the coolant distribution maps can more clearly reflect the qualitative discrepancies between the different design approaches on a core result objective of the present work, being more related to heat transfer rather than aerodynamics.

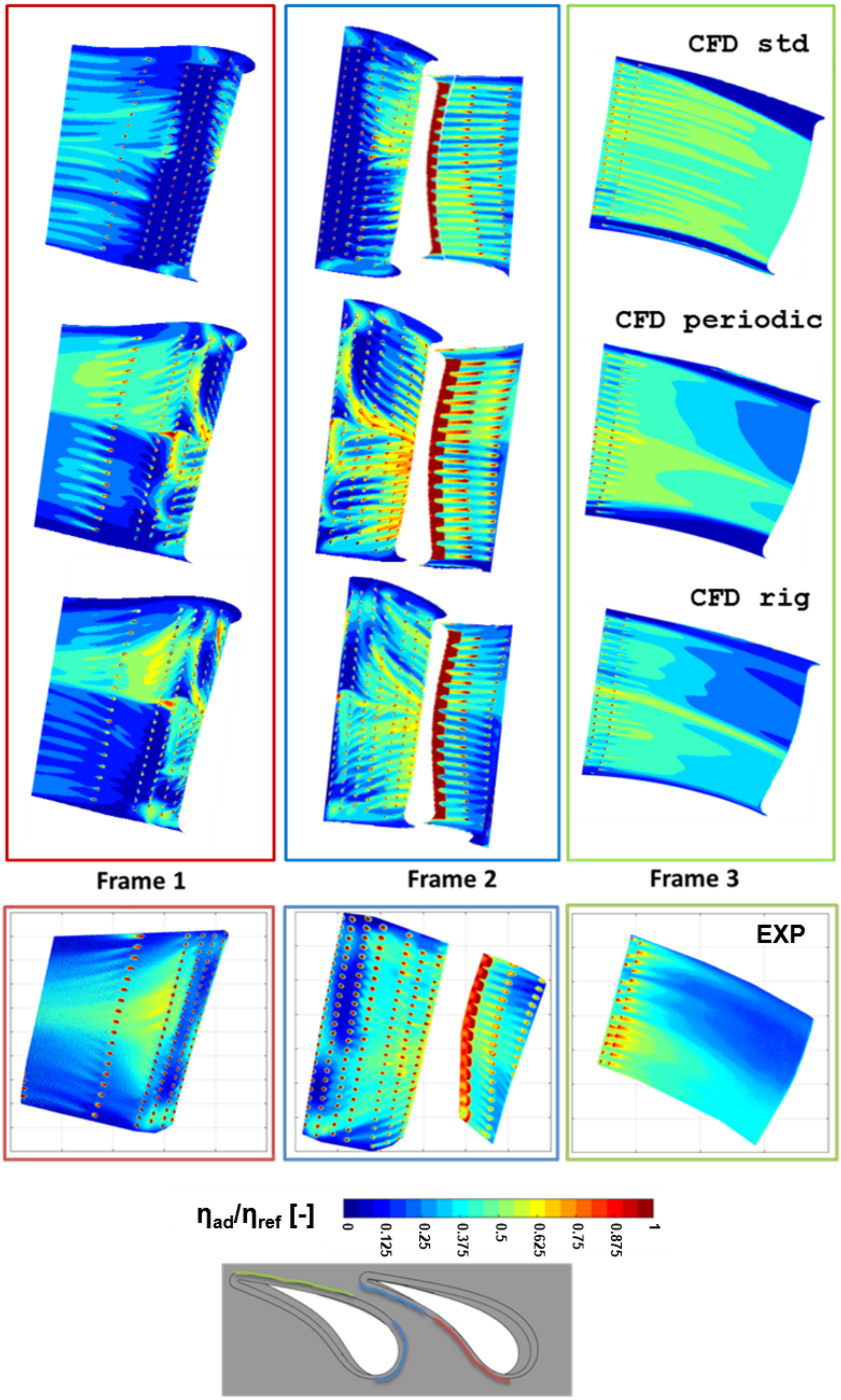

Figure 5.35: *STech* - Comparison of experimental vs. numerical film-cooling adiabatic effectiveness on the airfoils surfaces

Similar considerations to what already discussed relatively to Fig. 5.34 apply. Moreover it can be noticed that the rig *CFD* is the one to provide closer results to experimental measurements (only the "$1x\ m_c$" condition is herein reported). In particular, although non negligible differences are yet present between the rig *CFD* and experiments due to the adopted *RANS* modelling, the predicted coolant distribution sufficiently resembles the measured coverage both on the *PS* and the *SS* surfaces.

In fact, in the first part of the *PS* (Frame 1) the rig *CFD* is able to capture the coolant deflection due to the highly swirled inlet flow, which occurs only with a lower intensity in the periodic *CFD*, whereas is totally absent in the "std" case. This shows the impact of the full 2D inlet *BCs* specification in contrast to circumferentially averaged or uniform quantities. A similar behaviour is observed at the *LE* and the final part of the *PS*, even if it is to be recognised that none of the simulation cases is able to accurately reproduce the measured stagnation line.

Analysing the experimental maps on the *SS* surface, there is only a small appreciable corner vortex building up from the upper endwall over the airfoil, since the coolant distribution is again majorly dictated by the swirled main flow, which causes a remarkably different coverage over either the upper- or lower-half regions. In fact, while the lower half looks to be well protected by coolant, this is by contrast nearly missing over the whole upper one. This is qualitatively replicated in a better way by the numerical simulation over the rig rather than the periodic domain, since again the inlet *BCs* are more accurate. Once more and even at a larger extent, the "std" simulation does not capture any of the above, predicting an overly protected *SS* surface, which could be highly misleading during the thermal design of the component.

5.4 Concluding remarks

At last, a brief summary relative to the activities carried out within the *STech* programme can be drawn together with some preliminary conclusions and future perspectives. The design of a warm rig for the investigation of combustor-turbine interaction has been performed, on the basis of the experience gained during the previously conducted *FACTOR* project, in order to transfer both numerical and experimental practices from the aeronautic to the industrial technology field. The first objective of this programme was to design the rig from an aerodynamic perspective, respecting the flow field macroscopic features of the reference engine conditions, which are leveraged from *CFD* analyses and results available at *Baker Hughes* and based on the datamatch of tested performance of the heavy-duty gas turbine object of this study.

Engine conditions were scaled based on the Mach similitude, while the Reynolds number could not be fully achieved due to limitations in the plant hosting the test rig. However, temperature, velocity and turbulence intensity characteristics were reproduced within the rig also thanks to the implementation of some small modifications needed to compensate for the non-reactive nature of the combustor simulator, to allocate the required instrumentation and to ensure the quasi-periodicity of the central sector, i.e. in correspondence of the central vane passage. *uRANS* and *RANS* simulations were separately conducted on respectively the combustor and nozzles domains, in line with the conclusions drawn in the *FACTOR* project (see Section 4.4). However, although acceptable results were obtained in both combustor and nozzles modules, non negligible differences can be highlighted when comparing experimental results at both *Plane 40* and *41*.

A comparison of the film-cooling adiabatic effectiveness has also been performed between experimental and numerical results, which shows how the *CFD* simulation performed on the rig geometry resembles measurements in a better way than those carried out on the periodic domain either with rig or engine-like conditions, even though non negligible differences are noticeable. Moreover, the commonly employed design procedure largely fails in predicting the coolant distribution due to the hypothesis of uniform velocity inlet field, whereas the periodic case (rig conditions) delivers similar yet less accurate results than the rig configuration.

For these reasons, and recalling the *FACTOR* analyses, it is planned to continue the numerical activity by simulating the combined domain of combustor and turbine via Scale-Adaptive Simulation as to better capture unsteadiness and hence the combustor outlet flow field, in addition to transport fluctuations down in the stator vane passages. This will allow to study their related impacts on the airfoils aerothermal performance, which will bring to light any effective gap in the industrial aerothermal design practices.

Furthermore, it is to be added that the experimental phase is still ongoing at the time this thesis is being prepared. In fact, as shown in Table 3.2, the heat transfer coefficient is going to be measured via infrared thermography and transient technique, completing the investigation over the nozzles aerothermal behaviour and bringing also some added value with respect to the *FACTOR* test campaign.

Chapter 6

Conclusions

In this work the subject of combustor-turbine interaction has been investigated, with special focus on establishing suitable numerical methodology and strategy as to properly study the impact of the predicted turbine inlet conditions on the *NGVs* aerothermal performance. The activities were conducted in relation to the test campaigns of two non-reactive rigs, which were assembled at the *University of Florence*, Italy. The rigs, both composed of a lean combustor and a first stage film-cooled nozzles cascade, were operated in similitude conditions to mimic an aero-engine and an industrial gas-turbine arrangements. The rigs were designed to reproduce the real engine periodic flow field on the central sector, allowing also for *CFD*-friendly measurements to enable comparisons between numerical and experimental results. The periodicity condition at the central sector was enforced in both cases by the installation of circular ducts at the injectors outlet section as to preserve the non-reactive swirling flow down to the nozzles inlet plane.

The aero-engine simulator rig was developed within the European project *FACTOR* (Full Aerothermal Combustor-Turbine interactiOn Research) that has also been the context of two previous PhD works, focused on the conducted experimental campaigns, of which the present is a continuation. During such works the flow field within the combustion chamber was investigated via particle-image velocimetry (*PIV*) and velocity, pressure and turbulence fields at both turbine inlet and outlet sections were experimentally characterised by means of a five-hole pressure plus thermocouple probe and hot-wire anemometers, mounted on an automatic traverse system. Lastly, the film-cooling adiabatic effectiveness distribution over the airfoils was evaluated via coolant concentration measurements based on pressure sensitive paints (*PSP*) application.

Based on this, numerical analyses were carried out in order to review the turbine standard design practices. In fact, since the design of industrial high-pressure turbines historically relies on 1D, circumferentially-averaged profiles of pressure, velocity and temperature at the combustor/turbine interface in conjunction with Reynolds-averaged Navier-Stokes (RANS) models, this thesis describes how measurements can be leveraged to improve numerical modelling procedures.

For such purpose the nozzle guide vanes were first studied with a standard industrial approach, i.e. with a *RANS* modelling approach and turbine inlet aero-thermal conditions derived from the *CFD* analysis of the combustor alone. In particular, the considered combustor exit conditions were obtained from both *RANS* and Scale-adaptive simulation (*SAS*). Eventually an integrated combustor-turbine domain was created and simulated through the *SAS* technique, since the investigation of the two components within the same integrated simulation enables the transport of unsteady fluctuations from the combustor down to the first stage nozzles, with the aim of improving the accuracy of the simulation.

These strategies were first compared in terms of flow and temperature fields at the *NGVs* exit as well as adiabatic wall temperature on the airfoils. The flow field showed little sensitivity to the chosen approach, suggesting that simulating with scale-resolving models the combustor alone or in combination with the *NGV* is not worth the additional effort if the focus is just aerodynamics. Different conclusions are drawn in case the radial temperature profile at the nozzles exit or heat transfer are of paramount importance. In such scenario providing more accurate inlet conditions through *SAS* can strongly improve the prediction.

Moreover, providing inlet conditions with *RANS* appeared to be very dangerous in a design perspective, since, if compared to *SAS*, it may provide local errors in the adiabatic wall temperature estimation exceeding 100 K for uncooled vanes and 150 K when film cooling is accounted for. However, only an integrated approach considering both combustor and turbine can successfully take into account the effect of flow unsteadiness on turbulent mixing. This strategy provided a reduced misestimation on radial temperature profile at the *NGVs* exit by up to 50-70% and a more accurate reproduction of the coolant distribution on the airfoils. Similarly, also the heat transfer coefficient appears more reliable, even if an experimental validation would have given a higher degree of confidence.

An additional comparison against uniform velocity/temperature conditions at the inlet has been provided, confirming that the presence of a non-uniform swirl/temperature pattern exacerbates the intensity of the heat loads, both in terms of adiabatic wall temperature and heat transfer coefficient. This indicates once again that integrated approaches based on high-fidelity *CFD* are highly recommended for the estimation of thermal conditions in order to ensure an adequate lifespan without waste of coolant.

The experience gained in the aeronautical field within the *FACTOR* project was then exploited and transferred to the industrial sector, which was made possible through the *STech* programme. Within *STech* a second non-reactive combustor/turbine interaction rig was realised, including a real lean-premix combustor and a real high-pressure first-stage nozzle sector of a gas turbine in the *Baker Hughes* (formerly *GE Oil & Gas*) portfolio. In order to verify the goodness of the original design and to find possible improvements eligible for future versions of the same engine or, in general, for new products, basically the same measurements campaign of *FACTOR* has been scheduled, except for *PIV*.

As the project is still ongoing at the time this manuscript is being written, only the design phase and some preliminary measurements and numerical results could be included. The warm rig design was based on the objective of replicating the main flow features of the selected combustor, which led to the identification of some non-dimensionalised parameters of interest, to be matched at the combustor/turbine interface plane, i.e.: temperature, velocity components and turbulence intensity. These targets were set on the basis of a Large-eddy simulation of one combustor sector in engine operating (reactive) conditions, representative of the gas turbine full load. The rig design was therefore scaled to match the Mach number at the sections of interest (combustor/turbine interface and nozzles exit), while Reynolds similitude could not be achieved due to the limitations in flow rate and pressure as available in the plant. The aerodynamic design of the nozzles module was then based on inlet boundary conditions derived by *uRANS*, since, as shown in *FACTOR*, this proved to be sufficient for the purpose.

Experimental results obtained through five-hole pressure probe and hot wire anemometry measurements have confirmed the different behaviour of the same swirler geometry if operated in non-reactive conditions, requiring the installation of ducts at the injectors exit in order to preserve the swirling motion of flow further downstream and to ensure the periodicity condition at the central sector. On the other hand, the nozzles' outlet plane has been investigated via hot wire anemometry and a discrete number of pressure probes, showing that some better numerical representation of the flow through all the vane passages is needed to be achieved to correctly reproduce experimental data.

In addition, the film-cooling adiabatic effectiveness was measured on the test rig by means of the pressure sensitive paint (*PSP*) method, as previously mentioned. Results show that the swirled inflow has a noticeable impact on the coolant coverage over the airfoils, since it is able to deflect the coolant away from the intended region leaving parts of the airfoils barely protected. Moreover, non negligible differences have also been observed between the herein presented analyses and the commonly-adopted industrial design procedure, which further emphasises the need for a joint analysis of combustor and first stage nozzles, especially when focusing on thermal design.

Future measurements will include also the external heat transfer coefficient through infrared thermography and transient technique, which will allow for a more complete characterisation of the whole combustor/turbine system and probably be subject of future publications.

In conclusion, this work gives an overview of the possible design choices available for studying combustor/turbine interaction and the possible lack-of-accuracy areas. In fact, standard design practices are challenged based on the definition of inlet boundary conditions, analysis domain and methodology. In fact, results show that integrated simulations of combustor and turbine even via hybrid scale-resolving techniques, such as Scale-adaptive simulation (SAS), can suit the purpose, whilst containing computational costs, since the transport of unsteady fluctuations from the combustor down to the first stage nozzles is ensured, which highly improves predictions when studying thermal aspects and in the presence of film cooling.

The *FACTOR* (Full Aerothermal Combustor-Turbine interactiOns Research) Consortium is thankfully acknowledged for allowing the herein reported results to be published. *FACTOR* is a collaborative project co-funded by the European Commission within the Seventh Framework Programme (2010-2016) under the Grant Agreement n° 265985.

With the same thankfulness, *Regione Toscana* and the industrial partner *Baker Hughes* are acknowledged for the possibility of publishing the presented results relatively to the *STech* programme. *Regione Toscana* is co-funder and *Baker Hughes* is the coordinator partner of the *STech* Smart Technologies programme 2017-2019 (FAR-FAS 2014 public notice).

Bibliography

[1] Virginia Tech Wadley Research Group. High temperature coatings. *Available @ https://www2.virginia.edu/ms/research/wadley/high-temp.html*, 2013. ix, 2

[2] D. Ballal and J. Zelina. Progress in aeroengine technology (1939-2003). *Journal of Aircraft*, 41:43–50, 2004. ix, 2

[3] International Air Transport Association. Press release n° 57. Technical report, October 2014. 3

[4] Advisory Council for Aeronautics Research in Europe. Strategic research agenda. Technical report, ACARE, 2000. 3

[5] Advisory Council for Aeronautics Research in Europe. Strategic research and innovation agenda. Technical report, ACARE, 2017. 3

[6] European Energy Agency. Greening the power sector: benefits of an ambitious implementation of europe's environment and climate policies. *Available @ https://www.eea.europa.eu/themes/industry/industrial-pollution-in-europe/benefits-of-an-ambitious-implementation*, 2018. 3

[7] A.H. Lefebvre and D.R. Ballal. *Gas Turbine Combustion*. Taylor & Francis, 2010. ix, 4, 5, 12, 13

[8] Y. Huang and V. Yang. Dynamics and stability of lean-premixed swirl-stabilized combustion. *Progress in Energy and Combustion Science*, 5(4):293–364, 2009. ix, 5, 12, 14, 15, 20

[9] A. Innocenti. Numerical analysis of the dynamic response of practical gaseous and liquid fuelled flames for heavy-duty and aero-engine gas turbines. *PhD thesis, University of Florence*, 2015. ix, 7

[10] T.C. Lieuwen and V. Yang. *Gas Turbine Emissions*. Cambridge University Press, 2013. 8

[11] R.G. McKinney, D. Sepulveda, W. Sowa, and A.K. Cheung. The Pratt & Whitney TALON X low emissions combustor: revolutionary results with evolutionary technology. *AIAA Journal, the 45th AIAA Aerospace Sciences Meeting*, 386, 2007. 8

[12] S.M. Correa. Carbon monoxide emissions in lean premixed combustion. *Journal of Propulsion and Power*, 8(6):1144–1151, 1992. 9

[13] R. Banck, C. Berat, M. Cazales, and S. Hardling. Organisation of european aeronautic ultra-low NO_x combustion research. *25TH INTERNATIONAL CONGRESS OF THE AERONAUTICAL SCIENCES*, 2006. 9

[14] General Electric. Taps II combustor
final report - continuous lower energy, emissions and noise (CLEEN) program. Technical report, Federal Aviation Administration, 2013. ix, 10

[15] C.L. Ford, J.F. Carrotte, and A.D. Walker. The impact of compressor exit conditions on fuel injector flows. *Journal of Engineering for Gas Turbines and Power*, 134:111504–111504, 2012. doi: 10.2514/3.11455. ix, 10

[16] D. Dunn-Rankin. Lean combustion: technology and control. *Academic Press*, 2011. 12

[17] Y. Ohkubo. Low-nox combustion technology. *Target*, 20(35), 2005. 12

[18] G. Ceccherini and R. Modi. Gas turbine combustion. *Technical report, GE Oil & Gas*, 2013. ix, 13, 14

[19] L.B. Davis and S.H. Black. Dry Low NOx combustion systems for GE heavy duty gas turbine. *GER-3568G document, GE Power Systems, Schenectady NY*, 2000. 13

[20] G. Caciolli. A close investigation on the aerothermal behaviour of modern aero-engine combustors. *PhD thesis, University of Florence*, 2014. 16, 53, 54

[21] T. Bacci. Experimental investigation on a high pressure ngv cascade in the presence of a representative lean burn aero-engine combustor outflow. *PhD thesis, University of Florence*, 2017. 16, 58

[22] C. Koupper. Unsteady multi-component simulations dedicated to the impact of the combustion chamber on the turbine of aeronautical gas turbines. *PhD thesis, Institut National Polytechnique de Toulouse*, 2015. ix, xi, 20, 45, 48, 93

[23] B.F. Hall, K.S. Chana, and T. Povey. Design of a non reacting combustor simulator with swirl and temperature distortion with experimental validation. *Proc. ASME Turbo Expo*, (GT2013-95499), 2013. 20, 21, 40

[24] A Andreini, B. Facchini, R. Becchi, A. Picchi., and F.Turrini. Effect of slot injection and effusion array on the liner heat transfer coefficient of a scaled lean-burn combustor with representative swirling flow. *J. Eng. Gas Turbines Power*, 138(4):041501-041501-10, 2015. doi: 10.1115/1.4031434. 21

[25] A Andreini, B. Facchini, L. Mazzei, R. Becchi, A. Picchi., and F.Turrini. Adiabatic effectiveness and flow field measurements in a realistic effusion cooled lean burn combustor. *J. Eng. Gas Turbines Power*, 38(3):031506-031506-11, 2015. doi: 10.1115/1.4031309. 21

[26] A. Andreini, R. Becchi, B. Facchini, L. Mazzei, A. Picchi, and A. Peschiulli. Effusion cooling system optimization for modern lean burn combustor. *ASME Conference Proceedings*, GT2016-57721, 2016. doi: 10.1115/GT2016-57721. 21

[27] M. Berrino, F. Satta, M. Ubaldi, P. Zunino, S. Colantuoni, and P. Di Martino. Experimental characterization of the flow-field downstream of an innovative ultra low nox injection system. *ASME Conference Proceedings*, (GT2014-25459), 2014. 21

[28] M. Berrino, D. Legnani, F. Satta, M. Ubaldi, P. Zunino, S. Colantuoni, and P. Di Martino. Investigation of the dynamics of an ultra low NO_x injection system by pod data post-processing. *ASME Conference Proceedings*, (GT2015-42638), 2015. 21

[29] S. Wang, V. Yang, G. Hsiao, S. Hsieh, and C. Mogiah. Large eddy simulations of gas-turbine swirl injector flow dynamics. *J. Fluid Mech*, 583:99, 2007. 21

[30] S. Roux, G. Lartigue, and T. Poinsot. Studies of mean and unsteady flow in a swirled combustor using experiments, acoustic analysis, and large eddy simulations. *Combustion and Flame*, 141(1-2):40–54, 2005. 21

[31] L. Selle, G. Lartigue, and T. Poinsot. Compressible large eddy simulation of turbulent combustion in complex geometry on unstructured meshes. *Combustion and Flame*, 137(4):489–505, 2004. 21

[32] M. Kern, S. Marinov, P. Habisreuther, N. Zarzalis, A. Peschiulli, and F. Turrini. Characteristics of an ultra-lean swirl combustor flow by LES and comparison to measurements. *ASME Conference Proceedings*, GT2011(45300), 2011. 21

[33] S. Marinov, M. Kern, K. Merkle, N. Zarzalis, A. Peschiulli, and F. Turrini. On swirl stabilized flame characteristics near the weak extinction limit. *ASME Conference Proceedings*, GT2010(22335), 2010. 21

[34] T. Povey, K.S. Chana, T.V. Jones, and H. Hurrion. The effect of hotstreaks on HP vane surface and endwall heat transfer: An experimental and numerical study. *ASME J. Turbomach.*, 129, 2007. ix, 21, 22

[35] C.M. Cha, S. Hong, P.T. Ireland, P. Denman, and V. Savarianandam. Experimental and numerical investigation of combustor-turbine interaction using an isothermal, nonreacting tracer. *J. Eng. Gas Turb. Power*, 134, 2012. ix, 21, 22, 25, 26

[36] T. Povey, A. Beretta, and I. Qureshi. Effect of simulated combustor temperature nonuniformity on hp vane and end wall heat transfer: An experimental and computational investigation. *J. Eng. Gas Turbines Power*, (031901-1), 2011. ix, x, 22, 23, 24, 25, 40

[37] T. Povey and I. Qureshi. Developments in hot-streak simulators for turbine testing. *ASME J. Turbomach.*, 131(3):031009–031009, 2009. ISSN 0889-504X. 22, 23

[38] M.D. Barringer, K.A. Thole, and M.D. Polanka. An experimental study of combustor exit profile shapes on endwall heat transfer in high pressure turbine vanes. *Proc. ASME Turbo Expo*, (GT2007-27156), 2007. 25

[39] W.F. Colban, A.T. Lethander, and K.A. Thole. Combustor turbine interface studies - part 2: flow and thermal field measurements. *Journal of Turbomachinery*, 2003. 25

[40] S. Nasir, J.S. Carullo, W.F. Ng, K.A. Thole, H. Wu, L.J. Zhang, and H.K. Moon. Effects of large scale high freestream turbulence and exit Reynolds number on turbine vane heat transfer in a transonic cascade. *ASME J. Turbomach.*, 131: 021021–021021, 2009. 25

[41] M.D. Barringer, K.A. Thole, and M.D. Polanka. Effects of combustor exit profiles on vane aerodynamic loading and heat transfer in a high pressure turbine. *ASME J. Turbomach.*, 131(2):021008–021008, 2009. ISSN 0889-504X. 25

[42] S. Jenkins, K. Varadarajan, and D.G. Bogard. The effects of high mainstream turbulence and turbine vane film cooling on the dispersion of a simulated hot streak. *ASME J. Turbomach.*, 126(1):203–211, 2004. 25

[43] S.C. Jenkins and D.G. Bogard. Superposition predictions of the reduction of hot streaks by coolant from a film-cooled guide vane. *ASME J. Turbomach.*, 131(4): 041002–041002, 2009. ISSN 0889-504X. x, 25, 37, 38

[44] C.M. Cha, P.T. Ireland, P.A. Denman, and V. Savarianandam. Turbulence levels are high at the combustor-turbine interface. *ASME Conference Proceedings*, (GT2012-69130), 2012. 26

[45] P. Ligrani. Aerodynamic losses in turbines with and without film cooling, as influenced by mainstream turbulence, surface roughness, airfoil shape, and mach number. *International Journal of Rotating Machinery*, (957421), 2012. doi: http://dx.doi.org/10.1155/2012/957421. 27, 29

[46] D.G. Ainley and G.C.R. Mathieson. An examination of the flow and pressure losses in blade rows of axial-flow turbines. Technical report, Aeronautical Research Council Reports and Memoranda, 1955. 27

[47] J.H. Horlock. Losses and efficiencies in axial-flow turbines. *Int. J. Mech. 8ci. Pergamon Press*, 2:48–75, 1959. 27

[48] O. Zweifel. *The Spacing of Turbo-Machine Blading Especially with Large Angular Deflection*. Brown Boveri Review, 1945. 27

[49] B. Lakshminarayana and J.H. Horlock. Review: secondary flows and losses in cascade and axial flow turbomachines. *Int. J. Mech. 8ci. Pergamon Press*, 5: 287–307, 1962. 27

[50] L.S. Langston. Secondary flows in turbines - a review. *Ann. N.Y. Acad. Sci.*, 934:11–26, 2001. 27, 28

[51] I. Qureshi, A. Smith, and T. Povey. HP vane aerodynamics and heat transfer in the presence of aggressive inlet swirl. *ASME J. Turbomach.*, 135(2):021040–021040, 2012. ISSN 0889-504X. 28, 40

[52] J. P. Bouchez and R. J. Goldstein. Impingement cooling from a circular jet in a cross flow. *Int. J. Heat Mass Transfer*, 18:719–730, 1975. x, 28

[53] J. Han, S. Dutta, and S. Ekkad. *Gas Turbine Heat Transfer and Cooling Technology*, pages 129–249. Taylor & Francis, 2000. x, 29, 30

[54] M.R. L'Ecuyer and F.O. Soechting. A model for correlating flat plate film cooling effectiveness for rows of round holes. In *AGARD Heat Transfer and Cooling in Gas Turbines 12p (SEE N86-29823 21-07)*. 1985. 30, 55

[55] D.R. Pedersen, E. Eckert, and R. Goldstein. Film cooling with large density differences between the mainstream and the secondary fluid measured by the heat-mass transfer analogy. *ASME Journal of Heat Transfer*, 99, 1977. 31, 32

[56] Li Y., Zhang Y., Su X., and Yuan X. Experimental and numerical investigations of shaped hole film cooling with the influence of endwall cross flow. *International Journal of Heat and Mass Transfer*, 120, 2018. x, 32

[57] S. Baldauf, M. Scheurlen, A. Schulz, and S. Wittig. Heat flux reduction from film cooling and correlation of heat transfer coefficients from thermographic measurements at enginelike conditions. *ASME J. Turbomach.*, 124:699–709, 2002. x, 31, 32, 33

[58] K.A. Thole, A.K. Sinha, D.G. Bogard, and M.E. Crawford. Mean temperature measurements of jets with a cross flow for gas turbine film cooling application. *Rotating Machinery Transport Phenomena*, 1992. x, 32, 33

[59] D.P. Narzary, K.C. Liu, A.P. Rallabandi, and J.C. Han. Influence of coolant density on turbine blade film-cooling using pressure sensitive paint technique. *Journal of Turbomachinery*, 134(3), 2010. doi: 10.1115/1.4003025. x, 32, 34

[60] R.E. Mayle, F.C Kopper, M.F. Blair, and D.A. Bailey. Effect of streamline curvature on film cooling. *ASME Journal of Eng for Power*, 99, 1977. 32

[61] S. Ito, R.J. Goldstein, and E.R.G. Eckert. Film cooling of a gas turbine blade. *ASME Journal of Engineering for Power*, 100:476–481, 1978. 32

[62] R.G. Boyle and A.A. Ameri. A correlation approach to predicting film cooled turbine vane heat transfer. *Proceedings of ASME Turbo Expo, (GT2010-23597)*, 2010. 32

[63] J. Andreopoulos. On the structure of jets in a cross-flow. *J. Fluid Mechanics*, 157, 1985. 34

[64] D.K. Walter and J.H. Leylek. A detailed analysis of film-cooling physics: part I - streamwise injection with cylindrical holes. *J. Turbomach.*, 122, 2000. 34

[65] T.F. Fric and A. Roshko. Vortical structure in the wake of a transverse jet. *Journal of Fluid Mechanics*, 279:1–47, 1994. x, 35

[66] R.G. Stabe, W.J. Whitney, and T.P. Moffit. Performance of a high-work low aspect ratio turbine tested with a realistic inlet radial temperature profile. *NASA Technical Memorandum Report*, AIAA Paper No. 84-1161, 1984. x, 35, 36

[67] T.L. Butler, O.P. Sharma, H.D. Joslyn, and R.P. Dring. Redistribution of inlet temperature distortion in an axial flow turbine stage. *J. Propul. Power*, 5(1): 64–71, 1989. x, 36

[68] T. Shang, G.R. Guenette, A.H. Epstein, and A.P. Saxer. The influence of an inlet temperature distortion on rotor heat transfer in a transonic turbine. *AIAA*, 95, 1995. x, 37

[69] W.P. Jones and B.E. Launder. The prediction of laminarization with turbulence. *Int. J. Heat Mass Transfer*, 15, 1972. 37, 75

[70] M.D. Barringer, K.A. Thole, and M.D. Polanka. Experimental evaluation of an inlet profile generator for high pressure turbine tests. *Proceedings of ASME TURBOEXPO 2006: Power for Land, Sea, and Air*, (GT-2006-90401), 2006. x, 37, 38

[71] S. Jacobi, C. Mazzoni, B. Rosic, and K. Chana. Investigation of unsteady flow phenomena in first vane caused by combustor flow with swirl. *Journal of Turbomachinery*, 139, 2017. x, 38, 39

[72] I. Qureshi and T. Povey. A combustor-representative swirl simulator for a transonic turbine research facility. *Proceedings of the Institution of Mechanical Engineers: Journal of Aerospace Engineering*, 2011. 39

[73] A. Krichbaum, H. Werschnik, M. Wilhelm, H.PH.P. Schiffer, and K. Lehmann. A large scale turbine test rig for the investigation of high pressure turbine aerodynamics and heat transfer with variable inflow conditions. *ASME Conference Proceedings*, (GT2015-43261), 2015. 40

[74] G. Schmid, A. Krichbaum, H. Werschnik, and H.P. Schiffer. The impact of realistic inlet swirl in a 1-1/2 stage axial turbine. *ASME Conference Proceedings*, (GT2014-26716), 2014. x, 40, 41

[75] C. Koupper, G. Caciolli, L. Gicquel, F. Duchaine, G. Bonneau, L. Tarchi, and B. Facchini. Development of an engine representative combustor simulator dedicated to hot streak generation. *ASME J. Turbomach.*, 136(11):111007–111007, 2014. ISSN 0889-504X. 41, 45, 53

[76] G. Dufour, N. Gourdain, F. Duchaine, O. Vermorel, L.Y.M Gicquel, J.F. Boussuge, and T. Poinsot. Numerical investigations in turbomachinery: A state of the art. *Notes prepared for the von Karman Institute for Fluid Dynamics*, 2009. 42

[77] X. Wu, S. Kim, J. Alonso, H. Pitsch, and J. Schluter. Coupled RANS-LES computation of a compressor and combustor in a gas turbine engine. $40^{th} AIAA - ASME - SAE - ASEE Joint Propulsion Conf. and Exh.$, 2004. 43

[78] X. Kim, S. Shankaran, S. Alonso, J. Pitsch, H. Schluter, and J. Wu. A framework for coupling Reynolds-averaged with large-eddy simulations for gas turbine applications. *Journal of Fluids Engineering*, 127(4):806–815, 2005. x, 43

[79] E.V. Klapdor. Simulation of combustor - turbine interac- tion in a jet engine. *Darmstadt University, PhD Thesis*, 2011. x, 43, 44

[80] E.V. Klapdor, S. Pyliouras, R.L.G.M. Eggels, and J. Janicka. Towards investigation of combustor turbine interaction in an integrated simulation. *Proc. ASME Turbo Expo*, (GT2010-22933), 2010. 43

[81] E. Collado-Morata. Impact of the unsteady aerothermal environment on the turbine blades temperature. *PhD thesis, Institut National Polytechnique de Toulouse*, 2012. x, 44, 45

[82] S. Vagnoli. Assessment of advanced numerical methods for the aero-thermal investigation of combustor-turbine interactions. *PhD thesis, University of Florence*, 2015. x, 44, 46

[83] M. Insinna. Investigation of the aero-thermal aspects of combustor/turbine interaction in gas turbines. *PhD thesis, University of Florence*, 2016. x, 44, 47

[84] C. Koupper, G. Bonneau, L. Gicquel, and F. Duchaine. Large eddy simulations of the combustor turbine interface: study of the potential and clocking effects. *Proc. ASME Turbo Expo*, (GT2016-56443), 2016. 45

[85] C. Battisti, F. Kost, N. Atkins, W. Playford, M. Orain, G. Caciolli, L. Tarchi, M. Mersinligil, and J. Raffel. Full aerothermal combustor turbine interaction research. *Proceedings of the EASN workshop on Flight Physics and Propulsion*, 2012. 50

[86] A. Andreini, G. Caciolli, B. Facchini, A. Picchi, and F. Turrini. Experimental investigation of the flow field and the heat transfer on a scaled cooled combustor liner with realistic swirling flow generated by a lean-burn injection system. *ASME J. Turbomach.*, 137(3):031012–031012, 2014. 53

[87] B. Wurm, A. Schulz, H.J. Bauer, and M. Gerendas. Impact of swirl flow on the cooling performance of an effusion cooled combustor liner. *ASME J Eng Gas Turb Power*, 134(12):121503–121503, 2012. ISSN 0742-4795. 53

[88] U. Meier, J. Heinze, M. Schroll, C. Hassa, S. Bake, and T. Doerr. Optically accessible multisector combustor: Application and challenges of laser techniques at realistic operating conditions. *ASME Conference Proceedings*, (GT2015-43391), 2015. doi: 10.1115/GT2015-43391. 53

[89] T. Bacci, G. Caciolli, B. Facchini, L. Tarchi, C. Koupper, and J.L. Champion. Flowfield and temperature profiles of a combustor simulator dedicated to hot streaks generation. *Proc. ASME Turbo Expo*, (GT2015-42217), 2015. xi, 53, 54

[90] T.V. Jones. Theory for the use of foreign gas in simulating film cooling. *International Journal of Heat and Fluid Flow*, 20:349–354, 1999. 57, 58

[91] R.J. Goldstein and H.H. Cho. A review of mass transfer measurements using naphthalene sublimation. *Experimental Thermal and Fluid Science,*, 10(4):416–434, 1995. doi: 10.1016/0894-1777(94)00071-F. 57

[92] D. Charbonnier, P. Ott, M. Jonsson, F. Cottier, and T. Kobke. Experimental and numerical study of the thermal performance of a film cooled turbine platform. *ASME Conference Proceedings*, (GT2009(60306)), 2009. 58

[93] J.D. Anderson. *Computational Fluid Dynamics: The Basics with Applications*. McGrawhill Inc, NJ USA, 1995. xi, 65, 66

[94] S.B. Pope. *Turbulent Flows*. Cambridge University Press, 2000. 66, 67, 69, 77, 78, 80

[95] H. Choi and P. Moin. Grid-point requirements for large eddy simulation: Chapman's estimate revisited. *Physics of Fluids*, 2012. 66, 67

[96] U. Piomelli. Large-eddy and direct simulation of turbulent flows. *VKI Lecture Notes*, 1997. 66

[97] D.R. Chapman. Computational aerodynamics development and outlook. *AIAA Journal*, 1979. 67

[98] L.Y.M. Gicquel, G. Staffelbach, and T. Poinsot. Large eddy simulations of gaseous ames in gas turbine combustion chambers. *Progress in Energy and Combustion Science*, 2012. 67

[99] E. Collado-Morata, N. Gourdain, F. Duchaine, and L.Y.M. Gicquel. Effects of free-stream turbulence on high pressure turbine blade heat transfer predicted by structured and unstructured LES. *Heat and Mass Transfer*, 2012. 67

[100] M. Peric and J.H. Ferziger. *Computational Methods for Fluid Dynamics*. Springer Science and Business Media, Dordrecht, the Netherlands, 2012. 67

[101] P. Sagaut, S. Deck, and M. Teraccol. *Multiscale and Multiresolution Approaches in Turbulence, 2nd edn.* Imperial College Press, London UK, 2013. 67

[102] D. von Terzi and J. Frohlich. Hybrid LES-RANS methods for the simulation of turbulent flows. *Prog. Aerosp. Sci*, 2008. 67, 82

[103] K. Hanjalic, M. Hadziabdic, L. Temmerman, and M. Leschziner. *Merging LES and RANS strategies: Zonal or seamless coupling?, Direct and Large Eddy Simulation V*. Kluwer Academic Publishers, 2004. 68, 82

[104] H. Tennekes and J. Lumley. *A first course in turbulence*. The MIT Press, 1972. xi, 70

[105] R. Schiestel. *Modeling and Simulation of Turbulent Flows*. ISTE Ltd and J. Wiley, 2008. 72

[106] K. Hanjalic and B.E. Launder. *Modelling Turbulence in Engineering and the Environment, Second-moment Route to Closure*. Cambridge University Press, 2011. 72

[107] M.A. Leschziner and D. Drikakis. Turbulence modelling and turbulent-flow computation in aeronautics. *Aeronaut. J.*, 2002. 72

[108] D.C. Wilcox. *Turbulence Modeling for CFD, 2nd edition*. DCW Industries, Inc., La Canada, California, 1998. 72, 76

[109] B.E. Launder, G.J. Reece, and W. Rodi. Progress in the development of a Reynolds-stress turbulent closure. *Journal of Fluid Mechanics*, 68, 1975. 74

[110] P.R. Spalart and S.R. Allmaras. A one-equation turbulence model for aerodynamic flows. *Recherche Aerospatiale*, 1, 1994. 75

[111] F.R. Menter. Two equation eddy viscosity turbulence model for engineering applications. *AIAA Journal*, 32:1598–1604, 1994. 76

[112] U. Piomelli. Large eddy simulation: Achievement and challenges. *Progress Aeros. Sci.*, 35, 1999. 77

[113] B. Chaouat and R. Schiestel. A new partially integrated transport model for subgrid-scale stresses and dissipation rate for turbulent developing flows. *Physics of Fluids Journal*, 17, 2005. xi, 77, 83

[114] J. Smagorinsky. General circulation experiments with the primitive equations. *Monthly Weather Review 91*, 1963. 78, 80

[115] M. Germano, U. Piomelli, P. Moin, and W.H. Cabot. A dynamic subgrid-scale eddy viscosity model. *Physics and Fluids*, 3(7), 1991. 78

[116] U. Schumann. Subgrid scale model for finite difference simulations of turbulent flows in plane channels and annuli. *Journal of Computation and Physics*, 18, 1975. 78, 81

[117] J.W. Deardoff. The use of subgrid transport equations in a three-dimensional model of atmospheric turbulence. *Journal of Fluids Engineering*, 95, 1973. 78

[118] U. Piomelli and E. Balaras. Wall-layer models for large-eddy simulations. *Annual Review of Fluid Mechanics*, 34, 2002. 78

[119] Kolmogorov A.N. The local structure of turbulence in incompressible viscous fluid for very large Reynolds numbers. *C. R. Acad. Sci. , USSR*, 1941. 80

[120] D.K. Lilly. The representation of small-scale turbulence in numerical simulation experiments. *Proceedings of the IBM Scientific Computing Symposium on Environmental Sciences, Yorktown Heights, USA*, 1967. 80

[121] A. Yoshizawa and K. Horiuti. statistically derived subgrid scale kinetic model for the large-eddy simulation of turbulent flows. *Journal of Physics Society of Japan*, 54, 1985. 81

[122] D.K. Lilly. A proposed modification of the germano sub-grid closure method. *Physics and Fluids Journal*, 1992. 81

[123] F. Ducros, F. Nicoud, and T. Poinsot. Wall-adapating local eddy-viscosity models for simulations in complex geometries. *ICFD*, 44, 1998. 81

[124] P.R. Spalart, W. Jou, M. Strelets, and S.R. Allmaras. Comments on the feasibility of LES for wings, and on a hybrid RANS/LES approach. *Liu, C., Liu, Z. (eds.) Advances in DNS/LES, Greyden Press, Columbus*, 1997. 82, 83

[125] L. Davidson and M. Billson. Hybrid les-rans using synthesized turbulent fluctuations for forcing in the interface region. *Internnational Journal of Heat Fluid Flow*, 27, 2006. 82

[126] P.R. Spalart. Detached-eddy simulation. *Annual Review of Fluid Mechanics*, 41, 2009. 83

[127] P.R. Spalart, S. Deck, M.L. Shur, K.D. Squires, M.K. Strelets, and A. Travin. A new version of detachededdy simulation, resistant to ambiguous grid densities. *Theoretical Computational Fluid Dynamics*, 20, 2006. 83

[128] C.G. Speziale. Turbulence modeling for time-dependent RANS and VLES: A review. *AIAA Journal*, 36, 1998. 83

[129] R. Schiestel and A. Dejoan. Towards a new partially integrated transport model for coarse grid and unsteady turbulent flow simulations. *Theoretical Computational Fluid Dynamics*, 18, 2005. 83

[130] S.S. Girimaji and K. Abdol-Hamid. Partially averaged navier stokes model for turbulence: Implementation and validation. *AIAA paper n.0502*, 2005. 84

[131] F.R. Menter and Y.A. Egorov. A scale-adaptive simulation model using two-equation models. *AIAA paper n.1095*, 2005. 84, 85, 86

[132] J.C. Rotta. Statistische theorie nichthomogener turbulenz. *Z. Physik*, 129, 1951. 85, 86

[133] P. Aillaud, L.Y.M. Gicquel, and F. Duchaine. Investigation of the concave curvature effect for an impinging jet flow. *Physical Review Fluids*, 2(11):114608, 2017. 90

[134] F.R. Menter. *Best Practice: Scale-Resolving Simulations in ANSYS CFD*. ANSYS Germany GmbH, April 2012. 90

[135] A. Andreini, T. Bacci, M. Insinna, L. Mazzei, and S. Salvadori. Hybrid RANS-LES modeling of the aerothermal field in an annular hot streak generator for the study of combustor–turbine interaction. *ASME J Eng Gas Turb Power*, 139(2): 021508, 2017. xi, xii, 90, 92, 94, 95, 96, 97

[136] S.B. Pope. Ten questions concerning the large-eddy simulation of turbulent flows. *New Journal of Physics*, 6:1–24, 2004. doi: 10.1088/1367-2630/6/1/035. 91

[137] S. Mendez and F. Nicoud. Adiabatic homogeneous model for flow around a multiperforated plate. *AIAA Journal*, 46(10):2623–2633, 2008. 91

[138] A. Andreini, B. Facchini, M. Insinna, L. Mazzei, and S. Salvadori. Hybrid RANS-LES modeling of a hot streak generator oriented to the study of combustor-turbine interaction. *Proc. ASME Turbo Expo*, (GT2015-42402), 2015. xi, 92, 93

[139] S. Cubeda, L. Mazzei, T. Bacci, and A. Andreini. Impact of the predicted combustor outlet conditions on the aerothermal performance of film-cooled HPT vanes. *Journal of Engineering for Gas Turbines and Power*, 141(5), 2018. 96

[140] T. Bacci, T. Lenzi, A. Picchi, L. Mazzei, and B. Facchini. Flow field and hot streak migration through high pressure cooled vanes with representative lean burn combustor outflow. In *Proceedings of ASME Turbo Expo 2018*, number GT2018-76728, 2018. 98

[141] S. Cubeda, L. Mazzei, and A. Andreini. External heat transfer on nozzle guide vanes under highly swirled combustor outlet flow. *Proceedings of 13th ETC*, ETC2019-293, 2019. 112

[142] I. Qureshi, A. Beretta, and T. Povey. Effect of simulated combustor temperature nonuniformity on HP vane and end wall heat transfer: An experimental and computational investigation. *ASME J Eng Gas Turb Power*, 133(3):031901–031901, 2010. ISSN 0742-4795. 114

[143] ANSYS. *ANSYS CFX-Solver Modeling Guide*, release 19.2 edition, 2019. 130, 137